ABSTRACT

Title of Dissertation: SIMULTANEOUS MEASUREMENTS OF THE VELOCITY AND VORTICITY VECTOR FIELDS IN THE TURBULENT NEAR WAKE OF A CIRCULAR CYLINDER

Phúc Ngọc Nguyễn, Doctor of Philosophy, 1993

Dissertation co-directed by: Dr. Barsam Marasli, Assistant Professor
Dr. James M. Wallace, Professor
Department of Mechanical Engineering

Hot-wire measurements of all components of the instantaneous velocity and vorticity vectors in the wake of a circular cylinder are presented. The experiments were performed at $x/d = 20$ and 30, at $Re_d = 2000$, using a miniature 12-sensor probe for the simultaneous velocity-vorticity measurements and a 4-sensor probe for the velocity-only measurements.

A calibration and a data reduction method for multi-sensor hot-wire probes are introduced. The calibration technique is independent of the number of sensors and requires minimal information about probe geometry. The data reduction scheme involves the solution of an overdetermined nonlinear algebraic system of equations in a least-squares sense.

The measurements indicate that the Kármán vortices are accurately resolved. Statistical characteristics of the velocity and vorticity fields in this flow, including moments, probability distributions and one-dimensional spectra components are documented for the first time. Conditional analysis of the measurements at $x/d = 30$ with respect to the passage of the Kármán vortices are presented. The vortex center and the saddle regions are identified and characterized. The instanteaneous velocity and vorticity signals are decomposed into mean, coherent and incoherent parts

using the triple decomposition technique. A significant percentage of the incoherent fluctuations are observed to be phase-locked to the Kármán vortices. The enstropy balances are computed for three decomposed parts. The generation of incoherent enstrophy due to incoherent vortex stretching is detected to be the most dominant term and is balanced by the viscous dissipation.

SIMULTANEOUS MEASUREMENTS OF THE VELOCITY AND VORTICITY VECTOR FIELDS IN THE TURBULENT NEAR WAKE OF A CIRCULAR CYLINDER

by

Phúc Ngọc Nguyễn

Dissertation submitted to the faculty of the Graduate School
of The University of Maryland in partial fulfillment
of the requirements for the degree of
Doctor of Philosophy
1993

Advisory Committee:

Assistant Professor Barsam Marasli, Co-Chairman
Professor James M. Wallace, Co-Chairman
Associate Professor James H. Duncan
Associate Professor Ugo Piomelli
Associate Professor Richard V. Calabrese

ACKNOWLEDGEMENTS

I want to thank my advisors, Drs. Barsam Marasli and Jim Wallace, for dedicated guidance and support, and for working closely with me to complete this ambitious project. Their commitment to turbulence research is quite inspirational. I also would like to thank other members of the committee, Drs. Ugo Piomelli, Jim Duncan, and Richard Calabrese for fruitful suggestions on several occasions. I am very grateful for all the help from my fellow students and friends, Dr. Lawrence Ong, Dr. Seong-Ryong Park, and Mr. John Wright. Their willing support for the experiments has been very helpful, and sometimes crucial. Lawrence and Seong-Ryong have even showed me how to be a graduate student sometimes.

I would like to thank my sponsors, Drs. Frank Peterson and Bruce Douglas at David Taylor Model Basin, and Dr. Pat Purtell at the Office of Naval Research. Their support during these changing times is much appreciated. I also want to thank my previous mentors, Dr. Demetri Telionis at VPI & SU, and Dr. Om Sharma at Pratt & Whitney. They have helped shape my interest in fluid mechanics.

I am grateful to my family for understanding. Most deserving are my older sisters, who have carried some of my responsibility. My in-laws have also been very helpful, especially in lending me a computer for the thesis work. Finally, I want to thank my wife, Ti, for sharing all the good and bad times during the course of the PhD work. Without her, this project might not get done. She has even listened a few times to my monologues about some of the "neat things" in turbulence.

TABLE OF CONTENTS

LIST OF TABLES

LIST OF FIGURES

NOMENCLATURE

A_j	calibration coefficients for each sensor
c_i	sensor y-coordinate relative to the center of the sensing area
d_i	sensor z-coordinate relative to the center of the sensing area
d	diameter of cylinder
e	sensor voltage reading
f_i	error function for each sensor in Eq. (3.11)
F	sum of the squares of errors for each sensor in Eq. (3.12)
f_s	vortex shedding frequency
$\mathbf{G}$	gradient vector defined in Eq. (3.19)
$\mathcal{H}$	Hessian matrix defined in Eq. (3.20)
k	turbulent kinetic energy
L_o	wake half-width
$\mathcal{L}$	locking parameter defined in Eq. (6.20)
N_c	number of calibration points
N_p	number of periods in total sampling interval
N_P	number of phases in a period
N_s	number of sensors
$P(u)$	probability distribution function for variable u
$P(u,v)$	joint probability distribution function for variables u and v
$\mathcal{P}(e)$	polynomial curve-fit of the square of the sensor cooling velocity
Q	centerline velocity at exit of calibration jet
r_{1-2}	magnitude of phase locking defined in Eq. (6.21)
Re	Reynolds number
s_{ij}	symmetric part of the stress tensor

t	time
U	instantaneous streamwise velocity
u	total fluctuating streamwise velocity
u_o	centerline velocity deficit
u_i	velocity vector
U_∞	freestream velocity
U_B	binormal cooling velocity
U_{eff}^2	effective cooling velocity defined in Eq. (3.1)
U_N	normal cooling velocity
U_T	tangential cooling velocity
v	total fluctuating transverse velocity
w	total fluctuating spanwise velocity
x	streamwise direction
y	transverse, or lateral direction
z	spanwise direction

Greek symbols

α, β	empirical parameters in Eq. (4.1) for mean streamwise velocity
ϵ	dissipation rate
ε	enstrophy
η	y position normalized by wake half-width
γ	pitch angle
ϕ_u	spectrum of variable u
θ	momentum thickness
ψ	yaw angle
Ω_x	instantaneous streamwise vorticity
ω_x	total fluctuating streamwise vorticity

ω_y total fluctuating transverse vorticity

ω_z total fluctuating spanwise vorticity

Special notations

u^* rms value of the total fluctuating u

u' incoherent part of an instantaneous turbulent variable U

$<u>$ coherent part of an instantaneous turbulent variable U

$\overline{U}$ time average of U

$<u>$ phase average of u

1 Introduction

Wake flows can be found behind vehicles moving in air or water, or, in general, behind bodies moving in a fluid medium. Except at very low Reynolds number, wake flows in most practical applications are turbulent. Experimental measurements have been useful in a great number of applications. Wake measurements of velocity and static pressure have been used to determine the drag of a body moving in a fluid [27]. In the vibration control of lifting surfaces, one needs to measure the turbulent wake characteristics such as wake thickness, magnitude of the turbulent kinetic energy and its spatial and spectral distributions. Fluctuating velocity measurements by Huang *et al.* [24] in airfoil wake flow, and pressure measurements by Gershfeld *et al.* [20] indicated that minor geometrical changes of the trailing edge results in measurable and distinctly different characteristics of the turbulent wake and the trailing edge pressure spectra. Therefore, understanding the effects of changes in these parameters and their interelation are necessary to predict the flow past lifting surfaces and to design them for minimum vibration.

Most prediction procedures involve some empiricism to model the Reynolds stresses in the time-averaged momentum equations. One of the goals of this dissertation is to provide high quality measurements of the Reynolds stresses and the physical generation/transport mechanisms for these stresses in order to improve turbulence models. Schlichting [55] used a one-dimensional integral method to calculate the mean streamwise velocity profile in the region where the streamwise pressure gradient is negligible, and obtained good agreement with measurements. Huang *et al.* [24] calculated the wake of lifting surfaces using a modified boundary-layer method. This method was able to calculate the entire wake, but the predicted center of the wake needed to be shifted to agree with the measurements. Nguyen & Gorski [44] calcu-

lated the wake flows of lifting surfaces using the Reynolds-averaged Navier-Stokes equations. This method, in general, predicted accurately the mean streamwise velocity and the Reynolds stress distributions, but it did poorly in the flow region immediately behind the trailing edge due to an inadequate turbulence model. Miner *et al.* [40] attributed this to the poor near-wall modelling based on comparison with a direct simulation of channel flow. To date, no large-eddy simulation or direct numerical simulation has been attempted for a turbulent plane wake. Compared to the direct simulation by Kim & Moin [31] on the turbulent channel flow, the wake simulations would involve growing boundaries and would be very expensive in computational resources. Therefore, experiments have been the only means so far used to investigate the fundamental physics of wake flows.

1.1 Characteristics of the Velocity Field

One of the early fundamental questions about wake flows was in what Reynolds number range does the flow become turbulent. In 1954, Roshko [53] found that for Reynolds number based on cylinder diameter, Re_d, greater than 300, the wake is fully turbulent after 40-50 diameters downstream of the circular cylinder. For the region 0-40 diameters, the discrete energy of the vortex shedding gradually feeds the continuous spectrum. The nondimensional vortex shedding frequency, called the Strouhal number $S \equiv f_s d/U_\infty$ where f_s is the shedding frequency, d the cylinder diameter and U_∞ the freestream velocity, increases with the Reynolds number, reaching an asymptotic value of approximately 0.21 above $Re_d \approx 700$. For Re_d between 150 and 300, he characterized the flow as in "transition" in which turbulent velocity fluctuations exists along with periodic formation of the Kármán vortices. He also suggested that these turbulent velocity fluctuations are initiated by the "laminar-turbulent transition in the free layers" developing at the separation points on the cylinder. Williamson [68] found that there are two stages in the transition to the

three-dimensional structures of the near wake. Each stage corresponds to a discontinuity in the Strouhal-Reynolds number relationship, and both stages have distinct characteristics. The first discontinuity, at $Re_d \approx 180$, is associated with the inception of vortex loops and is hysteretic. These vortex loops are developed from the Kármán vortices, and become stretched afterward to evolve into a pair of counter-rotating quasi-streamwise vortices. The second discontinuity, at $Re_d \approx 250$, corresponds with a change to a finer-scale streamwise vortex structure, and is not hysteretic.

In wake experiments, one of the first concerns is to ensure the two-dimensionality of the mean flow. Eisenlohr & Eckelmann [16] investigated end effects on cylinder wake flows. They used smoke-wire flow visualization to detect oblique vortex shedding in the wake. At $Re_d = 130$, i.e. in the transition range, with an aspect ratio (AR) of 60, flow visualization showed that vortex shedding can be inclined with respect to the cylinder up to 30°. When end-plates and end-cylinders were attached to the circular cylinder, the vortex shedding became parallel to the body. For AR > 100 and higher Reynolds numbers, they anticipated that, based on the data of Roshko [53], vortex shedding would be parallel to the body without the need of end-plates and end-cylinders.

Early research concentrated on characterizing the mean variation in the streamwise and transverse directions in wake flows. Andreopoulos & Bradshaw [2], using a temperature-conditional sampling technique, observed 3 layers in the transverse direction of the near-wake region of a flat plate: a turbulent inner-layer, and 2 intermittent outer layers. They noted that the wake interaction involves significant fine-scale mixing shear layers, and recommended using shear stress transport to model the outer layer, and eddy-viscosity to model the inner layer. Based on the measurements, they suggested an empirical relationship which shows logarithmic growth of the wake centerline velocity with respect to the streamwise direction.

Pot [49], Alber [1] and Ramaprian *et al.* [51] studied the streamwise variation of

the mean streamwise velocity of a turbulent wake. Alber presented a semi-empirical relationship in which the wake centerline velocity is a logarithmic function of the streamwise direction. Ramaprian *et al.* measured the streamwise and transverse velocity components of a tapered flat plate wake, and suggested that this turbulent wake has 3 regions in the streamwise direction. In the near-wake ($x/\theta < 25$, where θ is the momentum thickness), mixing of the inner shear-layer occurs. In the middle-wake ($25 < x/\theta < 350$), mixing of the outer layer occurs, and self-similarity of the mean velocity exists. This means that the mean velocity profiles are the same at every streamwise station when normalized by the local wake half-width and velocity-deficit. In the far wake ($x > 350\,\theta$), all large scale mixing is completed and the wake reaches an "asymptotic" state where self-preservation exists. According to Ramaprian *et al.* , this state means that "the turbulent structure becomes independent of the initial conditions", and a far-wake model can be used to predict the flow. Schlichting [55] showed that in the far wake region where the pressure gradient is negligible, the momentum equation simplifies significantly. When a mixing length turbulence model was used for the Reynolds shear stress $\overline{uv}$, the momentum balance yielded a mean streamwise velocity profile that is self-similar. These predictions agreed well with the data for x/d=80 to 208.

The streamwise velocity at the wake centerline also exhibits a shape equivalent to the universal velocity profile for the sublayer and the "log" regions in the turbulent boundary-layer of a flat plate. The data of Pot [49] and Ramaprian *et al.* [51] showed the logarithmic growth of the centerline velocity along the streamwise direction where Alber's formula matched the data quite well. Haidari & Smith [22] used hot-film anemometry in water to study the near-wake of a tapered flat plate. They found that the centerline velocity varied linearly with x^+ for $0 < x^+ < 100$, and varied as $\log x^+$ for $x^+ > 270$ (x^+ is the streamwise distance from the trailing-edge normalized with the wall shear stress at a certain distance upstream of the trailing-edge). Here,

one momentum thickness θ is approximately 90 x^+. These patterns are similar to those in the viscous sublayer, and in the so-called wake region of a turbulent boundary layer, respectively. They suggested a linear relationship between the x^+ for the wake streamwise position, and the y^+ for the boundary-layer normal position. With this relationship, they showed that the velocity at the wake centerline and the velocity of a boundary layer collapse to the same empirical relationships, for both the very-near wake and the "log" region.

Narasimha & Prabhu [42] investigated the relaxation process necessary to reach an equilibrium state of turbulent wakes and suggested universal relationships for the wake half-width L_o and the velocity deficit u_o. The assumption for these relationships is that the equilibrium wakes are independent of initial conditions originated from the wake generators. Wygnanski *et al.* [69], however, found that the initial conditions dictate how the wakes approach the self-preserving state. They studied the wakes behind different two-dimensional wake generators such as circular cylinders, flat plates, airfoils, and screens. They systematically measured the mean velocity profiles and the Reynolds stresses at different streamwise stations. Their results indicated that u_o, L_o, and the Reynolds stresses, $\overline{u^2}$ and $\overline{uv}$, depend on the wake generator shapes, but the mean streamwise velocity does not. They also found that the nondimensional quantities $(U_\infty/u_o)^2$ and $(L_o/\theta)^2$ varied linearly with respect to the streamwise direction as predicted by the self-preservation arguments, but the slopes and intercepts of these lines were different for different wake generators.

Yamada *et al.* [70] made measurements at various streamwise stations for a circular cylinder, from x/d=30 to 475. The mean streamwise velocity, and the various Reynolds stress components were found to approach the self-preserved data curves of Townsend [60] as the downstream distance was increased. At the x/d=30 station, the rms of the transverse velocity component was highest, and the streamwise and spanwise components were approximately the same. In the far-wake, the stream-

wise component was highest, and the other two components were approximately the same. Since Yamada *et al.* used X-wires for their measurements the three velocity components were not measured simultaneously.

Fabris [17] used a 4-sensor probe to measure simultaneously the three velocity components and the temperature in a circular cylinder wake at x/d=200 and 400. The skewness factor was negative across the wake for the streamwise velocity, and anti-symmetric for the transverse velocity. From the positive sign of the transverse velocity component skewness, it can be deduced that the author was reporting data from the upper wake. The spanwise component skewness was reported to be very close to zero, though it was not shown. The flatness factor was approximately 2.9 for about 4 diameters from the wake centerline, but was quite high beyond this region. The intermittency factor was also shown to be self-similar.

To achieve a more complete description of turbulent wakes, researchers have used multi-point measurements which reveal the dynamics of the turbulent structures. Browne *et al.* [9] used a temperature-conditional sampling technique to detect large-scale structures in the far wake region of a circular cylinder. They decomposed the fluctuating velocity components into a "random" part, and a "coherent" part which corresponds to the detected events. At $x/d = 420$, the contribution from the random motion is much larger than that of the coherent motion.

Considerable physics of turbulent wakes have been discovered from velocity measurement using mostly single-sensor or X-array probes. However, all three components of the velocity or vorticity vectors have never been measured in the near-wake to study the three-dimensional flow structures. The following section will describe the development of multi-component velocity and vorticity probes. The use of these powerful techniques will undoubtedly reveal some of the missing pieces of the turbulence puzzle.

1.2 Multi-Component Velocity and Vorticity Measurement Techniques

Single-sensor and X-wire probes have been widely used in turbulence research. In the X-array, or V-array hot-wire measurement technique (Bradshaw [8]), two simultaneous algebraic equations are obtained from the two sensor readings which relate the two unknown velocity components to the cooling velocity of each sensor. These types of probes can either be used to measure the u and v components or the u and w components. The measuring volume is assumed to experience uniform flow. Commercial X-wire probes often have about 1 mm spacing between the two sensors. This spacing can be too large to properly assume uniform flow in the measuring volume for highly turbulent flows. Reducing the wire spacing can increase the measurement accuracy, but the effect of the third component still cannot be accounted for by X-wire probes.

Only in the last decade have three-component velocity measurements become a common tool in turbulence research. As mentioned above, Fabris [17] used a 4-sensor probe to measure velocity in the far-wake region of a cylinder, with one sensor used for temperature measurement. Four coupled nonlinear equations were solved to obtain the flow temperature and the 3 velocity components. Lekakis *et al.* [36] made measurements in a turbulent pipe flow with a 3-sensor velocity probe which has a third sensor orthogonal to an X-wire probe. They developed a probe calibration method and a fast data reduction scheme that can also account for small non-orthogonalities in the geometry. They pointed out that a unique solution can only be achieved when the flow angle is within the cone of acceptance of the probe. This uniqueness problem is due to the nonlinearity of the cooling equations which can have multiple solutions. Vukoslavčević & Wallace [62] developed a 4-sensor Kovasznay-type probe, to be discussed below, that was able to measure all three velocity components in a turbulent boundary-layer. The probe had the configuration

of two orthogonal X-probes. Samet & Einav [54] developed a 4-sensor probe to measure 3 components of velocity in a turbulent jet flow. The probe consisted of a pair of orthogonal V-probes with the inner prongs shorter than the outer prongs. Least-squares surfaces were fitted to the calibration data, and the solutions were found as intersections of the surfaces. Two values of the streamwise velocity were calculated by this method, and they were averaged to yield the final value. They obtained either unique solutions or non-convergence; the later occured when the angles of attack of the velocity vector to the probe axis were outside the range of calibration. Döbbeling *et al.* [14] also used a 4-sensor probe for measurements in a turbulent jet flow. The probe was configured as a pair of orthogonal V-probes with the inner prongs longer than the outer prongs. They showed that using a 4-sensor probe to measure 3 components of velocity can yield a unique set of physical solutions, whereas a 3-sensor probe yields multiple sets of physical solutions.

Measurement of vorticity in turbulent flows has been rare due to the difficulty in the estimation of velocity gradients. The following discussion will briefly describe the development of vorticity measurement techniques (readers will find the definition of the coordinate axes in Fig. 1.1 useful). Here, the focus will be on methods that estimate vorticity components from velocity gradient measurements. A more comprehensive review of different techniques is given in Wallace [64] and Foss & Wallace [19].

In 1950, Kovasznay [33] developed a 4-sensor probe to measure the three velocity components and the streamwise component of the vorticity vector. This probe had only four supporting prongs so that all sensors are electrically connected together through the prongs. The probe was thought to be uniquely sensitive only to the streamwise vorticity component, but Kistler [32] found that second-order cooling from the cross-stream velocity components can strongly affect the measured streamwise vorticity. Kastrinakis *et al.* [29] confirmed this finding with extensive analytical

and experimental studies, and proposed a Kovasznay-type vorticity probe without common prongs. From this suggestion, Vukoslavčević & Wallace [62] developed a 4-sensor probe with eight prongs. Four equations were derived to solve for the three velocity components and the streamwise vorticity component. They showed that gradients of the streamwise velocity, which are neglected in these equations, can be very high for near-wall boundary-layer flows thereby causing significant errors in the measured cross-stream velocity components and, in turn, the streamwise vorticity.

Foss [18] developed a four-sensor probe to measure the spanwise vorticity component ω_z. The probe consisted of two parallel sensors and two X-sensors. The parallel sensors measured $\partial U/\partial y$, and the X-sensors measured U and V. Taylor's hypothesis was used to estimate $\partial V/\partial x$. The effect of neglecting the spanwise velocity component W was corrected. Lang & Dimotakis [34] used four pairs of laser beams to measure the spanwise vorticity component in shear layers. The streamwise velocity gradient was measured directly so the use of Taylor's hypothesis was not necessary. Hussain & Hayakawa [26] used an array of X-probes to make multi-point measurements of ω_z in the turbulent wake of a circular cylinder. The X-probes were separated in the transverse direction. Each X-probe measured the U and V velocity components, and $\partial U/\partial y$ was estimated from two adjacent pairs of X-probes. Taylor's hypothesis was used for $\partial V/\partial x$. Hayakawa & Hussain [23] also measured the transverse vorticity component ω_y using a similar technique. With this arrangement, ω_y and ω_z were measured at different times during their experiments.

Eckelmann *et al.* [15] developed a five-sensor probe to measure simultaneously ω_y and ω_z. A unique arrangement of a single sensor, a V-probe and an X-probe was used to get $\partial U/\partial z$ and $\partial U/\partial y$. Recently, Kim & Fiedler [30] developed a six-sensor probe to measure ω_x and ω_z. Taylor's hypothesis was used to estimate the streamwise gradients with both of these probes.

There have been some efforts to measure all three components of vorticity by using

different combinations of X-probes. Antonia *et al.* [3] measured at different times the spanwise and normal components using two pairs of X-probes separated in the appropriate lateral directions. The two velocity gradients of the streamwise vorticity component were not measured simultaneously. Theoretically, it is possible to measure simultaneously all three components of the vorticity vector with four X-probes. Two probes in the $x-z$ planes separated in the y direction can measure the gradients $\partial U/\partial y$, and $\partial W/\partial y$. Two additional probes in the $x-y$ planes separated in the z direction can measure the gradients $\partial U/\partial z$, and $\partial V/\partial z$. The streamwise gradients $\partial V/\partial x$, and $\partial W/\partial x$ can be obtained from the Taylor's hypothesis. However, putting all these X-probes in a small measuring volume is quite a problem. Bisset *et al.* [7] arranged seven X-probes, with total sensing area of approximately 9 mm by 14 mm, to measure simultaneously the large-scale parts of the vorticity components. They used the probe to study the vortical structures in the far-wake of a circular cylinder.

Recent breakthroughs have allowed reasonably accurate vorticity measurement without having to use a great number of X-probes. Vukoslavčević *et al.* [63] developed a miniature 9-sensor probe to measure simultaneously the velocity and vorticity vectors. The probe had three arrays with the sensors arranged in a "T" shape in each array. Each array had a common prong to minimize the sensing area, which fits inside a circle with a diameter of 2.5 mm. Nine coupled equations were derived for the nine sensors. These equations for the cooling of each individual sensor were Taylor series expansions, to first order, around the probe centroid, thus incorporating the cross-stream velocity gradients. An iterative technique was used to solve for the three components of velocity and the six velocity gradient components in the spanwise and transverse directions. The streamwise velocity gradients were estimated using Taylor's hypothesis. Thus they were able to measure simultaneously the velocity and vorticity vectors. Balint *et al.* [5] used this probe in a turbulent boundary-layer, and were able to resolve all but the smallest turbulent scales at Re_θ=2685.

In this dissertation, an improved version of the miniature nine-sensor vorticity probe, constructed by P. Vukoslavčević (private communication), was used to study the vortical structures in the near wake of a circular cylinder. This new probe has twelve sensors to help obtain the unique solutions to the cooling equations. More details are provided in Sections 2.2 and 3.3.

1.3 Characteristics of the Vorticity Field

For the turbulent wake of a circular cylinder, there were only a few experiments which documented the basic statistics of the fluctuating vorticity such as moments, spectra and probability distributions. Antonia *et al.* [3] measured separately the vorticity components at $x/d = 420$ using a pair of X-probes. The rms of ω_x was the largest maximum value, and the other two components were about the same. The skewness factors for ω_x and ω_y were quite high, which could indicate an accuracy problem since the skewness factors of these vorticity components should be near zero due to the symmetry of the mean flow. Reasonable agreement was seen when the rms values and the probability distributions were compared to calculations based on local isotropy.

Bisset *et al.* [7] simultaneously measured the large-scale approximations of the vorticity vectors in the far-wake of a circular cylinder, using a very large probe made from seven X-probes as described earlier. The rms values of ω_x and ω_y were about the same throughout the wake. The ω_z rms component was higher than the other two by approximately 20% in the region $\pm L_o/2$ around the wake centerline. With a cold wire in the array probe, they measured temperature and used a temperature-conditional sampling technique to detect the turbulent structures at $x/d = 420$.

The existing literature yields a fairly consistent picture of the vortical structures for the turbulent plane wake. However, a complete description of the dynamics of the turbulent structures has not yet emerged. This would require time-varying infor-

mation across the entire spatial domain of the turbulent wake for a wide Reynolds number range. The vorticity measurements in this project will shed some light on this very complicated problem as vorticity is the fundamental variable in the dynamics of the "coherent" structures. This view is shared by many investigators such as Willmarth [67], and Hussain & Hayakawa [26].

Grant [21] made two-point velocity measurements in the turbulent far-wake to form correlation coefficients. He proposed a model of the vortical structure which is consistent with the spatial distribution of these correlation coefficients. These structures consisted of counter-rotating vortex pairs with their axes separated in the spanwise direction and approximately aligned in the direction of the mean shear (see Fig. 1.2). The existence of these structures, sometimes called the "double-roller" vortices, were also proposed by Mumford [41], and Payne & Lumley [47]. The other type of structure observed in the far-wake is the spanwise vortex. This vortex is part of the "secondary vortex street", which has scale much larger than the original Kármán vortex street according to Cimbala *et al.* [12]. The spanwise vortices and their dynamics have also been studied by Mumford [41], Townsend [61], and Browne *et al.* [9]. The "double-roller" structures consist of mainly the ω_x and ω_y components, and the spanwise structures consist of mainly the ω_z component of the vorticity vector.

To study the secondary spanwise vortices, Browne *et al.* [9] measured in the far-wake of a slightly heated circular cylinder with an assembly of X-wires and temperature sensors as mentioned above. Using relatively large temperature change between consecutive samples as a detection criterion of the flow structures, they constructed a velocity vector plot (see Fig. 1.3) in the plane of the mean shear ($x-y$ plane). The vortex centers and the saddles were clearly seen on both sides of the wake. The authors called the region that connects one spanwise vortex to the next the "converging separatrix" where fluid converges toward the saddle. At about 90°

from the "converging separatrix" is the "diverging separatrix" where fluid diverges away from the saddle toward the freestream or toward the wake centerline. These diverging separatrices are approximately aligned with the mean shear, a characteristic which the double-roller structures also have. Therefore, it is possible that the double-roller structures are related to the diverging separatrix flow regions. With the ω_x and ω_y vorticity data, it is possible to further characterize these structures as will be discussed later.

In the near-wake of a circular cylinder, Hussain & Hayakawa [26] measured the large-scale spanwise vorticity by a rake of X-probes positioned in the plane of the mean shear. They specified the trigger signal as the passing of a large amplitude spanwise vortex. For the measurement range of x/d=10 to 40, they found that the spanwise vortex center was less than one wake half-width from the centerline. From analysis of other data and their own, Hussain & Hayakawa proposed a mechanism for the dynamics of the turbulent plane wake (see Fig. 1.4). In this mechanism, the wake can be viewed as "a superposition of two coherent vorticity layers consisting of large-scale, nominally spanwise vortex rolls of opposite circulation". Each "layer" would consist of vortical structures with the same sense of rotation separated by saddles. The diverging separatrices, or "braids", oriented in the direction of the mean shear connect the top of one structure to the bottom of another structure in the same layer. Their proposed mechanism lacked the ω_x and ω_y data. Later, Hayakawa & Hussain [23] measured both the large-scale ω_y and ω_z components, though not simultaneously. From the ω_y contours, they claimed to see the "apparent signatures" of the "braids". From the simultaneous measurements of all three vorticity components in this dissertation, it is possible to relate the braids to the double-roller vortices described earlier.

Cantwell & Coles [10] investigated the entrainment and transport processes in the turbulent near wake of a circular cylinder. They measured in the region within 8

diameters downstream of the cylinder using two X-wire probes mounted on a pair of whirling arms. This arrangement increases the velocity along the sensor axis which decreases the angles of attack of the velocity vector on the sensor, thus making very-near wake measurement possible. They used a pressure reading on the cylinder surface to detect the vortex shedding and deduced a pattern of moving vortex centers and saddles by phase-averaging the measured streamwise and transverse velocity components. They found that a substantial part of the turbulence production is concentrated near the saddles and suggested that the mechanism of turbulence production is "probably vortex stretching at intermediate scales". Their data showed that the normal Reynolds stresses due to the random motion have maxima near each vortex center, and the magnitude of the random Reynolds shear stress is maximum near the saddle between the vortices.

Meiburg & Lasheras [39] investigated experimentally and numerically the laminar wake of a flat plate subjected to periodic spanwise pertubations. Computational results from the inviscid vortex technique agreed qualitatively with the laser-induced flow visualization. They showed that the redistribution, reorientation, and stretching of vorticity lead to the formation of counter-rotating pairs of streamwise vortices, which superimpose on the spanwise Kármán vortices. The streamwise vortices were shown to be located in the braids connecting the spanwise vortices with opposite rotation on the two sides of the wake. This picture is slightly different from those of Browne *et al.* [9] and Hussain & Hayakawa [26] where the braids connect structures on the same side of the wake. But, in the x–y plane, the filaments of these streamwise vortices calculated by Meiburg & Lasheras [39] were approximately aligned with the mean shear (shown in Fig. 1.5), which agreed with the model of Grant [21]. These uncertainties underscore the need to obtain simultaneous measurements of the three vorticity components together with the velocity components.

1.4 Objectives and Approach

The above literature review points out that simultaneous three-component velocity measurement is lacking for wake flows. Some data existed in the far-wake, but these are either non-simultaneous, or are very coarse in spatial resolution. Simultaneous three-component vorticity data for near-wake flow are non-existent. Therefore, the main objectives of this work is to measure simultaneously and with reasonably good spatial resolution the three components of the velocity and vorticity vectors in the cylinder wake, and to analyze these measured data in order to determine:

1. Basic properties such as the moments, spectra and probability distribution functions of the velocity and vorticity vectors.

2. Locations of the saddle and the vortex center and the wake flow characteristics at these locations.

3. Mechanisms of the different processes of vorticity transport in the wake.

The following steps were taken to achieve the above objectives:

1. Simultaneous measurements of velocity and vorticity in the turbulent near-wake of a circular cylinder. The experimental program had three phases. The first phase, which involved preliminary experiments, was mainly for identifying problems with the experimental setup and for optimizing the experimental conditions. The second phase was for velocity component measurement, and the third phase was for simultaneous velocity and vorticity measurement. These experiments are described in Chapter 2.

2. Development of the data calibration and reduction software for measuring the velocity and vorticity vector fields using multi-sensor hot-wire probes. This is addressed in Chapter 3.

3. Characterization of the velocity and vorticity fields of the turbulent plane wake with various statistical properties including moments up to the fourth order, probability distributions, and spectra. These are discussed in Chapters 4 & 5.

4. Investigation of the vortical structure dynamics in the turbulent plane wake with a joint probability distribution analysis of the velocity components, the vorticity components, and the generation terms in the vorticity transport equations. This is discussed at the ends of Chapters 4 & 5.

5. Characterization of the vortical structures by conditional analyses of the Reynolds stresses, the turbulent kinetic energy, the enstrophy and its components, and the energy dissipation rate relative to the passage of the Kármán vortex. This is discussed in Chapter 6.

6. Computation of the mean and fluctuating enstrophy balances by decomposing the instantaneous signal into its components. These balances give quantitative description of the different vorticity transport processes. This is discussed in Chapter 7.

2 Equipment and Experimental Program

2.1 Wind Tunnel and Calibration Jet

The experiments were performed at the low speed wind tunnel of the Turbulence Research Laboratory at the University of Maryland. This tunnel is an open-return type (see Fig. 2.1) with a total length of 15.2 m. A centrifugal blower takes air from the test room and outputs to an adjacent room which contains the tunnel inlet. The blower can produce flow up to 5.5 m/s, with freestream turbulence level of 0.5 %. The inlet section is 4.40 m by 2.20 m, and covered by filters. Downstream of the filters are 17.5 cm long, 5 cm diameter tubes to break down large-scale eddies. The tunnel contracts to the test section with a contraction ratio of 11.2 to 1 over a distance of 5.0 m. A honeycomb 7.6 cm long with 0.94 cm hexagonal cells, and four stainless steel screens help reduce the flow turbulence at the beginning of the test section. The test cross section is 1.26 m by 0.68 m with corner fillets to reduce secondary flows and is 8.8 m long with the top and bottom walls diverging to account for pressure gradients created by the thickening boundary-layers. The measurements were performed in the last one meter before the tunnel exit.

The traversing mechanism is at the tunnel exit and allows motion in the vertical and spanwise directions with accuracies of 0.03 mm and 0.015 mm, respectively. The multi-sensor hot-wire probes were calibrated in an axisymmetric jet tunnel (see Fig. 2.2) built by P. Vukoslavčević. This jet can produce stable, uniform, and low turbulence flow in the range $0.2 - 10$ m/s. The total length of the calibrating tunnel is about 2.0 m. Air enters the jet tunnel through a filter, is accelerated by a centrifugal blower through a long tubular flow straightener and exits from a 4:1 nozzle. A pitch/yaw mechanism is attached to the nozzle exit and can rotate through $\pm 20°$ with $5°$ increments. The pitch and yaw angles are defined in Fig. 2.3.

2.2 Hot-Wire Probes

Four different types of probes were used in the present project: single-sensor, 4-sensor, 9-sensor and 12-sensor. The preliminary measurements were made with a rake of single sensors. The rake consists of 20 wires approximately 2 mm apart. All the following multi-sensor probes were built by P. Vukoslavčević. The 4-sensor probes were used to measure simultaneously all three components of velocity. Two different probes were used: (1) a Kovasznay-type 4-sensor probe (see Fig. 2.4) similar to one first used by Vukoslavčević & Wallace [62], and a plus-shaped 4-sensor probe (see Fig. 2.5). The Kovasznay-type consists of 2 pairs of orthogonal X-probes, and the plus-shaped consists of 2 pairs of orthogonal V-probes (hereinafter referred to as the square probe and plus probe, respectively). The 9-sensor and 12-sensor probes were used to measure all three components of velocity and vorticity. The 9-sensor probe in Fig. 2.6 had been used successfully in boundary-layer measurements as reported by Vukoslavčević *et al.* [63] and Balint *et al.* [5]. Each of the 3 arrays of this probe has a common prong connected to other prongs in a T-shape. The 12-sensor probe in Fig. 2.7 consists of 3 arrays arranged at the corners of an equilateral triangle. Each array is a plus probe with no common prongs. The 12-sensor probe was developed to help obtain more accurate measurements with the extra sensors. This issue is discussed in more detail in the next chapter. All probes have 2.5 micron Tungsten sensor wires and prong spacings of approximately 0.5 mm. The 12-sensor probe sensing area can fit inside a circle of 2.4 mm diameter.

2.3 Other Equipment

The anemometer, custom-made by AA Labs, has 12 constant-temperature channels, with built-in circuitry for gain, offset and low-pass filters, and "low noise", "low drift" options.

Data acquisition was performed with a 12-channel, 12-bit A/D converter with

simultaneous sample and hold circuitry connected to a PDP 11/23 microcomputer. The system is capable of no-gap data transfer directly to hard disk at a maximum rate of approximately 30000 samples/sec. Data processing were performed on a network of Sun Sparcstations. During the experiments, the tunnel speed was continuously monitored by a Pitot tube connected to a Barocel pressure transducer (model 1174).

2.4 Experimental Procedure

The experimental procedure consisted of 3 phases: preliminary wake measurement tests, velocity measurements with the 4-sensor probes, and vorticity measurements with the 9-sensor and 12-sensor probes.

2.4.1 Preliminary Experiments

These experiments were performed to establish the optimum conditions for wake measurements. Early in the experimental program, it was found that the measurement station (streamwise location of probe tip) should be about 0.5 m upstream to be free of the blockage effect of the traversing mechanism. Two Pitot tubes were used to measure the freestream velocity, one fixed on one side of the tunnel, the other riding on the traverse. Measurements started with the two probes separated by only a few centimeters. This position had the most blockage from the traversing mechanism. The probe on the traverse was then moved a short distance in the spanwise direction away from the stationary probe. Measurements were taken for many spanwise locations across the tunnel width. The streamwise distance from the probe tips to the traversing mechanism were increased gradually until the variation between the two probe readings were within 1% of the measured velocity.

The streamwise velocity component was measured with the single-sensor rake. Several velocity profiles were taken in the range $x/d = 70 - 220$ downstream of the cylinder. These measurements indicated that, in this region, the velocity deficit is

from 5% to 10% of the freestream velocity ($\approx$ 3 m/s) and the maximum mean shear varies only from 10 s^{-1} to 20 s^{-1}. These values of mean shear are of the same order as the noise level of the 9-sensor vorticity probe. Therefore, it was decided that all vorticity field measurements should be carried out in the region $x/d < 50$.

The single-sensor rake experiments also indicated some unsteadiness in the tunnel speed. It was determined that, prior to any measurements, the tunnel must be left running for at least 3 hours without any disturbance to stabilize the flow. Low speeds (below 3 m/s) tended to be more unstable than high speeds. To obtain stable flow and large velocity gradients, it was decided that measurements should be carried out at the highest speed possible, approximately 5 m/s for this tunnel.

Preliminary measurements of the streamwise velocity components were all for the horizontal cylinder orientation. The tunnel width is larger than its height; therefore the horizontal position provides a larger cylinder length to diameter ratio, or aspect ratio (AR), than the vertical position. Larger AR is desirable to achieve two-dimensionality of the flow. For the horizontal orientation, however, the freestream flow region of the wake is less than that for the vertical orientation. This is a consequence of the fact that the tunnel was originally designed for boundary-layer measurements, and the traversing mechanism is strategically placed where the boundary-layer is thickest. The AR for a vertical orientation of the cylinder was approxiately 107 for which Roshko [53] indicated that two-dimensionality of the wake flow can be achieved with $Re_d > 500$. To obtain more confidence for multi-component velocity measurements, flow visualization was performed with the vertical cylinder arrangement. Fig. 2.8 shows the parallel shedding of the Kármán vortex behind the cylinder which indicates that the flow was two-dimensional. Therefore, all definitive measurements were performed with the vertical cylinder orientation.

2.4.2 Velocity Measurements

Velocity measurements were performed after the preliminary experiments indicated the optimum experimental conditions. Both 4-sensor probes were used during this phase. The tachometer connected to the jet fan was first calibrated against a Pitot tube over the range 2 m/s – 7 m/s, so that the jet velocity could be obtained from the fan input voltage. Then, the dynamic range of the sensors was determined by finding the maximum and minimum voltage drops for all sensors. The anemometer outputs were offset and amplified to maximize the range of the sensor response to nearly the extent of the A/D range. The temperature drift had been studied earlier, and determined to be negligible provided the entire calibration and data acquisition process could be done in under 3 hours. This was possibly due to several factors: (1) the anemometer channels have low drift components, (2) the anemometer bridges were turned on at least two hours before the calibration process, and (3) the hot-wire overheat ratio was set relatively high at 1.4. The probe was pitched and yawed in the core region of the calibration jet flow with 5 second sampling times at each position. The pitch-yaw data were obtained at two speeds, one at the wind tunnel freestream velocity, the other about 3 wake deficits lower. Measurements were also obtained for a range of speeds at zero pitch and yaw. This limited set of calibration data was found to be adequate as the velocity variation in wake flow is not as great as in boundary-layer flow. Although more data would be better, a compromise is required between the number of calibration points and the total calibration time. With the existing manual pitch/yaw mechanism, the calibration process takes approximately 90 minutes. The long calibration time is undesirable because of the voltage drift.

Tests were performed with both 4-sensor probes before definitive measurements were obtained. The effect of moving the probes from the calibration jet to the wind tunnel was studied and found to be negligible. A wake profile was taken at

$x/d = 120$ using the square probe. This was performed to determine the quality of the experimental conditions, and to test the 4-sensor data reduction software. Results from these measurements showed that the flow was stable, and that the data reduction method produced physically realistic measurements if the angles of the velocity vectors were within $\pm 20°$.

The definitive velocity measurements were performed at x/d=20 and 30 using the plus probe. These stations were chosen to maximize the signal-to-noise ratio without the extremely high angles of attack of locations closer to the cylinder. This probe was used for comparison with the 12-sensor probe measurements, because the 4-sensor probe resembles one array of the vorticity probe. The cylinder, a 1/4 inch drill rod, was fastened to the top and bottom walls of the tunnel and held under tension by external fasteners. The streamwise displacement was achieved with an adjustable probe extender mounted on the traversing mechanism. For all definitive measurements reported in the following chapters, the experimental conditions were:

- downstream locations $x/d = 20$ and 30
- cylinder diameter $d = 6.3$ mm and $L/d = 107$
- tunnel freestream speed $U_\infty = 5.00$ m/s
- Reynolds number $Re_d = 2000$
- data sampling period = 90 seconds
- data sampling frequency = 2000 Hz
- hot-wire effective overheat ratio = 1.4

The sampling period was determined from previous studies which showed that after 90 seconds the variances of all the velocity and vorticity components varied

within 0.3 %. The 2000 Hz sampling frequency was limited by the total throughput of the A/D converters.

2.4.3 Vorticity Measurements

The vorticity measurements began with preliminary experiments to establish the flow quality and probe capability, and to develop the data reduction software.

The first preliminary experiments were performed in the calibration jet with the 9-sensor vorticity probe described by Vukoslavčević *et al.* [63]. Data were obtained with pitch and yaw variation as described in the previous section. As the flow was nominally irrotational all velocity gradients should be nearly zero. Any non-zero velocity gradients represent the noise level of the overall system which includes the probe and measurement system, the calibration and data reduction methods, and any low level rotationality of the calibration flow. Several experiments were performed in the jet to establish the accuracy of velocity and vorticity measurements. One conclusion from these measurements was that some of the measured spurious gradients at the extreme angles ($\pm 20^{\circ}$ pitch/yaw) can have values higher than the anticipated maximum mean shear in the wake region $x/d = 50 - 120$.

The next preliminary experiments were wake measurements with the 9-sensor probe at $x/d = 120$. Repeated measurements confirmed the earlier indications that the maximum mean shear is of the same order of magnitude as the spurious gradients for this x/d location. Even though the fluctuating gradients can be an order of magnitude larger than the mean shear, it was decided that a confidence test would be how well the directly measured mean shear agrees with the derivative of the mean streamwise velocity profile. This test was not satisfied for these measurements. The skewness factors of the velocity and vorticity components also shed light on the accuracy of the measurements. The skewness factors of the spanwise velocity and the streamwise and transverse vorticity components should all be approximately zero

across the turbulent wake due to the two-dimensionality of the mean flow. These measured skewness factors showed a variation of ± 0.7, which is quite high. These experiments thus indicated that wake measurements at this x/d station need more accuracy than the 9-sensor probe can provide due to the low signal-to-noise ratio.

Further measurements in nominally irrotational, uniform flow provided by the calibration jet confirmed that the 12-sensor probe can yield greater accuracy than the 9-sensor probe. The spurious velocity gradients were lower than those measured with the 9-sensor probe for the same conditions. Definitive measurements were performed in the wake with the 12-sensor probe at $x/d = 20$, and 30 for the same conditions as the velocity measurements with the plus probe. More details about the accuracy of the plus probe and the 12-sensor probe are given in Section 3.5.

3 Calibration and Data Reduction Methods

3.1 Calibration Method

In the probe calibration method developed by Marasli *et al.* [37], Jorgensen's law [28] is used to express the effective cooling velocity of each sensor as a nonlinear function of 3 velocity components for any inclined sensor in uniform flow, i.e.

$$U_{eff}^2 = U_N^2 + C_T U_T^2 + C_B U_B^2, \tag{3.1}$$

where U_N, U_T, and U_B are the normal, tangential and binormal components of the cooling velocity with respect to the sensor (see Fig. 3.1), and C_T and C_B are the tangential and binormal cooling coefficients, respectively. For each sensor, the effective cooling velocity is expressed as a 4th order polynomial, $\mathcal{P}(e)$, of the voltage drop across the sensor:

$$U_{eff}^2 = \mathcal{P}(e) = A_1 + A_2 e + A_3 e^2 + A_4 e^3 + A_5 e^4. \tag{3.2}$$

One can transform U_N, U_T, and U_B from a coordinate system attached to the sensor to a more convenient system, where the x-direction is along the probe axis, giving

$$U_N = n_1 U + n_2 V + n_3 W, \tag{3.3}$$

$$U_T = t_1 U + t_2 V + t_3 W, \tag{3.4}$$

$$U_B = b_1 U + b_2 V + b_3 W, \tag{3.5}$$

where n_i, t_i and b_i $(i = 1, 2, 3)$ are the coefficients of the coordinate transformation which can be determined by measuring the angles the sensors make with the probe axis. However, accurate measurement of these angles for a miniature, multi-sensor

probe is very difficult. It is more convenient to combine these geometric coefficients with the cooling velocity coefficients and determine them by direct calibration.

Substituting Eqs. (3.3) to (3.5) into Jorgensen's cooling law yields

$$\mathcal{P}(e) = U^2 + A_6V^2 + A_7W^2 + A_8UV + A_9UW + A_{10}VW. \tag{3.6}$$

The coefficients A_j $(j = 1, 10)$ can be calculated for each sensor by calibrating the probe in a known irrotational flow with preset flow angles. For flow speed Q at given pitch γ and yaw ψ angles (illustrated in Fig. 2.3), the induced velocity components at the sensor are:

$$U = Q\cos\gamma\cos\psi, \tag{3.7}$$

$$V = Q\sin\gamma\cos\psi, \tag{3.8}$$

$$W = Q\sin\psi. \tag{3.9}$$

To get the 10 coefficients A_j for each sensor, more than 10 calibration points are required to account for the range of speeds and angles of attack the probe encounters in a turbulent flow. For each sensor, given the bridge voltage e_i corresponding to the known calibration velocity components U_i, V_i and W_i $(i = 1, N_c)$, where N_c is number of calibration points, the unknown coefficients A_j can be determined by a linear least-square method from the following linear system of equations:

$$\begin{pmatrix}
N_c & \overline{e} & \overline{e^2} & \overline{e^3} & \overline{e^4} & \overline{v^2} & \overline{w^2} & \overline{uv} & \overline{uw} & \overline{vw} \\
\overline{e} & \overline{e^2} & \overline{e^3} & \overline{e^4} & \overline{e^5} & \overline{ev^2} & \overline{ew^2} & \overline{euv} & \overline{euw} & \overline{evw} \\
\overline{e^2} & \overline{e^3} & \overline{e^4} & \overline{e^5} & \overline{e^6} & \overline{e^2v^2} & \overline{e^2w^2} & \overline{e^2uv} & \overline{e^2uw} & \overline{e^2vw} \\
\overline{e^3} & \overline{e^4} & \overline{e^5} & \overline{e^6} & \overline{e^7} & \overline{e^3v^2} & \overline{e^3w^2} & \overline{e^3uv} & \overline{e^3uw} & \overline{e^3vw} \\
\overline{e^4} & \overline{e^5} & \overline{e^6} & \overline{e^7} & \overline{e^8} & \overline{e^4v^2} & \overline{e^4w^2} & \overline{e^4uv} & \overline{e^4uw} & \overline{e^4vw} \\
\overline{v^2} & \overline{ev^2} & \overline{e^2v^2} & \overline{e^3v^2} & \overline{e^4v^2} & \overline{v^4} & \overline{v^2w^2} & \overline{uv^3} & \overline{uv^2w} & \overline{v^3w} \\
\overline{w^2} & \overline{ew^2} & \overline{e^2w^2} & \overline{e^3w^2} & \overline{e^4w^2} & \overline{v^2w^2} & \overline{w^4} & \overline{uvw^2} & \overline{uw^3} & \overline{vw^3} \\
\overline{uv} & \overline{euv} & \overline{e^2uv} & \overline{e^3uv} & \overline{e^4uv} & \overline{uv^3} & \overline{uvw^2} & \overline{u^2v^2} & \overline{u^2vw} & \overline{uv^2w} \\
\overline{uw} & \overline{euw} & \overline{e^2uw} & \overline{e^3uw} & \overline{e^4uw} & \overline{uv^2w} & \overline{uw^3} & \overline{u^2vw} & \overline{u^2w^2} & \overline{uvw^2} \\
\overline{vw} & \overline{evw} & \overline{e^2vw} & \overline{e^3vw} & \overline{e^4vw} & \overline{v^3w} & \overline{vw^3} & \overline{uv^2w} & \overline{uvw^2} & \overline{v^2w^2}
\end{pmatrix}
\begin{bmatrix} A_1 \\ A_2 \\ A_3 \\ A_4 \\ A_5 \\ A_6 \\ A_7 \\ A_8 \\ A_9 \\ A_{10} \end{bmatrix}
=
\begin{bmatrix} \overline{u^2} \\ \overline{eu^2} \\ \overline{e^2u^2} \\ \overline{e^3u^2} \\ \overline{e^4u^2} \\ \overline{u^2v^2} \\ \overline{u^2w^2} \\ \overline{u^3v} \\ \overline{u^3w} \\ \overline{u^2vw} \end{bmatrix}$$

where the lower case characters are used here to fit the above matrix in the available space, and

$$\overline{e} = \sum_{i=1}^{N_c} e_i, \qquad \overline{e^2} = \sum_{i=1}^{N_c} e_i^2, \quad \text{etc.} \tag{3.10}$$

A typical calibration data set and the calibration curve $\mathcal{P}(e)$ for one of the sensors is shown in Fig. 3.2. In this data set, the pitch and yaw angles were varied within $\pm 20°$ at two different speeds, Q=5 m/s, and 3.2 m/s. In addition, data were obtained at zero pitch and yaw for speeds over the range 2.6−5.7 m/s. In Fig. 3.2, the ordinate values of the symbols correspond to the right-hand-side of Eq. (3.6), where all the velocity components are the known induced values given by Eqs. (3.7) to (3.9). The solid line is the fourth order polynomial curve fit which represents the left-hand-side of Eq. (3.6). The collapse of all points on one curve indicates that Jorgensen's cooling equation represents well the response of a hot-wire in a combined pitch and yaw orientation. Lekakis *et al.* [35] previously reached the same conclusion. This calibration method has the additional advantage that it is independent of probe geometry, and sensor orientation. The technique can be used for both velocity and vorticity measurements, where for the latter, only the spacings between the prongs are required for the data reduction.

The calibration space is divided into 9 zones as shown in Fig. 3.3 for more accurate calculations of the calibration coefficients. Four zones are at the corners of the pitch-yaw plane having angles higher than $\pm 10°$. Another zone is at the center having angles smaller than $\pm 10°$. The last 4 zones fill in the remaining space. For the $x/d = 30$ measurement set, about 95% of the samples fall within the zone having angles less than $\pm 10°$; less than 1% fall within each of the other zones. In the solution procedure of turbulent flow samples, the global ("global" refers to the entire calibration set) calibration coefficients were used first to estimate the pitch and yaw angles. These angles determined which calibration zone the turbulent sample is in and the appropriate zonal calibration set was used for better accuracy. The solution

was flagged if the calculated flow angles jump outside the appropriate zone. The use of these methods for wake velocity measurements has been briefly documented by Nguyen *et al.* [44].

3.2 Data Reduction Method for Velocity Measurement

The following method is applied to a 4-sensor probe, but it can be used for any probe with 3 or more sensors. The method assumes that the spatial resolution of the probe is sufficiently small so that the gradients across the sensing volume can be neglected. In order to reduce the uniqueness problem (addressed in Section 3.4) associated with the triple-sensor response equations reported by Döbbeling *et al.* [14], the present data reduction scheme uses the information from all four sensors simultaneously and solves the overdetermined nonlinear system of equations in a least-square sense. For each sensor, one can rewrite Eq. (3.6) as

$$f_j \equiv \mathcal{P}_j(e_j) - (U^2 + A_{6j}V^2 + A_{7j}W^2 + A_{8j}UV + A_{9j}UW + A_{10j}VW) = 0. \quad (3.11)$$

Here, the subscript j denotes a sensor. In this equation, A_{ij} $(i = 1, 10)$ and $\mathcal{P}_j(e_j)$ are known from the calibration and the anemometer output voltage; $\mathbf{U} \equiv (U, V, W)$ is the unknown velocity vector. Thus, we have a system of 4 nonlinear algebraic equations with 3 unknowns. The goal of the solution scheme is to determine $\mathbf{U}$ which minimizes the error defined as

$$F \equiv \sum_{j=1}^{N_s} f_j^2, \quad (3.12)$$

where N_s is the number of sensors, which is four.

A variety of iterative techniques are available for the solution of nonlinear algebraic systems. The simplest one is Newton's method. With an initial guess for the unknown vector, the incremental correction $\Delta\mathbf{U}$ to the solution $\mathbf{U}$ is obtained from

$$\begin{pmatrix} \frac{\partial^2 F}{\partial U^2} & \frac{\partial^2 F}{\partial U \partial V} & \frac{\partial^2 F}{\partial U \partial W} \\ \frac{\partial^2 F}{\partial U \partial V} & \frac{\partial^2 F}{\partial V^2} & \frac{\partial^2 F}{\partial V \partial W} \\ \frac{\partial^2 F}{\partial U \partial W} & \frac{\partial^2 F}{\partial V \partial W} & \frac{\partial^2 F}{\partial W^2} \end{pmatrix} \begin{bmatrix} \Delta U \\ \Delta V \\ \Delta W \end{bmatrix} = \begin{bmatrix} -\frac{\partial F}{\partial U} \\ -\frac{\partial F}{\partial V} \\ -\frac{\partial F}{\partial W} \end{bmatrix}. \quad (3.13)$$

The solution at the nth iteration step is updated using

$$\mathbf{U}^{n+1} = \mathbf{U}^n + (\Delta\mathbf{U})^n, \tag{3.14}$$

where the superscripts denote the iteration level. The procedure is repeated until convergence is achieved within a specified tolerance. For the results presented here the solution was usually obtained within five iterations. Another solution method, called Broyden-Fletcher-Goldfarb-Shanno [49], was also tried and was found to be less dependent on the initial guesses than Newton's method, but it took almost twice the calculation time. For the plus probe (in Fig. 2.5), an initial guess was obtained by treating the probe as 2 V-arrays which only need the pitch-only and yaw-only calibration data for calibration coefficients.

The calibration data were tested to see whether the calibration velocities were recovered from the bridge voltages. Most velocities were usually recovered to within less than 0.5% and none were more than 1% of the flow speed. Calculated turbulent velocity solutions were rejected if the computed angles of the velocity vectors were outside the calibration range. For the $x/d = 30$ measurement station, there were practically no rejection.

3.3 Data Reduction Method for Vorticity Measurement

When a multi-sensor probe is used in a shear flow, the velocity vector seen by each sensor will be different, i.e., the flow is not uniform across the sensing volume. The effect of the velocity gradients on multi-sensor probe performance has been demonstrated by Vukoslavčević & Wallace [62] and Park & Wallace [46]. Vukoslavčević *et al.* [63] used a 9-sensor probe to measure the spanwise and cross-stream velocity gradients in addition to the three components of the instantaneous velocity vector in a turbulent boundary-layer. They calculated the streamwise gradients from the temporal gradients using Taylor's hypothesis and thus were able to obtain all three components of the instantaneous vorticity vector as well. The 12-sensor probe is

an extension of the 9-sensor probe and the extra sensors were added to widen the cone of acceptance and to eliminate some of the uniqueness problems. Dracos *et al.* [13] presented gradient measurements from a turbulent grid flow obtained with a 12-sensor probe; however, their calibration and reduction algorithm were quite different from the present one.

The data reduction for the 12-sensor probe follows a very similar procedure to that of the 4-sensor probe presented earlier, except now the gradients across the sensing volume are taken into account. Following Vukoslavčević *et al.* [63], one can expand the velocity measured by each wire, $\mathbf{U}_j$, in a Taylor series to first order around the centroid of the frontal area of the probe, i.e.,

$$\mathbf{U}_j = \mathbf{U} + c_j \frac{\partial \mathbf{U}}{\partial y} + d_j \frac{\partial \mathbf{U}}{\partial z}, \tag{3.15}$$

where the right-hand-side is evaluated at the probe centroid. The constants c_j and d_j are the vertical and horizontal distances from the centroid of each wire to the centroid of the probe, respectively. Thus, in this procedure, instead of the velocity, all velocity *gradients* are assumed to be uniform across the sensing volume. Substitution of Eq. (3.15) into Eq. (3.11) yields 12 nonlinear algebraic equations given by

$$\begin{aligned} f_j \equiv\ & -\mathcal{P}_j + U^2 + 2c_j U \frac{\partial U}{\partial y} + 2d_j U \frac{\partial U}{\partial z} \\ & - A_{6j}\left[V^2 + 2c_j V \frac{\partial V}{\partial y} + 2d_j V \frac{\partial V}{\partial z}\right] \\ & - A_{7j}\left[W^2 + 2c_j W \frac{\partial W}{\partial y} + 2d_j W \frac{\partial W}{\partial z}\right] \\ & - A_{8j}\left[UV + c_j\left(U\frac{\partial V}{\partial y} + V\frac{\partial U}{\partial y}\right) + d_j\left(U\frac{\partial V}{\partial z} + V\frac{\partial U}{\partial z}\right)\right] \\ & - A_{9j}\left[UW + c_j\left(U\frac{\partial W}{\partial y} + W\frac{\partial U}{\partial y}\right) + d_j\left(U\frac{\partial W}{\partial z} + W\frac{\partial U}{\partial z}\right)\right] \\ & - A_{10j}\left[VW + c_j\left(V\frac{\partial W}{\partial y} + W\frac{\partial V}{\partial y}\right) + d_j\left(V\frac{\partial W}{\partial z} + W\frac{\partial V}{\partial z}\right)\right] = 0, \end{aligned} \tag{3.16}$$

with the 9 unknowns

$$\mathbf{U} \equiv U_k \equiv \left(U\,,\,V\,,\,W\,,\,\frac{\partial U}{\partial y}\,,\,\frac{\partial U}{\partial z}\,,\,\frac{\partial V}{\partial y}\,,\,\frac{\partial V}{\partial z}\,,\,\frac{\partial W}{\partial y}\,,\,\frac{\partial W}{\partial z}\right). \tag{3.17}$$

This nonlinear system can also be solved in a least-square sense using Newton's method, where the error, defined by Eq. (3.12), is minimized. The incremental correction to the solution at the nth iteration step can be computed from the 9×9 linear system

$$\mathcal{H} \cdot \Delta \mathbf{U} = -\mathbf{G}, \tag{3.18}$$

where

$$\mathbf{G} \equiv \frac{\partial F}{\partial U_k} \tag{3.19}$$

is the gradient vector consisting of the derivatives of F with respect to each of the unknowns, and

$$\mathcal{H} \equiv \frac{\partial^2 F}{\partial U_i \partial U_k} \tag{3.20}$$

is the Hessian matrix composed of all possible second derivatives of F with respect to each of the unknowns. An initial guess for the velocity components was obtained by treating each 4-wire array as two independent V-arrays. The initial gradients were computed by differencing the velocities from the three 4-wire arrays. Convergence, within a specified tolerance, was usually achieved within five iterations. The pitch and yaw angles encountered by each sensor were checked *a posteriori* in order to verify the integrity of the solution. The solutions that were outside the calibration range were rejected.

The present calibration and data reduction scheme can easily be applied to probes with different geometries. The only geometrical information needed is the distance from the center of each wire to the centroid of the frontal sensing area of the probe. The number of sensors need not be fixed at 12, but a minimum of 9 is necessary.

3.4 Solution Uniqueness

For the 4-sensor probe, using only 3 sensors can result in non-convergence for certain probe orientations whereas using all 4 sensors results in convergence to one solution

for all the calibration angles within $\pm 20°$. To illustrate the convergence characteristics of the velocity measurements, error contours are drawn in the $U - V$ plane demonstrating the minimum error region containing the solution. Here, the error F in Eq. (3.12) is expressed in terms of U and V. This is done by eliminating W from the four expressions in Eq. (3.11). One can further eliminate U or V to obtain F as a function of only one variable (see for example Vukoslavčević *et al.* [63]). For a calibration point at $+20°$ pitch and $-20°$ yaw, Fig. 3.4 shows the error contours in the $U - V$ plane with the inner contours having lower values than the outer ones. The data reduction converges in 3 iterations to the physical solution represented by the unique minimum when all 4 sensors are used, as seen in Fig. 3.4(a). When only 3 sensors are used, the topology of the solution surface changes. Instead of the unique minimum, a valley containing many local minima develops, as depicted in Fig. 3.4(b). In this case, the solution algorithm jumps from one local minimum to the next, as a clear indication of the nonuniqueness. These convergence characteristics are consistent with the findings of Döbbeling *et al.* [14].

For the 12-sensor data, there are 9 unknowns which are the 3 velocity components at the probe centroid, and the 6 velocity gradients as shown in the previous section. Since the equations are nonlinear, it is not possible to eliminate enough unknowns to depict the error as a contour plot as was done for the velocity-only measurements. However, the uniqueness study for the 4-sensor measurements indicates that, for relatively high angles of attack (greater than $\pm 15°$), neglecting the sensor with the lowest effective cooling velocity within one array can lead to nonuniqueness problem. Conversely, for all the calibrations points within $\pm 20°$, neglecting the sensor with the highest effective cooling velocity in one array leads to unique solution which is close to that obtained with all 4 sensors. For the 12-sensor data, using all sensors converges in 5 iterations whereas neglecting the 3 sensors having lowest cooling velocity in each array leads to divergence. This, however, does not prove uniqueness of the 12-sensor

data.

For a turbulent sample in the centerline region at $x/d = 30$, one-dimensional error curves for the 3 velocity components are shown in Fig. 3.5. In each plot, the remaining 8 variables are held at their converged values. In Fig. 3.5(a), the error curve for U has two minima; therefore, U can have two possible solutions. However, only one minimum has positive U; the other does not have a physical meaning. Plots (b) and (c) for velocity components V and W show only one minimum, indicating one solution each. The error function F in Eq. (3.12) are fourth-order polynomials in U, V, and W. The components V and W have only one minimum because the fourth-power term is the most dominant. Similar plots for the velocity gradients show only one minimum for each since F in Eq. (3.12) is parabolic in these gradients.

3.5 Measurement Accuracy

To estimate the accuracy of the data reduction system and the probe, one can apply the data reduction method on the calibration data. This means giving the data reduction system the calibration sensor voltages and the calibration coefficients to calculate the induced calibration flow velocity components. Any nonzero velocity gradients computed from the calibration data will be spurious since the probe was calibrated in a steady, uniform, nominally irrotational flow. For this purpose, zone 1 in Fig. 3.3, which has angles between $10° - 20°$, was chosen. Note that every zone needs the additional zero-angle calibration points for accurate calculation of the calibration coefficients. Table 1 shows the calculated velocity components, and the errors between the measured values and the known, induced values from Eqs. (3.7 – 3.9). These errors are normalized by the calibration speed Q. Most of the large angle points have higher errors than the small angle points, as expected. All of the calibration points have relatively low errors which are less than or equal to 1% of the calibration speed. Table 2 shows the calculated spurious velocity gradients for

the same calibration points. Again, here the large angle points usually have higher spurious gradients than the small angle points. Most of the spurious values are much smaller than the maximum mean shear which is approximately 65 s^{-1}.

From Table 1, the average error is 0.008 m/s for U, 0.005 m/s for V and 0.007 m/s for W. When normalized with u_o=0.82 m/s at $x/d = 30$, these uncertainty values are 1.0 % for U, 0.6 % for V, and 0.9 % for W. For the global calibration set, these uncertainty values are 1.7 % for U, 1.5 % for V and 1.8% for W. From Table 2, the largest average spurious velocity gradients are about 5.2 s^{-1}, or 5.4 % of the ratio u_o/L_o for $x/d = 30$. For the global calibration set, this value is about 14.7 s^{-1}. These average spurious gradients can give an estimate of the uncertainty limits for the measured vorticity.

3.6 Summary

The discussion in the above sections has demonstrated the following:

1. The present calibration and data reduction method is independent of the probe geometry and sensor orientation. For vorticity measurements, the only geometrical information needed is the distance from the center of each wire to the centroid of the frontal sensing area of the probe.

2. The error minimization method, when used with more sensors than the number of unknowns, can produce unique solutions of the measured velocity for angles of attack within $\pm 20°$.

3. For calibration angles within $\pm 20°$, neglecting the sensor with the lowest cooling velocity from the plus probe results in divergence during data reduction. Conversely, neglecting the sensor with the highest cooling velocity results in convergence to practically the same solution as when all sensors are used.

4. The zonal calibration scheme can improve measurement accuracy.

#	U	V	W	%error of (U,V,W)			pitch	yaw
1	4.582	1.671	0.860	-0.1	0.0	0.0	20.	10.
2	4.505	1.635	1.279	0.1	0.0	-0.1	20.	15.
3	4.385	1.592	1.695	0.0	-0.1	-0.1	20.	20.
4	4.508	1.211	1.697	0.0	0.1	0.0	15.	20.
5	4.639	1.243	1.284	0.1	0.0	0.0	15.	15.
6	4.720	1.267	0.858	0.1	0.1	-0.1	15.	10.
7	4.806	0.847	0.867	-0.2	0.0	0.1	10.	10.
8	4.719	0.834	1.287	-0.1	0.0	0.0	10.	15.
9	4.595	0.810	1.698	0.0	0.0	0.0	10.	20.
10	4.948	-0.005	-0.005	-0.3	-0.1	-0.1	0.	0.
11	4.983	-0.005	-0.007	0.1	-0.1	-0.1	0.	0.
12	3.159	-0.002	0.006	-0.2	-0.1	0.2	0.	0.
13	2.941	1.066	0.558	0.1	-0.1	0.2	20.	10.
14	2.877	1.055	0.831	0.0	0.2	0.3	20.	15.
15	2.769	1.036	1.110	-1.0	0.5	0.8	20.	20.
16	2.875	0.767	1.094	-0.1	-0.1	0.3	15.	20.
17	2.973	0.790	0.815	0.5	-0.1	-0.2	15.	15.
18	3.022	0.797	0.555	0.1	-0.4	0.1	15.	10.
19	3.067	0.541	0.539	0.0	0.0	-0.3	10.	10.
20	3.015	0.528	0.810	0.5	0.0	-0.2	10.	15.
21	2.930	0.514	1.078	0.4	0.0	0.0	10.	20.
22	3.172	-0.001	0.000	0.2	0.0	0.0	0.	0.
23	3.161	0.002	-0.006	0.1	0.1	-0.2	0.	0.
24	2.578	0.006	0.005	0.0	0.2	0.2	0.	0.
25	2.760	0.010	-0.004	-0.2	0.4	-0.2	0.	0.
26	2.980	0.001	-0.005	-0.4	0.0	-0.2	0.	0.
27	3.184	0.002	-0.004	-0.4	0.1	-0.1	0.	0.
28	3.401	0.001	-0.003	0.0	0.0	-0.1	0.	0.
29	3.664	-0.002	0.006	0.0	-0.1	0.2	0.	0.
30	3.868	-0.001	-0.002	0.0	0.0	-0.1	0.	0.
31	4.035	-0.003	-0.001	0.1	-0.1	0.0	0.	0.
32	4.308	-0.003	-0.002	0.0	-0.1	0.0	0.	0.
33	4.529	-0.005	-0.004	-0.2	-0.1	-0.1	0.	0.
34	4.715	-0.002	-0.001	0.0	0.0	0.0	0.	0.
35	4.949	-0.006	-0.003	0.0	-0.1	-0.1	0.	0.
36	5.139	0.000	0.000	0.0	0.0	0.0	0.	0.
37	5.347	0.000	0.000	0.1	0.0	0.0	0.	0.
38	5.553	0.005	0.005	0.2	0.1	0.1	0.	0.
39	5.721	0.011	0.010	0.0	0.2	0.2	0.	0.

Table 1: Data reduction of velocity components (in m/s) for the calibration data of the 12-sensor probe. The errors are non-dimensionalized by the calibration speed.

#	dU/dy	dU/dz	dV/dy	dV/dz	dW/dy	dW/dz	pitch	yaw
1	-1.	-1.	-2.	-1.	-1.	3.	20.	10.
2	-2.	-2.	-1.	2.	2.	1.	20.	15.
3	7.	-7.	-7.	5.	-7.	1.	20.	20.
4	-2.	-4.	5.	5.	5.	0.	15.	20.
5	-5.	-1.	6.	1.	9.	-1.	15.	15.
6	-3.	0.	0.	-2.	3.	0.	15.	10.
7	1.	-1.	-5.	-2.	-7.	2.	10.	10.
8	-1.	-1.	2.	0.	0.	0.	10.	15.
9	-2.	-1.	2.	2.	1.	-2.	10.	20.
10	2.	-6.	3.	-9.	-6.	0.	0.	0.
11	2.	-6.	3.	-9.	-6.	0.	0.	0.
12	0.	-5.	2.	-1.	2.	-2.	0.	0.
13	7.	2.	8.	3.	-1.	-6.	20.	10.
14	-2.	13.	10.	-7.	4.	-6.	20.	15.
15	-2.	28.	3.	-26.	0.	-6.	20.	20.
16	7.	14.	-7.	-14.	-9.	2.	15.	20.
17	3.	8.	1.	-2.	-4.	-1.	15.	15.
18	5.	1.	2.	7.	-7.	-2.	15.	10.
19	6.	2.	-4.	6.	-4.	1.	10.	10.
20	4.	5.	-5.	0.	-1.	2.	10.	15.
21	7.	5.	-12.	-8.	-6.	6.	10.	20.
22	0.	-5.	4.	-2.	0.	-2.	0.	0.
23	-2.	-3.	0.	3.	0.	-2.	0.	0.
24	-4.	-9.	-1.	19.	22.	2.	0.	0.
25	-4.	-8.	0.	12.	8.	1.	0.	0.
26	-3.	-5.	1.	6.	3.	0.	0.	0.
27	-2.	-2.	1.	3.	0.	-1.	0.	0.
28	-1.	-1.	1.	0.	-1.	-2.	0.	0.
29	0.	1.	1.	-2.	-2.	-2.	0.	0.
30	0.	1.	0.	-4.	-3.	-2.	0.	0.
31	-1.	1.	1.	-5.	-5.	-1.	0.	0.
32	-1.	0.	1.	-5.	-6.	-1.	0.	0.
33	-2.	0.	1.	-4.	-6.	0.	0.	0.
34	-2.	0.	1.	-4.	-6.	0.	0.	0.
35	-2.	1.	0.	-2.	-4.	1.	0.	0.
36	-1.	1.	0.	0.	-2.	1.	0.	0.
37	0.	2.	-1.	3.	2.	1.	0.	0.
38	1.	4.	-2.	7.	7.	1.	0.	0.
39	3.	5.	-4.	9.	13.	0.	0.	0.

Table 2: Data reduction of velocity gradients (in s^{-1}) for the calibration data of the 12-sensor probe.

4 Characteristics of the Velocity Field

4.1 Statistical Properties

In this section, the mean streamwise velocity, the moments of the fluctuating velocity components and the Reynolds shear stresses are presented. These measurements were obtained with the 12-sensor probe. Any 4-sensor measurements used for comparison were obtained with the plus probe. For the $x/d = 30$ measurement station, the wake half-width L_o, used to normalize the wake position, is 8.5 mm, and the centerline wake deficit u_o, used to normalized all Reynolds stresses, is 0.82 m/s. Unless otherwise noted, all measured variables are nondimensionalized by u_o or L_o, which are obtained from

$$(U_\infty - \overline{U})/u_o = \mathrm{sech}^2(\alpha\eta + \beta\eta^3), \tag{4.1}$$

where $\eta = y/L_o$, $\alpha = 0.88$, and $\beta = \cosh^{-1}\sqrt{2} - \alpha = 0.00137$. The values for α and β are empirically determined to give the best-fit curve to the measurements. Generally, it is found that the value for α decreases for measurement locations further downstream of the cylinder and settles on the value 0.78 for the self-preserving wake (Marasli *et al.* [36]). The measured $\overline{U}$ profile is quite symmetric, as shown in Fig. 4.1 (a) along with the best-fit curve. Both the $\overline{V}$ and $\overline{W}$ distributions are nearly zero and are not shown in the plot. From the above curve-fit of $\overline{U}$ and the continuity equation, $\overline{V}$ is calculated to have maximum value of only 2% of the wake deficit, which is of the same order as the measurement uncertainty.

Fig. 4.1(b) shows that the maximum rms value of v is slightly higher than that of u due to the vortex shedding in the near-wake region; the maximum rms value of w is considerably lower. The average turbulence intensity in the freestream is about 1/20 of those near the centerline, which indicates a high signal-to-noise ratio.

The $x/d = 30$ measurement station is in the region where the energy of the Kármán vortex is still quite distinct. Roshko [53] found that the Kármán vortex persists up to $x/d = 50 - 70$. Downstream of this region, Yamada *et al.* [70] measured all three components of the velocity vector and found that the rms for the u component is highest, with the other two about the same. For the current measurements, the u and w components have small double peaks approximately $0.7L_o$ from the wake centerline, while the rms value of v peaks at the wake centerline. The rms values of the velocity components from the 4-sensor velocity probe have the same trends and approximately the same magnitudes, and therefore are not shown.

The skewness factors of the velocity components in Fig. 4.1(c) show symmetry of the u component, antisymmetry of the v component, and nearly zero values of the w component. The u skewness is negative on both sides of the wake because the wake is always spreading outward; low momentum fluid from the centerline is being transferred to the wake edges. At the centerline, the u skewness value is about $+0.1$, consistent with observation of Fabris [17] in the far-wake region. This positive skewness value could indicate that a small transfer of high momentum fluid from the wake edges is occuring. The skewness value decreases to a minimum of about -3.0 at approximately $\eta = \pm 3$ then goes back to zero in the freestream region. The v skewness is negative in the lower wake and positive in the upper wake. This is consistent with the outward spreading of the wake, which is characterized by negative lateral velocity in the lower wake, and positive lateral velocity in the upper wake. The w skewness is nearly zero across the wake as expected from the two-dimensionality of the mean flow.

The flatness factors for all three velocity components in Fig. 4.1(d) are about 3.0 around the wake centerline, indicating an almost Gaussian distribution in this region. The wake edge regions, however, have extremely high values due to the intermittent turbulence there. Also, the maximum v flatness factor is higher than that of the u

flatness factor and occurs nearer the wake edges. A similar pattern is noted for the skewness factor. This pattern was also observed in the measurements at $x/d = 400$ of Fabris [17]. Presently, a satisfactory explanation has not been found. In general, the skewness and flatness data at $x/d = 30$ agree well with the measurements of Fabris which were much further downstream.

Fig. 4.2 shows the comparison of the nondimensional rms values (denoted by superscript $*$) at $x/d = 20$ and 30. For $x/d = 20$, $L_o = 6.5$ mm and $u_o = 0.93$ m/s, and the u^* and w^* values are only slightly higher than those at $x/d = 30$. The v^* values, however, are significantly higher, reaching as much as 25% higher in the centerline region. This is likely due to the Kármán vortices. The differences between the nondimensional rms values at the two downstream locations indicate that the wake is not yet in the self-preserving region, which Wygnanski *et al.* [69] have found to occur more than $300d$ downstream of the cylinder. The Kármán vortex decays in the region $0 - 50d$ according to Roshko [53], as is most evident in the large decrease in the v^* values. Higher moments at $x/d = 20$ have similar characteristics as those at $x/d = 30$ thus are not shown.

To illustrate the effect of accounting for velocity gradients and for the third velocity component in the probe sensing area, the 12-sensor rms data at $x/d = 30$ are compared with the V-probe values from one array of the 12-sensor probe (hereafter referred to as the "V-probe data") in Fig. 4.3. For the V-probe data, the u component represents the average of the two orthogonal V-probes. All three rms components are slightly higher than those from the 12-sensor probe. The 12-sensor probe has a larger sensing area, but it accounts for the velocity gradients. The 12-sensor data should be more accurate. The small difference between the two probes indicates that neglecting the third component and the velocity gradients have a small effect in the rms data of plane wake flow. However, Park & Wallace [46], and Vukoslavčević *et al.* [63] found that neglecting the velocity gradients, as must

be done with the V-probes and the plus probe, can lead to large errors in near-wall regions of the boundary-layer.

The 12-sensor rms data at $x/d = 30$ are also compared with X-probe measurements of Yamada *et al.* [70] in Fig. 4.3. The Yamada *et al.* data are at the same x/d location, but at $Re_d = 4000$, and were measured with commercial X-probes which have sensor spacing of approximately 1 mm, i.e. about twice that of the 12-sensor probe. The X-probe does not account for the velocity gradients and the third velocity component, but these effects have been shown to be small in the previous paragraph. What remain are the Reynolds number and the sensor spacing effects, which cannot be separated out. The Kolmogorov scale in Yamada *et al.* was smaller than that in the current measurements due to a higher Reynolds number, but they were not able to provide estimates of the Kolmogorov scale. The 12-sensor probe can measure all the necessary velocity gradients in the expression for the dissipation. For $Re_d = 2000$ and $x/d = 30$, the Kolmogorov scale is approximately $0.2 - 0.4$ mm across the wake.

In Fig. 4.3, the u rms component from the 12-sensor probe is slightly lower, and the v and w components are significantly lower than the X-probe data. Analysis of a direct numerical database by Suzuki & Kasagi [56] indicated that the sensor spacing has a strong effect on the measured rms velocity components. They showed that for an X-probe configuration, the v and w rms values are overestimated significantly when the sensor spacing is increased. Park & Wallace [46], and Tagawa *et al.* [57] came to the same conclusion when they evaluated the X-probe response in a simulated wall turbulence flow. These previous studies indicate that the rms data obtained with the miniature 12-sensor probe are likely to be closer to the true values.

The Reynolds shear stresses are shown in Fig. 4.4. The $-\overline{uv}$ stress is negative in the lower wake, zero on the centerline, and positive in the upper wake. This is consistent with the u and v skewness factors which have the same signs in the lower

wake, and opposite signs in the upper wake. The difference between the 4-sensor and 12-sensor probe measurements is also illustrated. For the $-\overline{uv}$ component, the two sets of data are about the same. The $-\overline{uw}$ stress, which should be zero everywhere, is about 25% of the peak $-\overline{uv}$ stress at the centerline for the 4-sensor data. For the 12-sensor data, it is considerably smaller everywhere across the wake. The $-\overline{vw}$ stress is about zero for both sets. The non-zero $\overline{uw}$ from the 4-sensor probe is spurious. It is inconsistent with the nearly zero values of $\overline{W}$ and w skewness, which reflects the equal probability of negative and positive w fluctuations. Also, flow visualization in Fig. 2.8 showed that the vortex shedding was quite parallel to the cylinder, which indicates two-dimensionality of the mean flow, and implies no preference for either negative or positive w fluctuations. The cause of this error must therefore be the assumption for the 4-sensor probe that the velocity is uniform within the sensing area of the probe. This assumption is least applicable in the centerline region where the turbulence is highest.

In the comparison in Fig. 4.5, the $-\overline{uv}$ values of Yamada *et al.* are almost twice the 12-sensor data near the centerline, consistent with the higher u and v rms values. Again, the differences might also be attributed to their higher Reynolds number. The V-probe $-\overline{uv}$ data are about the same as those from the 12-sensor probe, which is consistent with the rms comparison. For the $-\overline{uw}$ component, the V-probe and 12-sensor data are about the same, but the $-\overline{vw}$ stress for the V-probe reaches 35% of the peak $-\overline{uv}$ stress. X-probe data from Yamada *et al.* were not available for comparison, and to the author's knowledge, there are no other published X-probe data for these stresses. In summary, the comparisons for all the Reynolds stresses indicate that the 12-sensor probe data show the greatest self-consistency.

4.2 Velocity Spectra

The spectra for all components of the velocity vector are presented and discussed in this section. Six cross-stream locations covering both the lower and upper layers were chosen for this purpose. The spectra are normalized by the local variance of the individual component so that the area under each is unity. The discussion is representative of all the 21 wake locations where data were taken.

The u and v spectra in Figs. 4.6 and 4.7 show strong peaks at the vortex shedding frequency, $f_s = 168$ Hz. This frequency corresponds to a Strouhal number of 0.21, in excellent agreement with the value reported by Roshko [53] at this Reynolds number. The w spectra in Fig. 4.8 do not have any distinct peak above the background; this indicates that the shed vortex is parallel to the cylinder. The Kármán vortex, if it is shed parallel to the cylinder, is in the $z-$direction so it can only influence flow in the $x-y$ plane. The proper detection of the shedding frequency is another indication of the accuracy of the measurements made by the 12-sensor probe.

The peaks for the u spectra disappear in the centerline region, and reach maximum values around $\eta = \pm 1$ from the centerline. On the other hand, the peaks for the v spectra are most prominent in the centerline region, and diminish toward the wake edges. This pattern of the power peaks for these two components can be predicted by linear stability theory (see for example Mattingly & Criminale [38]).

The w spectra show little change across the wake. All w spectra have relatively flat distributions up to about the shedding frequency, then drop off at higher frequencies. This pattern is also observed for the v spectra at the wake edges. For the v spectra near the centerline region, the neighboring frequencies of f_s have high energy content. This is because the background $v-$spectrum has a local maximum at a frequency slightly smaller than f_s which corresponds to the locally neutral frequency from linear stability theory (Marasli *et al.* [36]). All frequencies above f_s are damped, which is consistent with the fact that the Kármán vortex street decays

with downstream distance.

4.3 Probability Density Functions of the Velocity Components

The probability density functions (PDFs) for all three components of the fluctuating velocity are presented in Figs. 4.9 to 4.11. Each velocity component is normalized by the wake deficit u_o. The area under the PDF curve is unity by definition. The six wake locations in these figures are for the same locations as in the spectra plots for ease of comparison. The following discussion is representative of all positions measured.

In Fig. 4.9, the PDFs for the u components are skewed at the wake edges and quite symmetric in the centerline region. This symmetry reflects the near-zero skewness in the wake centerline. For both the upper and lower wake, the PDFs have most probable $+u$ values but have longer $-u$ tails indicating penetration of low momentum fluid from the centerline region into the outer edges of the wake. This corresponds to the negative skewness values in this region. The PDFs for the wake edge ($\eta = -1.65$) have very high peaks near the mean value. This is why the flatness values are so high in these regions. High fluctuations, about 2 times the wake deficit, rarely occur. Near the wake centerline, the peak values are much lower, with wider distributions around the mean, which is also indicated by the high rms values there. This pattern reflects the high degree of mixing occuring in the centerline region. The PDFs are closer to the Gaussian distributions in the centerline region than in the wake edges.

In Fig. 4.10, the PDFs for v show the antisymmetry expected from the skewness distribution. For the lower wake, the PDFs have most probable $+v$ values but have longer $-v$ tails, which means that v has negative skewness values in this region. For the upper wake, the opposite pattern occurs. At both wake edges, large v fluctuations occur much less frequently than small fluctuations which is why the flatness values

are high there. In the centerline region ($\eta = 0.12$), the PDF is quite symmetric so that the skewness value is approximately zero.

In Fig. 4.11, the PDFs for w are symmetric for all the positions across the wake, indicating a two-dimensional mean flow. For the wake edges where the turbulence is more intermittent, the PDFs have asymmetric tails which explain the non-zero skewness values here.

4.4 Joint Probability Analysis of the Velocity Components

The joint probability density functions (JPDFs) of two variables indicate the probability of the two variables having specified values at the same time. The orientation of the JPDF contours reflects the preferred simultaneous states of the two variable fields. Thus, some turbulence structure information can be deduced, even from single-point measurements. JPDF analysis was utilized by Wallace & Brodkey [65] to examine the structure of the correlation $\overline{uv}$ in a turbulent channel flow. Ong [45] used JPDF analysis in the buffer region of a turbulent boundary-layer to detect the presence of inclined vortices. The covariance of two variables, v_1 and v_2, can be related to the JPDF by

$$\overline{\mathrm{v}_1\mathrm{v}_2} = \int_{-\infty}^{+\infty}\int_{-\infty}^{+\infty} \mathrm{v}_1\mathrm{v}_2 P(\mathrm{v}_1,\mathrm{v}_2)\,d\mathrm{v}_1 d\mathrm{v}_2. \tag{4.2}$$

The JPDFs for all combinations of the velocity components have been determined for six locations across the wake. Numerical values of the contributions from all four quadrants, Q1, Q2, Q3 and Q4, of the two velocity component hodograph plane are also presented. The quadrants are defined in Fig. 4.12. For all JPDFs, the velocity components are normalized by the centerline velocity deficit u_o.

Fig. 4.13 shows the JPDF, $P(u,v)$, and the covariance integrand contours, $uvP(u,v)$. For the lower wake, the JPDF contours show a preferred orientation of 45° from the horizontal axis u. The covariance integrand contours show this even more clearly with the contribution coming mainly from Q1 and Q3 in the outer part

of the lower wake. The Q3 activity has lower probability but larger fluctuations than the Q1 activity, and, in fact, contributes more to the covariance than Q1 as seen in Fig. 4.14. In the centerline region ($\eta = 0.12$) the contours are symmetric in v but not in u, as expected. The upper wake has a preferred Reynolds stress orientation of $-45°$ from the horizontal axis, and most of the activity is in Q4 and Q2. The Q2 activity has lower probability but larger fluctuations than the Q4 activity, and is the greater contributor to the $\overline{uv}$ covariance, as also seen in Fig. 4.14. These patterns mean that the covariance $\overline{uv}$ is positive in the lower wake, near zero in the centerline region, and negative in the upper wake. The quadrant contribution distributions in Fig. 4.14 quantify these qualitative trends. The total covariance $\overline{uv}$ (the sum of the quadrant contributions) is the Reynolds shear stress given in Fig. 4.4.

The preferred $\pm 45°$ angles of the JPDF contours indicates a tendency to maximize generation of $\overline{uv}$. The following illustration explains why. For a unit two-dimensional vector with angle α, the x and y components are, respectively,

$$\mathrm{v}_1 = \cos\alpha, \tag{4.3}$$

$$\mathrm{v}_2 = \sin\alpha. \tag{4.4}$$

The product of these two components is

$$\mathrm{v}_1\mathrm{v}_2 = \cos\alpha \ \sin\alpha. \tag{4.5}$$

Since the right-hand-side can be expressed as

$$\cos\alpha \ \sin\alpha = \frac{1}{2}\sin(2\alpha), \tag{4.6}$$

maximizing the product $\mathrm{v}_1\mathrm{v}_2$ is equivalent to maximizing the function $\sin(2\alpha)$. This function is maximum at $90°$ which makes $\alpha = 45°$.

The shear stress $\overline{uv}$ reflects the momentum deficit transport of the streamwise momentum from the centerline region to the outer wake. The streamwise momentum

deficit can be seen clearly in the negative skewness of u away from the centerline. This momentum deficit transport from the centerline toward the wake edges also can be seen in the negative skewness value of v in the lower wake, and positive skewness value in the upper wake. The combination of the u and v skewness values is consistent with the sign change of the $\overline{uv}$ covariance across the wake.

The quadrant contribution distribution in Fig. 4.14 gives more details about the momentum deficit transport. In the lower wake, the larger contributions in Q1 and Q3 quadrants means that $+u$ is most likely to occur with $+v$, and $-u$ is most likely to occur with $-v$. In the upper wake, $+u$ is most likely to occur with $-v$, and $-u$ with $+v$, which are the Q4 and Q2 quadrants, respectively.

This pattern of momentum transport can be better visualized with the aid of a velocity vector plot covering the lower and upper wakes. The vector plot in Fig. 1.3 shows the vortex centers and saddle regions in both layers. Around the saddle regions, the diverging legs and converging legs indicate flow away or toward the saddle, respectively. In the lower wake, the converging legs would correspond to Q1 and Q3 flow activity, and the diverging legs would correspond to Q2 and Q4. Since Q1 and Q3 are preferred in this region, the converging legs are the dominant $\overline{uv}$ generators in the lower wake. Following similar arguments, it can be seen that the converging legs are also the dominant $\overline{uv}$ generators in the upper wake.

For $P(u,w)$, Fig. 4.15 shows that the JPDF and covariance integrand contours are symmetric with respect to w, which must be the case for a two-dimensional mean flow. The symmetry in w results in the almost zero $\overline{uw}$ covariance across the wake. Due to the negative skewness of u across the wake, the maximum probability contours are on the $+u$ side. The negative skewness also implies that the largest contribution to the total covariance should come from Q2 and Q3. This observation is confirmed in the quadrant plots of Fig. 4.16.

For $P(v,w)$, Fig. 4.17 shows that the JPDF and covariance integrand contours are symmetric with respect to w, for the same reason as for $P(u,w)$, and the total covariance still is almost zero across the wake due to this symmetry. The skewness of v changes sign across the wake, which is reflected in the maximum probability contours. The covariance integrand contours show high probability of low-fluctuation activity in Q1 and Q4 in the lower wake, and in Q2 and Q3 in the upper wake. This pattern implies that the large fluctuations should produce high correlation values in the opposite quadrants. This is confirmed in the quadrant plots of Fig. 4.18 with larger magnitudes in Q2 and Q3 for the lower wake, and Q1 and Q4 in the upper wake.

4.5 Summary

The discussion in the above sections has demonstrated the following:

1. At $x/d = 20$ and 30, the maximum rms of the transverse velocity component is higher than the streamwise, followed by the spanwise component. This trend is consistent with X-probe measurements of Yamada *et al.* [70] at $x/d = 30$.

2. The small prong spacing of the 4-sensor and 12-sensor probes results in more accurate measurements.

3. The skewness and flatness values of the velocity components show the proper characteristics of a turbulent plane wake.

4. The 12-sensor probe accounts for velocity gradients in the measuring volume and can measure the Reynolds shear stresses more accurately than the 4-sensor probe.

5. The velocity spectra show peaks at the vortex shedding frequency f_s for the streamwise and transverse components. The spanwise velocity spectra donot have any peak at f_s, indicating parallel shedding.

6. The JPDFs of the streamwise and transverse velocity components show preferred orientations at $+45°$ from the centerline for the lower wake and at $-45°$ for the upper wake. The other correlations are about zero across the wake due to flow symmetry.

7. The converging legs of the saddle region are the dominant $\overline{uv}$ generators. These flow regions are along the direction normal to the mean shear.

5 Characteristics of the Vorticity Field

5.1 Statistical Properties

The statistical properties described in this section include the mean vorticity components and moments of the fluctuating vorticity components. These properties at $x/d = 30$ are shown in Fig. 5.1, and are normalized by the ratio $u_o/L_o = 96.5$ s^{-1}. The mean vorticity components $\overline{\Omega}_x$ and $\overline{\Omega}_y$ are nearly zero as expected for a two-dimensional wake flow. The directly measured $\overline{\Omega}_z$ distribution is very close to that obtained by differentiating the curve-fit of $\overline{U}$ given by Eq. (4.1). Both the magnitude and the symmetry of $\overline{\Omega}_z$ are in good agreement, thus providing a rather stringent test of the accuracy of the vorticity measurements. As expected, the lower half of the wake has positive and the upper wake negative $\overline{\Omega}_z$.

The nondimensional rms values of the vorticity components (denoted by superscript $*$) have sufficiently high signal-to-noise ratios, as indicated by the ratio of the centerline to the freestream value of about 200:1, and peak near the wake centerline. The peak magnitudes of all components are quite close to each other, with ω_x^* the largest, followed by ω_y^*, and then ω_z^*. The relatively low value for ω_z^* clearly shows that the Kármán vortex does not the dominate the enstrophy at $x/d = 30$.

The skewness and flatness values shown are limited to within $\eta = \pm 2.5$, because the intermittent region of the wake produces extremely high values. The freestream values at approximately $\eta = \pm 5$ are also shown for comparison; the skewness values are close to zero as they should be. The freestream flatness values are near the Gaussian value of 3 which is also reasonable. The skewness factors for ω_x and ω_y are nearly zero across the wake within the fully rotational flow region, consistent with the two-dimensional nature of the mean flow. Within the intermittent region they take on non-zero values but return to nearly zero in the freestream. The ω_z skewness

factor is positive for the lower wake, crosses zero at the centerline, and is negative for the upper wake, following the sign of $\overline{\Omega}_z$. The flatness factors are approximately the same for all three components, and are about 5.0 in the fully rotational centerline region.

There are some vorticity data in the literature for comparison. Antonia *et al.* [3] measured separately the 3 components of vorticity at $x/d = 420$ and $Re_d = 1170$, with various combinations of X-probes. Their maximum vorticity rms values, when normalized by u_o/L_o, are in the range $1.4 - 1.6$ in the centerline region. Bisset *et al.* [7] measured simultaneously the 3 vorticity components using a very large probe (described in Section 1.2) for the same location and condition as in Antonia *et al.* . Their maximum nondimensional rms values are in the range $1.0 - 1.3$ in the centerline region. Both of these rms results give significantly lower values than the present rms data, which are more than 2.2 for all components. The relatively high rms values in present data are due to: (1) the closer wake location, (2) higher Reynolds number, (3) higher spatial resolution therefore lower signal attenuation of the miniature 12-sensor probe.

In Fig. 5.2, the rms values at $x/d = 20$ are compared with those at $x/d = 30$. For $x/d = 20$, the normalizing length scale L_o and velocity scale u_o are 6.5 mm, and 0.93 m/s, respectively. Even though the dimensional values are all higher than those at $x/d = 30$, the normalized rms values at $x/d = 20$ are all lower due to the large normalization scale u_o/L_o. The results are not expected to collapse on one curve since the measurement stations are far upstream of the self-preserving region. All components at $x/d = 20$ have about the same peak value of approximately 2.1. The difference between the two streamwise locations is greatest for ω_x, followed by ω_y, and then ω_z.

Other moments and characteristics at $x/d = 20$ have similar patterns as those at $x/d = 30$ and therefore are not shown. The expected trends of the mean vorticity

components and the skewness values at the two wake locations give further confidence that the vorticity measurements are reasonably accurate.

5.2 Streamwise Velocity Gradients

The transverse and spanwise vorticity components in the previous section have streamwise velocity gradient terms that cannot be measured directly with the 12-sensor vorticity probe. In fact, due to severe blockage effects, the streamwise gradients cannot be measured accurately by any hot-wire anemometry technique. For the current measurements, Taylor's hypothesis is used to estimate these streamwise gradients. In effect, the relationship assumes that the turbulent flow is frozen over a short time interval so the streamwise gradient for a turbulent variable can be calculated from its temporal variation. Mathematically, the hypothesis is expressed as

$$\frac{\partial}{\partial t} + U_c \frac{\partial}{\partial x} \approx 0. \tag{5.1}$$

This relationship is somewhat like a substantial derivative operator, with the variable U_c being the local convection velocity. For the current measurements, the instantaneous streamwise velocity is used for U_c. Taylor's hypothesis is widely used in processing turbulence measurements. Cenedese *et al.* [11] tested Taylor's hypothesis by Laser-Doppler measurements in a rectangular pipe flow. They found that the hypothesis is still applicable in high turbulence flows, but the integral scales have large errors. Piomelli *et al.* [47] have compared boundary-layer measurements with large-eddy and direct numerical simulation databases and found that the hypothesis holds reasonably well even into the buffer layer.

The transverse and spanwise vorticity components are computed from the measured signals as

$$\Omega_y = \frac{\partial U}{\partial z} + \frac{1}{U_c}\frac{\partial W}{\partial t}, \tag{5.2}$$

$$\Omega_z = -\frac{\partial U}{\partial y} - \frac{1}{U_c}\frac{\partial V}{\partial t}. \tag{5.3}$$

For the time derivatives, $\partial V/\partial t$ and $\partial W/\partial t$, central-differencing (C-D) yields more accurate vorticity results than backward-differencing (B-D). When the measured data were first analyzed, the B-D scheme was used since the scheme is sometimes used by other researchers [3,26], and it gives double the temporal resolution compared to the C-D scheme. However, it also introduces a phase misalignment of one-half time step, as discussed below. During calculation of the enstrophy production, the B-D scheme was discovered to give unrealistic results. The term $\overline{v\omega_z}d\overline{\Omega}_z/dy$, is responsible for producing the fluctuating enstrophy from the gradient of the mean spanwise vorticity. The term represents a loss for the mean enstrophy and should have negative values across the wake. The B-D scheme gave significant positive values for the wake centerline region, as shown in Fig. 5.3. The C-D scheme, on the other hand, gives negative values for the term throughout the wake. The dramatic sign change is probably due to (1) low magnitude of the correlation $\overline{v\omega_z}$ as shown in Section 7.6, and (2) low sampling rate.

The difference between results from the two schemes is due to the phase misalignment of variables v and ω_z in the correlation $\overline{v\omega_z}$. There is also phase misalignment within ω_z itself, between the estimated value of $\partial v/\partial x$ from Taylor's hypothesis and the directly measured value of $\partial u/\partial y$. The B-D scheme calculates the time derivative from two *consecutive* samples, the current time and the previous. The C-D scheme uses the samples before and after the current time. In effect then, the B-D scheme is like the C-D scheme with two different features: (1) the B-D scheme evaluates the time derivative one-half time step earlier, and (2) the B-D scheme evaluates the time derivative over one time step rather than two. Feature (1) indicates that when the sampling rate is not high enough, as in the current measurements, the one-half time step phase difference between two variables such as v and ω_z can give erroneous results. This was observed when the correlation $\overline{v\omega_z}$ was calculated with variable

time delay to evaluate the effect of feature (1) as described below. Feature (2) of the B-D scheme is an advantage because it doubles the usable frequency range of the data, but it must be sacrificed here in order to maintain the phase alignment.

Fig. 5.4 shows the production term $\overline{v\omega_z}d\overline{\Omega}_z/dy$ versus time delay for $\eta = 0.12$. The calculation was done for a range of ± 2 time steps (± 1 ms) for both the C-D and B-D schemes. The plot clearly shows that after the B-D curve is shifted by one-half time step in the direction of negative time, it falls almost on top of the C-D curve. This time-delay calculation was repeated for a few other wake locations, and the results were similar. This indicates that the positive (erroneous) enstrophy production is due to the phase difference of the B-D scheme.

Since B-D evaluates the time derivative over only one time step, it does not attenuate the turbulent signal as much as the C-D scheme. Time series data of ω_z are shown for both schemes in Fig. 5.5. The two match quite well except that the B-D curve sometimes has higher peaks and resolves higher frequencies. The latter difference shows up more clearly in the spectra in Fig. 5.6. For ω_z, the two spectra are virtually identical up to approximately twice the shedding frequency. Beyond this, the B-D curve is clearly higher than the C-D curve. Therefore, it is clear that the B-D scheme resolves more of the high frequency fluctuations, but the half time step phase difference between the estimated value of $\partial v/\partial x$ from Taylor's hypothesis and the directly measured value of $\partial u/\partial y$ makes the B-D scheme inaccurate. The high frequency values of the B-D scheme compared to the C-D scheme are erroneous as shown below.

The signal attenuation and phase shift of the two differencing schemes can be calculated analytically. A time dependent variable can be expressed in a Fourier series as

$$\mathrm{v}(t) = \sum_{n=1}^{N} a_n \varphi_n(t), \tag{5.4}$$

where a_n = Fourier coefficient for $n = 1$ to N components. Each Fourier component can be expressed as

$$\varphi(t) = e^{i\kappa t}, \tag{5.5}$$

where $i = \sqrt{-1}$, $\kappa = 2\pi f$, and f = frequency, and differentiation of $\varphi(t)$ gives

$$\varphi'(t) = i\kappa\varphi(t). \tag{5.6}$$

It can be shown easily that differentiation with the C-D scheme gives

$$\varphi'_{CD}(t) = i\kappa\frac{\sin\kappa\Delta t}{\kappa\Delta t}\varphi(t). \tag{5.7}$$

where Δt = sampling interval. Comparison between Eq. (5.6) and Eq. (5.7) shows that a modified wave number, κ_{CD}, can be defined as

$$\kappa_{CD} \equiv \kappa\frac{\sin\kappa\Delta t}{\kappa\Delta t}. \tag{5.8}$$

Physically, this relationship means that the C-D scheme attenuates a signal by the factor $\frac{\sin\kappa\Delta t}{\kappa\Delta t}$. However, there is no phase shift because this is a real number.

Similarly, it can be shown easily that differentiation with the B-D scheme gives

$$\varphi'_{BD}(t) = i\kappa\left[\frac{\sin\kappa\Delta t}{\kappa\Delta t} + i\frac{\cos\kappa\Delta t - 1}{\kappa\Delta t}\right]\varphi(t). \tag{5.9}$$

Again, comparison between Eq. (5.6) and Eq. (5.9) shows that a modified wave number, κ_{BD}, can be defined as

$$\kappa_{BD} \equiv \kappa\left[\frac{\sin\kappa\Delta t}{\kappa\Delta t} + i\frac{\cos\kappa\Delta t - 1}{\kappa\Delta t}\right]. \tag{5.10}$$

Physically, this relationship means that the B-D scheme attenuates a signal, and introduces a phase shift because κ_{BD} has a complex component. The magnitude of the signal attenuation can be shown to be

$$|\kappa_{BD}/\kappa| = \frac{[2 - 2\cos\kappa\Delta t]^2}{\kappa\Delta t}. \tag{5.11}$$

The phase angle ξ for the vector κ_{BD}/κ can be shown to be

$$\xi = \arctan(\cot \Delta t - \csc \Delta t). \tag{5.12}$$

The ratios κ_{CD}/κ and $|\kappa_{BD}/\kappa|$ are shown in Fig. 5.7 (a) and ξ is shown in Fig. 5.7 (b) as functions of the frequency f for the range used in this experiment. In Fig. 5.7 (a), both the C-D and B-D schemes have low attenuation for low frequencies and significant attenuation for high frequencies.

At half the sampling frequency, the C-D scheme attenuates all the differentiated signal intensity, but the B-D scheme retains about 63% of the signal. This high value is erroneous and comes from the complex component, which also indicates a phase shift. This phase lag (negative values) is shown in Fig. 5.7 (b) to vary linearly with f. It is practically zero for low frequency and is 90° at half the sampling frequency. At the vortex shedding frequency (about 168 Hz), the C-D scheme, which does not introduce any phase shift, attenuates only about 5% of the signal. At this frequency, the B-D scheme attenuates only 1% of the signal but introduces a 16° phase lag. If a higher sampling frequency had been possible, the phase lag would be smaller. In the present results, the C-D scheme has been used to calculate all time derivatives.

5.3 Vorticity Spectra

The spectra for three components of the vorticity vector are presented and discussed. The spectra are for 6 wake locations covering both the lower and upper layers, and they are normalized by the local variance of the individual component. The discussion is representative of all the 21 wake locations where data were taken.

Fig. 5.8 shows that the spectra for ω_x are similar in the region $|\eta| < 1.35$. The distributions are all broad band, and there are no distinct peaks at the shedding frequency. Since the Kármán vortices are aligned only in the z-direction (if they are not obliquely shed), there should not be any evidence of the vortex shedding in the x-direction vorticity. Therefore, the ω_x spectra provide another indication that the

12-sensor vorticity probe accurately resolves the components of the vorticity field. All these spectra have relatively flat distributions up to about the shedding frequency and then drop off for higher frequencies.

Fig. 5.9 shows that the spectra for ω_y are also similar in the region $|\eta| < 1.65$. The distributions are also all broad band with no distinct peaks at the shedding frequency, reflecting the parallel nature of the Kármán vortices. The ω_y spectra are quite close to the ω_x spectra, in both magnitude and in the distribution. However, the ω_y spectra have very low energy content in the high frequency range, undoubtedly due to the attenuation effect of central differencing. At the highest frequency, the ω_y spectral value is about one half the ω_x value.

The spectra for ω_z in Fig. 5.10 show a strong intensity narrow band spike at the vortex shedding frequency, $f_s = 168$ Hz. This strong peak is a signature of the Kármán vortex. At locations $\eta = -0.47$ and 0.71, the peaks seem to be highest indicating that these locations are somewhere near the centers of the vortices shed on either side of the wake. Near the centerline ($\eta = 0.12$), the peak is a little lower. The effect of the vortices can be seen, from these peaks, to extend beyond $\eta = 1.29$ but less than $\eta = 1.65$. The cross-stream distribution of the spectral peak can be predicted by the linear stability theory [38]. For the same reason as in the ω_y spectra, the ω_z spectra have very low energy content in the high frequency range. All three spectra span about one decade in magnitude indicating that the sampling frequency was really two low. However, the vortex shedding frequency is not in the attenuated high frequency range of the spectra, and thus the filtered ω_z signal can still serve as a phase reference for conditional analysis of the measured turbulent flow field, as described in Chapter 6.

5.4 Probability Density Functions of the Vorticity Components

The probability density functions (PDFs) for all three components of the fluctuating vorticity are presented in Fig. 5.11 for the freestream and centerline regions. Each vorticity component is normalized by the scale u_o/L_o. The narrow widths of the distributions for the freestream PDFs compared to those for the centerline PDFs demonstrate the high signal-to-noise ratio (up to two orders of magnitude) of the vorticity measurements. Figs. 5.12 to 5.14 show the PDFs of all three vorticity components for six wake locations. For each location, a Gaussian distribution with the same rms value is plotted for comparison with the PDFs. These six locations are the same as those in the spectra plots for ease of comparison.

In Figs. 5.12 and 5.13, the PDFs for the ω_x and ω_y components have similar patterns. Both have symmetric shapes which reflects the near-zero skewness values in this region. The differences from Gaussian distributions can be quantified with the flatness factor, which is 3 for a Gaussian. The differences are smallest near the centerline region where ω_x and ω_y have flatness values of approximately 5 (see Fig. 5.1(d)). Near the lower wake edge ($\eta = -1.65$), the ω_x and ω_y PDFs have much lower probability away from the mean vorticity than the Gaussian distributions, which indicates high intermittency. Note that these vorticity components are not as close to the Gaussian distributions as the velocity components are in Figs. 4.9 to 4.11, especially for the centerline region. For both components, the PDF at $\eta = -1.65$ has a very high peak around the mean vorticity. This means that the ω_x and ω_y fluctuations in this region are most probably quite small. The high fluctuating values, approximately 15 times the scale u_o/L_o, occur very rarely. Near the wake centerline, the peak value is much lower, with a wider distribution around the mean. This pattern reflects the intense vortical activity taking place in the center region.

In Fig. 5.14, the PDFs for ω_z show the asymmetry expected for a skewed variable.

These PDFs are significantly different from the Gaussian distributions even at the centerline region. For the lower wake, the PDFs have $-\omega_z$ peaks but have longer $+\omega_z$ tails, giving positive skewness values. For the upper wake, the opposite pattern is seen, and this yields negative skewness values. Near the lower wake edge ($\eta = -1.65$), the tails are long relative to the width of most of the distribution, which is why the flatness value is so high in this region. In the centerline region ($\eta = 0.12$), the PDF is quite symmetric so that the skewness value is approximately zero. Near the mean spanwise fluctuating vorticity value ($\omega_z = 0$), the PDF in the centerline region is broader than those in the outer wake, indicating more intense vortical activity.

5.5 Joint Probability Analysis of the Vorticity Components

The contours of the joint probability distribution functions (JPDFs) $P(\omega_x, \omega_y)$, and the covariance integrand $\omega_x \omega_y P(\omega_x, \omega_y)$, where

$$\overline{\omega_x \omega_y} = \int_{-\infty}^{+\infty} \int_{-\infty}^{+\infty} \omega_x \omega_y P(\omega_x, \omega_y) d\omega_x d\omega_y, \tag{5.13}$$

are shown in Fig. 5.15 for positions $\eta = -1.65$ to 1.29. The contours of the JPDFs are inclined about the horizontal axis by approximately $-45°$ for the lower wake, and about $+45°$ for the upper wake. The contours of the covariance integrand offer the additional information that there is a greater contribution to the covariance, $\overline{\omega_x \omega_y}$, from Q2 and Q4 than from Q1 and Q3 for the lower wake, and vice versa for the upper wake. Fig. 5.16 quantifies the quadrant contributions. These plots show that there is a strongly preferred orientation in the direction of the mean shear of the projection of the vorticity vector on the $x - y$ plane. This quantitatively illustrates the presence of vortical structures that are most probably inclined at approximately $\pm 45°$ from the wake centerline, which is consistent with the computational results of Meiburg & Lasheras [39] in Fig. 1.5. This preferred orientation is along the diverging legs (or braids) shown in Figs. 1.3 and 1.4, which is parallel to the axis of maximum positive strain rate. Approximately perpendicular to this is the preferred

orientation for the $\overline{uv}$ correlation, which is along the converging legs. The most probable inclination angles of $\pm 45°$ show that the vortical structures called braids tend to maximize the covariance $\overline{\omega_x \omega_y}$, as shown in Section 4.4.

In the quadrant analysis of $\overline{\omega_x \omega_y}$ in Fig. 5.16, the Q1 curve is almost identical to the Q3 curve, and Q2 curve is almost identical to the Q4 curve. This is consistent with the almost perfect symmetry observed in the JPDF and covariance integrand contours. The asymmetry of the total correlation from one side of the wake to the other (higher magnitude in the lower wake) is probably due to experimental accuracy, which also is evident in the asymmetry of $-\overline{uv}$ in Fig. 4.4.

Meiburg & Lasheras [39] calculated the dynamics of the laminar wake of a flat plate with a corrugated trailing edge. They showed that flow structures with streamwise vortices interact with the Kármán vortices to produce the three-dimensional closed vortex loops illustrated in Fig. 5.17. The two legs of these closed vortex loops have the orientation and rotation similar to the "double-roller" model of the vortical structure suggested by Grant [21] in Fig. 1.2, and also the diverging/converging flow structures around the saddle from the results of Browne *et al.* [9] in Fig. 1.3.

In the current measurements, the correlation $\overline{\omega_x \omega_y}$ is positive for the upper wake, which indicates that the diverging leg is the preferred orientation of the projection on the $x-y$ plane and has a larger contribution than the converging one. The positive value of $\overline{\omega_x \omega_y}$ is interpreted by Ong [44] as an indication of "hairpin" vortex structures in a turbulent boundary-layer. Perhaps the closed vortex loop in plane wake flow is a two-sided "hairpin" vortex. Since the current measurements are single-point and the Meiburg & Lasheras calculation is for a laminar wake, all of these speculations point to the need for a direct simulation or a large-eddy simulation of the turbulent plane wake.

The contours of the JPDF $P(\omega_x, \omega_z)$ and the covariance integrand $\omega_x \omega_z P(\omega_x, \omega_z)$ are shown in Fig. 5.18. There is symmetry in the distributions of both ω_x and ω_z

which is reflected in the JPDF plots. The covariance integrand contours show some slight preference in certain quadrants which is likely due to experimental uncertainty. The quadrant analysis in Fig. 5.19 indicates that the total correlation is slightly positive in the centerline region and slightly negative in the outer regions (roughly for $\eta > 0.7$), but this is within the accuracy of the data.

For $P(\omega_y, \omega_z)$, contours of the JPDFs and the covariance integrand are shown in Fig. 5.20. These contours and the quadrant plots in Fig. 5.21 clearly show almost zero correlation across the wake.

5.6 JPDF Analysis of Vorticity and Velocity Gradients

The correlations between the vorticity and the velocity gradient components make up the stretching/compression and reorientation term in the mean vorticity transport equation

$$\overline{U}_j \frac{\partial \overline{\Omega}_i}{\partial x_j} = \overline{\omega_j \frac{\partial u_i}{\partial x_j}} - \overline{u_j \frac{\partial \omega_i}{\partial x_j}} + \overline{\Omega}_j \overline{S}_{ij} + \frac{1}{Re} \frac{\partial^2 \overline{\Omega}_i}{\partial x_j \partial x_j}. \tag{5.14}$$

This term, the first on the right hand side, consists of nine correlations: $\overline{\omega_x \partial u/\partial x}$, $\overline{\omega_y \partial u/\partial y}$, $\overline{\omega_z \partial u/\partial z}$, $\overline{\omega_x \partial v/\partial x}$, $\overline{\omega_y \partial v/\partial y}$, $\overline{\omega_z \partial v/\partial z}$, $\overline{\omega_x \partial w/\partial x}$, $\overline{\omega_y \partial w/\partial y}$, $\overline{\omega_z \partial w/\partial z}$. JPDF analysis of the individual correlations can shed some light on the question: how do the reorientation, stretching and compression processes of the velocity gradients increase or decrease the vorticity?

Schematic models in Fig. 5.22 of the different physical processes will aid in the discussion of the individual correlations. As illustrated in the top sketch, the ω_x component of either sign is stretched by $+du/dx$, and conversely, compressed by $-du/dx$. In the bottom sketch, the velocity gradient du/dy will shear and reorient ω_y about the $z-$axis into ω_x. This latter process represents a transfer of ω_y vorticity into ω_x. Similarly, in the same sketch, the dw/dx gradient will reorient ω_x about the $y-$axis into ω_z.

Figs. 5.23 to 5.40 show the JPDF contours, covariance integrand contours and the quadrant analysis of the above nine correlations. The quadrant analysis plots indicate that two correlations which involve the gradients of the spanwise velocity, $\overline{\omega_x \partial w/\partial x}$ and $\overline{\omega_y \partial w/\partial y}$, have the largest magnitudes (due to limitations of the graphics software, the partial derivative symbol is represented as regular derivative symbol in all figures). The other correlations are almost zero across the wake. Quadrant analysis of the individual correlations can also explain how the velocity gradients increase or decrease the vorticity components.

Fig. 5.23 shows that $P(\omega_x, \partial u/\partial x)$ is symmetric with respect to the vertical axis ($\omega_x = 0$). Even though it is not so obvious in the covariance integrand contours, the vortex stretching (Q1 & Q2) contribute more to the covariance than the vortex compression (Q3 & Q4) as seen in Fig. 5.24, yielding a net gain in ω_x. Q2 and Q4 have higher magnitudes than Q1 and Q3 in the lower wake resulting in a small negative correlation there, but this is due to measurement inaccuracy.

For $P(\omega_y, \partial u/\partial y)$, Fig. 5.25 shows that the four quadrants have almost the same level of contributions, as seen in both the JPDFs and the covariance integrand contours. There seems to be preference in certain quadrants even though the contour levels for such cases are quite small. The quadrant plots in Fig. 5.26 confirm that, for the lower wake, the Q3 and Q4 contributions are higher than Q1 and Q2, and vice versa in the upper wake. The term represents the shearing of ω_y vortex lines by the velocity gradient $\partial u/\partial y$ into the streamwise direction. The gain of $+\omega_x$ by $+\partial u/\partial y$ shearing on $+\omega_y$ is balanced by the gain of $-\omega_x$ by $+\partial u/\partial y$ shearing on $-\omega_y$. Similar conclusion can be drawn about the shearing due to $-\partial u/\partial y$. The total correlation is almost zero across the wake, which indicates that there is no net gain of ω_x by $\partial u/\partial y$ shearing.

For $P(\omega_z, \partial u/\partial z)$, Fig. 5.27 shows the symmetry with the horizontal axis ($\partial u/\partial z = 0$). In the covariance integrand contours, there seems to be preference in certain

quadrants which distorts the symmetry picture but the contour levels for such cases are quite small, and this is very likely just due to measurement error. The quadrant plots in Fig. 5.28, which show that the magnitude of Q1 is almost the same as Q4, and Q2 is almost the same as Q3, confirm this observation. These plots also show that, for the lower wake, the Q1 contribution is higher than Q3, and Q4 is higher than Q2, and vice versa in the upper wake, although all four quadrants are more nearly equal there. This small asymmetry is probably due to measurement limitations. Similar to $\overline{\omega_y \partial u/\partial y}$, discussed above, the total correlation here is about zero across the wake, which indicates that there is no net gain of ω_x by $\partial u/\partial z$ shearing.

For $P(\omega_x, \partial v/\partial x)$, Fig. 5.29 shows that the four quadrants have almost the same level of contribution as seen in both the JPDFs and the covariance integrand contours. There seems to be preference in certain quadrants but the contour levels for such cases are again quite small, and the difference is within the measurement accuracy. This quadrant equality is confirmed in Fig. 5.30. The correlation represents the shearing action of the velocity gradient $\partial v/\partial x$ on the streamwise vortex lines reorienting them into the transverse direction. The nearly zero net correlation value indicates that there is no net gain or loss of ω_x to ω_y due to $\partial v/\partial x$ shearing. The gradient $\partial v/\partial x$ is one component of ω_z, and the patterns of all quadrants in $\overline{\omega_x \partial v/\partial x}$ in Fig. 5.30 are almost the same as those of $\overline{\omega_x \omega_z}$ in Fig. 5.19 except for the magnitudes.

For $P(\omega_y, \partial v/\partial y)$, the correlation represents a stretching/compression term and Fig. 5.31 shows that the four quadrants have almost the same level of activity as seen in both the JPDFs and the covariance integrand contours. The quadrant plots in Fig. 5.32 confirm this with the total correlation about zero across the wake. For part of the upper wake, the Q1 contribution is slightly higher than Q3, and Q2 is slightly higher than Q4. But these differences are certainly due to measurement error. In any case, Fig. 5.32 clearly shows that the stretching and compression processes balance

out so no net gain or loss of ω_y occurs.

For $P(\omega_z, \partial v/\partial z)$, Fig. 5.33 shows general symmetry about the horizontal axis ($\partial v/\partial z = 0$). In the covariance integrand contours, there seems to be some small preference in certain quadrants which distorts the symmetry picture, but the contour levels for such cases are again quite small, and these differences are within the noise of the data. The quadrant plots in Fig. 5.34 confirm the symmetry showing that the magnitudes for all quadrants are about the same. The total correlation is almost zero across the wake indicating that the transverse vorticity component has no net gain or loss from $\partial v/\partial z$ shearing on the spanwise vorticity component.

For $P(\omega_x, \partial w/\partial x)$, Fig. 5.35 shows that the JPDF contours are tilted approximately $+25°$ from the ω_x axis at $\eta = -1.65$ and $-25°$ at $\eta = 1.29$. All other correlations between vorticity components and velocity gradients discussed so far have been symmetric around either the horizontal, or vertical axis. Part of the reason for the non-zero correlation here is because $\partial w/\partial x$ is one component of ω_y. The JPDF contours for ω_x and ω_y have been shown above to be inclined at approximately $\pm 45°$. The quadrant plots in Fig. 5.36 show that the JPDF contours are almost perfectly symmetric. The Q1 curve lies on top of the Q3 curve, and the Q2 curve is on top of the Q4 curve. The correlation $\overline{\omega_x \partial w/\partial x}$ is antisymmetric across the wake; its value is positive for the lower wake and negative for the upper wake. This means that $\partial w/\partial x$ predominantly shears ω_x of like sign to increase positive ω_z in the lower wake, and predominantly shears ω_x of unlike sign to increase negative ω_z in the upper wake.

For $P(\omega_y, \partial w/\partial y)$, Fig. 5.37 shows that Q1 contribution is about the same as that for Q3, and Q2 is the same as Q4, as seen in both the JPDFs and the covariance integrand contours. This pattern is confirmed in the quadrant plots in Fig. 5.38 in which the Q1 curve is almost on top of the Q3 curve, and likewise for Q2 and Q4. Across the wake, Q1 and Q3 generates $+\omega_z$; Q2 and Q4 generates $-\omega_z$. The

equal contributions from Q1 and Q3 means that the generation of $+\omega_z$ by $+\partial w/\partial y$ shearing of $+\omega_y$ is the same as that by $-\partial w/\partial y$ shearing of $-\omega_y$. Similar deduction can be made about the equal contributions from Q2 and Q4 across the wake. The Q2 and Q4 contributions are dominant in the lower wake so that the total correlation $\overline{\omega_y \partial w/\partial y}$ is negative there. The opposite is true in the upper wake. This means the correlation reduces the strength of $\overline{\Omega}_z$ which is positive in the lower wake and negative $\overline{\Omega}_z$ in the upper wake. These reductions are approximately balanced by the enhancements of $\overline{\Omega}_z$ due to the correlation $\overline{\omega_x \partial w/\partial x}$ discussed in the previous paragraph and seen in Fig. 5.36. Therefore, one can deduce for plane wake flows that

$$\overline{\omega_x \frac{\partial w}{\partial x}} + \overline{\omega_y \frac{\partial w}{\partial y}} \approx 0. \tag{5.15}$$

Physically, this approximation means that for plane wake flows, whatever intensity ω_z gains from ω_x is mainly taken by ω_y, and whatever intensity ω_z gains from ω_y is, in turn, taken by ω_x. In this regard, the ω_z just serves as the vehicle for vorticity exchange between ω_x and ω_y.

Now we come to the last stretching/compression term, $\overline{\omega_z \partial w/\partial z}$. This correlation is also the last among the three that can generate spanwise vorticity. For $P(\omega_z, \partial w/\partial z)$, the JPDF contours in Fig. 5.39 are almost symmetric about the horizontal axis ($\partial w/\partial z = 0$). But, the covariance integrand contours indicate a weak preference for Q1 in the lower wake and for Q2 in the upper wake. This pattern is confirmed in the quadrant plots in Fig. 5.40. These plots clearly show that the magnitudes of Q1 and Q2 curves are larger than those for Q3 and Q4 in the lower and upper wake wake regions, respectively. This means vortex stretching (Q1 & Q2) of either sign ω_z dominates vortex compression (Q3 & Q4) of either sign ω_z. The total correlation is thus approximately zero across the wake indicating no net gain of ω_z.

5.7 Summary

The discussion in the above sections has demonstrated the following:

1. The miniature 12-sensor probe can measure simultaneously velocity and vorticity with good accuracy in the near-wake of a circular cylinder for $x/d = 20-30$.

2. Central-differencing, which results in proper phase alignment of the streamwise velocity gradients with the directly measured variables, should be used in applying Taylor's hypothesis.

3. The measured mean spanwise vorticity component agrees well with the derivative of the mean streamwise velocity. The other mean vorticity components are about zero. This is a good test of the accuracy of the measurements.

4. At $x/d = 30$, the rms of the streamwise vorticity is highest, followed by the transverse and the spanwise components. The rms values for the transverse and spanwise components are somewhat attenuated due to the low sampling rate.

5. The skewness and flatness values for the vorticity components have the proper characteristics for a plane wake. These values are high at the wake edges and have nearly Gaussian values in the centerline region.

6. Only the spectra of the spanwise vorticity component show intensity peaks at the shedding frequency, indicating parallel shedding.

7. The extremely narrow PDFs of all vorticity components in the freestream compared with the centerline region indicate a high signal-to-noise ratio of up to 2 orders of magnitude.

8. The JPDF contours of $\overline{\omega_x \omega_y}$ show a preferred orientation that is along the direction of the mean shear. Therefore, ω_x and ω_y are negatively correlated

in the lower wake and positively correlated in the upper wake. The pattern is consistent with the computational results of Meiburg & Lasheras [39]. Other vorticity correlations are about zero across the wake.

9. The correlations of vorticity and velocity gradients are about zero across the wake except for those that involve gradients of the spanwise velocity.

10. Quadrant analysis of the correlation $\overline{\omega_x \partial u/\partial x}$ and $\overline{\omega_z \partial w/\partial z}$ show more stretching than compression activity across the wake.

11. The ω_z component serves as the vehicle for vorticity exchange between the ω_x and ω_y components.

6 Conditional Analysis

6.1 Motivation

The goal of this chapter is to characterize the "coherence" of the turbulent fluctuating velocity and vorticity fields with the shedding vortices. "Coherence" here means the phase locking of the fluctuating velocity (or vorticity) field with a certain phase of the periodic shedding vortices. In the near-wake of a bluff body, the vortex shedding is regular and the shedding frequency is governed by the Strouhal-Reynolds number relationship. This has been illustrated in the spectra of the variables u, v, and ω_z in Chapters 4 & 5.

Using a phase of the vortex shedding as a conditioning detection criterion is just one of many different possibilities of conditional averaging. Browne *et al.* [9] conditionally sampled on temperature to detect large-scale coherent structures in the far wake region ($x/d = 420$) of a circular cylinder. They decomposed the fluctuating velocity components into the incoherent, and coherent parts. For these structures detected by Browne *et al.* , the contribution to the Reynolds shear stress from the incoherent motion is much larger than that from the coherent motion. As described in Section 1.3, Cantwell & Coles [10] measured in the region within 8 diameters downstream of a circular cylinder using two X-wire probes mounted on a pair of whirling arms. They deduced a pattern of moving vortex centers and saddles (these flow regions are illustrated in Fig. 1.4) by analyzing the decomposed signals and found that a substantial part of the turbulence production is concentrated near the saddles. Their data showed that the Reynolds normal stresses due to the incoherent motion have maxima near each vortex center, and the magnitude of the incoherent shear stress has a maximum near the saddle between the vortices. In the near-wake of a circular cylinder, Hussain & Hayakawa [26] measured the large-scale spanwise

vorticity using a rake of X-probes positioned in the plane of the mean shear. They deduced the passage of the spanwise vortices using the measured coherent vorticity as the trigger signal. For the measurement station of $x/d = 30$, they found that the spanwise vortex center was slightly less than one cylinder diameter from the centerline. They observed similar patterns for the Reynolds shear stresses and turbulent kinetic energy as had Cantwell & Coles. No observations about enstrophy was made, because only the spanwise component of vorticity was measured. These investigations point to a need for simultaneous measurements of all the velocity and vorticity vector components to elucidate some basic characteristics of the vortical structures. Therefore, in this chapter, the simultaneous measurements of velocity and vorticity will be analyzed using the passage of the shed vortex for phase referencing. The following section will describe the detection scheme.

6.2 Description of the Conditioning Detection Scheme

The detected event used as the conditioning criterion was chosen to be the passage of the shed vortex. This was achieved by: (1) band-pass filtering the time series of the spanwise vorticity component in a narrow band around the shedding frequency, and (2) using a phase of this periodic time series as the phase reference for ensemble averaging all other variables considered.

First, the ω_z spectrum was narrow band-pass filtered around the shedding frequency f_s, and an inverse Fourier transformation was performed to produce a time series of the phase reference signal. A square band-pass filter was used over 3 frequency bins ($\approx$ 4 Hz bandwidth) with the shedding frequency centered in the middle one. The two additional bins are for smoothing the spectrum of the background turbulence signal which is the difference between the total fluctuating signal and the phase reference signal. The square filter has negligible leakage effects on neighboring frequency bins. Because the inverse Fourier transform was performed on blocks

containing 512 samples out of approximately 180000 samples to obtain a time series, a moving window technique was used to smooth out the difference between blocks of data in the transformation. This technique simply overlaps consecutive blocks resulting in an averaging effect for the overlapped regions.

The result of this process is illustrated in Fig. 6.1 which shows the spectra of the total fluctuating ω_z signal, the phase reference signal, and the background turbulence signal. The reference signal spectrum has a peak at the shedding frequency, and negligible energy at all other frequencies. The background turbulence spectrum is smooth in the filtered frequency band since it was designed to filter only the additional contribution of the shed vortex. For each wake position, this process was repeated to produce separate and local detection signals. Therefore, phase information between various wake locations is not directly available.

An instantaneous turbulent signal can be decomposed into 3 parts: mean, coherent, and incoherent. This technique was first introduced by Reynolds & Hussain [52] to study the dynamics of travelling waves in a turbulent flow. For a variable $F(x_i, t)$ one can write

$$F(x_i, t) = \overline{F}(x_i) + \tilde{f}(x_i, t) + f'(x_i, t), \tag{6.1}$$

where $\overline{F}(x_i)$ is the mean or time average, $\tilde{f}(x_i, t)$ is the coherent signal, and $f'(x_i, t)$ is the incoherent signal. The last two parts make up the total fluctuating signal

$$f(x_i, t) \equiv \tilde{f}(x_i, t) + f'(x_i, t). \tag{6.2}$$

The coherent signal $\tilde{f}$ can be obtained from the *phase average* of F which is defined as

$$<F(x_i, t)> \equiv \lim_{N\to\infty} \frac{1}{N} \sum_{j=1}^{N} F(x_i, t + jT) \equiv \overline{F} + \tilde{f}, \tag{6.3}$$

where T is the vortex shedding period and $N \approx 14700$ for this experimental data set. The phase information for the phase average comes from the reference signal

obtained with the filtering process described earlier. It follows that $<F>$ is periodic and

$$<f> = \tilde{f}, \text{ and } <f'> = 0. \tag{6.4}$$

The coherent and incoherent fields can be shown to be uncorrelated, i.e.,

$$<\tilde{f}f'> = \overline{\tilde{f}f'} = 0. \tag{6.5}$$

Therefore, it follows that

$$<(\tilde{f} + f')^2> = <\tilde{f}^2> + <f'^2> . \tag{6.6}$$

Fig. 6.2 shows the total fluctuating, coherent, and incoherent parts of ω_z. The $\tilde{\omega}_z$ signal is quite periodic except for some occasional small jitter. The period T is approximately 6 ms, because the shedding frequency is about 168 Hz. Hussain [25] and Hussain & Hayakawa [26] have indicated that the spanwise vorticity should be used to detect coherent structures in turbulent wake flows. Furthermore, they emphasized that using the local signal for phase-referencing smears the structure less than using an external phase-reference signal as was done by Cantwell & Coles [10]. The vortex center passage, they assumed, would be associated with a local maximum of $\tilde{\omega}_z$ in the lower wake, and a local minimum of $\tilde{\omega}_z$ in the upper wake. They described a saddle as the region between two consecutive spanwise vortices that is associated with a local minimum of $\tilde{\omega}_z$ in the lower wake and a local maximum of $\tilde{\omega}_z$ in the upper wake. Therefore, in the current work, an event detected by a local maximum in $\tilde{\omega}_z$ was presumed to be near the vortex center in the lower wake and to be near the saddle in the upper wake. To describe the saddle and vortex center locations in terms of $<\Omega_z>$ it is important to recall that the mean vorticity $\overline{\Omega}_z$ is positive in the lower wake and negative in the upper wake. One can visualize a vortex shedding pattern, detected by maxima in $\tilde{\omega}_z$ on either side of the wake, as depicted in Fig. 6.3. This model is derived from a combined analysis of the velocity vector plots and $\tilde{\omega}_z$ contours

of Hussain & Hayakawa [26], and of the present database. The streamwise and lateral dimensions of the vortices are estimated to give a rough idea where the vortex center and saddle regions are located. The vortex shedding period and mean streamwise velocity at the half-deficit point are used to estimate the streamwise extent of the vortices. The vortex center locations and their lateral extent are estimated from the $\tilde{\omega}_z$ contours at $x/d = 30$ of Hussain & Hayakawa. The vortices are shed alternately so that the vortex center on one side is ahead (or behind) a vortex on the other side by approximately half the distance between consecutive vortices. The arrows between the shed vortices illustrate the converging and diverging flow regions which drive fluid toward or away from the saddle region, respectively, creating a highly strained flow there. The streamwise location of the detected event can be visualized as a line approximately normal to the wake centerline, running through the vortex center in the lower wake, and the saddle region in the upper wake as indicated on Fig. 6.3. Interpretation of the following conditional analyses should take into account the fact that the current database was obtained by single-point measurements. Also, the locations of the vortex centers and the saddles in Fig. 6.3 are rough estimates since the Reynolds number in Hussain & Hayakawa is 13400, almost seven times that for the present data. For all analyses in this chapter, measurements at $x/d = 30$ were used.

6.3 Conditional Analysis of the Velocity Vector Field

The $<u>$ ($\equiv \tilde{u}$) values for 6 cross-stream locations are shown in Fig. 6.4. Here, and in subsequent plots, velocity is normalized by the wake deficit u_o and time is normalized by the period T of the vortex shedding. Note that, by definition, $\overline{<u>} = 0$. For $\eta = -1.06$, this component has a peak near the detection time which is associated with the passage of the vortex center in the lower wake. Positive time corresponds to upstream and negative to downstream of the vortex center. Therefore, for the

lower wake, $t/T = 0$ corresponds to the passing of the vortex center, and $t/T = \pm 0.5$ corresponds to the passing of the saddle regions. At $\eta = -1.06$, the peak near $t/T = 0.1$ indicates that u has strongest coherence at a location slightly upstream of the vortex center.

For $\eta = 0.71$ and 1.29 in Fig. 6.4, in the upper wake, the detected event corresponds to the saddle region so the velocity at $t/T = 0$ is negative, with positive values of $<u>$ on either side due to the passage of the vortex centers. The degree of phase coherence varies depending on the wake positions; it is low near the wake edges and around the wake centerline, and high in the region in between. The wake centerline region ($\eta = 0.12$) has almost zero phase coherence, probably because it is outside the domains of influence of the lower vortex center and the upper saddle regions (see the schematic model in Fig. 6.3).

Fig. 6.5 depicts the $<u^2>$ values. From Eq. (6.6),

$$<u^2> = <\tilde{u}^2> + <u'^2>, \tag{6.7}$$

hence both the intensity of the coherent part and the phase alignment of the incoherent part are represented in this quantity. Unlike $\overline{<u>}$, $\overline{<u^2>}$ is nonzero and represents the conditional variance of the total streamwise velocity fluctuations. The incoherent part, $<u'^2>$, is almost the same as the total, and thus is not shown in the figure. The values of $<\tilde{u}^2>$ are everywhere less than 0.007. One striking feature is that the vortex center has a maximum and the saddle has a minimum for this Reynolds normal stress. In the absence of vortex shedding $<u'^2>$ would have been a constant equal to the variance $\overline{u'^2}$. The fact that $<u'^2>$ oscillates around $\overline{u'^2}$ is an indication that a significant fraction of the incoherent fluctuations are phase locked to the vortex shedding. In Section 6.5, an attempt to quantify the degree of locking will be presented.

The schematic model in Fig. 6.3 can help to explain the patterns of $<v>$ in Fig. 6.6. For $\eta = -0.47$ and -1.06 (the lower wake) where the vortex center passage is at

$t/T = 0$, the downstream region should have an upward motion, as seen for $t/T < 0$, and the upstream region should have a downward motion, as seen for $t/T > 0$. For $t/T = \pm 0.5$, i.e. in the saddle region, $<v>$ returns to zero. Likewise, the combined effects of the converging and diverging legs of the saddle region in the upper wake ($\eta = 0.71$ and 1.29) produce positive v motion for $t/T < 0$ and negative for $t/T > 0$. Note further that the coherent $v-$fluctuations are strongest near the wake centerline and are weaker toward the wake edges. This is because the lower spanwise vortices combine their effects in the centerline region with the upper saddle regions for the vertical motion. The schematic model in Fig. 6.3 shows that, for $y/L_o > 0$ near the wake centerline, the downstream region ($x/L_o > 0$) of the saddle has upward flow. This is combined with the upward motion of the lower vortex at the same streamwise region. Similar reasoning can be made to show that the downward motion near the wake centerline receives contributions from both the vortex and saddle regions. The symmetry of the $<v>$ plots indicates that the vortex motions are symmetric in the $<v>$ field.

Fig. 6.7 shows the $<v^2>$ and $<v'^2>$ terms in the equation

$$<v^2> = <\tilde{v}^2> + <v'^2> . \tag{6.8}$$

Unlike $<\tilde{u}^2>$ in Eq. (6.7), $<\tilde{v}^2>$ is quite significant and is the difference between $<v^2>$ and the incoherent contribution $<v'^2>$. For $\eta = -0.47$, $<v'^2>$ peaks at $t/T = 0$, whereas $<v^2>$ peaks at $t/T = 0.2$. This is due to $\tilde{v}$, which has been shown in Fig. 6.6 to have maximum values around $t/T = \pm 0.25$. In the upper wake, for $\eta = 0.71$ and 1.29 where the vortex center is at $t/T = \pm 0.5$ and the saddle is at $t/T = 0$, the incoherent part has a minimum near $t/T = 0.25$. For $\eta = 0.71$, the total part is minimum near $t/T = 0$ due to zero contribution from $\tilde{v}$ here. Since $\overline{\tilde{v}^2}$ is largest in the wake centerline region where $\overline{\tilde{u}^2}$ is about zero, $\overline{v^2}$ is larger than $\overline{u^2}$ here even though $\overline{v'^2}$ is not. For $\eta = -1.06$, and -0.47, $<v'^2>$ is higher in the region upstream of a vortex center (which is in the converging leg of the saddle) than in

the region downstream. One can also see a similar pattern in the upper wake (where upstream of the saddle is equivalent to downstream of the vortex center) except near the centerline where there is almost symmetry. Therefore, this phenomenon reveals the significance of the converging leg of the saddle, which is also discussed in Section 4.4.

The $<w>$ values in Fig. 6.8 show weak coherence with the vortex motion. This is not surprising since the vortex shedding is parallel. The maximum $<w>$ is about 3% of the wake deficit u_o, and only slightly higher than the 1% measurement uncertainty reported in Section 3.5.

Fig. 6.9 shows the $<w^2>$ values in the equation

$$<w^2> = <\tilde{w}^2> + <w'^2> . \tag{6.9}$$

The incoherent part, $<w'^2>$, is not shown since it is practically the same as the total due to the extremely small values of $<\tilde{w}^2>$. In other words, $<w^2>$ is completely due to the phase locking of the incoherent w' fluctuations. This phase locking is small near the wake centerline and the wake edges, and is maximum near the centers of the upper and lower vortices ($t/T = 0$ at $\eta = -0.47$ and $t/T = \pm 0.5$ at $\eta = 0.71$). The values of $<u'^2>$ and $<v'^2>$ show similar behavior as seen in Figs. 6.5 and 6.7. Therefore, the incoherent Reynolds normal stresses have maxima near the vortex center. This is consistent with observations of Cantwell & Coles [10].

Fig. 6.10 presents the phase averages of the total and the incoherent turbulent kinetic energy, k, which is defined as

$$<k> = <\tilde{k}> + <k'>, \tag{6.10}$$

where

$$k \equiv \frac{1}{2}(u^2 + v^2 + w^2), \tag{6.11}$$

$$\tilde{k} \equiv \frac{1}{2}(\tilde{u}^2 + \tilde{v}^2 + \tilde{w}^2), \tag{6.12}$$

$$k' \equiv \frac{1}{2}(u'^2 + v'^2 + w'^2). \tag{6.13}$$

Across the wake, the total is only slightly higher than the incoherent contribution. For both the incoherent and total fluctuating parts, Fig. 6.10 shows a maximum coherence near the vortex center, at $t/T = 0$ for $\eta = -0.47$, and a minimum near the saddle region, at $t/T = 0$ for $\eta = 0.71$. The coherence is lower near the wake centerline and at the wake edges. The coherence shows near symmetry in the streamwise direction around the vortex center and saddle regions. These patterns are consistent with earlier observations for the component variances.

Fig. 6.11 depicts the phase averages of the stress uv and its incoherent part, $u'v'$, which are related by

$$<uv> = <\tilde{u}\tilde{v}> + <u'v'> . \tag{6.14}$$

Across the wake, the total is only slightly different from the incoherent contribution. The coherent contribution is very small mainly because $<u>$ is small. Fig. 6.11 reveals a strikingly clear pattern that at the vortex center, $<uv>$ has the lowest magnitude (≈ 0.01), and at the saddle, it has the highest (≈ 0.08). The left column is for the lower wake, and $<uv>$ has a positive sign except around $t/T = 0$ for $\eta = -0.47$; the right column is for the upper wake, and $<uv>$ has a negative sign everywhere except near the centerline ($\eta = 0.12$). The high $<uv>$ values in the saddle region (0.09 for $\eta = -0.47$ and -0.08 for $\eta = 0.71$) means that turbulence production is predominantly occuring there, and the vortex center just collects the turbulent kinetic energy produced in the saddle regions. The wake centerline region ($\eta = 0.12$) also has significant $<uv>$ values, but this high correlation does not result in high energy production since the average over the period is almost zero here. These observations are consistent with the findings of Hussain & Hayakawa [26] and Cantwell & Coles [10]. Hussain & Hayakawa reported a peak $<u'v'>$ value of approximately 0.006 U_∞^2 at $x/d = 30$. The peak $<u'v'>$ at $\eta = -0.47$ in Fig. 6.11 is

about 0.0025 U_∞^2. The value from Hussain & Hayakawa is higher probably because their accepted structures must have "large-scale vorticity concentration", whereas the structures in the current measurements are the periodic Kármán vortices.

An interesting feature revealed in Fig. 6.11 is that $\overline{u'v'}$ is a little higher than $\overline{uv}$ for $\eta = -0.47$, and a little lower than $\overline{uv}$ for $\eta = 0.71$. Therefore, Eq. (6.14) shows that $\overline{\tilde{u}\tilde{v}}$ has the opposite sign compared to $\overline{uv}$. This corresponds to negative coherent energy production (i.e., the vortex is decaying) as presented in the next chapter.

6.4 Conditional Analysis of the Vorticity Vector Field

The vorticity values are normalized with the wake deficit u_o and the wake half-width L_o for the plots in this section. Across the wake, the $<\omega_x>$ values are about zero as seen in Fig. 6.12. There is very low level of coherence upstream and downstream of the detected events but this is within the error of the data.

Fig. 6.13 presents the phase averages $<\omega_x^2>$. From Eq. (6.6),

$$<\omega_x^2> = <\tilde{\omega}_x^2> + <\omega_x'^2>, \tag{6.15}$$

but the incoherent part (not shown) is practically the same as the total due to the extremely small values of $<\tilde{\omega}_x^2>$. Therefore, $<\omega_x^2>$ is completely due to the phase locking of the incoherent ω_x' fluctuations. The $<\omega_x^2>$ values show strong coherence with the passage of the shed vortices as seen in Fig. 6.13. The $\eta = -1.06$ plot has a peak in $<\omega_x^2>$ for the region upstream of the vortex center ($t/T > 0$). This phenomenon is directly observed here for the first time due to the availability of these vorticity data. It can be explained with the aid of the vortex model in Fig. 6.3. With regard to lateral position, the $\eta = -1.06$ point is slightly outside of the vortex center and is about the level of the saddle region. At this lateral position, upstream of the detection event is the diverging leg, and downstream is the converging leg of the saddle region. At $\eta = -1.06$, the high $<\omega_x^2>$ in the upstream region compared to the downstream region means that the diverging leg is dominant over the converging

leg (the diverging leg is associated with stretching of ω_x, which increases $<\omega_x^2>$; by contrast, the converging leg is associated with compression).

This phenomenon can also be seen in the upper wake, at $\eta = 1.29$, where the detected event is the saddle region. The downstream region is the diverging leg of the saddle ($t/T < 0$) and has higher $<\omega_x^2>$ than the upstream converging leg. The schematic vortex model in Fig. 6.3 illustrates these flow regions as arrows in the plane of the mean shear. This diverging leg, commonly called "braid", could extend to the wake edges and join with the converging leg of the downstream saddle at a different spanwise location. This is a possible mechanism for the generation of three-dimensional flow structures. Hussain & Hayakawa [26] speculated that these braids with predominantly streamwise vorticity interact with the spanwise vortices to produce "small-scale, three-dimensional vorticity fluctutations". Meiburg & Lasheras [39] showed from inviscid vortex calculation that the braids containing streamwise vortices interact with the Kármán vortices to produce three-dimensional closed vortex loops illustrated in Fig. 5.17.

The $<\omega_y>$ values also show very low coherence with the vortex shedding across the wake as seen in Fig. 6.14. For the correlation ω_y^2, Eq. (6.6) shows that

$$<\omega_y^2> = <\tilde{\omega}_y^2> + <\omega_y'^2>, \tag{6.16}$$

but the incoherent part is practically the same as the total due to the extremely small $<\tilde{\omega}_y^2>$. Therefore, $<\omega_y^2>$, shown in Fig. 6.15, is completely due to the phase locking of the incoherent $<\omega_y'^2>$. The coherence is quite strong, although less than $<\omega_x'^2>$. Near the vortex centers, $\eta = -0.47$ for the lower wake and $\eta = 0.71$ for the upper wake, the coherence is stronger than at other wake locations. The high coherence lateral positions for $<\omega_x^2>$ are relatively closer to the wake edges. Note that even though the rms values of the fluctuating ω_x and ω_y are approximately the same across the wake, as seen in Fig. 5.1(b), the streamwise vorticity variance has

significantly higher coherence with the passage of the shed vortices than the lateral component.

The $<\omega_z>$ values obviously show high coherence at all wake positions in Fig. 6.16 since it is the phase reference variable. The peaks at $t/T = 0$ characterize the detection events and the phase averages are symmetric around these points. The large peak value of $<\omega_z>$ at $\eta = -0.47$ compared to other locations indicates that the vortex center is near this point. Also, the symmetry around the detection time $t/T = 0$ for all 6 locations show that the educed vortex center is probably half-way between two saddle regions. This observation is consistent with Hussain & Hayakawa [26].

For the correlation ω_z^2, Eq. (6.6) shows that

$$<\omega_z^2> = <\tilde{\omega}_z^2> + <\omega_z'^2>, \tag{6.17}$$

and Fig. 6.17 indicates that the incoherent contributions are almost the same as the total, except for small differences at the detected event of $\eta = -0.47$. Both show significant coherence with the vortex passage at all wake positions. One can deduce that the vortex center lies somewhere in the vicinity of $\eta = -0.47$ (or $\eta = 0.71$ for the upper wake) since the coherence is strongest there. At $\eta = -0.47$, the peak of $<\omega_z'^2>$ at $t/T = 0$ can be considered a signature of the vortex center. An interesting point is that the minimum level of $<\omega_z^2>$ is about 2 sample intervals upstream of the detected event in the upper wake. Recall that for $<\omega_x^2>$ in Fig. 6.13, the region upstream of the saddle also has lower coherence than the downstream region. These observations indicate that the region upstream of the saddle is characterized by lower vorticity fluctuations, relative to the region downstream.

Enstrophy, ε, is defined as one-half the sum of the vorticity variances, and the coherence of the enstrophy reflects a combination of the 3 variance phase averages. For the total ε, Eq. (6.6) shows that

$$<\varepsilon> = <\tilde{\varepsilon}> + <\varepsilon'>, \tag{6.18}$$

where ε, $\tilde{\varepsilon}$ and ε' are defined similarly to their kinetic energy analogs (Eqs. (6.11) to (6.13)). Fig. 6.18 indicates that the incoherent contributions are almost the same as the total across the wake. Only near the detected events, vortex center or saddle, is the difference significant. Fig. 6.18 shows that the peak coherence occurs at $\eta = -0.47$ at the detection event ($t/T = 0$) which is near the vortex center. At $\eta = 0.71$, the coherence is minimum at $t/T = 0.25$ or 3 sample intervals upstream of the saddle. This means that even though the turbulent vorticity field is predominantly incoherent, the magnitude of the vorticity fluctuations are intensified significantly when a vortex center passes by. The opposite is true when the saddle region passes by. Near the wake edges, the $\eta = -1.65$ location still exhibits some coherence, which indicates that the field of influence of the spanwise vortex probably extends greater than $1.6L_o$.

The phase averages of the dissipation rate, ϵ, are shown in Fig. 6.19. Eq. (6.6) shows that

$$<\epsilon> = <\tilde{\epsilon}> + <\epsilon'>, \tag{6.19}$$

but the incoherent contribution is practically the same as the total which is the only quantity shown in Fig. 6.19. The phase averages of the dissipation rate follow closely the pattern of the enstrophy (they should be identical if the fluctuating field was isotrophic).

6.5 Phase-Locking with the Vortex Shedding

In this section, the degree of coherence or phase locking of incoherent, turbulent fluctuating quantities with the vortex shedding will be quantified. Only locking of second order correlations will be presented.

The phase locking parameter, $\mathcal{L}$, for the incoherent components of two variables f_1 and f_2 is defined as

$$\mathcal{L} \equiv \frac{r_{1-2}}{r_1 r_2}, \tag{6.20}$$

where r_1 and r_2 are the rms values of the two variables. The magnitude of the phase locking, r_{1-2}, is defined as

$$r_{1-2} \equiv \sqrt{\frac{1}{N_P}\left(\sum_{i=1}^{N_P}(<f_1 f_2>_i - \overline{f_1 f_2})^2\right)}, \tag{6.21}$$

where N_P is the number of points per period of the vortex shedding (12 for the present data). For $f_1 = f_2 = u'$, the normalization factor $r_1 r_2$ becomes simply the local variance $\overline{u'^2}$. $\mathcal{L}$ would be zero in this case if $<u'^2>$ does not vary with respect to $\overline{u'^2}$ over the period of the shedding.

The phase locking values for the incoherent Reynolds normal stresses are shown in Fig. 6.20. For u'^2, the value of $\mathcal{L}$ reaches a maximum of 15% of $\overline{u'^2}$ at approximately $\eta = 0.7$. The centerline region has a lower phase locking value of 5%, about the same as those at the wake edges. The phase locking values for v'^2 are slightly higher than those for u'^2 and peak around $\eta = 1.0$. The value near $\eta = 0$ is also a minimum. Interestingly, although $\tilde{w}$ is about zero, w'^2 has the highest phase locking among the normal stresses. This illustrates strong phase-locking of spanwise velocity fluctuations to the vortex passage. The maximum locking values are also near $\eta = \pm 0.7$, locations determined in the previous sections to be near the vortex centers.

The values of $\mathcal{L}$ for the variances of the incoherent vorticity components are shown in Fig. 6.21. For $\omega_x'^2$, the value of $\mathcal{L}$ reaches a maximum of 18% of $\overline{\omega_x'^2}$ at approximately $\eta = 1.0$. The locking for $\omega_y'^2$ are much lower at approximately 5% of $\overline{\omega_y'^2}$ across the wake. The locking values for $\omega_z'^2$ are substantial higher than the other two values and reach maxima of approximately 26% of $\overline{\omega_z'^2}$ at the vortex center regions ($\eta = \pm 0.7$). Like the Reynolds normal stresses, the vorticity variances also have minimal locking around the centerline region.

The phase locking values for the incoherent Reynolds shear stress $u'v'$ are shown in Fig. 6.22 to reach a maximum of about 20% of $\overline{u'v'}$ at the wake centerline. Fig.

6.11 shows that the magnitude of phase locking for $<u'v'>$ is almost the same as the time average for most wake locations. This means practically all of $\overline{u'v'}$ generation is phase-locked with the vortex passage. The above 20% value is due to the normalization factor. In summary, a significant percentage of the incoherent fluctuations are phase locked with the Kármán vortex shedding. This is yet further evidence that the large-scale coherent structures affect the entire turbulent field.

6.6 Summary

The discussion in the above sections has demonstrated the following:

1. Detection at the peak of the periodic ω_z signal due to vortex shedding corresponds to passage of the vortex center in the lower wake and passage of the saddle in the upper wake.

2. The transverse velocity is more coherent with the shed vortex than the streamwise velocity, especially in the wake centerline region, which results in higher $\overline{v^2}$ there. The spanwise velocity is incoherent since the vortex shedding is parallel.

3. The incoherent Reynolds normal stresses and turbulent kinetic energy are maximum near the vortex center and minimum near the saddle region. The incoherent Reynolds shear stress $\overline{u'v'}$ is maximum near the saddle region and minimum near the vortex center. These observations are consistent with the findings of Cantwell & Coles [10] and Hussain & Hayakawa [26].

4. Although $\tilde{\omega}_x$ and $\tilde{\omega}_y$ are negligible, $<\omega_x'^2>$ and $<\omega_y'^2>$ are not. The variance of the streamwise vorticity has the strongest coherence in the diverging braids of the saddles, which suggests a three-dimensional vortex line orientation of these flow regions.

5. $<\omega_z'^2>$ has maximum coherence near the vortex center and minimum coherence near the saddle region.

6. The coherence of the enstrophy is maximum near the vortex center and minimum slightly upstream of the saddle region. The dissipation rate follows the same pattern.

7. The incoherent shear stress $u'v'$ is almost entirely phase-locked to the Kármán vortex shedding. The variance $\overline{w'^2}$ has the highest phase-locking compared with other incoherent normal stresses. The variance $\overline{\omega_z'^2}$ has the highest phase-locking compared with other vorticity components.

7 Enstrophy Balances

7.1 Motivation

Enstrophy, ε, is a scalar quantity defined as one half the trace of the tensor $\omega_i\omega_j$, i.e.,

$$\varepsilon \equiv \frac{1}{2}\omega_i\omega_i, \tag{7.1}$$

and it is analogous to kinetic energy k, since the latter is one half the trace of the Reynolds stress tensor u_iu_j. Therefore, ε is a measure of the vortical activity, or of the rotational intensity of turbulent flows. Although the governing transport equations for ε are well known [59], the use of these equations in practical calculations has not been widespread. One of the reasons is the lack of vorticity data in various turbulent flows to quantify the terms in the equations.

Recently enstrophy has been used in turbulence modeling. A mean vorticity and enstrophy transport model has been developed to calculate time averaged turbulent flows with some success [6]. The simultaneous measurements of velocity and vorticity available in the current database can contribute to turbulence modeling in two important ways: (1) providing benchmark data including many previously unavailable velocity-vorticity correlations, and (2) helping to improve turbulence models with insights derived from the data analysis. To guide theoretical modeling, the current database contributes to the development of a physical model, which should help to quantitatively characterize the various enstrophy transport processes.

Balint *et al.* [4] determined the balances of terms in the transport equations of mean and fluctuating enstrophies for a turbulent boundary-layer, using simultaneous measurements of velocity and vorticity. With a miniature 9-sensor vorticity probe, they measured all the terms in these equations except those that involve the

instantaneous vorticity gradients. For the present project, similar measurements were obtained in the near-wake of a circular cylinder. The rest of this chapter will present the turbulent energy production due to the coherent and incoherent fields, the derivation of the enstrophy transport equations, and the balances of the terms in these equations.

7.2 Distributions of Kinetic Energy Production

Before discussing the various terms in the enstrophy transport equations, it is helpful to look briefly at the energy equations. When the instantaneous quantities are decomposed into mean, coherent, and incoherent parts (see Section 6.2), the time averaged total kinetic energy must be equal to the sum of the time averaged kinetic energy of the three fields, i.e.,

$$\frac{1}{2}\overline{U_i U_i} = \frac{1}{2}\overline{U}_i\overline{U}_i + \frac{1}{2}\overline{\tilde{u}_i\tilde{u}_i} + \frac{1}{2}\overline{u_i' u_i'}. \tag{7.2}$$

As discussed in Chapter 6, the vortex shedding results in coherent velocity fluctuations which generate the coherent kinetic energy, $\frac{1}{2}\overline{\tilde{u}_i\tilde{u}_i}$. The transport equation for the mean kinetic energy, $\frac{1}{2}\overline{U}_i\overline{U}_i$, has two production terms coming from the coherent and incoherent fields. For the mean kinetic energy equation, Fig. 7.1 shows that the coherent production term, $\overline{\tilde{u}\tilde{v}}d\overline{U}/dy$, has small positive values whereas the incoherent production term, $\overline{u'v'}d\overline{U}/dy$, has large negative values across the wake. Positive value is a gain, and negative value is a loss in the mean energy equation. Therefore, the mean flow is gaining energy from the decaying Kármán vortices, but is losing a great deal more energy to the incoherent field. Similar energy transfer mechanisms between the coherent and incoherent fields are discussed by Hussain [25]. Thus, inspite of the presence of the shed coherent spanwise vortices, almost all the total energy is in the incoherent field. This chapter will study similar transport phenomena for enstrophy. To achieve this, the governing equations for the 3 parts of the total enstrophy will be derived next.

7.3 Derivation of the Enstrophy Equations

In the presence of coherent structures, one can decompose any instantaneous variable into mean, coherent, and incoherent parts, as discussed in Section 6.2. The transport equations for each decomposed component of the turbulent kinetic energy are given by Hussain [25]. Here the corresponding enstrophy transport equations will be presented. The derivation of these equations involves the following steps:

1. Substitute the triple-decomposition expression for each variable into the momentum equations for incompressible flows.

2. Phase average the resulting equations from step 1.

3. Time average the equations from step 2 to obtain the momentum equations for the mean field.

4. Subtract the time averaged equations from the phase averaged equations in step 2 to obtain the momentum equations for the coherent field.

5. Subtract the equations for the mean and coherent fields from the instantaneous equations in step 1 to obtain the momentum equations for the incoherent field.

6. Cross the momentum equations for each field with the gradient operator to obtain the vorticity equations.

7. Multiply the vorticity equations for each field by the corresponding mean, coherent or incoherent vorticity vector to obtain the enstrophy transport equations.

8. Time average the coherent and incoherent enstrophy equations.

As the intermediate momentum equations have been documented by Hussain [25], only the enstrophy balances for each field are presented here. All quantities have been nondimensionalized by the velocity deficit u_o and the wake half-width L_o.

The mean enstrophy equation is:

$$\overline{U}_j \frac{\partial}{\partial x_j}\left(\frac{1}{2}\overline{\Omega}_i\,\overline{\Omega}_i\right) = \underbrace{\overline{u'_j\omega'_i}\frac{\partial\overline{\Omega}_i}{\partial x_j}}_{(1)} + \underbrace{\overline{\tilde{u}_j\tilde{\omega}_i}\frac{\partial\overline{\Omega}_i}{\partial x_j}}_{(2a)} - \underbrace{\frac{\partial}{\partial x_j}\left(\overline{\Omega}_i\,\overline{u'_j\omega'_i}\right)}_{(2b)} - \underbrace{\frac{\partial}{\partial x_j}\left(\overline{\Omega}_i\,\overline{\tilde{u}_j\tilde{\omega}_i}\right)}_{(3a)} + \underbrace{\overline{\Omega}_i\frac{\partial}{\partial x_j}\left(\overline{U}_i\,\overline{\Omega}_j\right)}_{(3b)} + \underbrace{\overline{\Omega}_i\overline{\omega'_j s'_{ij}}}_{(4)} + \underbrace{\overline{\Omega}_i\overline{\tilde{\omega}_j\tilde{s}_{ij}}}_{(5a)} + \underbrace{\frac{1}{Re}\frac{\partial^2}{\partial x_j\partial x_j}\left(\frac{1}{2}\overline{\Omega}_i\overline{\Omega}_i\right)}_{(5b)} - \underbrace{\frac{1}{Re}\overline{\frac{\partial\Omega_i}{\partial x_j}\frac{\partial\Omega_i}{\partial x_j}}}_{(6)}. \tag{7.3}$$

The coherent enstrophy equation is:

$$\overline{U}_j \frac{\partial}{\partial x_j}\left(\frac{1}{2}\overline{\tilde{\omega}_i\tilde{\omega}_i}\right) = \underbrace{-\overline{\tilde{u}_j\tilde{\omega}_i}\frac{\partial\overline{\Omega}_i}{\partial x_j}}_{(1)} + \underbrace{\overline{<u'_j\omega'_i>\frac{\partial\tilde{\omega}_i}{\partial x_j}}}_{(2a)} - \underbrace{\frac{1}{2}\frac{\partial}{\partial x_j}\overline{\left(\tilde{\omega}_i\tilde{u}_j\tilde{\omega}_i\right)}}_{(2b)} - \underbrace{\frac{\partial}{\partial x_j}\overline{\left(\tilde{\omega}_i<u'_j\omega'_i>\right)}}_{(3a)} + \underbrace{\overline{\tilde{\omega}_i\tilde{\omega}_j\tilde{s}_{ij}}}_{(3b)} + \underbrace{\overline{\tilde{\omega}_i<\omega'_j s'_{ij}>}}_{(4a)} + \underbrace{\overline{\tilde{\omega}_i\tilde{\omega}_j\frac{\partial\overline{U}_i}{\partial x_j}}}_{(4b)} + \underbrace{\overline{\Omega}_j\overline{\tilde{\omega}_i\tilde{s}_{ij}}}_{(5a)} + \underbrace{\frac{1}{Re}\frac{\partial^2}{\partial x_j\partial x_j}\left(\frac{1}{2}\overline{\tilde{\omega}_i\tilde{\omega}_i}\right)}_{(5b)} - \underbrace{\frac{1}{Re}\overline{\frac{\partial\tilde{\omega}_i}{\partial x_j}\frac{\partial\tilde{\omega}_i}{\partial x_j}}}_{(6)}. \tag{7.4}$$

The incoherent enstrophy equation is:

$$\overline{U}_j \frac{\partial}{\partial x_j}\left(\frac{1}{2}\overline{\omega'_i\omega'_i}\right) = \underbrace{-\overline{u'_j\omega'_i}\frac{\partial\overline{\Omega}_i}{\partial x_j}}_{(1)} - \underbrace{\overline{<u'_j\omega'_i>\frac{\partial\tilde{\omega}_i}{\partial x_j}}}_{(2a)} - \underbrace{\frac{1}{2}\frac{\partial}{\partial x_j}\overline{\left(\omega'_i u'_j\omega'_i\right)}}_{(2b)} - \underbrace{\frac{1}{2}\frac{\partial}{\partial x_j}\overline{\left(\tilde{u}_j<\omega'_i\omega'_i>\right)}}_{(3a)} + \underbrace{\overline{\omega'_i\omega'_j s'_{ij}}}_{(3b)} + \underbrace{\overline{\tilde{\omega}_j<\omega'_i s'_{ij}>}}_{(4a)} + \underbrace{\overline{<\omega'_i\omega'_j>\tilde{s}_{ij}}}_{(4b)} + \underbrace{\overline{\omega'_i\omega'_j\frac{\partial\overline{U}_i}{\partial x_j}}}_{(4c)} + \underbrace{\overline{\Omega}_j\overline{\omega'_i s'_{ij}}}_{(5a)}$$

$$\underbrace{\qquad\qquad}_{(6)} \qquad\qquad \underbrace{\qquad\qquad}_{(7)}$$

$$+\frac{1}{Re}\frac{\partial^2}{\partial x_j \partial x_j}\left(\frac{1}{2}\overline{\omega_i'\omega_i'}\right) - \frac{1}{Re}\overline{\frac{\partial \omega_i'}{\partial x_j}\frac{\partial \omega_i'}{\partial x_j}}. \tag{7.5}$$

Tennekes & Lumley [59] derived the transport equations for the mean and the fluctuating enstrophies and presented interpretations of the resulting terms. The above triple-decomposition equations have additional interaction terms; therefore, all terms are interpreted here for ease of reference.

In the mean enstrophy equation:

- Term (1) represents the advection of the mean enstrophy.
- Term (2a) describes the loss of mean enstrophy to the incoherent field by gradient production.
- Term (2b) corresponds to the gain of mean enstrophy from the coherent field by gradient production.
- Term (3a) describes the transport of mean enstrophy by the incoherent velocity-vorticity interaction.
- Term (3b) represents the transport of mean enstrophy by the coherent velocity-vorticity interaction.
- Term (4) models the gain or loss of mean enstrophy from stretching/compression of the mean vorticity by the mean strain rate when $i = j$. The reorientation of mean vorticity (also in terms (5a) and (5b)) when $i \neq j$ results in no net change in mean enstrophy, as discussed in Section 5.5.
- Term (5a) is for the amplification/attenuation of the mean enstrophy through stretching/compression of the incoherent vorticity by the incoherent strain rate.

- Term (5b) represents the amplification/attenuation of mean enstrophy through stretching/compression of the coherent vorticity by the coherent strain rate.
- Term (6) represents the viscous diffusion of mean enstrophy.
- Term (7) describes the viscous dissipation of mean enstrophy.

In the coherent enstrophy equation:

- Term (1) corresponds to the advection of coherent enstrophy.
- Term (2a) describes the gain of coherent enstrophy from the mean field by gradient production. This term appears with opposite sign in the mean enstrophy equation.
- Term (2b) indicates the loss of coherent enstrophy to the incoherent field by gradient production.
- Term (3a) represents transport of coherent enstrophy by coherent velocity-vorticity interaction.
- Term (3b) corresponds to the transport of coherent enstrophy by incoherent velocity-vorticity interaction.
- Term (4a) models the amplification/attenuation of coherent enstrophy through stretching/compression of the coherent vorticity by the coherent strain rate when $i = j$. The reorientation of coherent vorticity (also in terms (4b), (5a) and (5b)) when $i \neq j$ results in no net change in coherent enstrophy.
- Term (4b) is for the amplification/attenuation of coherent enstrophy through stretching/compression of the incoherent vorticity by the incoherent strain rate.

- Term (5a) models the amplification/attenuation of coherent enstrophy through stretching/compression of the coherent vorticity by the mean strain rate.

- Term (5b) is interpreted by Tennekes & Lumley [59] as a mixed production term and it appears in the mean balance with the same sign. According to Tennekes & Lumley, this could mean that the stretching/compression of coherent vorticity by the coherent strain rate produces mean enstrophy and coherent enstrophy at the same rate.

- Term (6) describes the viscous diffusion of coherent enstrophy.

- Term (7) corresponds to the viscous dissipation of coherent enstrophy.

In the incoherent enstrophy equation:

- Term (1) represents the advection of the incoherent enstrophy.

- Term (2a) indicates the gain of incoherent enstrophy from the mean field by gradient production. This term appears in the mean enstrophy balance with opposite sign.

- Term (2b) describes the gain of incoherent enstrophy from the coherent field by gradient production. It has the opposite sign as the same term in the coherent enstrophy equation.

- Term (3a) represents the transport of incoherent enstrophy by incoherent velocity-vorticity interaction.

- Term (3b) corresponds to the transport of incoherent enstrophy by the interaction of incoherent vorticity with coherent velocity.

- Term (4a) represents the amplification/attenuation of incoherent enstrophy through stretching/compression of the incoherent vorticity by the incoherent

strain rate when $i = j$. The reorientation of incoherent vorticity (also in terms (4b), (4c), (5a) and (5b)) when $i \neq j$ results in no net change in incoherent enstrophy.

- Term (4b) appears with the same sign as term (4b) in the coherent enstrophy balance.
- Term (5a) models the amplification/attenuation of incoherent enstrophy through stretching/compression of incoherent vorticity by the mean strain rate.
- Term (5b) is for the amplification/attenuation of incoherent enstrophy through stretching/compression of the incoherent vorticity by the incoherent strain rate. It appears as term (5a) in the mean enstrophy equation which means that the stretching/compression of incoherent vorticity by the incoherent strain rate produces mean enstrophy and incoherent enstrophy at the same rate.
- Term (6) describes the viscous diffusion of incoherent enstrophy.
- Term (7) represents the viscous dissipation of incoherent enstrophy.

For a plane wake flow, the above equations simplify significantly. For example, the production term (2a) in the mean enstrophy equation includes only the correlation $\overline{v'\omega_z'}$ and the gradient $d\overline{\Omega}_z/dy$ instead of the full correlation and vorticity gradient tensors. The mean enstrophy equation becomes:

$$\begin{array}{ccccccccc} & \textbf{(1)} & & \textbf{(2a)} & & \textbf{(2b)} & & \textbf{(3a)} & \textbf{(3b)} \\ \overline{U}\dfrac{\partial}{\partial x}\left(\dfrac{1}{2}\overline{\Omega}_z^2\right) & = & \overline{v'\omega_z'}\dfrac{\partial \overline{\Omega}_z}{\partial y} & + & \overline{\tilde{v}\tilde{\omega}_z}\dfrac{\partial \overline{\Omega}_z}{\partial y} & - & \dfrac{\partial}{\partial y}\left(\overline{\Omega}_z\,\overline{v'\omega_z'}\right) & - & \dfrac{\partial}{\partial y}\left(\overline{\Omega}_z\,\overline{\tilde{v}\tilde{\omega}_z}\right) \end{array}$$

$$\begin{array}{ccccccc} & \textbf{(4)} & & \textbf{(5a)} & & \textbf{(5b)} & \\ + \overline{\Omega}_x\dfrac{\partial}{\partial y}\left(\overline{U}\,\overline{\Omega}_y\right) & + & \overline{\Omega}_z\overline{\omega_j' s_{3j}'} & + & \overline{\Omega}_z\overline{\tilde{\omega}_z\tilde{s}_{33}} & & \end{array}$$

$$\textbf{(6)} \qquad \textbf{(7)}$$

$$+ \frac{1}{Re}\frac{\partial^2}{\partial y^2}(\frac{1}{2}\overline{\Omega}_z^2) - \frac{1}{Re}\frac{\partial \overline{\Omega}_z}{\partial y}\frac{\partial \overline{\Omega}_z}{\partial y}. \tag{7.6}$$

The coherent enstrophy equation becomes:

$$\textbf{(1)} \qquad \textbf{(2a)} \qquad \textbf{(2b)} \qquad \textbf{(3a)} \qquad \textbf{(3b)}$$

$$\overline{U}\frac{\partial}{\partial x}(\frac{1}{2}\overline{\tilde{\omega}_z^2}) = -\overline{\tilde{v}\tilde{\omega}_z}\frac{\partial \overline{\Omega}_z}{\partial y} + \overline{<v'\omega_z'>\frac{\partial \tilde{\omega}_z}{\partial y}} - \frac{1}{2}\frac{\partial}{\partial y}\overline{(\tilde{\omega}_z\tilde{v}\tilde{\omega}_z)} - \frac{\partial}{\partial y}\overline{(\tilde{\omega}_z <v'\omega_z'>)}$$

$$\textbf{(4a)} \qquad \textbf{(4b)} \qquad \textbf{(5a)} \qquad \textbf{(5b)}$$

$$+ \overline{\tilde{\omega}_z\tilde{\omega}_z\tilde{s}_{33}} + \overline{\tilde{\omega}_z <\omega_i's_{3i}'>} + \overline{\tilde{\omega}_x\tilde{\omega}_y}\frac{\partial \overline{U}}{\partial y} + \overline{\Omega}_z\overline{\tilde{\omega}_z\tilde{s}_{33}}$$

$$\textbf{(6)} \qquad \textbf{(7)}$$

$$+ \frac{1}{Re}\frac{\partial^2}{\partial y^2}(\frac{1}{2}\overline{\tilde{\omega}_z^2}) - \frac{1}{Re}\overline{\frac{\partial \tilde{\omega}_z}{\partial x_j}\frac{\partial \tilde{\omega}_z}{\partial x_j}}. \tag{7.7}$$

The incoherent enstrophy equation becomes:

$$\textbf{(1)} \qquad \textbf{(2a)} \qquad \textbf{(2b)} \qquad \textbf{(3a)} \qquad \textbf{(3b)}$$

$$\overline{U}\frac{\partial}{\partial x}(\frac{1}{2}\overline{\omega_i'^2}) = -\overline{v'\omega_z'}\frac{\partial \overline{\Omega}_z}{\partial y} - \overline{<v'\omega_z'>\frac{\partial \tilde{\omega}_z}{\partial y}} - \frac{1}{2}\frac{\partial}{\partial y}\overline{(\omega_i'v'\omega_i')} - \frac{1}{2}\frac{\partial}{\partial y}\overline{(\tilde{v} <\omega_i'\omega_i'>)}$$

$$\textbf{(4a)} \qquad \textbf{(4b)} \qquad \textbf{(4c)} \qquad \textbf{(5a)} \qquad \textbf{(5b)}$$

$$+ \overline{\omega_i'\omega_j's_{ij}'} + \overline{\tilde{\omega}_z <\omega_i's_{3i}'>} + \overline{<\omega_i'\omega_j'>\tilde{s}_{ij}} + \overline{\omega_x'\omega_y'}\frac{\partial \overline{U}}{\partial y} + \overline{\Omega}_z\overline{\omega_i's_{3i}'}$$

$$\textbf{(6)} \qquad \textbf{(7)}$$

$$+ \frac{1}{Re}\frac{\partial^2}{\partial y^2}(\frac{1}{2}\overline{\omega_i'^2}) - \frac{1}{Re}\overline{\frac{\partial \omega_i'}{\partial x_j}\frac{\partial \omega_i'}{\partial x_j}}. \tag{7.8}$$

7.4 The Mean Enstrophy Balance

Before discussing the various terms in the enstrophy transport equations, it helps to study the time mean distributions of the 3 parts of the total enstrophy. Fig. 7.2 shows these distributions for the mean, coherent, and incoherent enstrophies across the wake at $x/d = 30$. The incoherent part is the largest and peaks near the wake centerline. Note that it is already divided by 10 to show some features of the other two parts. The mean and coherent enstrophies have roughly the same order of magnitude, and they are smaller than the incoherent part by a factor of 40 to 50. The mean enstrophy has a minimum at zero near the wake centerline since the mean vorticity is zero there. The coherent enstrophy value at the wake centerline is a little lower than the values at $\eta = \pm 0.5$ due to the presence of the vortex centers. In summary, the incoherent field contains much more enstrophy than the mean or the coherent fields.

The mean enstrophy balance is presented in Fig. 7.3. The various terms in Eq. (7.6) are grouped into 3 plots for clarity. Fig. 7.3(a) is for terms (1) to (3b). Fig. 7.3(b) is for terms (5a) and (5b) which are called the "vortex stretching/compression" terms. Fig. 7.3(c) shows the viscous diffusion, viscous dissipation, and residual terms.

The plane wake does not have a continuous source of enstrophy generation as does the turbulent boundary-layer; therefore, the mean enstrophy must decay in the streamwise direction. This is illustrated in Fig. 7.3(a) where term (1) is shown to be negative across the wake, demonstrating the loss of mean enstrophy by fluid particles as they advect downstream. Term (1) has two minima near $\eta = \pm 0.5$, and is approximately zero near the wake centerline since the mean enstrophy is zero all along it. Term (2a) is negative across the wake, representing the loss of mean enstrophy to the incoherent field, with a large minimum at the centerline. Term (2b) has very small positive values across the wake; it represents the gain of mean

enstrophy from the decaying Kármán vortices. Term (3a) is positive around the wake centerline region within $\eta = \pm 0.5$, and is negative in the outer region. This means the transport of mean enstrophy is from the outer wake to feed the centerline region. This is how the mean field has sufficient enstrophy to lose to the incoherent field (term (2a)) in the centerline region. The other transport term, (3b), is nearly zero across the wake. This term is due to the interaction of the coherent velocity and vorticity, and like other "coherent" terms, is quite small.

Term (5a), which represents enstrophy amplification/attenuation due to the incoherent strain rate s'_{ij}, is shown in Fig. 7.3(b) to be positive in the centerline region (roughly within $\eta = \pm 0.7$), and negative in the outer wake. It seems that amplification is occurring in the centerline region and attenuation in the outer wake, but the magnitudes are near the limit of the experimental error. The mean spanwise vorticity $\overline{\Omega}_z$ in term (5a) has the same sign on a given side of the wake so the sign change is entirely due to the change in sign of the correlation $\overline{\omega'_j s'_{3j}}$.

In Fig. 7.3(c), both the diffusion and dissipation terms are seen to be negligibly small across the wake. The residual term is the remainder after summing all the terms in Eq. (7.6). It therefore contains the cummulative measurement uncertainties of all terms in the balance. The residual varies in the range ± 0.03 across the wake. It is of the same order of magnitude as the largest term in the equation, i.e. about one-third of the maximum of term (2a). This fact should be kept in mind while interpreting the various terms in the mean enstrophy balance.

7.5 The Coherent Enstrophy Balance

In the coherent enstrophy balance from Eq. (7.7), all terms are practically within the noise level since the magnitudes are even smaller than the residual for the mean enstrophy. To analyze this balance properly, the amplitude should be one order of magnitude larger since the uncertainty level cannot be decreased much smaller. The

structure detection scheme of Hussain & Hayakawa [26] gave higher magnitudes for these coherent terms since they only detected structures with high magnitude of ω_z. Section 6.3 shows that their peak coherent Reynolds shear stress is more than twice that found from the current measurements for the same streamwise position.

Besides using a different structure detection scheme to increase the coherent signal-to-noise ratio, one can: (1) measure at higher speeds, (2) measure at wake locations closer than $x/d = 30$, and (3) measure with a higher data sampling rate to minimize data attenuation.

7.6 The Incoherent Enstrophy Balance

The incoherent enstrophy balance is presented in Fig. 7.4. The various terms in the balance are grouped in 3 plots as was done for the mean balance in Fig. 7.3. Similar to Fig. 7.3, all terms are plotted with their signs as presented in Eq. (7.8). These terms have much larger magnitudes than those in the mean and coherent enstrophy balances. Recall from Fig. 7.2 that the incoherent enstrophy is about 40 times larger than the mean enstrophy. All terms in this balance are, in principle, symmetric around the wake centerline, as for the mean enstrophy balance.

In Fig. 7.4(a), term (1) is positive across the wake, and represents the advection of the incoherent enstrophy by the mean streamwise velocity. Therefore, it means the advecting fluid particles gain incoherent enstrophy because the incoherent enstrophy increases in the downstream direction. This term has a minimum in the centerline region and maxima at roughly $\eta = \pm 1.0$, implying that the streamwise gradient of incoherent enstrophy is largest there. Term (2a) represents the gain of incoherent enstrophy from the mean field; it is the negative of term (2a) in the mean enstrophy equation. Term (2b) represents the interaction of the incoherent field with the coherent vorticity gradient; it is negligibly small. Term (3a) is the transport due to the incoherent field. It is negative within the region $\eta = \pm 1.5$, and positive in the

outer wake. This means incoherent enstrophy is drawn from the centerline region toward the wake edges, which is consistent with the wake spreading. Term (3b) is the transport due to the coherent lateral velocity, and it has similar trend as term (3a). The difference is that term (3b) is smaller by roughly a factor of 5, and it changes sign roughly at $\eta = \pm 1.0$.

Fig. 7.4(b) shows the "vortex stretching/compression" terms. Term (4a) corresponds to the incoherent enstrophy amplification due to the incoherent action; it is by far the largest term in the balance. This term is much larger than all the other terms and is scaled down by a factor of 10 in the plot. Vortex stretching increases enstrophy by straining of vortices to increase their component vorticity. The very large positive value across the wake indicates that, on balance, incoherent vortex stretching is much greater than vortex compression. This phenomenon is observed experimentally here for the first time for cylinder wake flows.

The source term involving coherent vorticity, (4b), is negligble compared to (4a). Term (4c) is stretching/compression of the incoherent vorticity by the coherent strain rate tensor. It is much smaller than term (4a), but is still about twice as large as the largest term in the mean balance. Term (5a) represents vortex stretching/compression due to the mean velocity gradient. It is the second largest source term, with peaks about one order of magnitude smaller than the peak of term (4a). This term is zero at the wake centerline, because the velocity gradient is zero there. The term comes from the mean velocity gradient $d\overline{U}/dy$, and the incoherent vorticity correlation $\overline{\omega_x'\omega_y'}$, which are shown in Fig. 5.1 and Fig. 5.16 to have maxima around $\eta = \pm 0.7$, respectively. Furthermore, the correlation $\overline{\omega_x'\omega_y'}$ is due to high stretching activity in the braid regions, as discussed in Section 5.5. Therefore, the two maxima of term (5a) at roughly $\eta = \pm 0.7$ are probably due to vorticity aligned with the mean strain field being stretched in the braid regions. Term (5b), which is the production of incoherent enstrophy involving the mean vorticity, and appears in

the mean enstrophy balance as term (5a) with the same sign, is negligible compared to other source terms.

Fig. 7.4(c) shows the diffusion term (6) and the residual term. Since the instantaneous vorticity gradients cannot be measured, the viscous dissipation is included in the residual; thus, the measurement uncertainties from all other terms are lumped with it. The diffusion is nearly zero across the wake, and is insignificant compared to the dissipation (plus measurement uncertainty). Note that the dissipation (residual) term is scaled down by a factor of 10 in the plot; it is just slightly smaller than the "vortex stretching" term (4a) in the Fig. 7.4(b). This means the enstrophy generated by the incoherent vortex stretching appears to be largely dissipated in the same flow region.

In 1938, Taylor [58] used dimensional analysis to show that turbulent vortex stretching is approximately balanced by viscous dissipation for a high Reynolds number flow. Basically, he showed that the other terms are of higher order and can be neglected. The current measurements support Taylor's findings. The incoherent vortex stretching/compression term (4a) is larger than all other terms by at least an order of magnitude, and it is approximately balanced by the viscous dissipation, i.e,

$$\overline{\omega_i' \omega_j' s_{ij}'} \approx \frac{1}{Re} \overline{\frac{\partial \omega_i'}{\partial x_j} \frac{\partial \omega_i'}{\partial x_j}}. \tag{7.9}$$

7.7 Summary

The discussion in the above sections has demonstrated the following for $x/d = 30$:

1. The mean flow field gains energy from decaying Kármán vortices, but loses a great deal more energy to the incoherent field.

2. The incoherent field has much more enstrophy than the mean or the coherent fields.

3. The mean enstrophy decreases with downstream direction.

4. The mean field loses enstrophy to the incoherent field in the centerline region and the transport terms balance it by taking enstrophy from the outer wake.

5. The terms in the coherent enstrophy balance are within the noise level. All coherent terms in the mean and incoherent equations are small compared with the other terms in these equations.

6. The incoherent enstrophy increases with the downstream direction.

7. Incoherent enstrophy generation by incoherent vortex stretching/compression is larger than any other terms by at least an order of magnitude. This term is approximately balanced by viscous dissipation.

8 Conclusions and Recommendations

The following conclusions are for the calibration and data reduction techniques.

1. The present calibration and data reduction method is independent of the probe geometry and sensor orientation. For vorticity measurements, the only geometrical information needed is the distance from the center of each wire to the centroid of the frontal sensing area of the probe.

2. The error minimization method, when used with more sensors than the number of unknowns, can produce unique solutions of the measured velocity for angles of attack within $\pm 20°$.

3. For calibration angles within $\pm 20°$, neglecting the sensor with the lowest cooling velocity from the plus probe results in divergence during data reduction. Conversely, neglecting the sensor with the highest cooling velocity results in convergence to practically the same solution as when all sensors are used.

4. The zonal calibration scheme can improve measurement accuracy.

The following conclusions are for the characteristics of the velocity field.

1. At $x/d = 20$ and 30, the maximum rms of the transverse velocity component is higher than the streamwise, followed by the spanwise component. This trend is consistent with X-probe measurements of Yamada *et al.* [70] at $x/d = 30$.

2. The small prong spacing of the 4-sensor and 12-sensor probes results in more accurate measurements.

3. The skewness and flatness values of the velocity components show the proper characteristics of a turbulent plane wake.

4. The 12-sensor probe accounts for velocity gradients in the measuring volume and can measure the Reynolds shear stresses more accurately than the 4-sensor probe.

5. The velocity spectra show peaks at the vortex shedding frequency f_s for the streamwise and transverse components. The spanwise velocity spectra donot have any peak at f_s, indicating parallel shedding. spanwise component.

6. The JPDFs of the streamwise and transverse velocity components show preferred orientations at $+45°$ from the centerline for the lower wake and at $-45°$ for the upper wake. The other correlations are about zero across the wake due to flow symmetry.

7. The converging legs of the saddle region are the dominant $\overline{uv}$ generators. These flow regions are along the direction normal to the mean shear.

The following conclusions are for the characteristics of the vorticity field.

1. The miniature 12-sensor probe can measure simultaneously velocity and vorticity with good accuracy in the near-wake of a circular cylinder for $x/d = 20-30$.

2. Central-differencing, which results in proper phase alignment of the streamwise velocity gradients with the directly measured variables, should be used in applying Taylor's hypothesis.

3. The measured mean spanwise vorticity component agrees well with the derivative of the mean streamwise velocity. The other mean vorticity components are about zero. This is a good test of the accuracy of the measurements.

4. At $x/d = 30$, the rms of the streamwise vorticity is highest, followed by the transverse and the spanwise components. The rms values for the transverse and spanwise components are somewhat attenuated due to the low sampling rate.

5. The skewness and flatness values for the vorticity components have the proper characteristics for a plane wake. These values are high at the wake edges and have nearly Gaussian values in the centerline region.

6. Only the spectra of the spanwise vorticity component show intensity peaks at the shedding frequency, indicating parallel shedding.

7. The extremely narrow PDFs of all vorticity components in the freestream compared with the centerline region indicate a high signal-to-noise ratio of up to 2 orders of magnitude.

8. The JPDF contours of $\overline{\omega_x \omega_y}$ show a preferred orientation that is along the direction of the mean shear. Therefore, ω_x and ω_y are negatively correlated in the lower wake and positively correlated in the upper wake. The pattern is consistent with the computational results of Meiburg & Lasheras [39]. Other vorticity correlations are about zero across the wake.

9. The correlations of vorticity and velocity gradients are about zero across the wake except for those that involve gradients of the spanwise velocity.

10. Quadrant analysis of the correlation $\overline{\omega_x \partial u/\partial x}$ and $\overline{\omega_z \partial w/\partial z}$ show more stretching than compression activity across the wake.

11. The ω_z component serves as the vehicle for vorticity exchange between the ω_x and ω_y components.

The following conclusions are from the analysis of the turbulent wake conditioned with the passage of the shedding vortex.

1. Detection at the peak of the periodic ω_z signal due to vortex shedding corresponds to passage of the vortex center in the lower wake and passage of the saddle in the upper wake.

2. The transverse velocity is more coherent with the shed vortex than the streamwise velocity, especially in the wake centerline region, which results in higher $\overline{v^2}$ there. The spanwise velocity is incoherent since the vortex shedding is parallel.

3. The incoherent Reynolds normal stresses and turbulent kinetic energy are maximum near the vortex center and minimum near the saddle region. The incoherent Reynolds shear stress $\overline{u'v'}$ is maximum near the saddle region and minimum near the vortex center. These observations are consistent with the findings of Cantwell & Coles [10] and Hussain & Hayakawa [26].

4. Although $\tilde{\omega}_x$ and $\tilde{\omega}_y$ are negligible, $<\omega_x'^2>$ and $<\omega_y'^2>$ are not. The variance of the streamwise vorticity has the strongest coherence in the diverging braids of the saddles, which suggests a three-dimensional vortex line orientation of these flow regions.

5. $<\omega_z'^2>$ has maximum coherence near the vortex center and minimum coherence near the saddle region.

6. The coherence of the enstrophy is maximum near the vortex center and minimum slightly upstream of the saddle region. The dissipation rate follows the same pattern.

7. The incoherent shear stress $u'v'$ is almost entirely phase-locked to the Kármán vortex shedding. The variance $\overline{w'^2}$ has the highest phase-locking compared with other incoherent normal stresses. The variance $\overline{\omega_z'^2}$ has the highest phase-locking compared with other vorticity components.

The following conclusions are for the enstrophy balances at $x/d = 30$ for the 3 parts of the measured flow field: mean, coherent, incoherent.

1. The mean flow field gains energy from decaying Kármán vortices, but loses a great deal more energy to the incoherent field.

2. The incoherent field has much more enstrophy than the mean or the coherent fields.

3. The mean enstrophy decreases with downstream direction.

4. The mean field loses enstrophy to the incoherent field in the centerline region and the transport terms balance it by taking enstrophy from the outer wake.

5. The terms in the coherent enstrophy balance are within the noise level. All coherent terms in the mean and incoherent equations are small compared with the other terms in these equations.

6. The incoherent enstrophy increases with the downstream direction.

7. Incoherent enstrophy generation by incoherent vortex stretching/compression is larger than any other terms by at least an order of magnitude. This term is approximately balanced by viscous dissipation.

The following recommendations can be drawn from the discussion of the results in the previous chapters. These suggestions can be useful in either further analysis of the current database or further experiments in turbulent wakes.

1. Develop techniques to make miniature probes more robust, and able to function properly in other fluids such as water.

2. Repeat the measurements in this project with higher sampling frequency. Also, perform parametric studies by varying the Reynolds number.

3. Build a vortex generator to calibrate the vorticity probe with known vortex strength.

4. Use the probes, and the data reduction technique to measure in the far-wake region ($x/d > 200$) where accuracy is critical, and in the very-near wake ($x/d < 20$) where the angles of attack are extremely high.

5. Perform two-point measurements using vorticity probes to investigate the three-dimensionality of the vortical structures.

6. Analyze the velocity gradients as thoroughly as the velocity and the vorticity components.

7. Improve the data reduction method to make use of the fact that the error equation is parabolic in all the velocity gradients.

8. Perform conditional analysis with trigger condition such that the incoherent vorticity has high magnitude with the same sign as the coherent vorticity.

9. Analyze the kinetic energy balances of the mean, coherent and incoherent flow fields.

10. Analyze the enstrophy balances for $x/d = 20$ to confirm findings at $x/d = 30$.

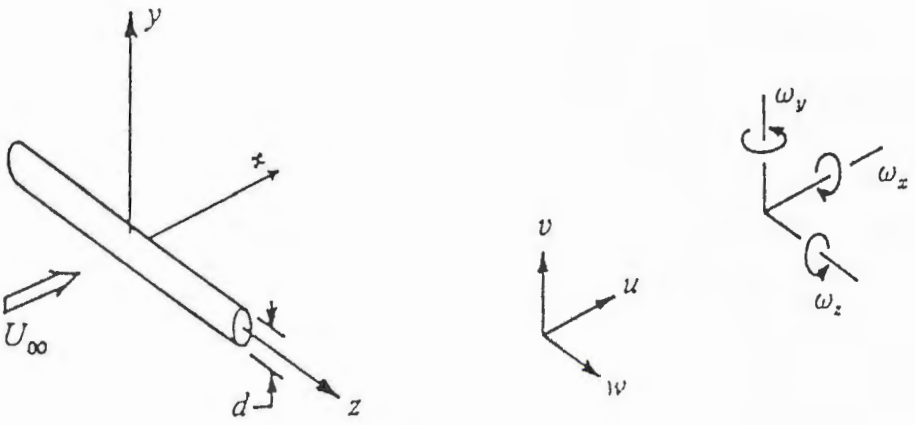

Fig. 1.1. Definition of the coordinate axes.

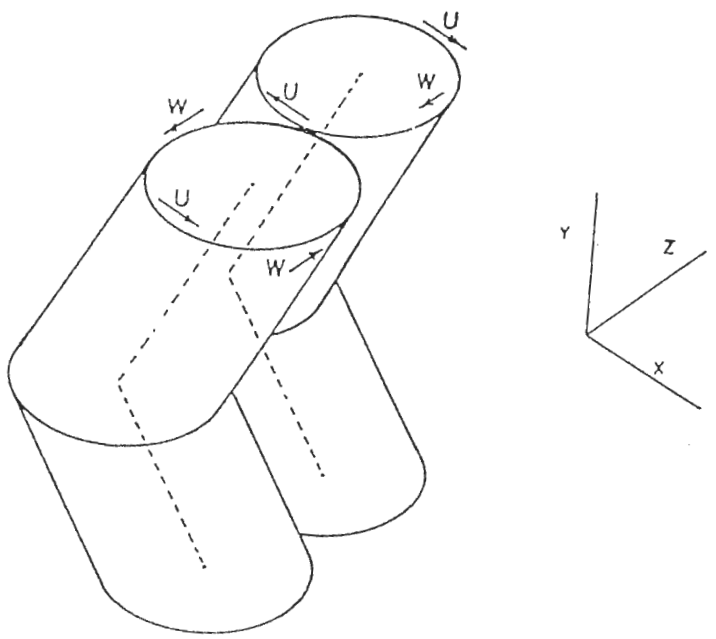

Fig. 1.2. Sketch of the double-roller model for the vortical structure of Grant [21].

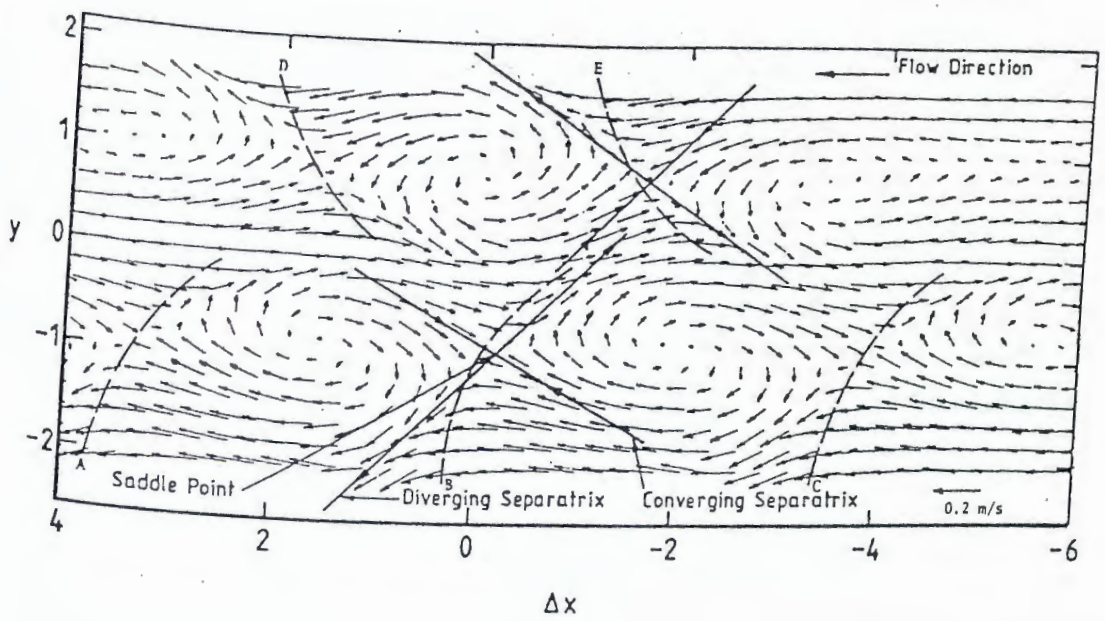

Fig. 1.3. Velocity vector plot in the x–y plane from Browne et al. [9]. The saddle region is between two consecutive vortices. The converging and diverging separatrices are regions of flow moving toward or away from the saddle.

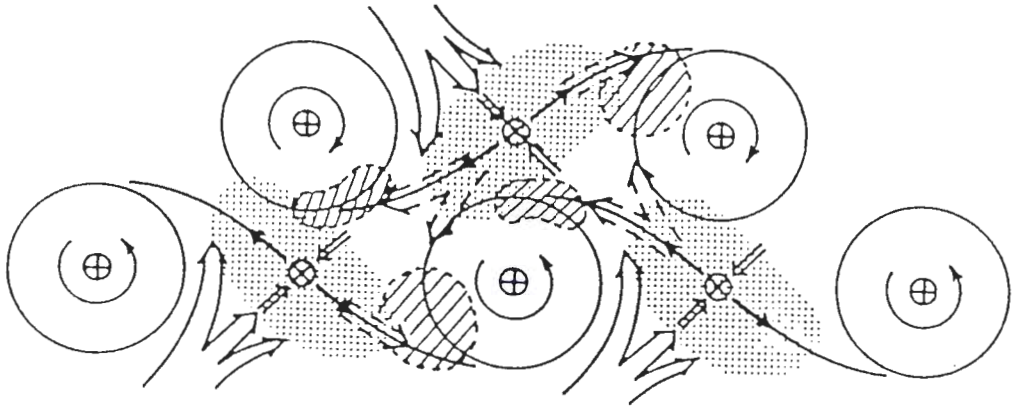

Fig. 1.4. Sketch of the model of the wake vortical structure from Hussain & Hayakawa [26]. The braids transfer fluid away from the saddles, which are marked by symbol X.

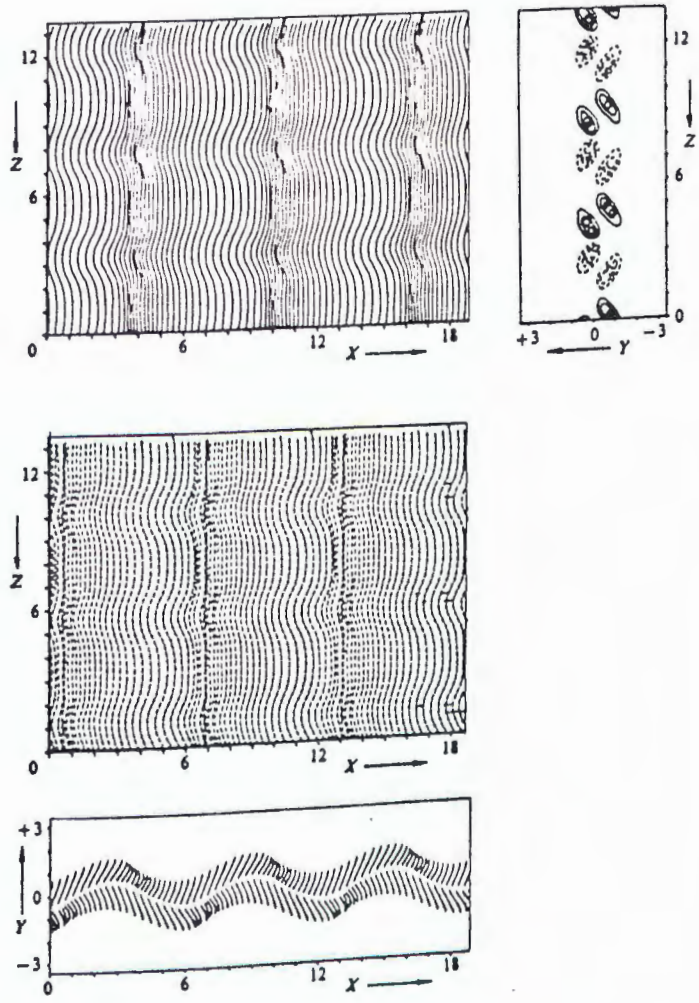

Fig. 1.5. Vortex lines at various section cuts in the wake calculated by Meiburg & Lasheras [39]. The flow is a laminar wake of a tapered flat plate. The upper wake is represented by solid lines, and the lower wake by dashed lines. The bottom plot in the x–y plane shows vortex lines inclined in the direction of the mean shear.

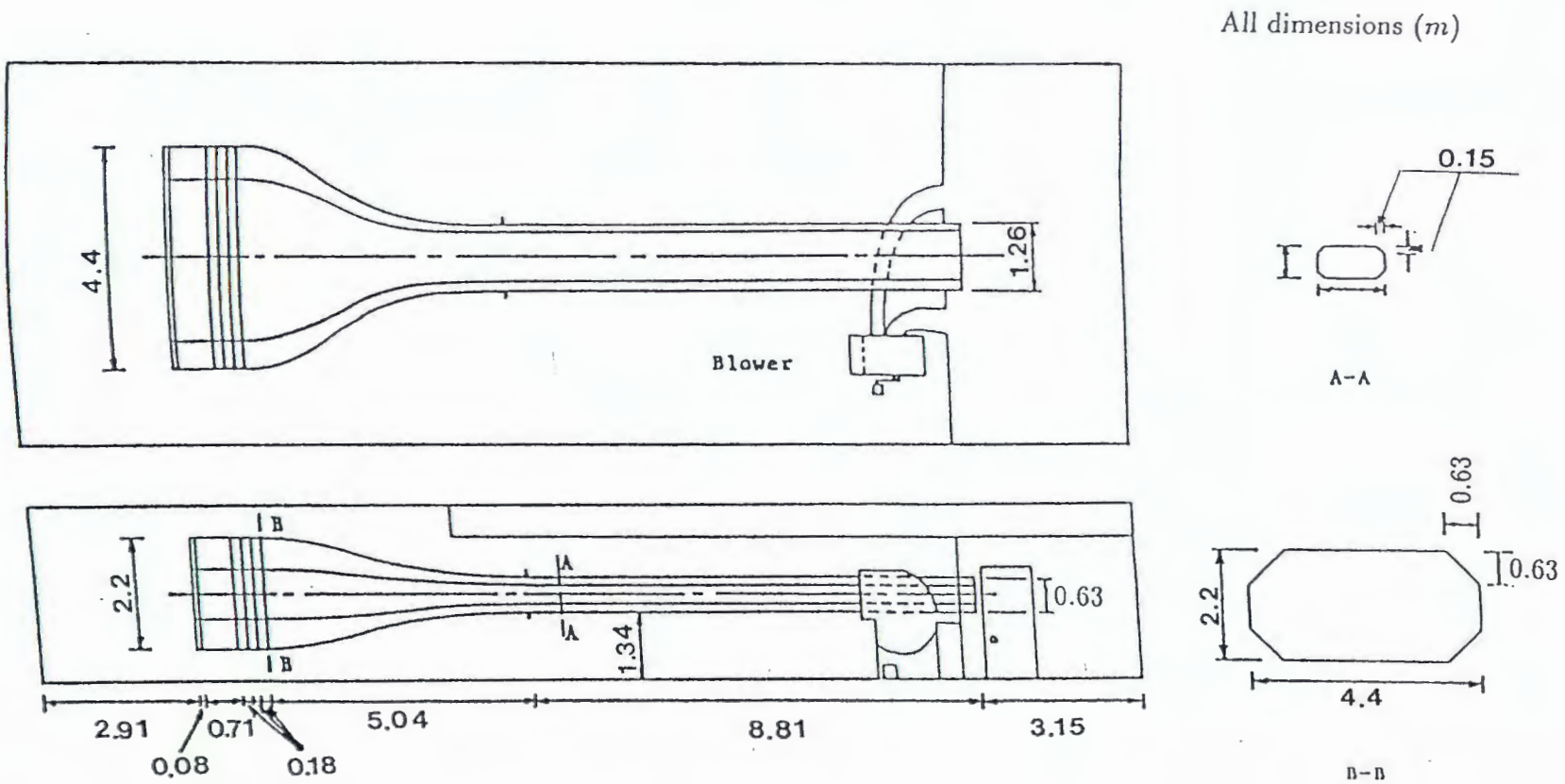

Fig. 2.1. Scale drawing of the wind tunnel.

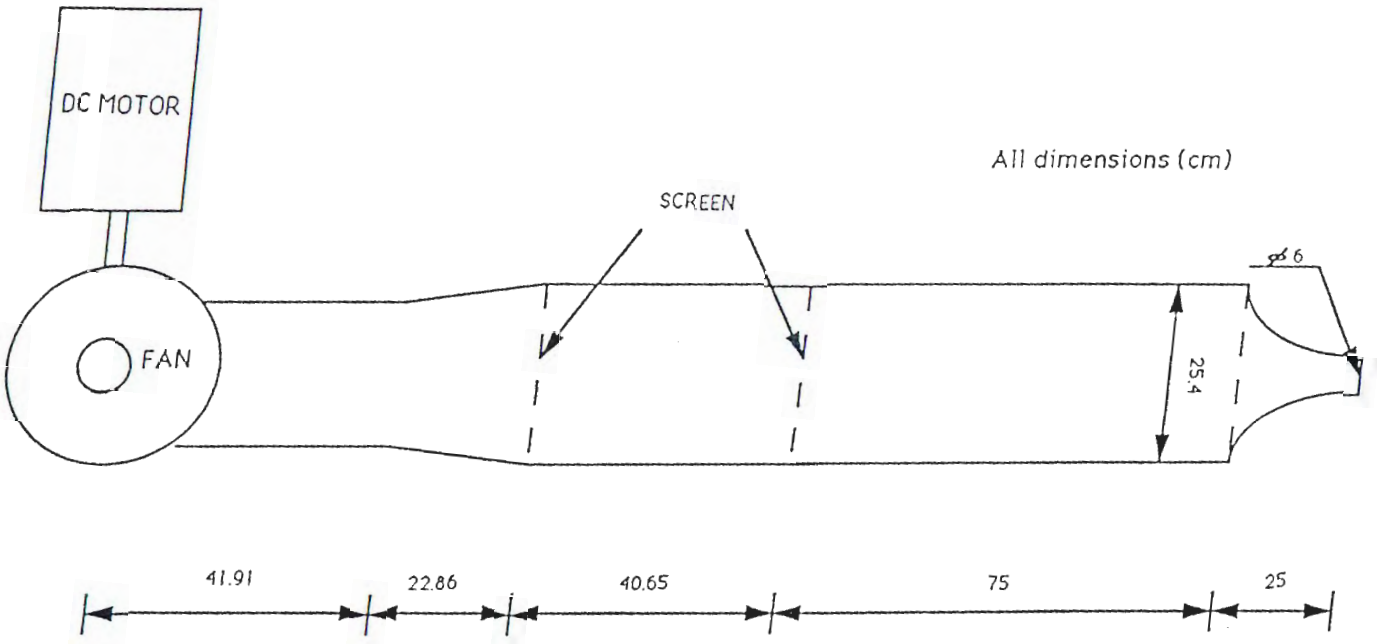

Fig. 2.2. Scale drawing of the calibration jet.

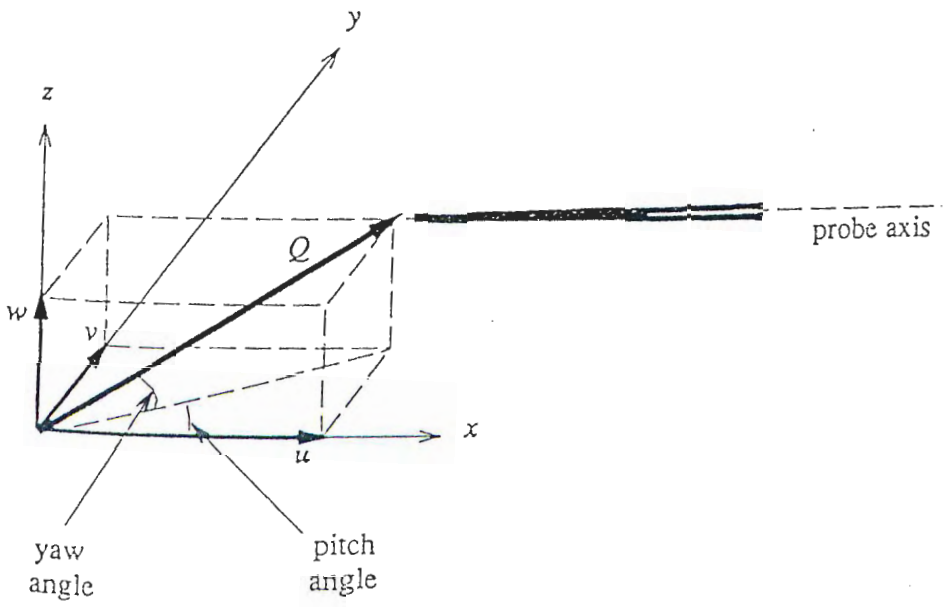

Fig. 2.3. Definition of the pitch and yaw angles.

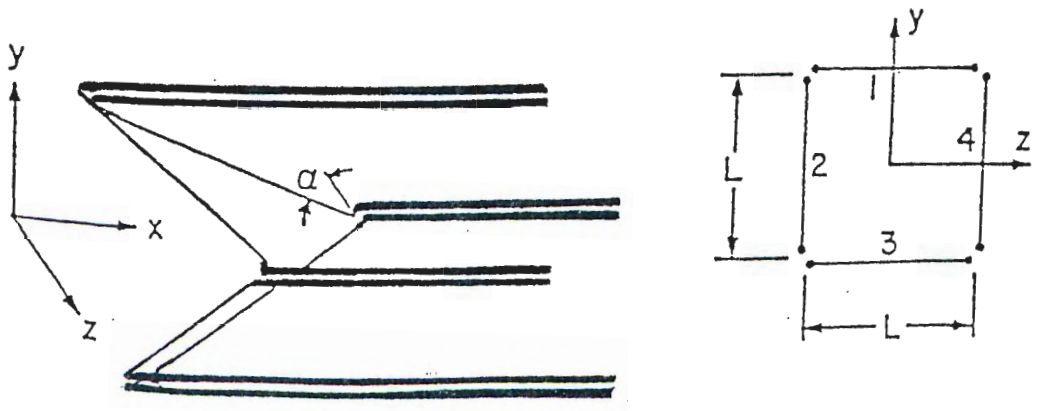

L = 0.51 mm, α = 42 °

Fig. 2.4. Schematic sketch of the Kovasznay–type 4–sensor probe.

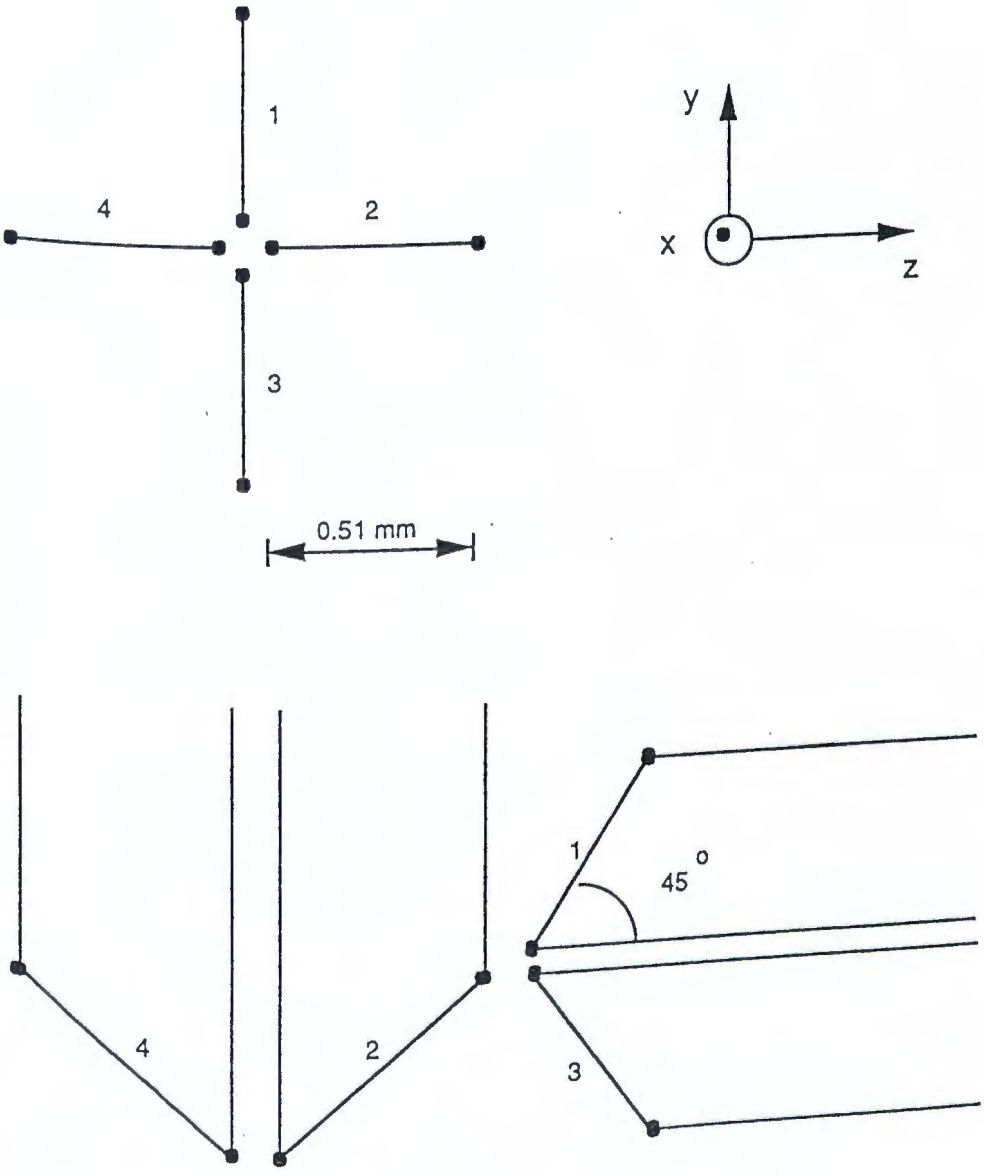

Fig. 2.5. Schematic sketch of the plus-shape 4-sensor probe.

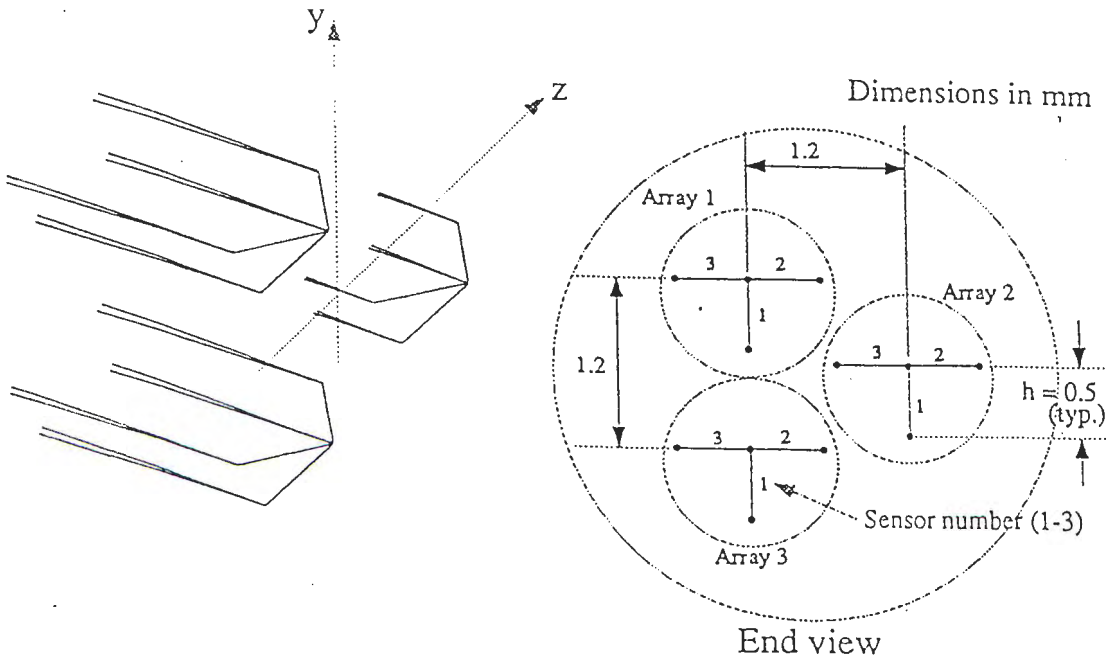

Fig. 2.6. Schematic sketch of the 9–sensor vorticity probe.

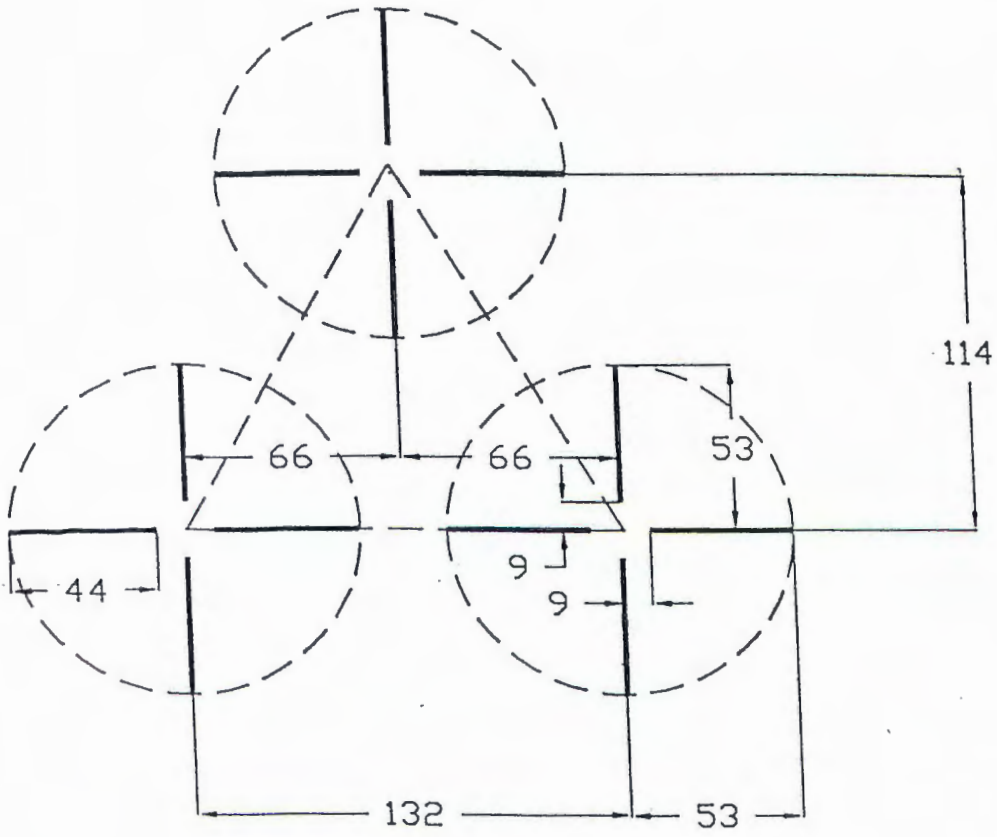

Dimensions in 1/100 mm

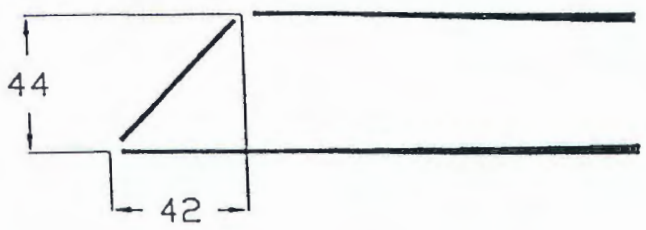

Fig. 2.7. Schematic sketch of the 12–sensor vorticity probe.

Fig. 2.8. Smoke flow visualization of the Kármán vortex lines showing parallel shedding.

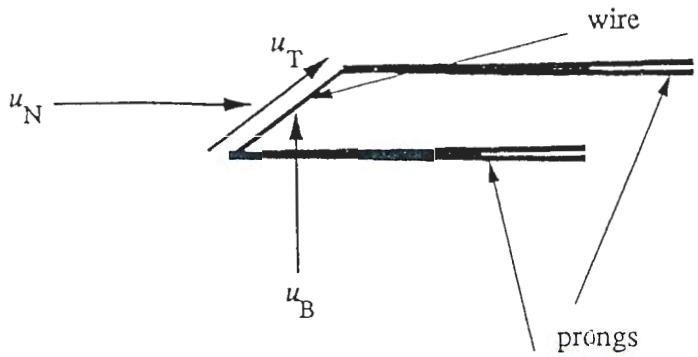

Fig. 3.1. Schematic sketch showing the three components of the cooling velocity for a hot-wire sensor.

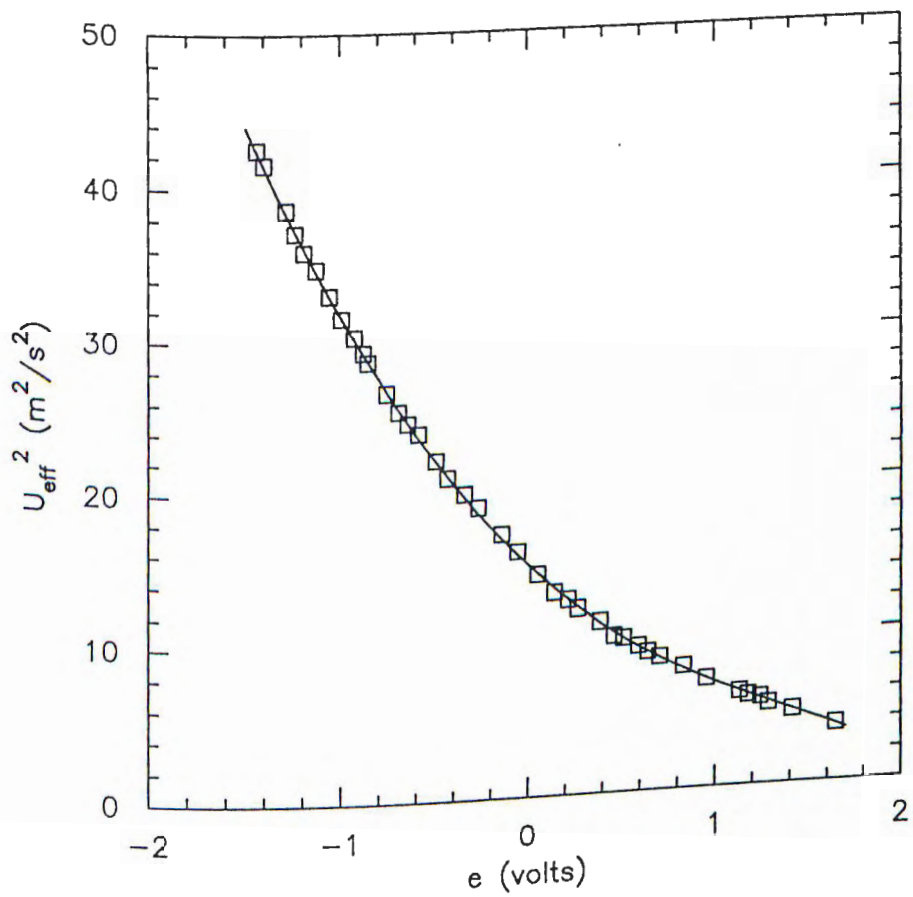

Fig. 3.2. Calibration curve of one sensor in the 12−sensor probe. The line is a 4th−order polynomial curve fit; the symbol is measurement.

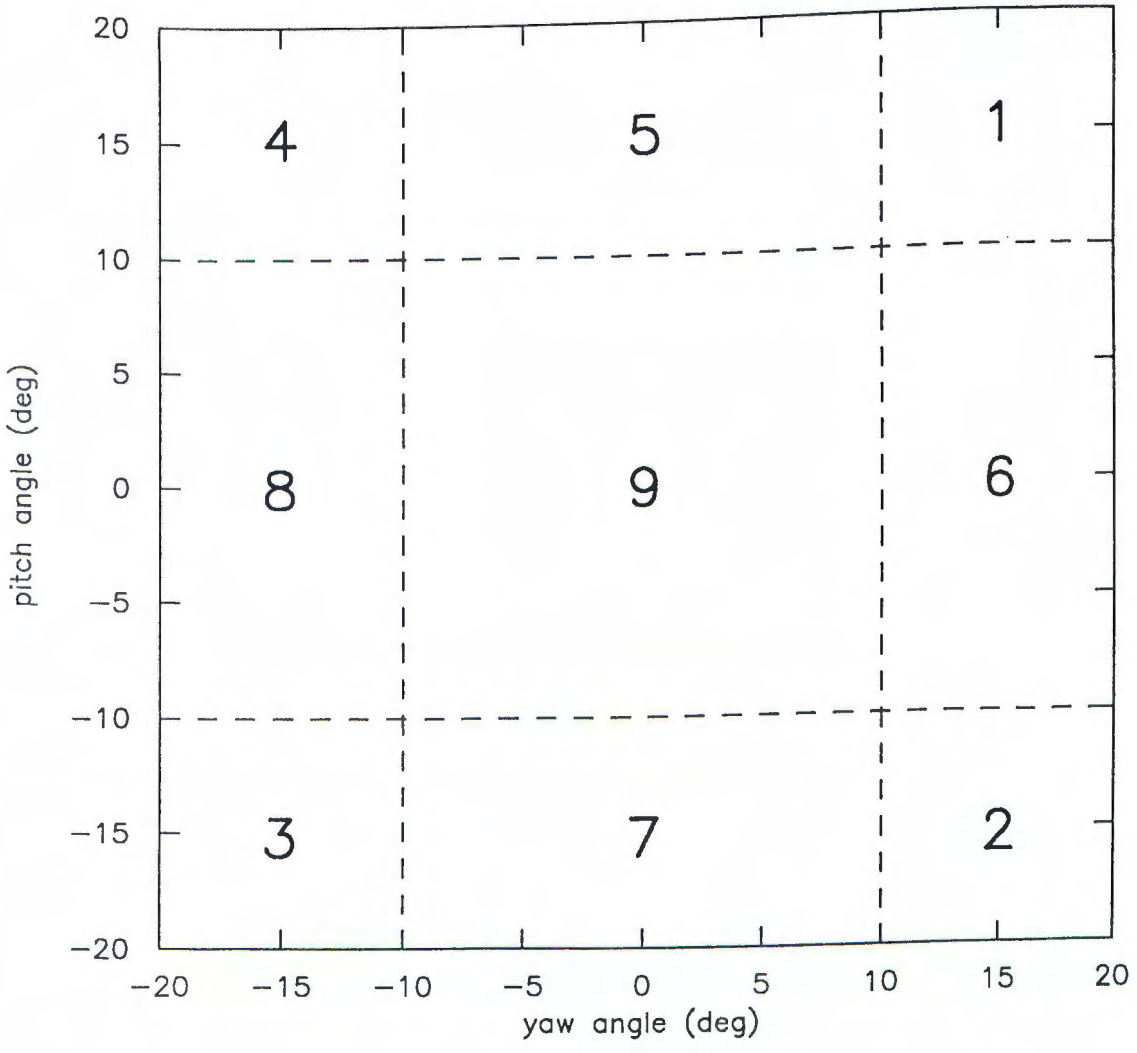

Fig. 3.3. Division of calibration angle space into calibration zones.

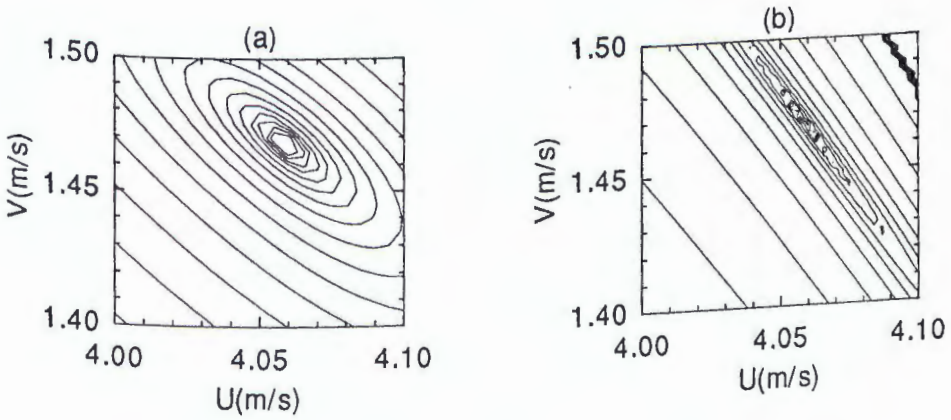

Fig. 3.4. Comparison of solution techniques for the plus probe: (a) 4 sensors used, and (b) 3 sensors used.

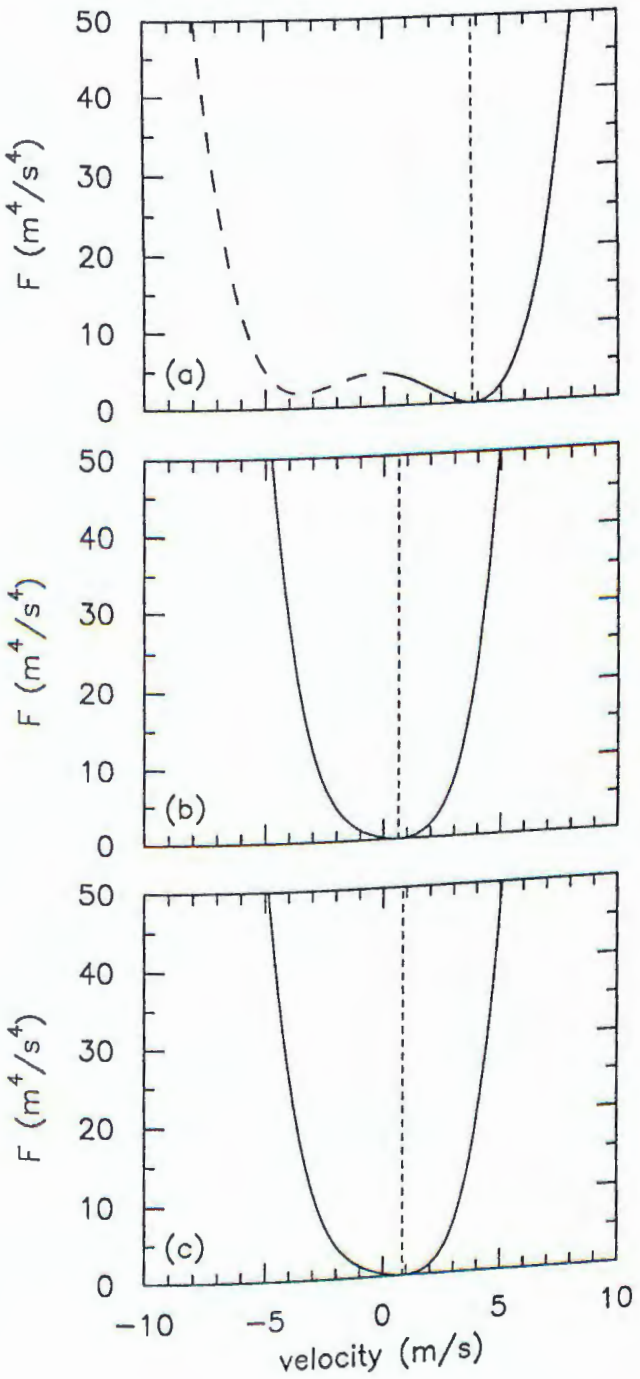

Fig. 3.5. Solution characteristics of the 12-sensor probe velocity components: (a) U, (b) V, and (c) W. The vertical dashed line indicates the solution. For each plot, all other flow variables are held at the converged values.

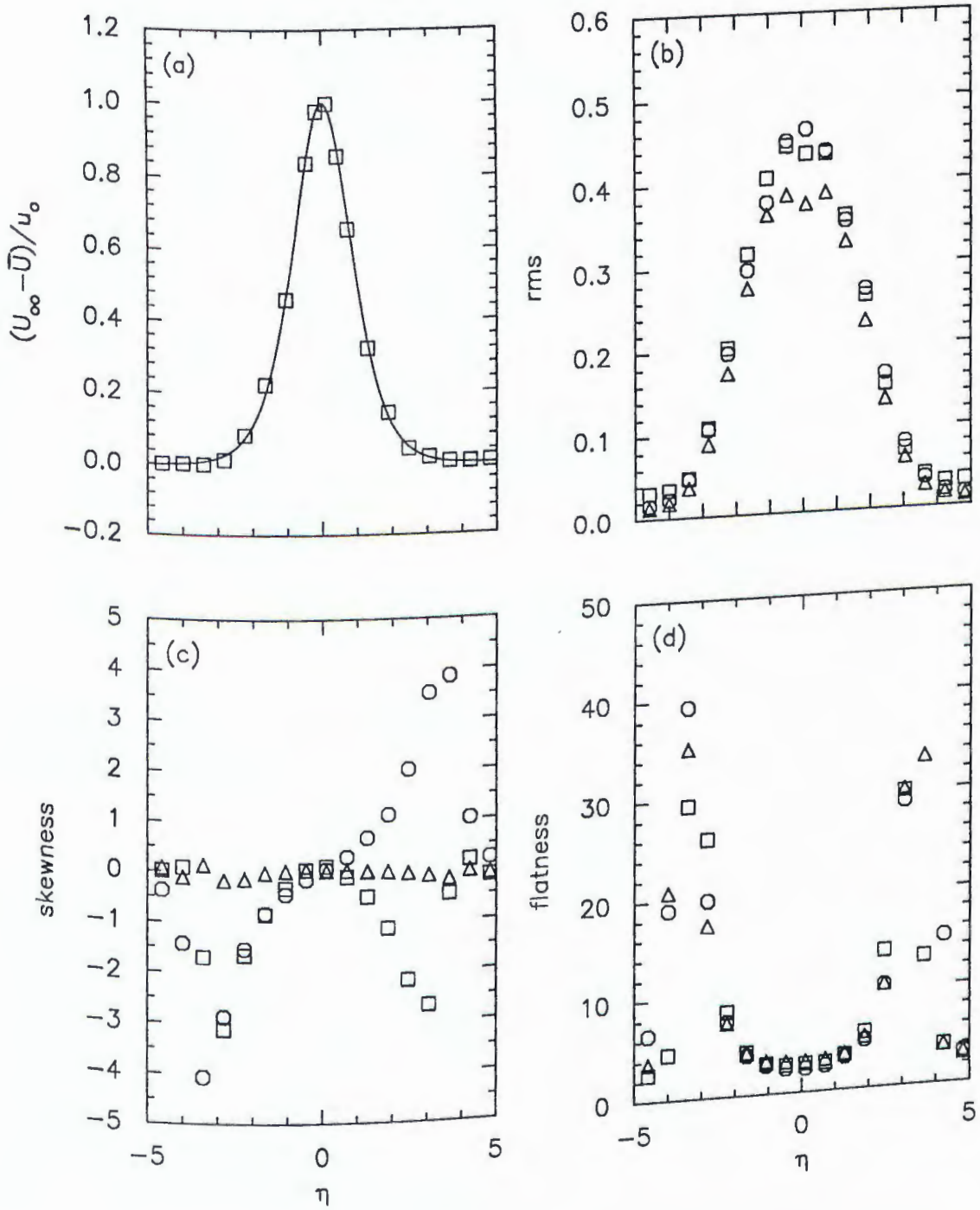

Fig. 4.1. Mean velocity and moments of the fluctuating velocity components at x/d=30: (a) mean velocity with the curve fit as solid line, (b) rms, (c) skewness, and (d) flatness. □, u; ○, v; △, w. The velocity component rms values are normalized by u_o in this and subsequent figures; $\eta = y/L_o$ in this and subsequent figures.

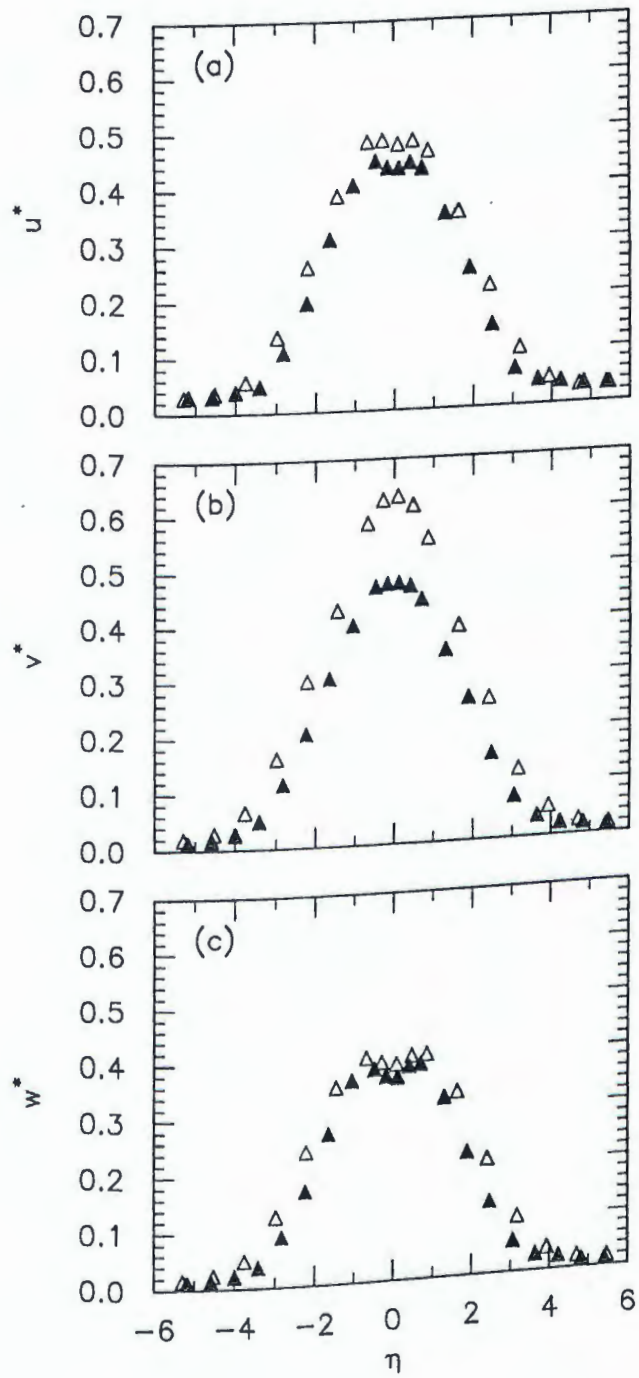

Fig. 4.2. Comparison of the velocity component rms values at two streamwise locations: (a) u^*, (b) v^*, and (c) w^*. The open symbols are for x/d=20, and the closed symbols are for x/d=30.

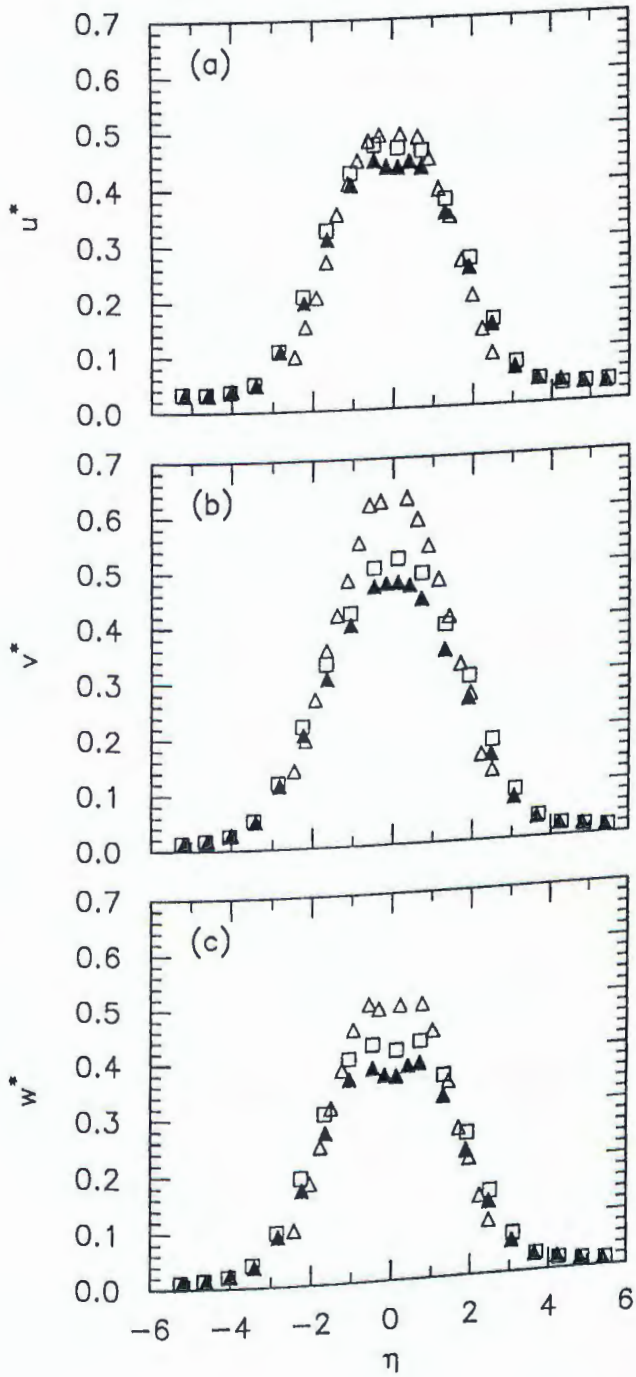

Fig. 4.3. Comparison of the velocity component rms values from 12−sensor probe measurements to V−probe and X−probe values at x/d=30: (a) u^*, (b) v^*, and (c) w^*. □, V−probe; △, X−probe; and ▲, 12−sensor probe. The V−probe comes from one array of the 12−sensor probe. The X−probe data are from Yamada et al. [70].

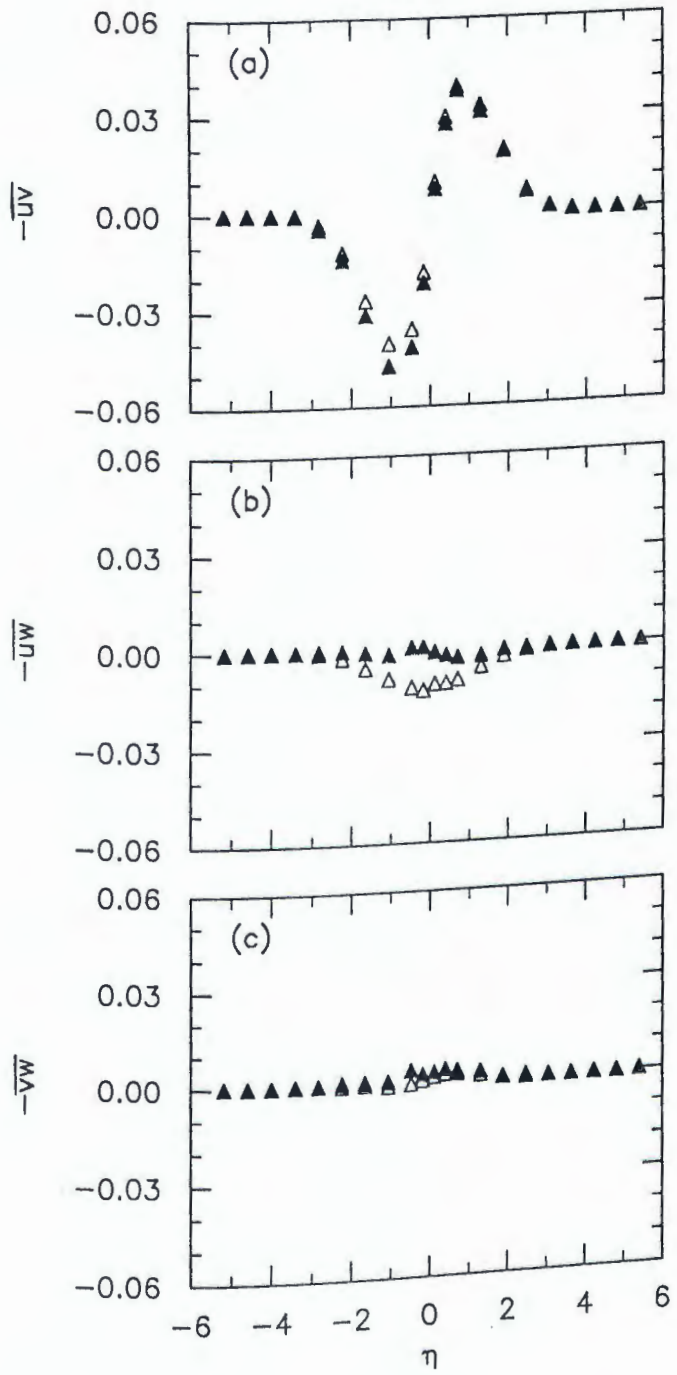

Fig. 4.4. Comparison between the 4−sensor and 12−sensor probe measurements of the Reynolds shear stresses at x/d=30: (a) $-\overline{uv}$, (b) $-\overline{uw}$, and (c) $-\overline{vw}$. The open symbols are for the 4−sensor probe, and the closed symbol for the 12−sensor probe. These stresses are normalized with u_o^2.

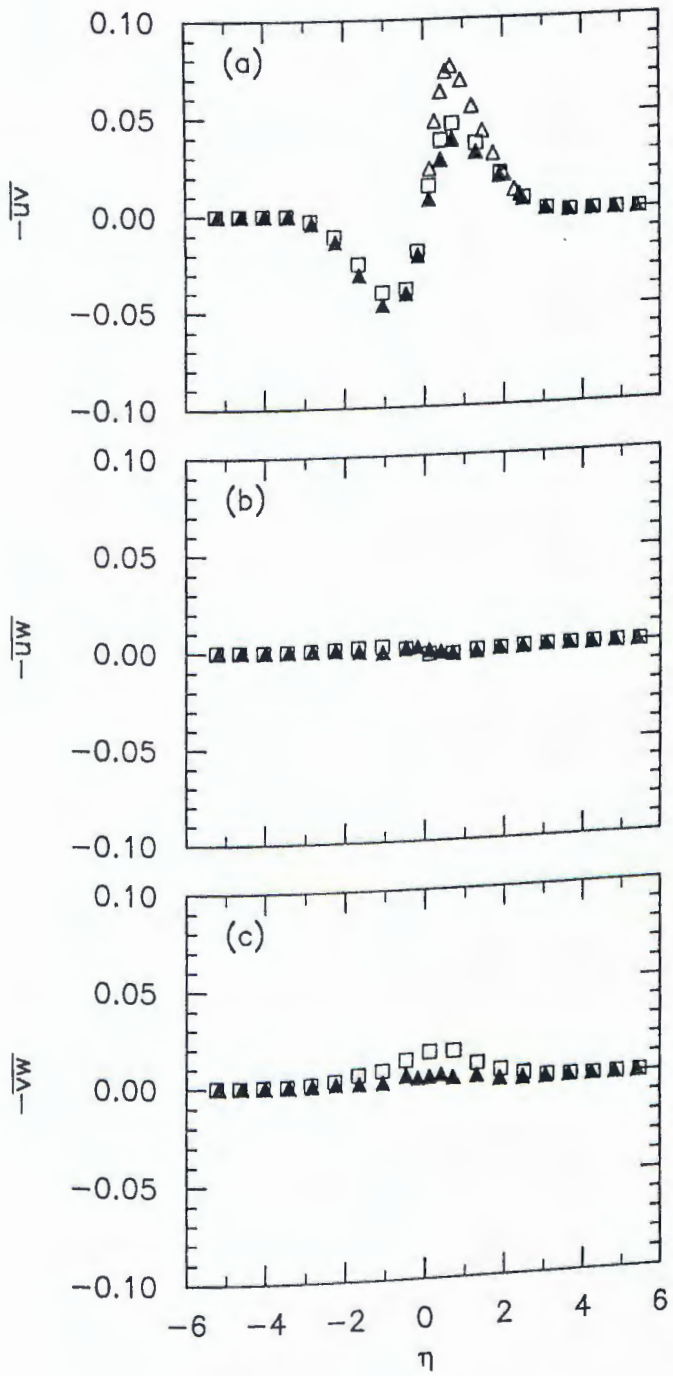

Fig. 4.5. Comparison of 12−sensor probe measurements of the Reynolds stresses to V−probe, and X−probe values at x/d=30: (a) $-\overline{uv}$, (b) $-\overline{uw}$, (c) $-\overline{vw}$. □, V−probe; △, X−probe; ▲, 12−sensor. The V−probe data are from one array of the 12−sensor probe. The X−probe data are from Yamada et al. [70]. These stresses are normalized with u_o^2.

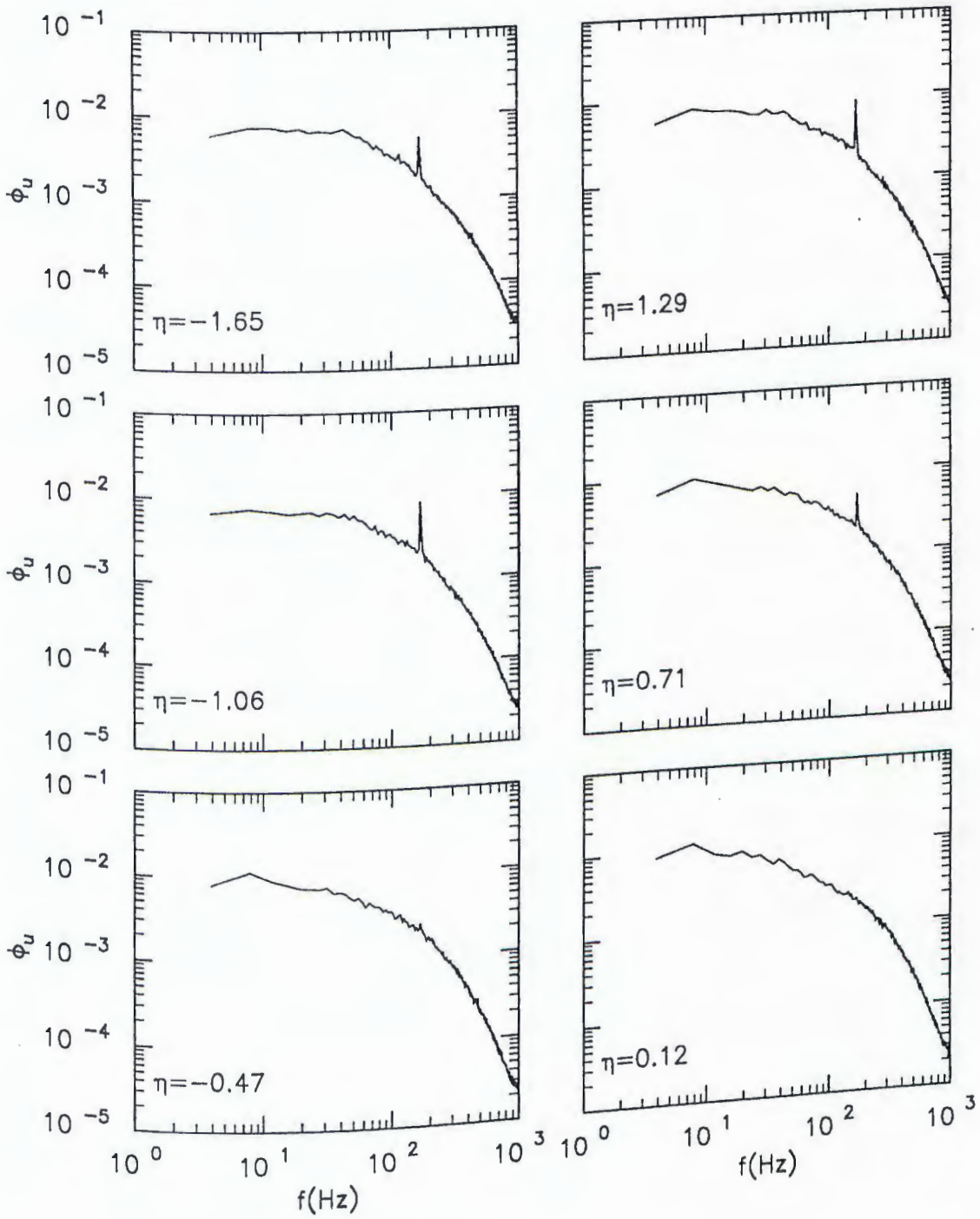

Fig. 4.6. Power spectra of the streamwise velocity. All spectra are normalized by the local variance and integrate to unity in this and subsequent figures.

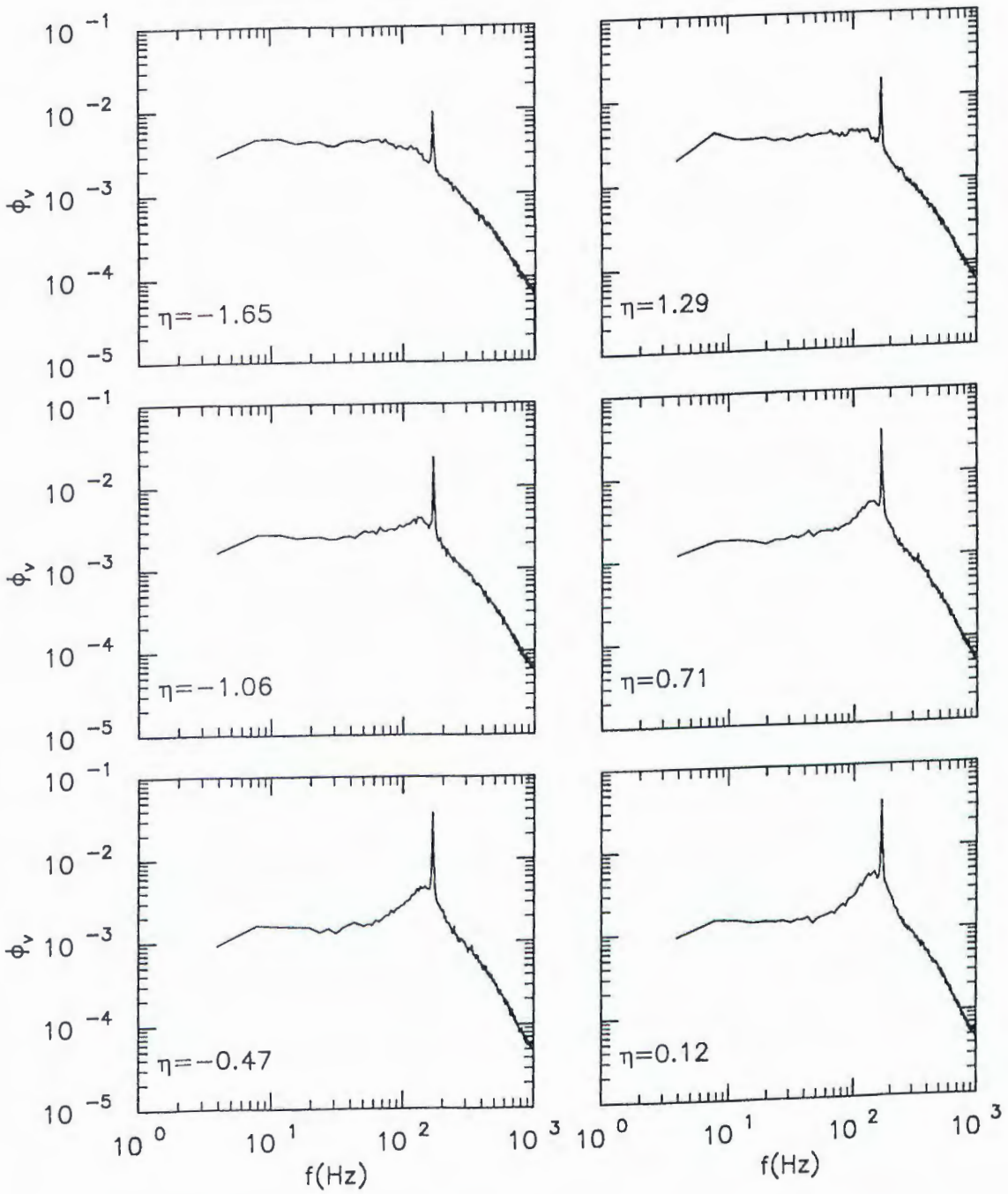

Fig. 4.7. Power spectra of the transverse velocity.

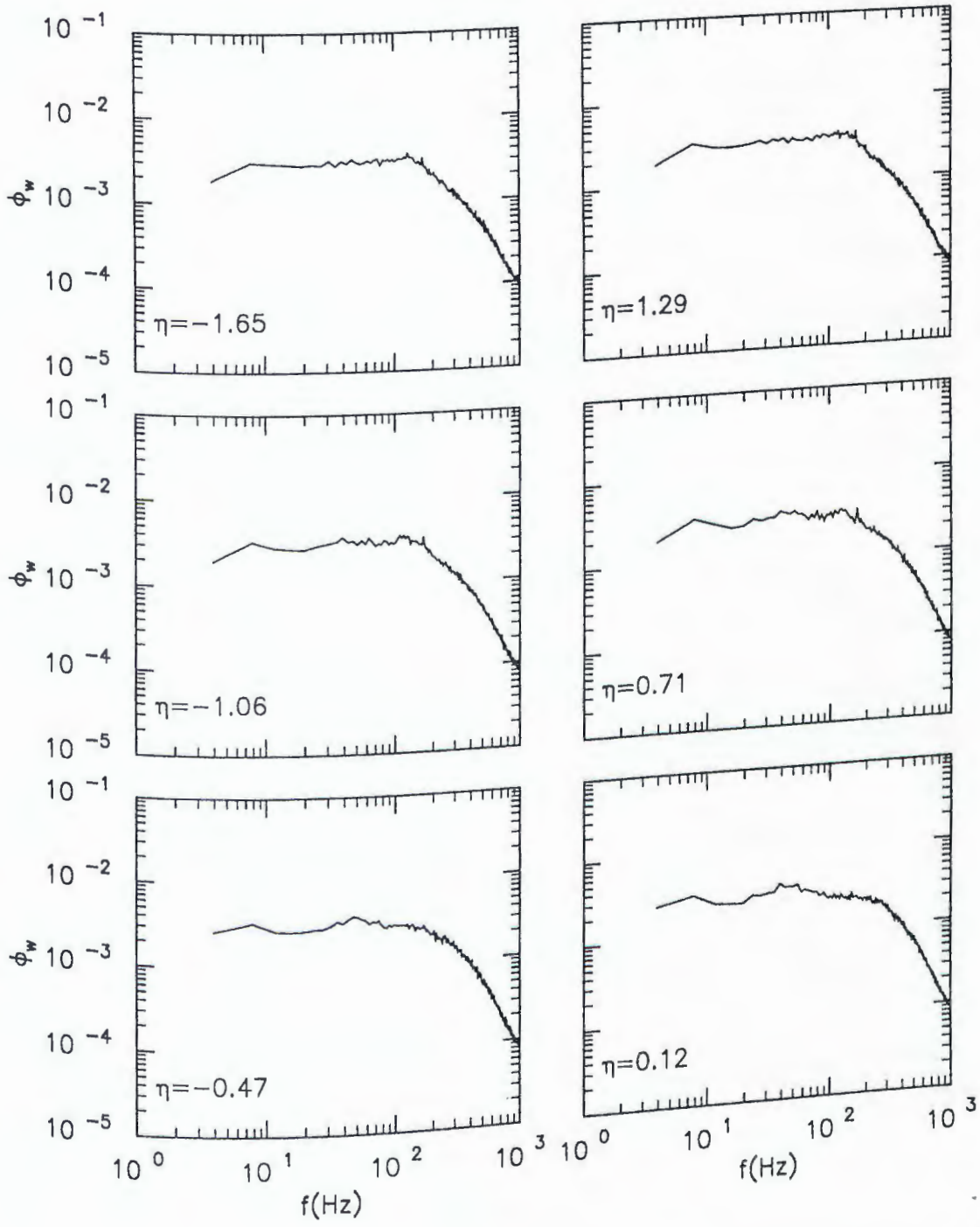

Fig. 4.8. Power spectra of the spanwise velocity.

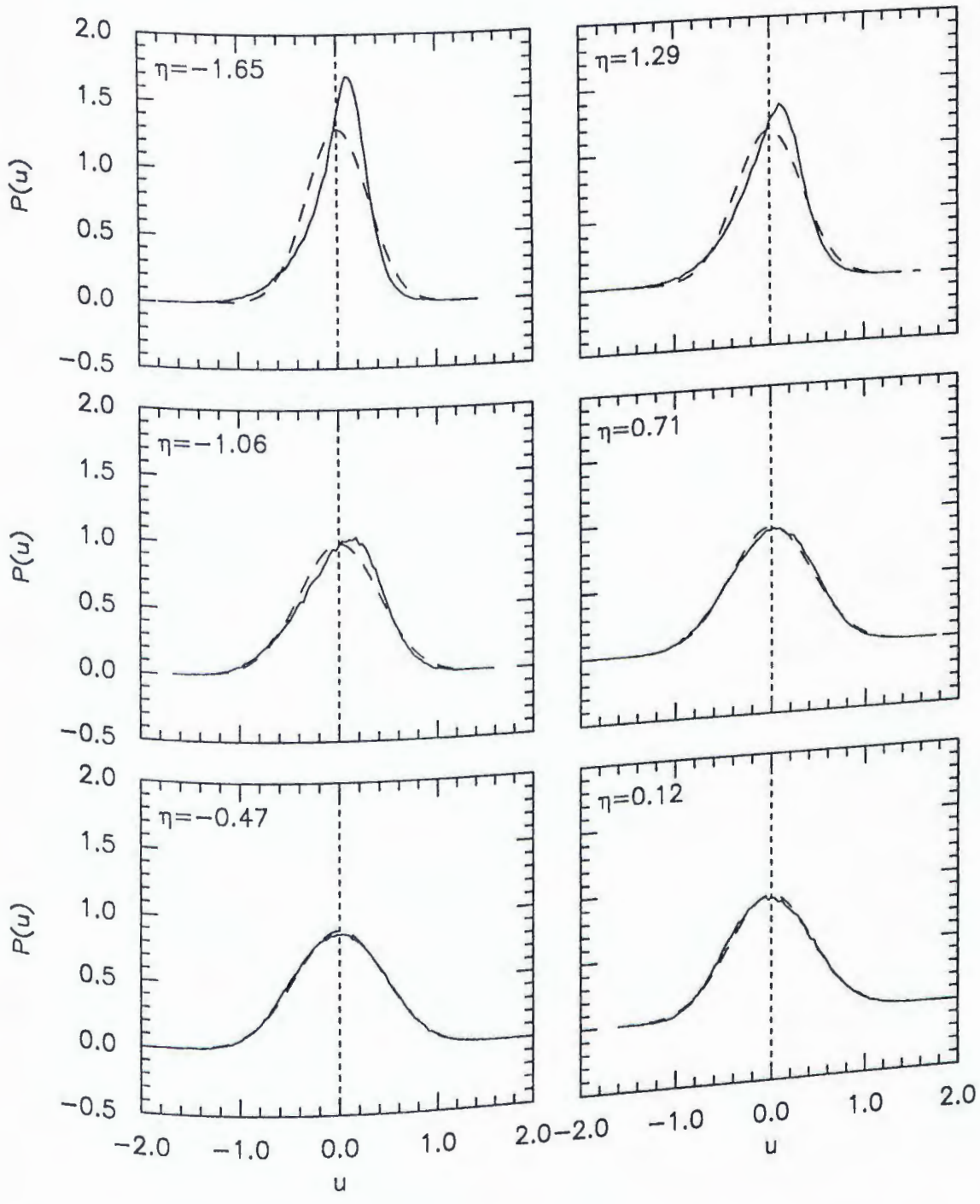

Fig. 4.9. Probability density function (PDF) of the streamwise velocity. Gaussian distributions are shown as dashed lines. The velocity components in this and subsequent PDF and JPDF figures are normalized by u_o.

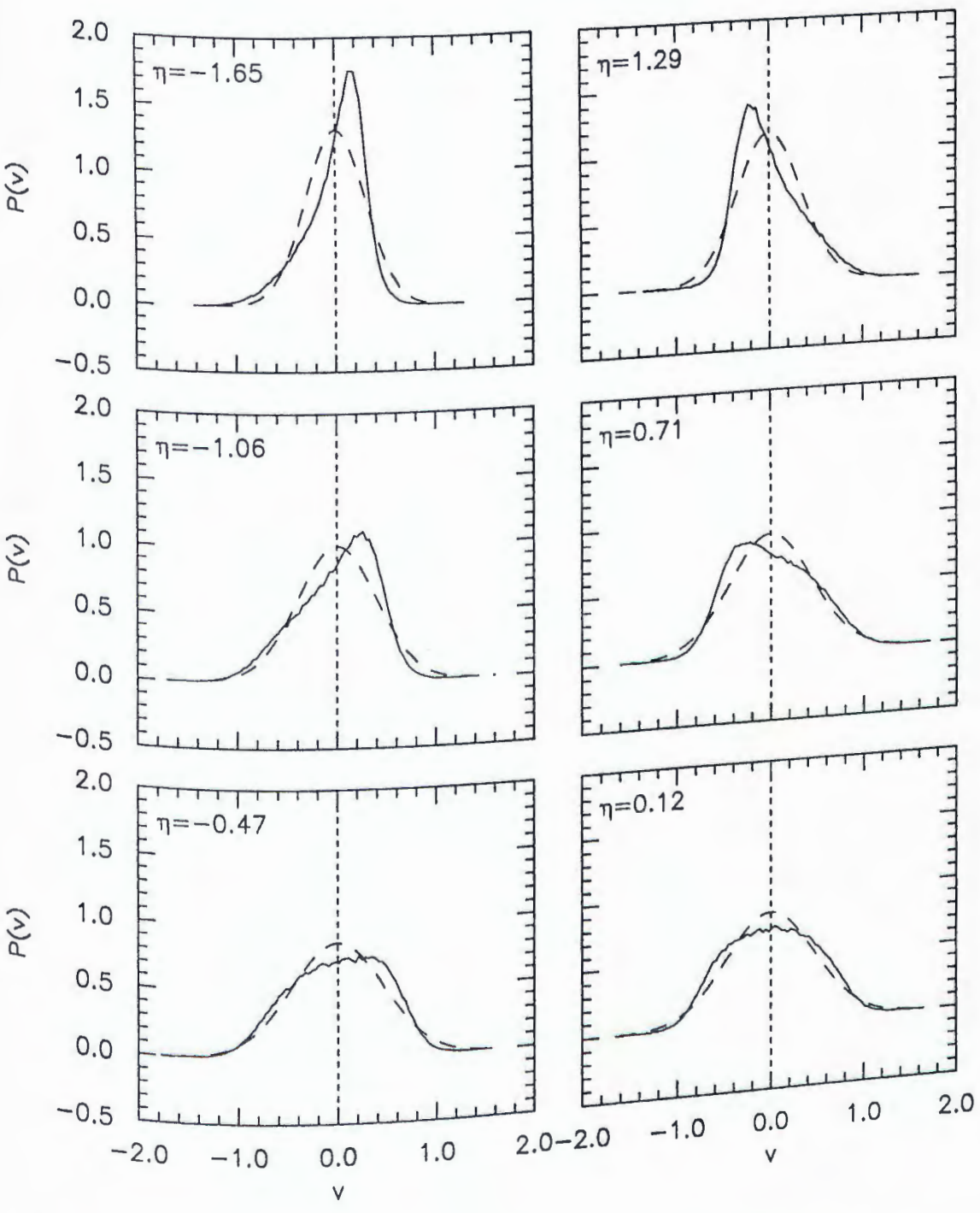

Fig. 4.10. PDF of the transverse velocity. Gaussian distributions are shown as dashed lines.

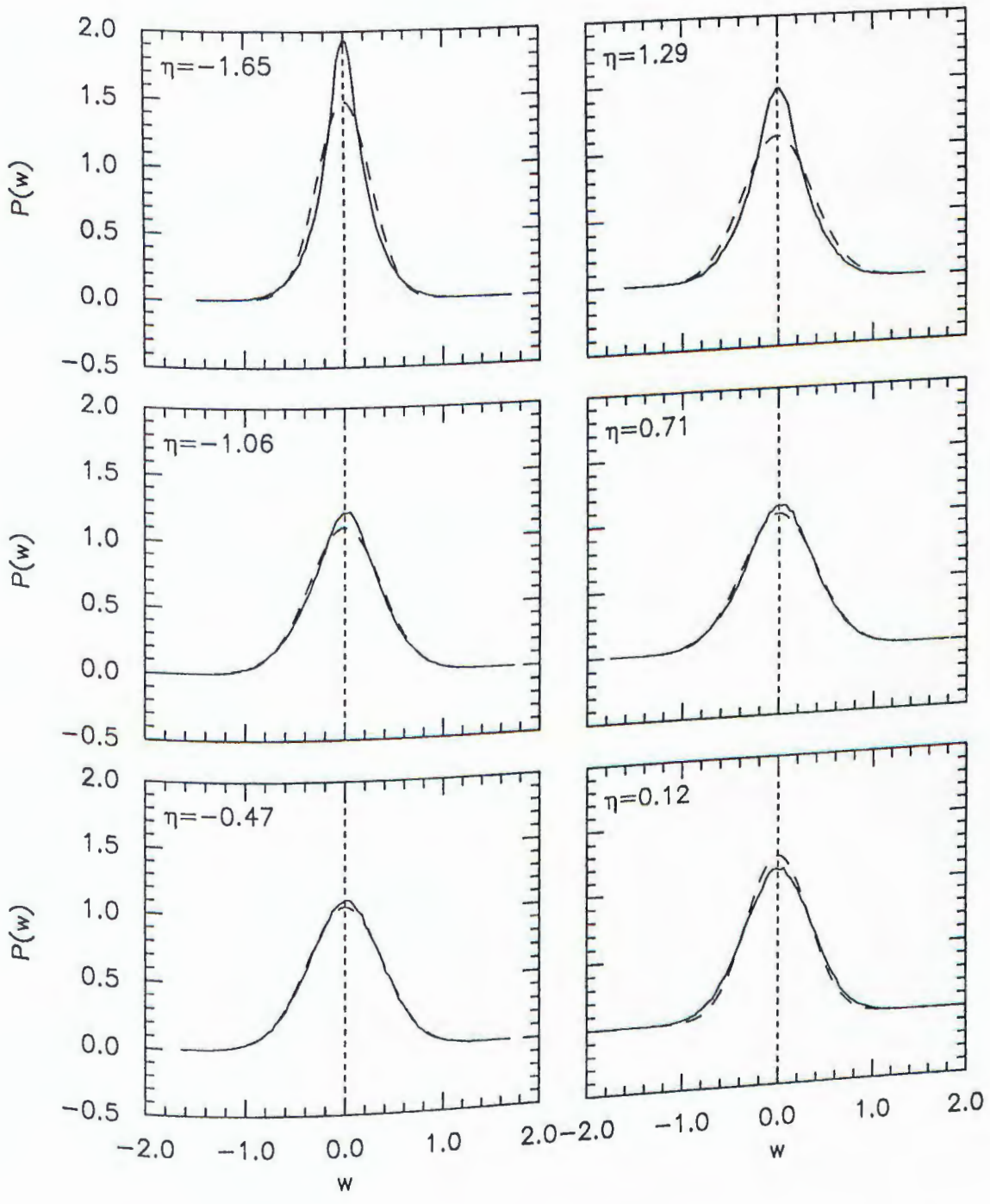

Fig. 4.11. PDF of the spanwise velocity. Gaussian distributions are shown as dashed lines.

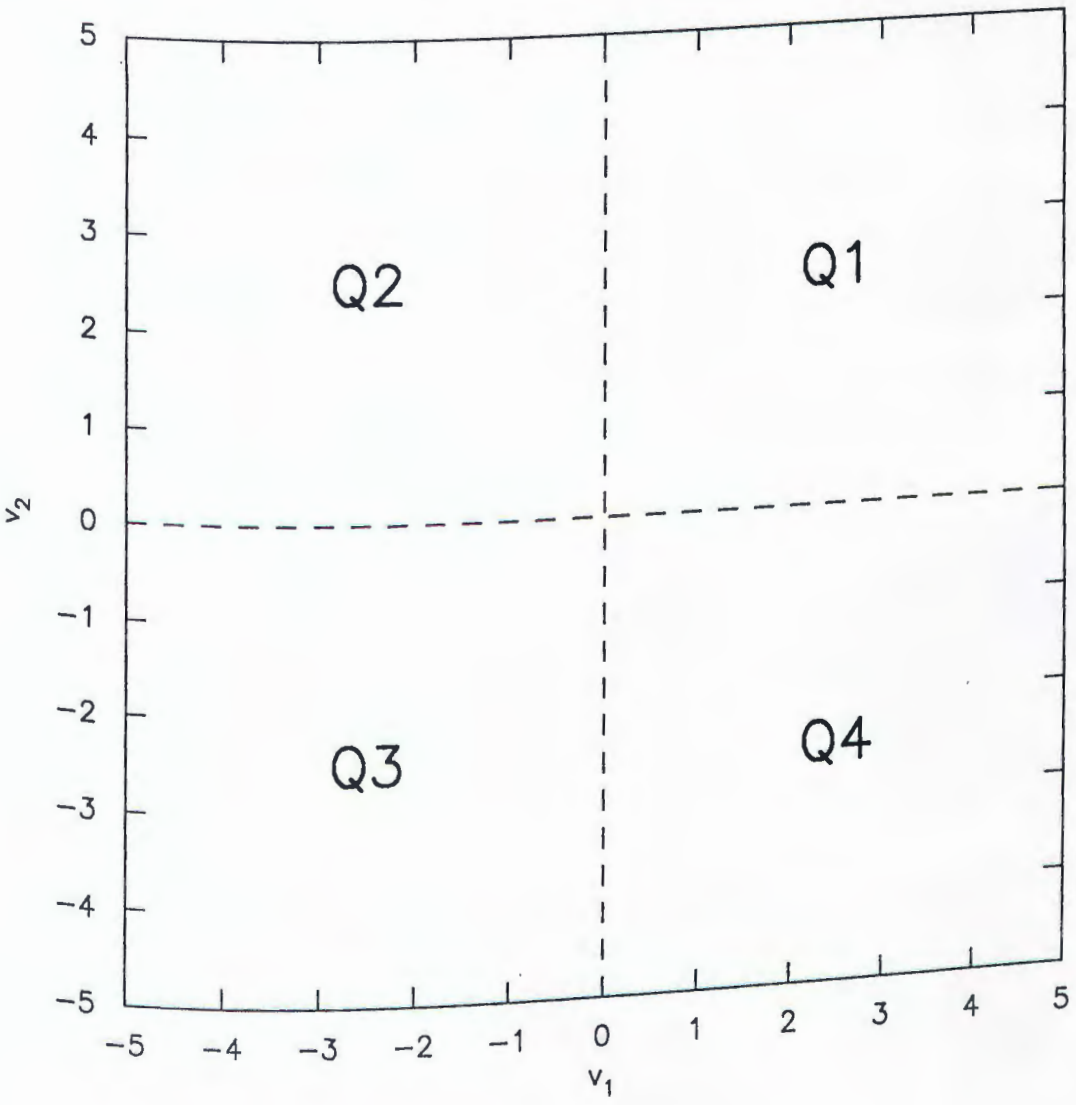

Fig. 4.12. Definition of the quadrants.

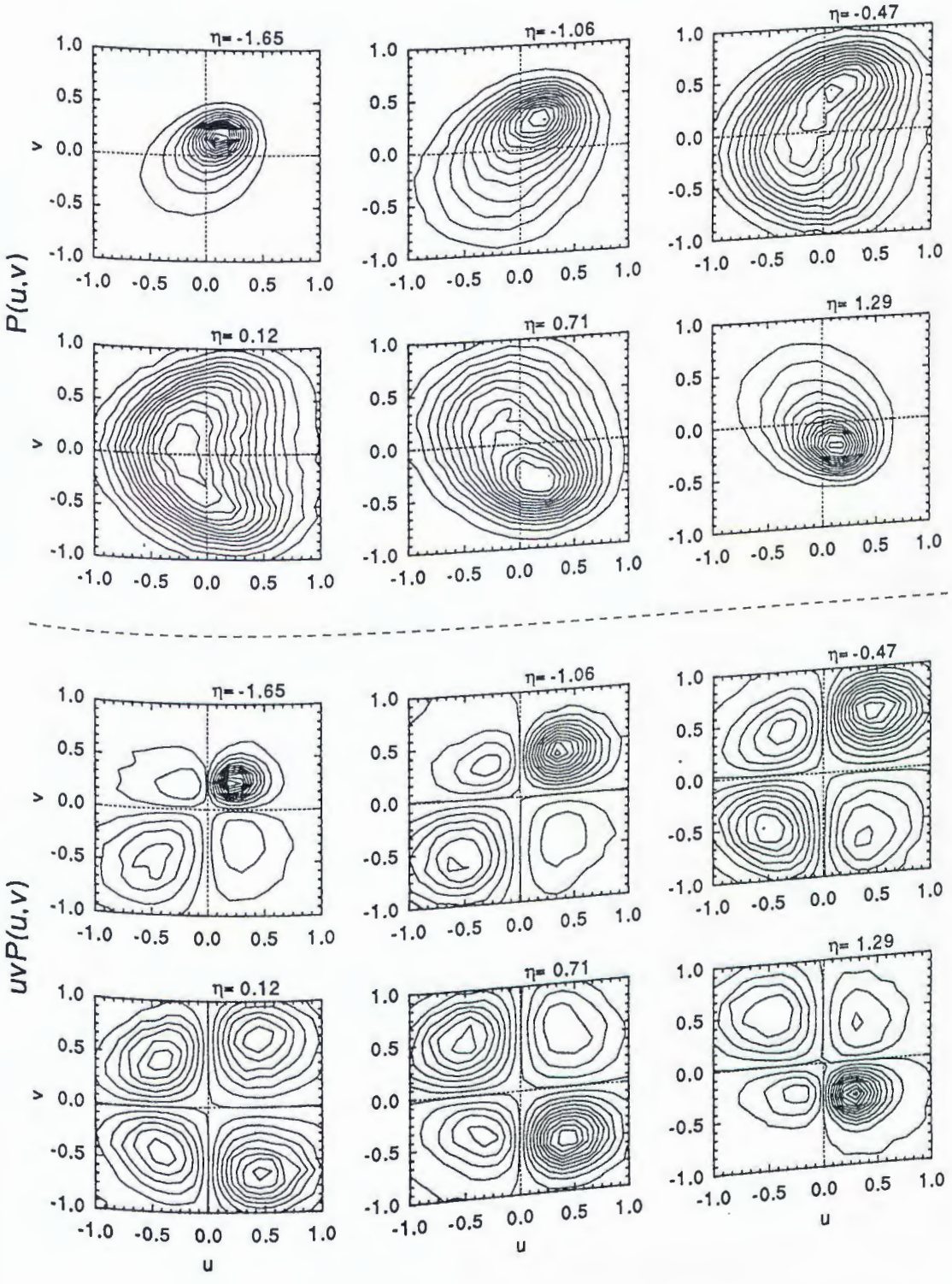

Fig. 4.13. Joint Probability density function (JPDF) (top) and covariance integrand (bottom) contours for the streamwise and transverse velocity components.

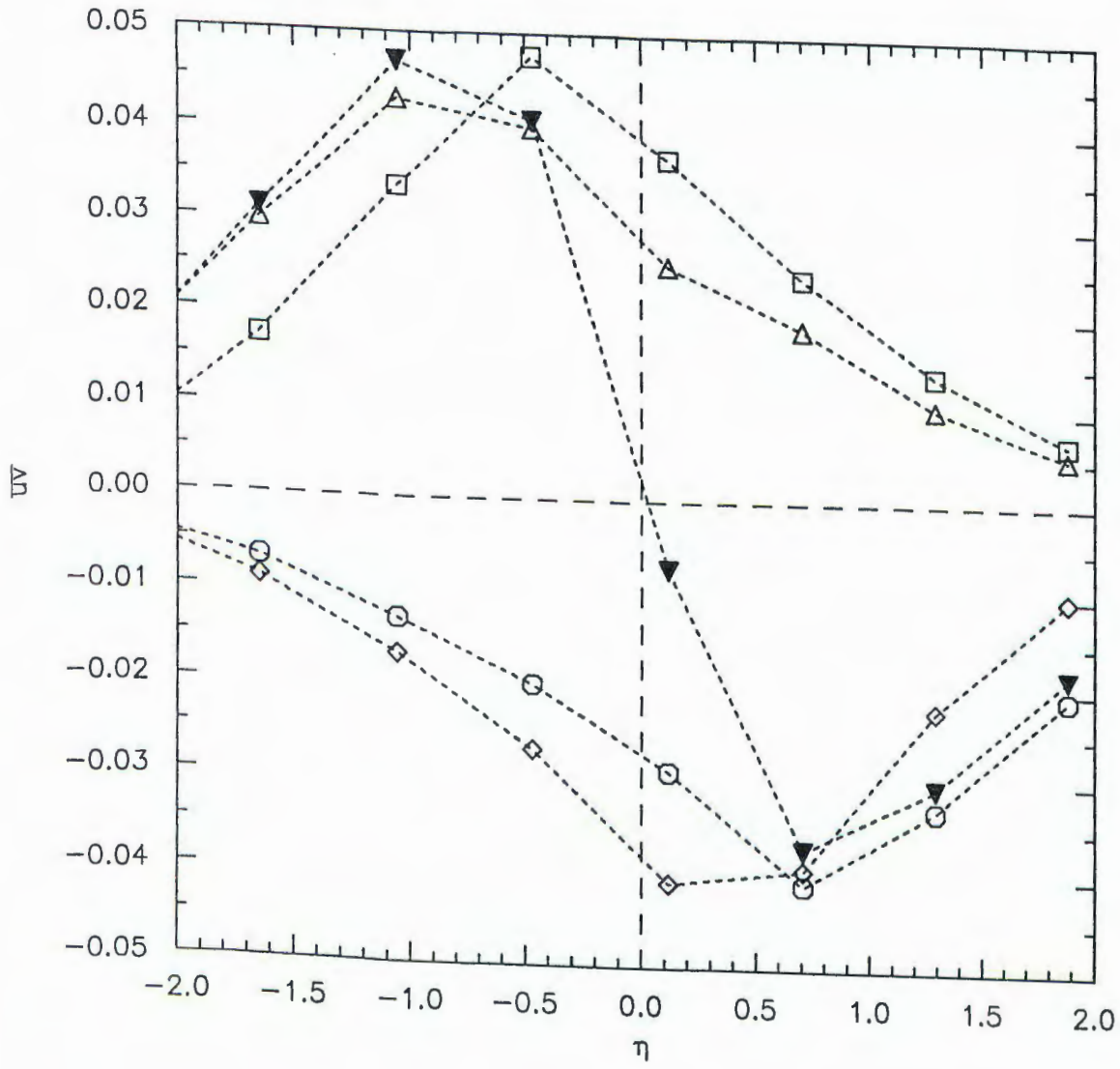

Fig. 4.14. Quadrant analysis for the correlation of the streamwise and transverse velocity components: □, Q1; ○, Q2; △, Q3; ◇, Q4; and ▼, total (sum of quadrant values in this and subsequent figures).

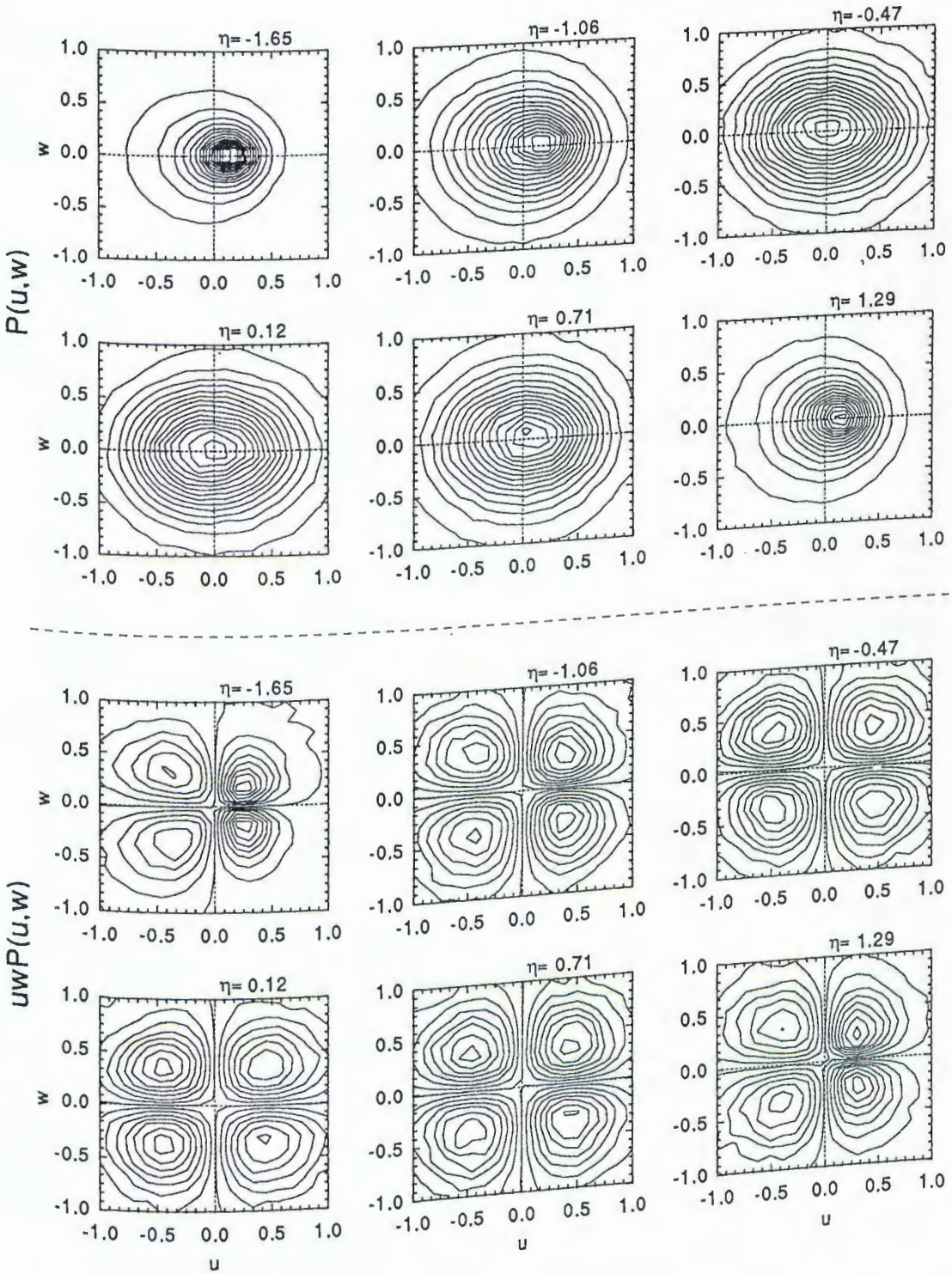

Fig. 4.15. JPDF (top) and covariance integrand (bottom) contours for the streamwise and spanwise velocity components.

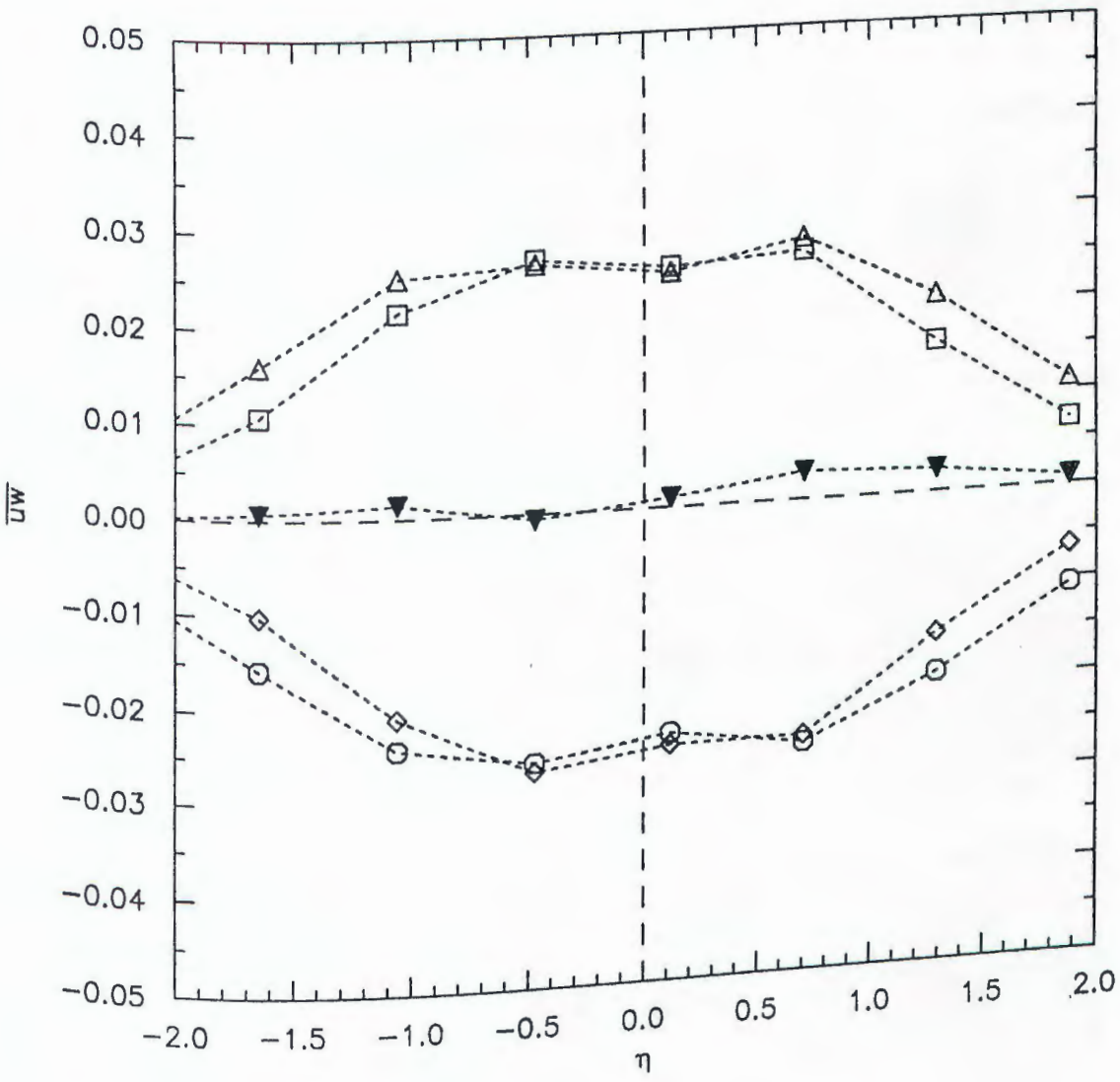

Fig. 4.16. Quadrant analysis for the correlation of the streamwise and spanwise velocity components: □, Q1; ○, Q2; △, Q3; ◇, Q4; and ▼, total.

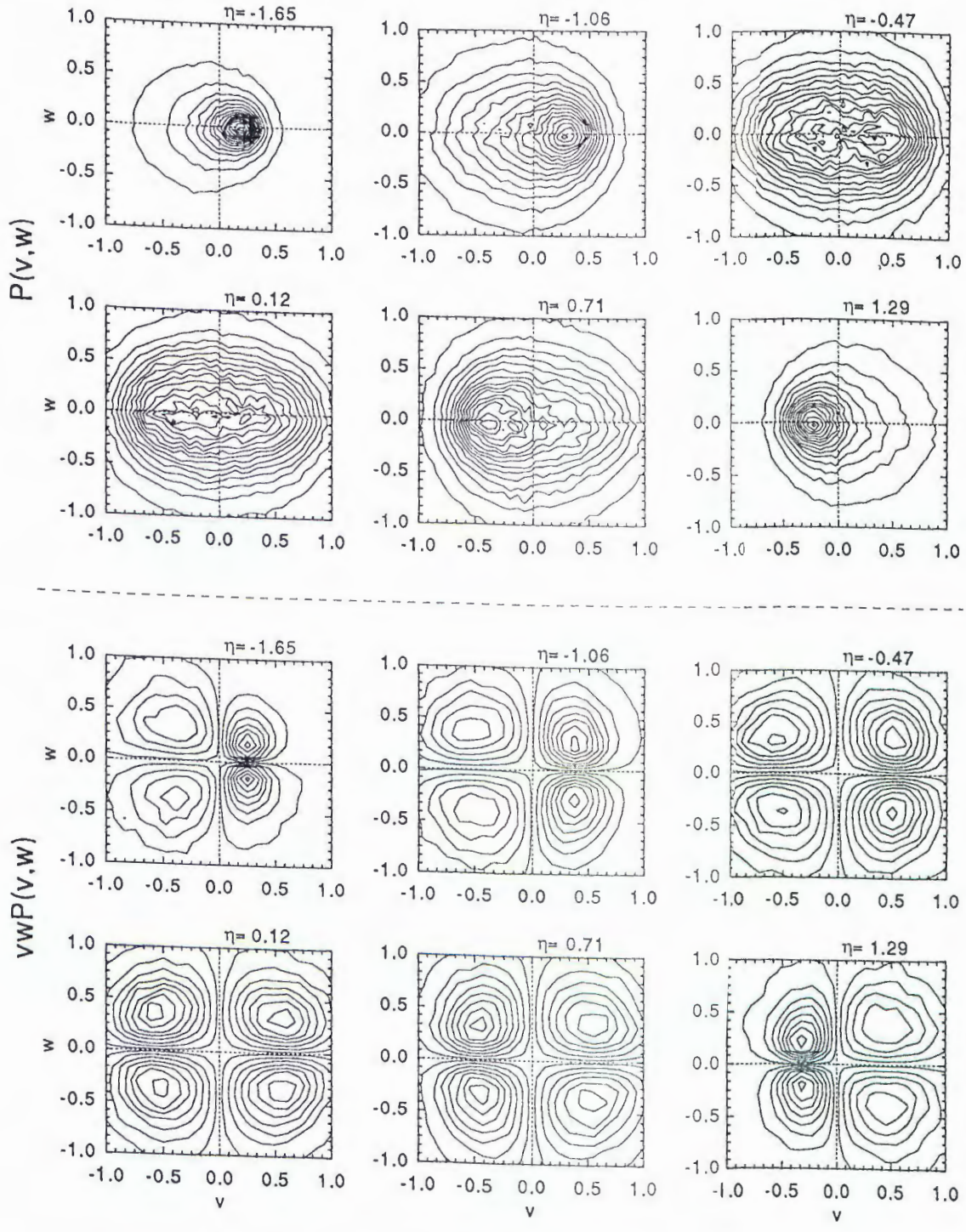

Fig. 4.17. JPDF (top) and covariance integrand (bottom) contours for the transverse and spanwise velocity components.

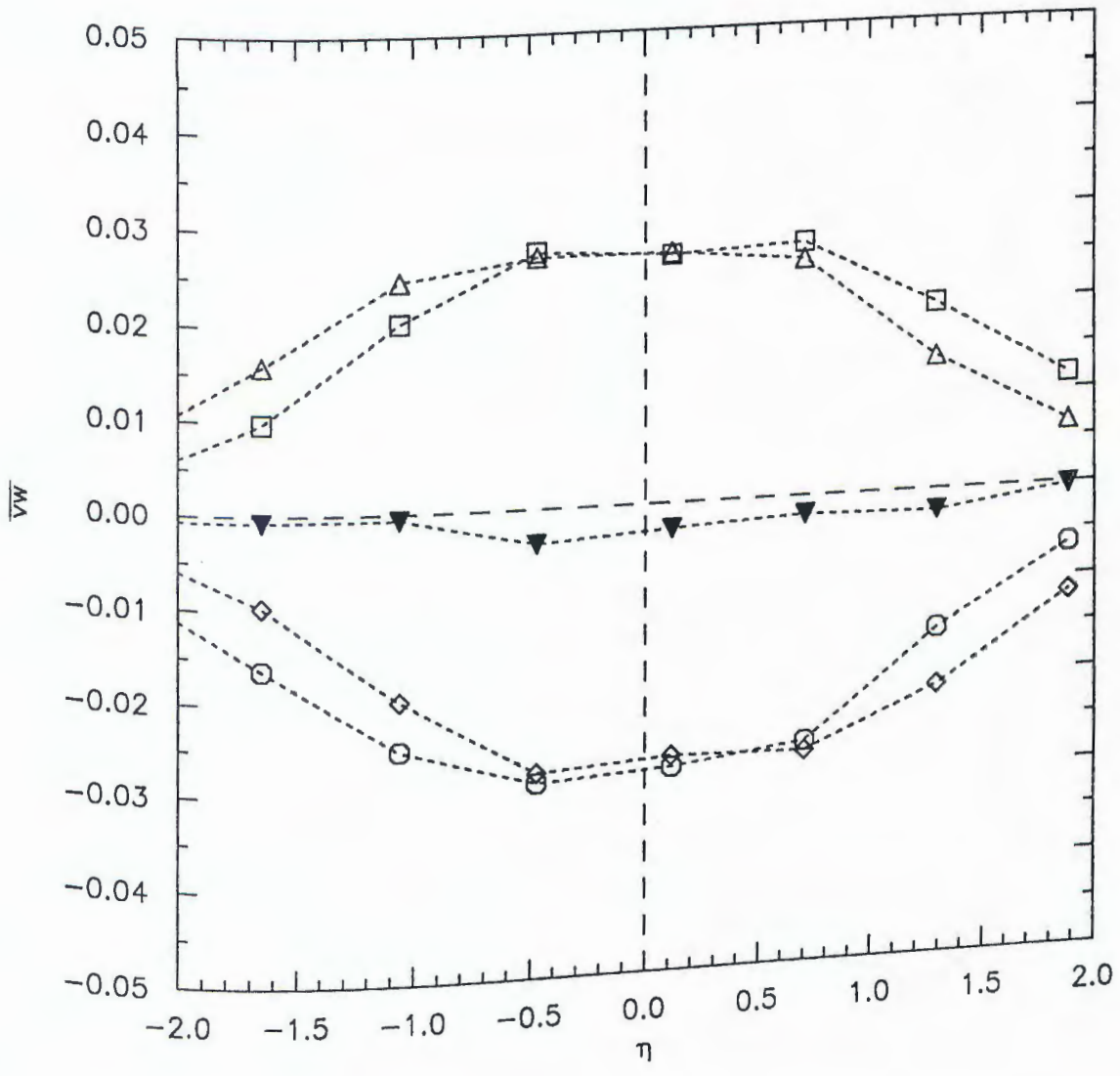

Fig. 4.18. Quadrant analysis for the correlation of the transverse and spanwise velocity components: □, Q1; ○, Q2; △, Q3; ◇, Q4; and ▼, total.

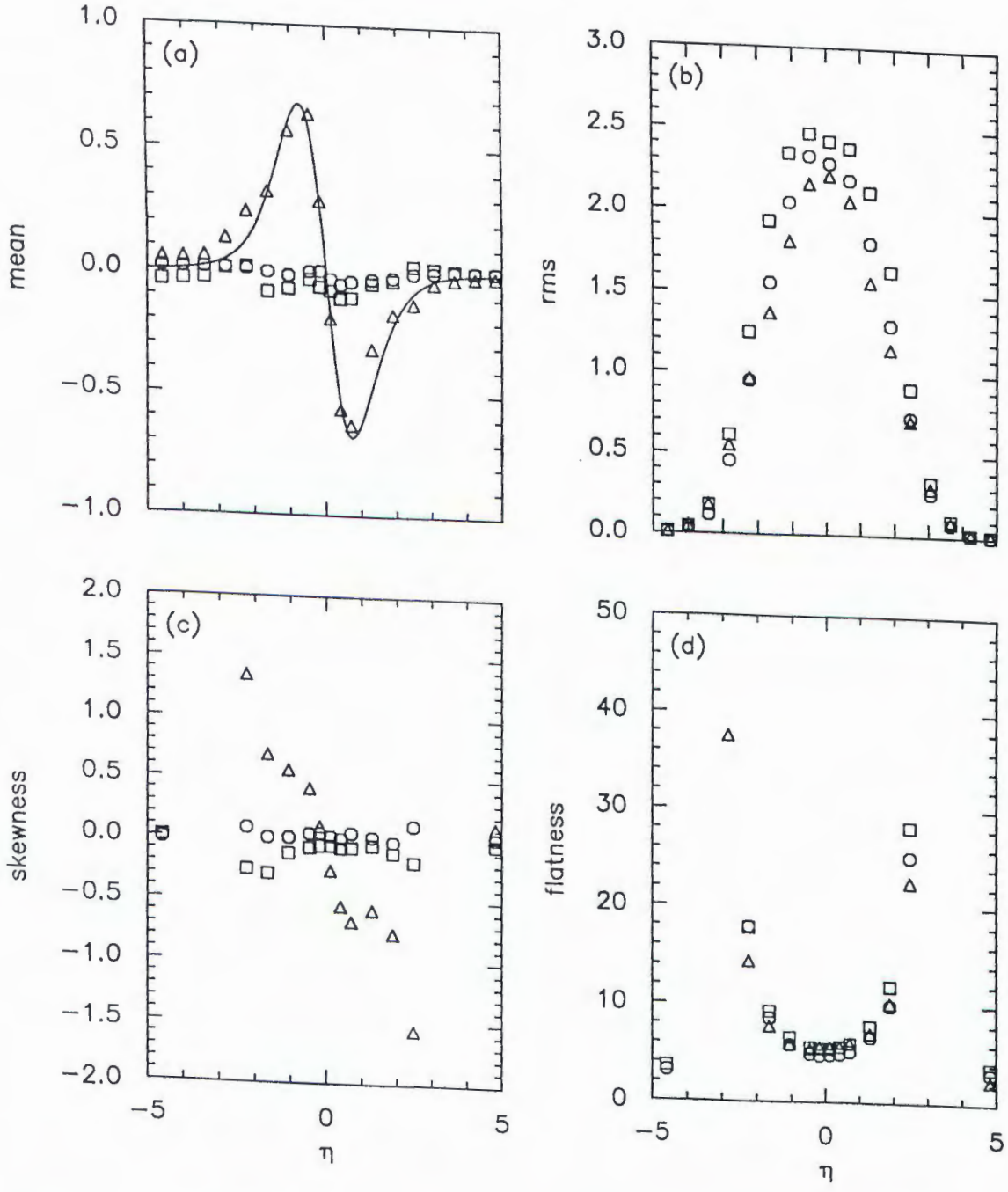

Fig. 5.1. Mean vorticity and moments of the fluctuating vorticity components at x/d=30: (a) mean vorticity with solid line as $-d\bar{U}/dy$, (b) rms, (c) skewness, and (d) flatness. □ , Ω_x; ○, Ω_y; △, Ω_z. The mean and rms values are normalized by u_o/L_o in this and subsequent figures; $\eta=y/L_o$ in this and subsequent figures.

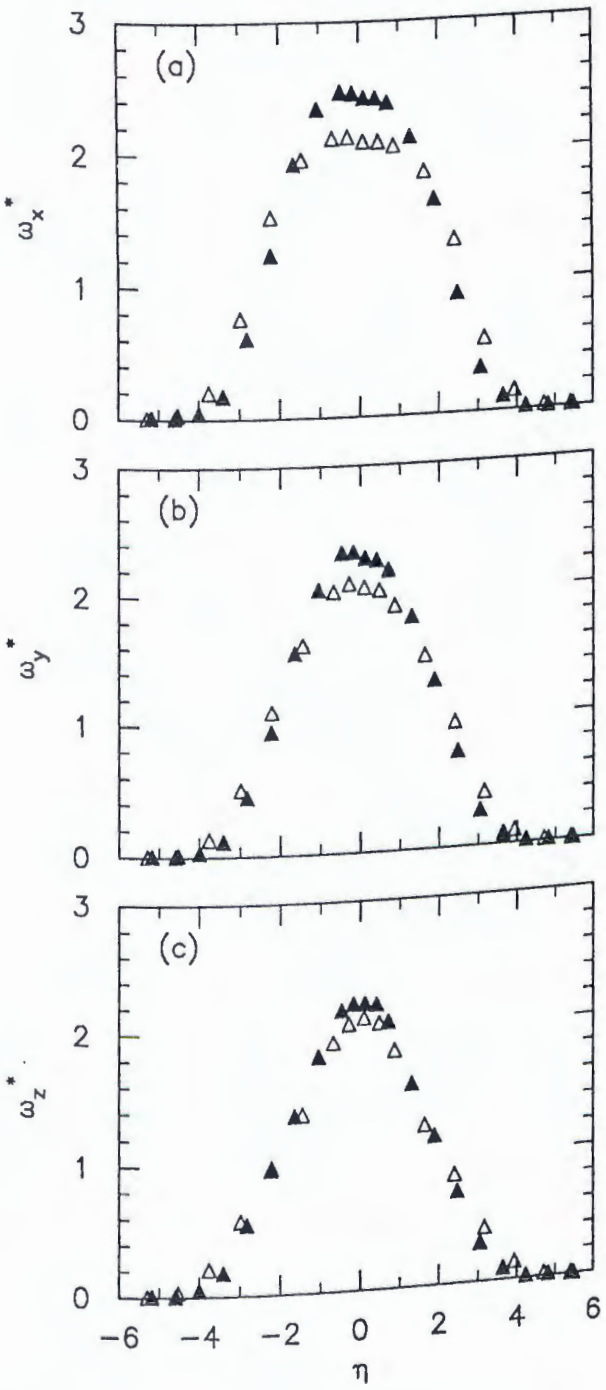

Fig. 5.2. Comparison of the vorticity component rms values at two streamwise locations. (a) ω_x^*, (b) ω_y^*, and (c) ω_z^*. The open symbols are for x/d=20; the closed symbols are for x/d=30.

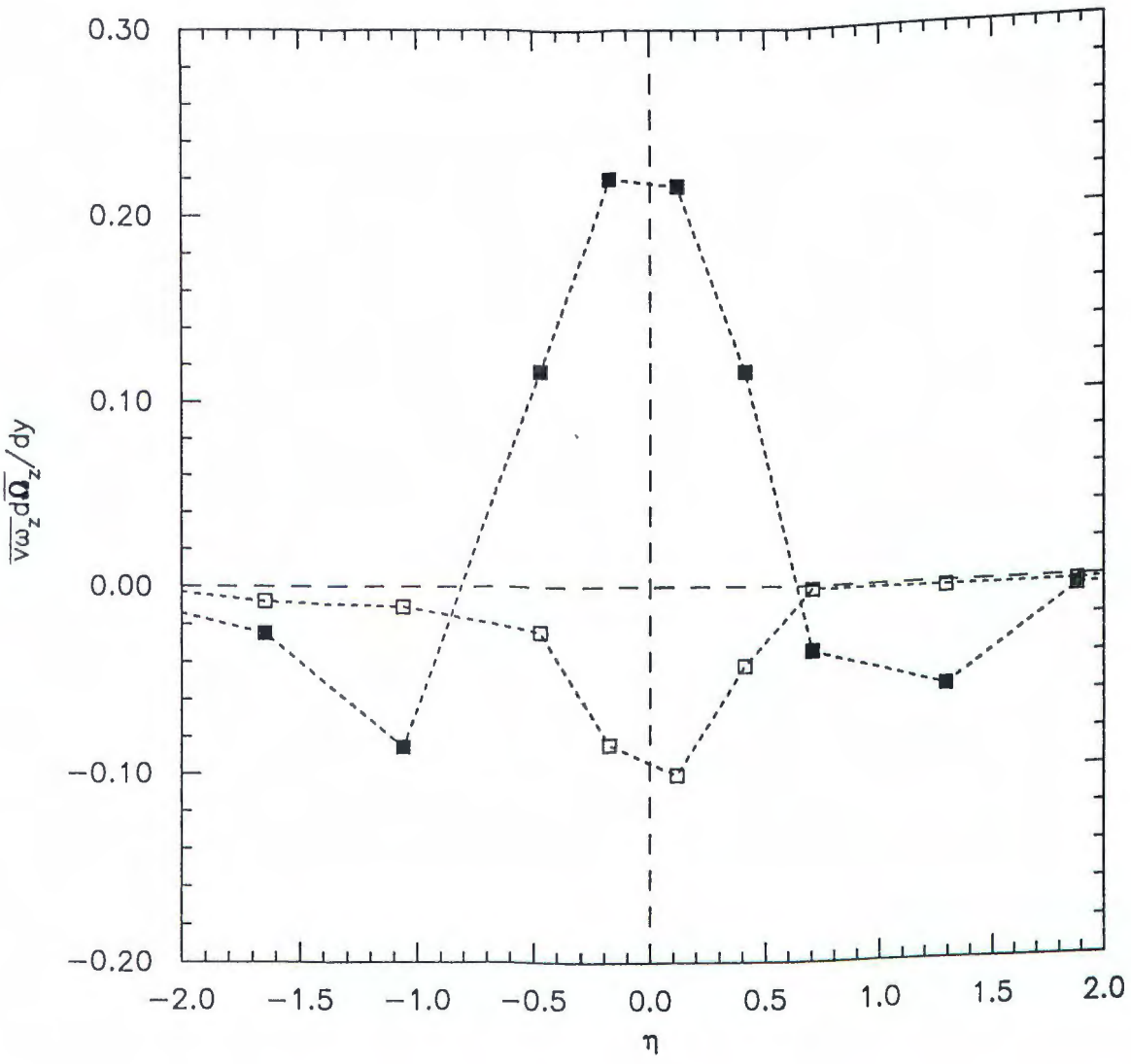

Fig. 5.3. Comparison between the central–difference scheme (C–D) (open symbols) and the backward–difference (B–D) (closed symbols) scheme. The affected term represents production in the mean enstrophy balance.

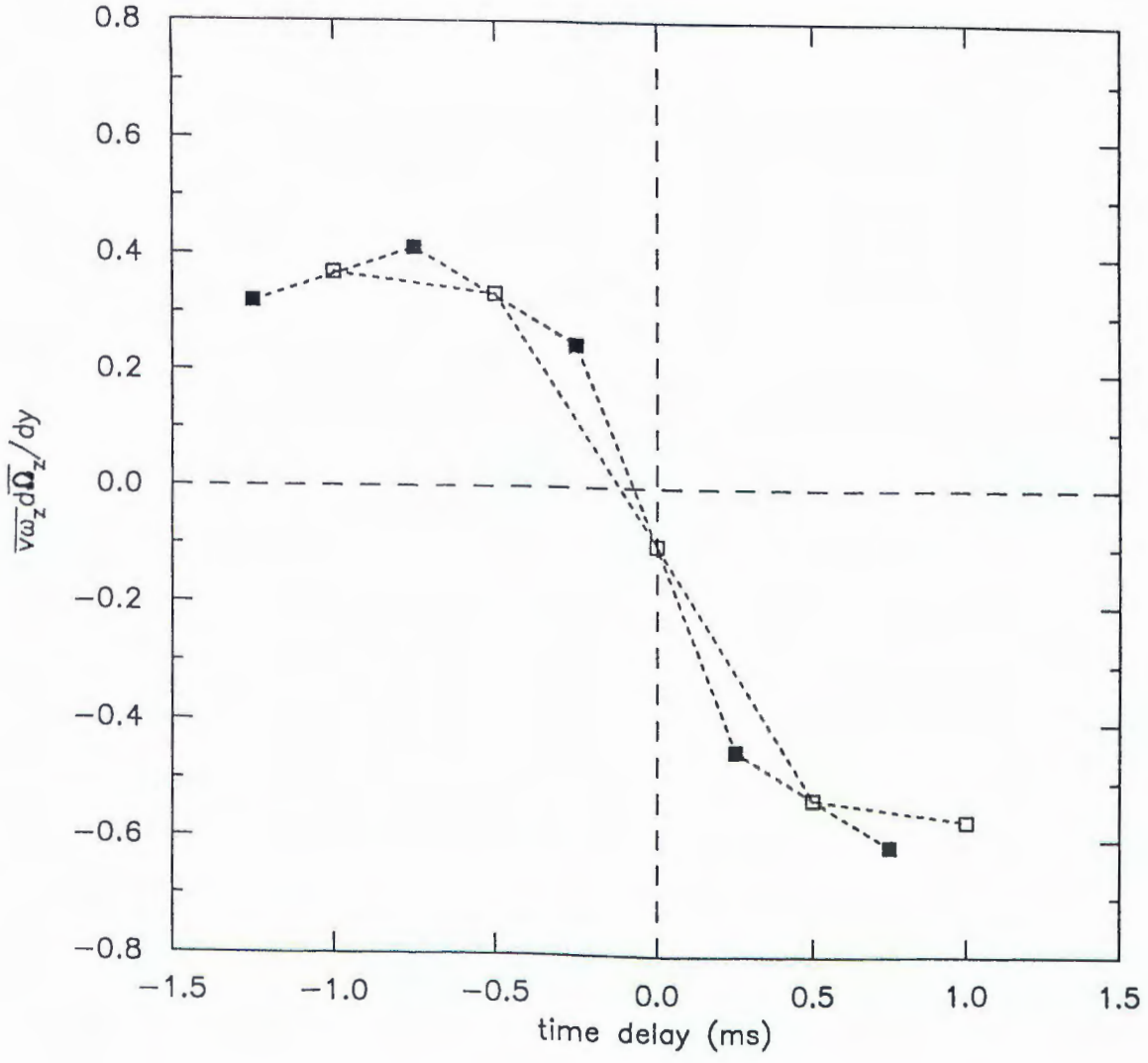

Fig. 5.4. Correlation $\overline{v\omega_z}$ with time delay using central–difference (C–D) (open symbols) and backward–difference (B–D) (closed symbols) schemes. The location is η=0.12. The B–D curve has been corrected by shifting to the left by half a time step or 0.25 ms. The gradient $d\overline{\Omega}_z/dy$ is included to compare with Fig. 5.3.

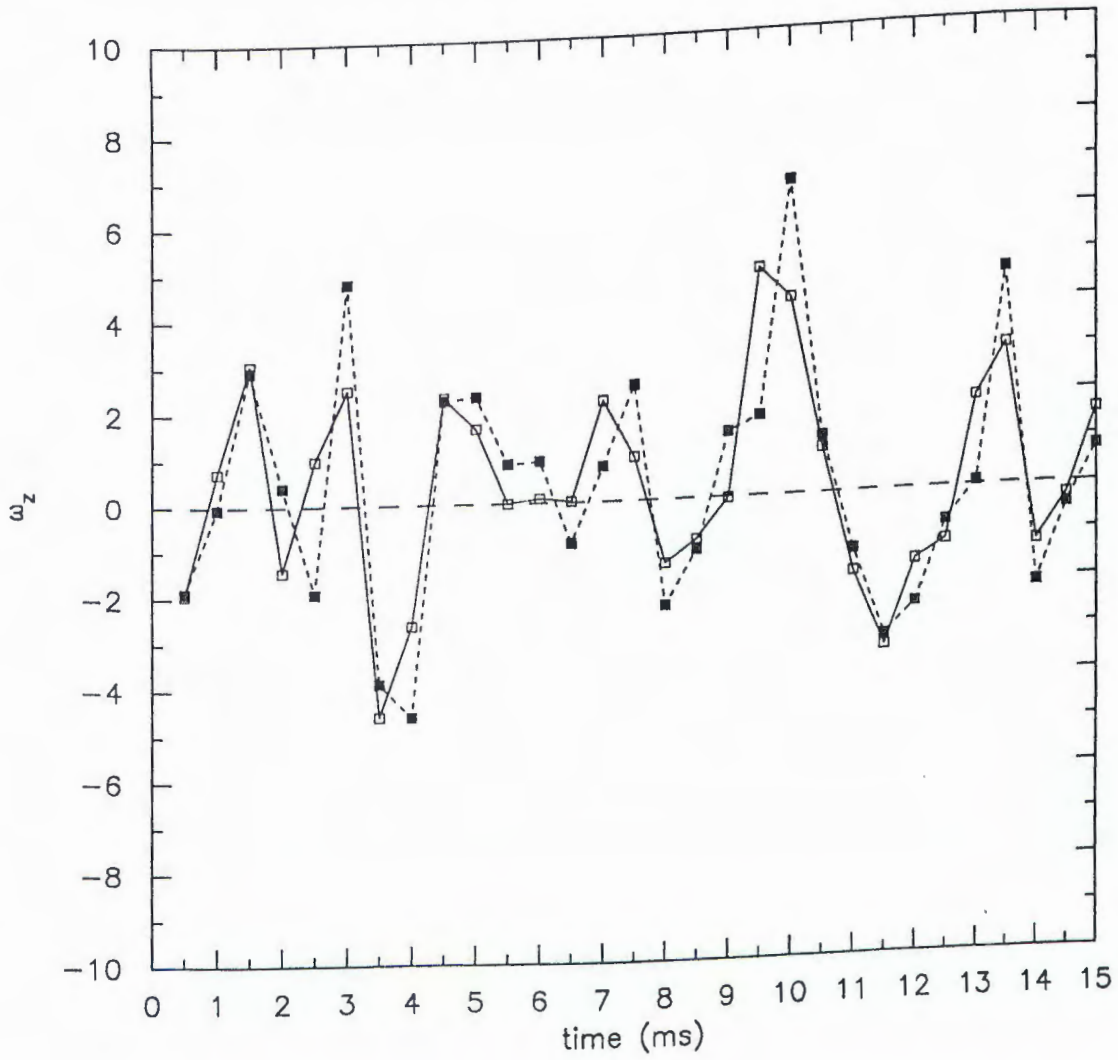

Fig. 5.5. Comparison of the ω_z time series from the central–difference (open symbols) and backward–difference (closed symbols) schemes. The location is η=0.12.

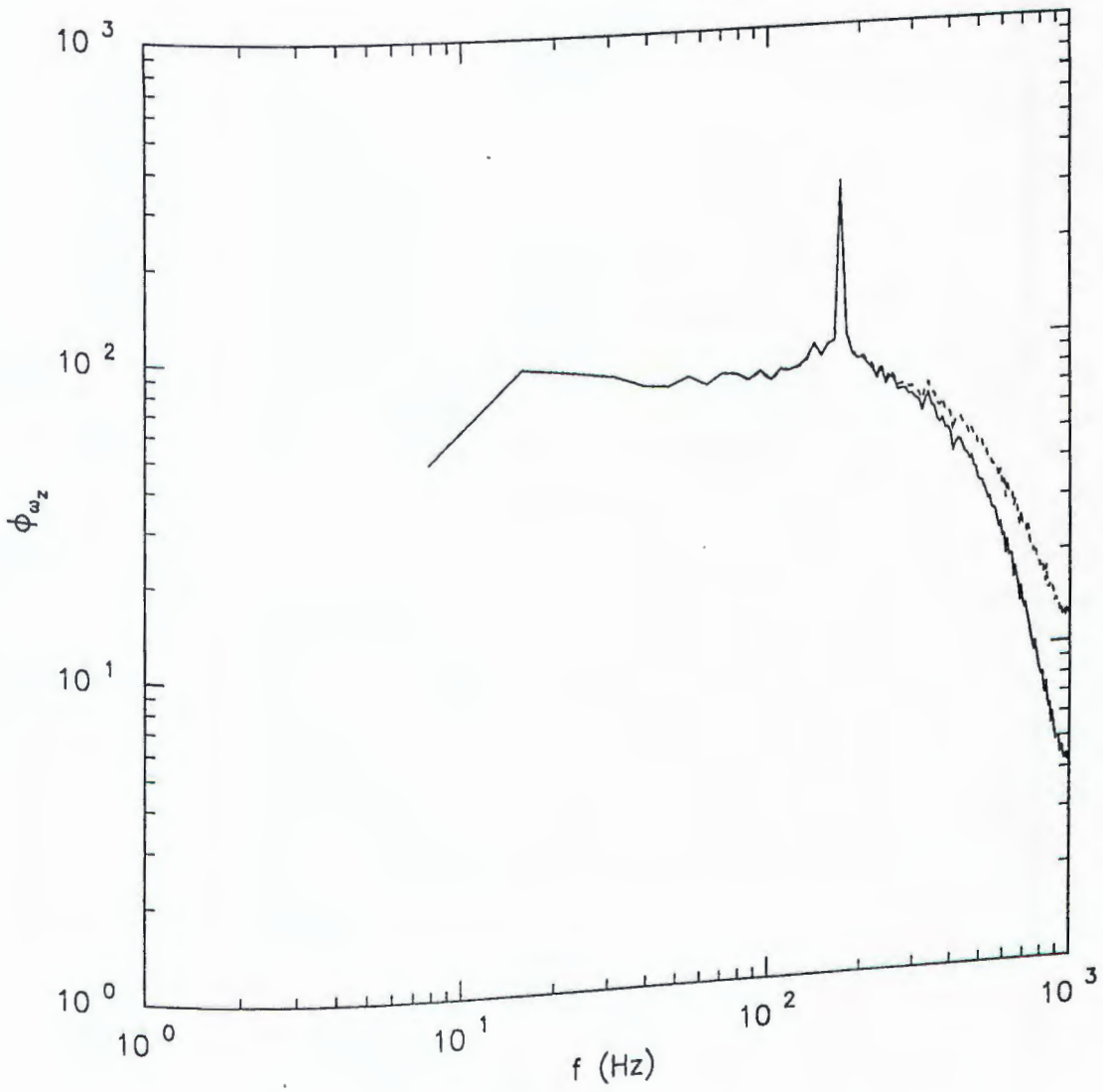

Fig. 5.6. Comparison of the ω_z spectra from the central–difference (solid line) and backward–difference (dashed line) schemes. The location is η=0.12.

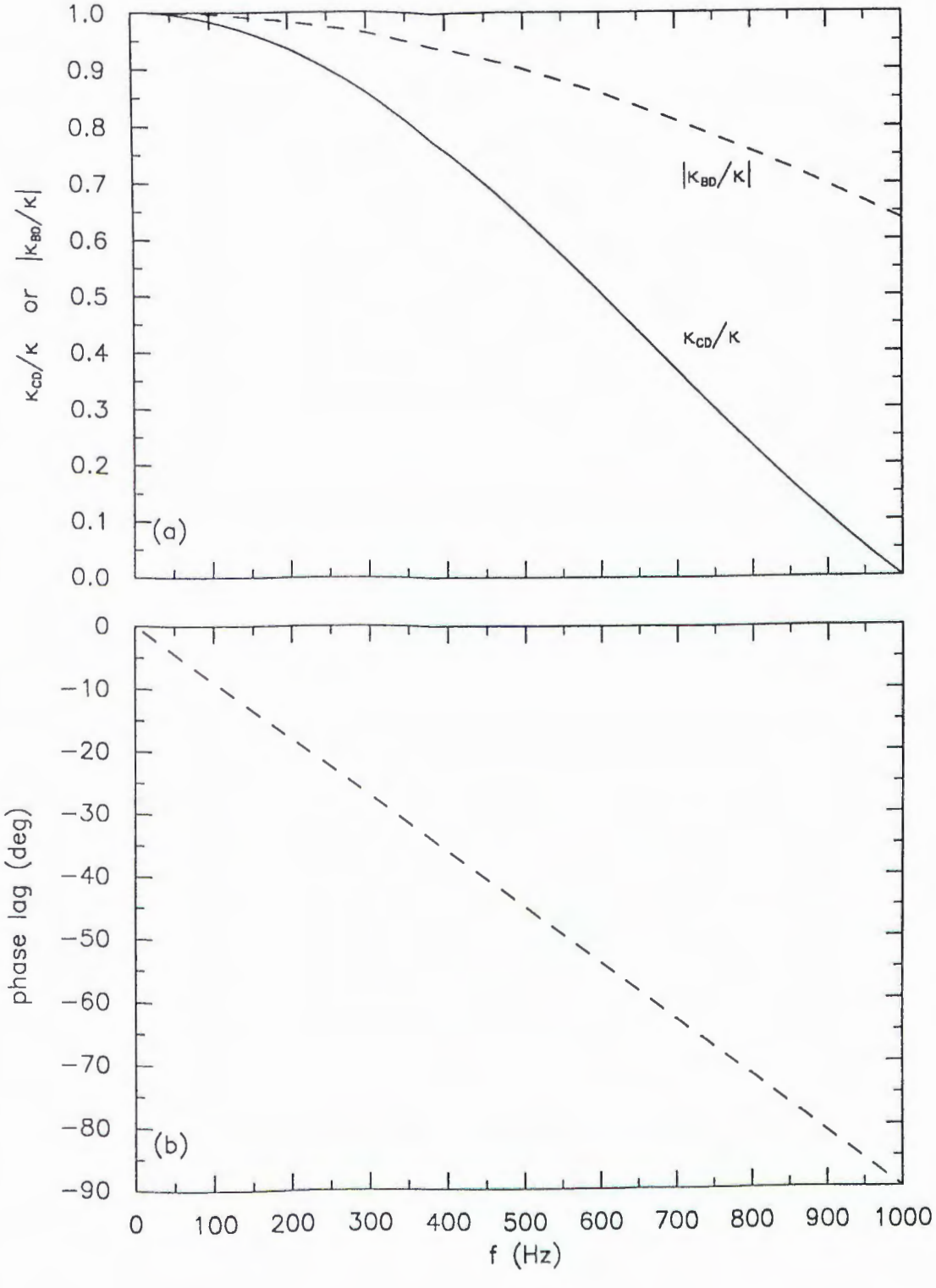

Fig. 5.7. Signal attenuation and phase shift of the two differencing schemes: (a) κ_{CD}/κ or $|\kappa_{BD}/\kappa|$, (b) phase shift due to the B−D scheme. Solid line is for the C−D scheme, dashed line is for the B−D scheme.

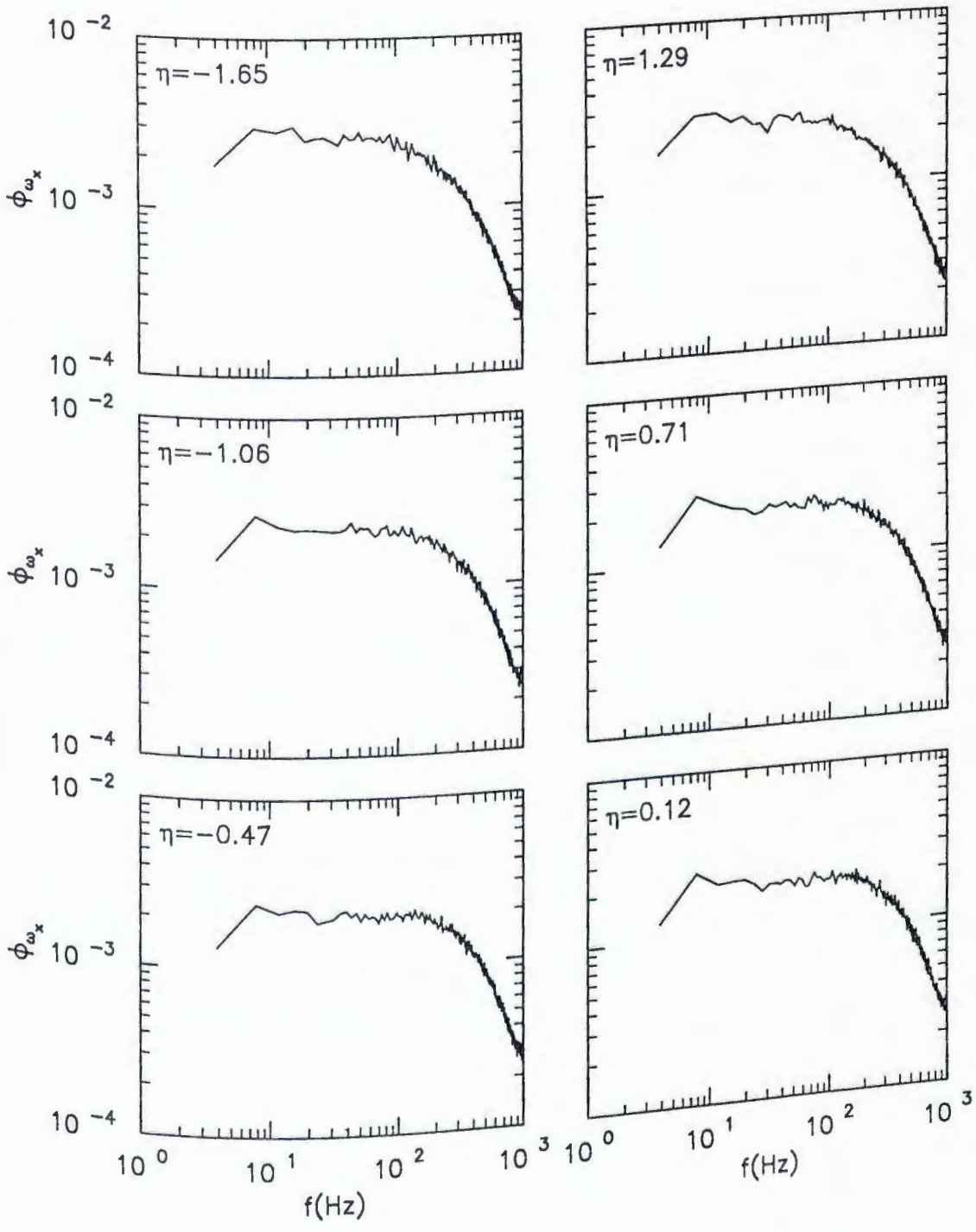

Fig. 5.8. Spectra of the streamwise vorticity component. All spectra are normalized by the local variance and integrate to unity in this and subsequent figures.

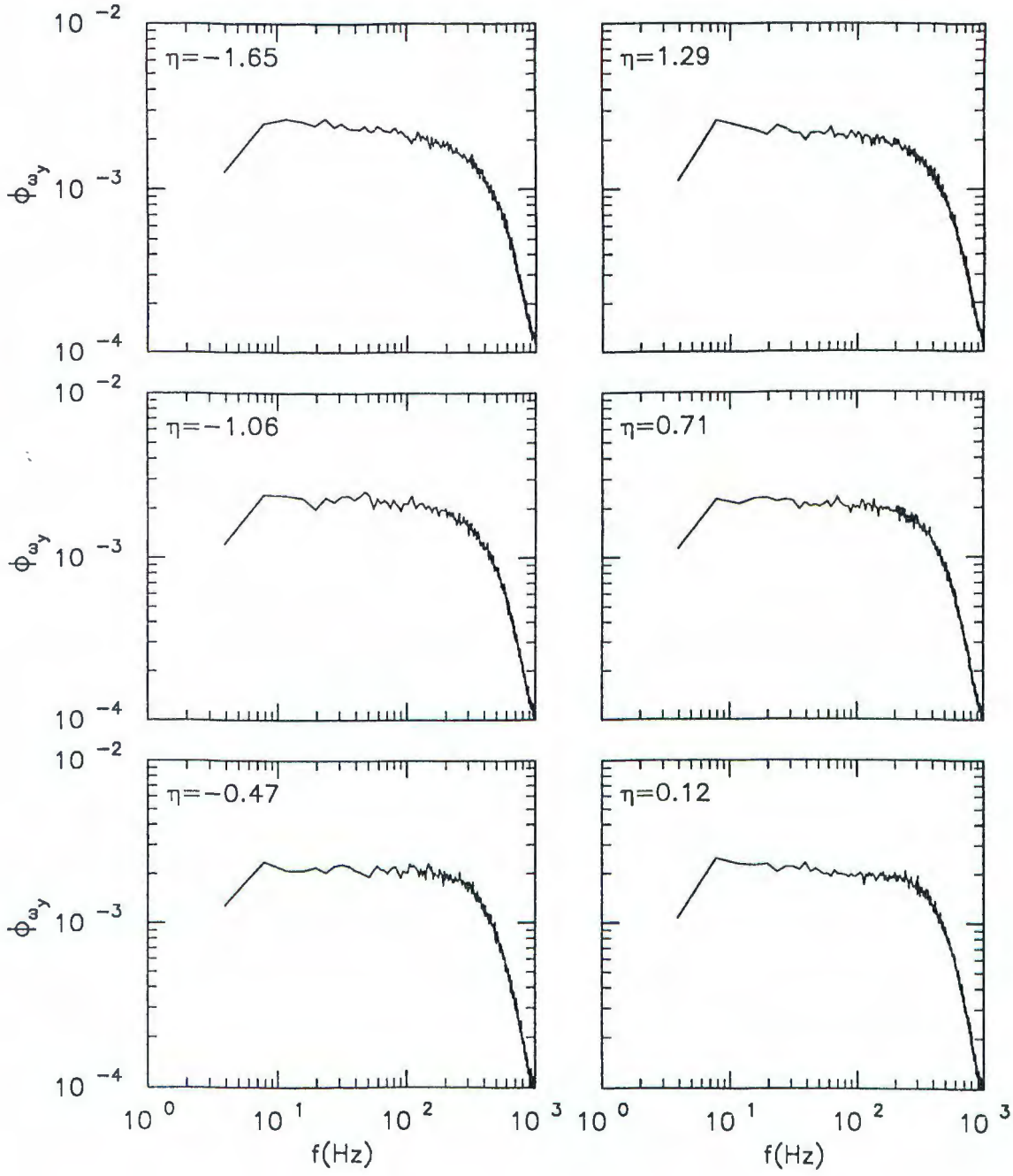

Fig. 5.9. Spectra of the transverse vorticity component.

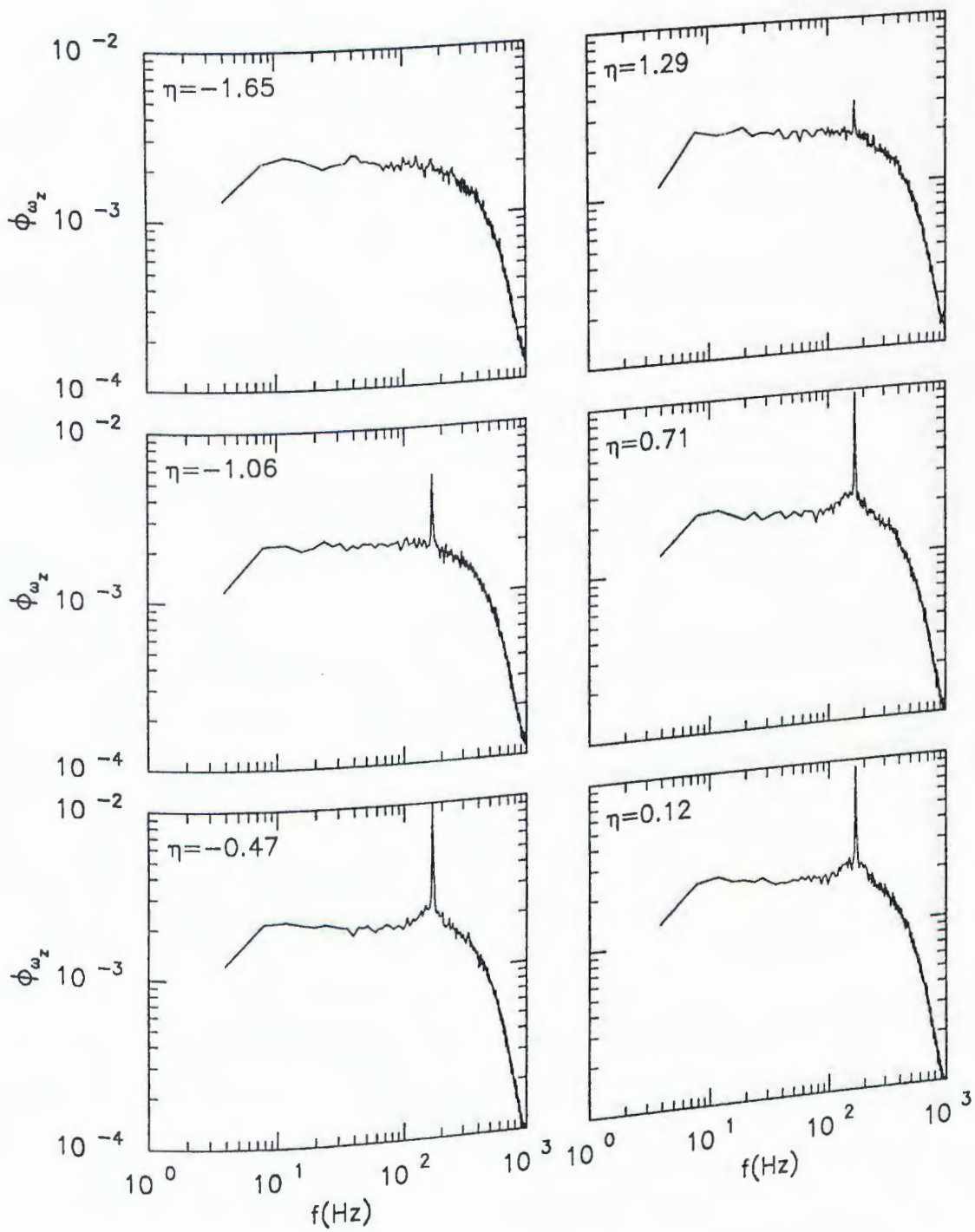

Fig. 5.10. Spectra of the spanwise vorticity component.

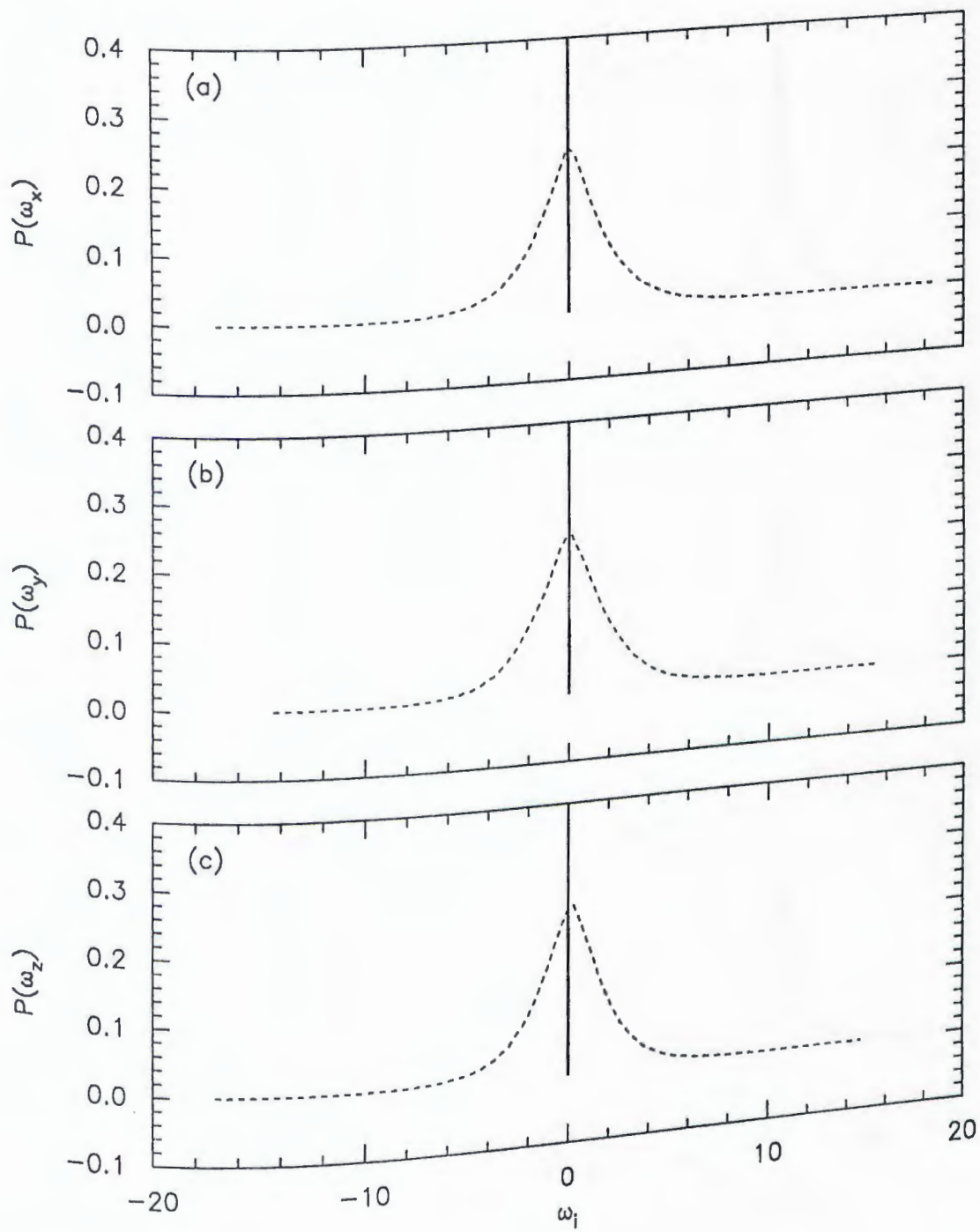

Fig. 5.11. PDF of the vorticity components in the freestream and the wake centerline: (a) ω_x, (b) ω_y, and (c) ω_z. The solid line is for the freestream; the dashed line is for η=0.12. The vorticity components in this and subsequent PDF and JPDF figures are normalized by u_o/L_o.

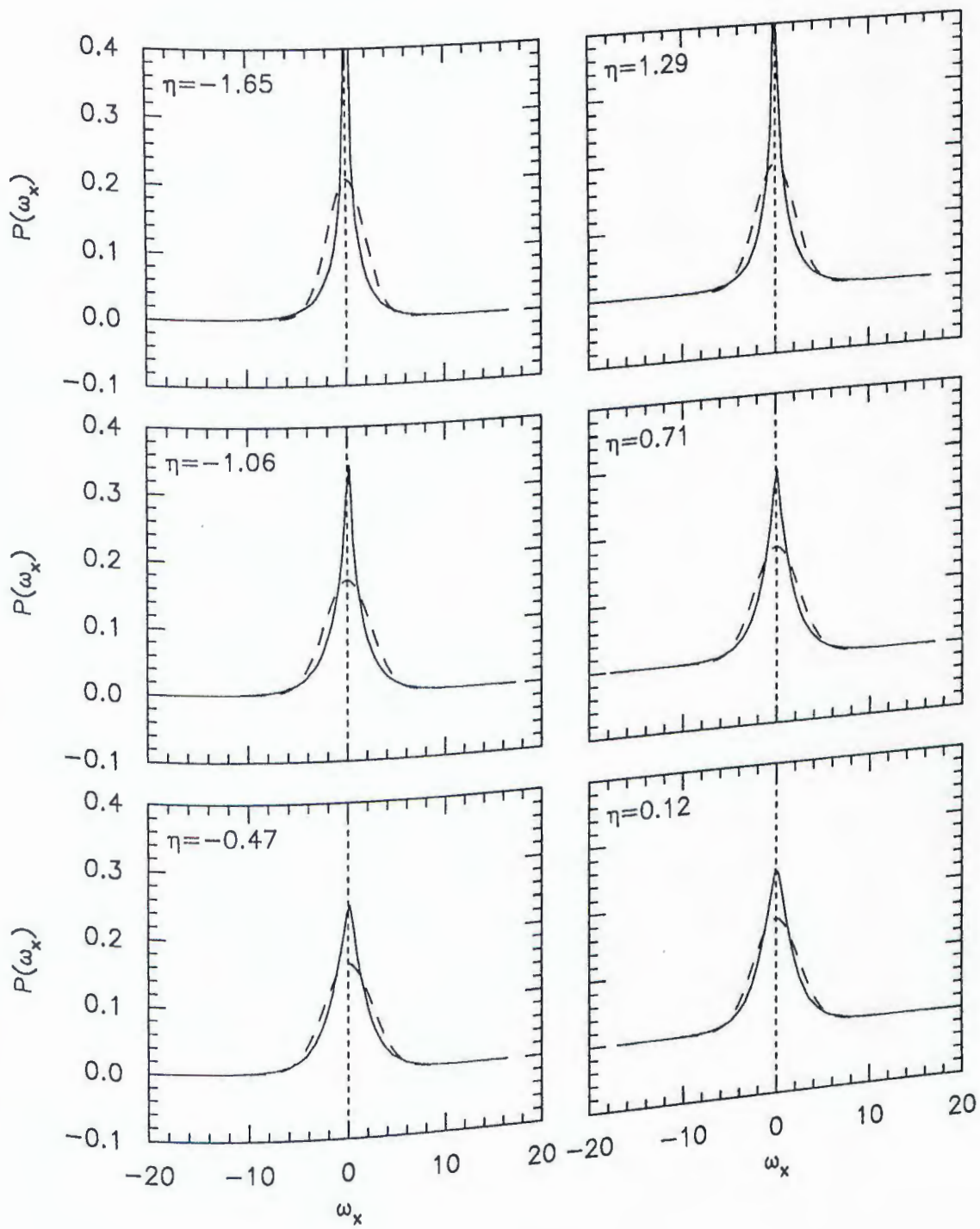

Fig. 5.12. PDF of the streamwise vorticity. Gaussian distributions are shown as dashed lines.

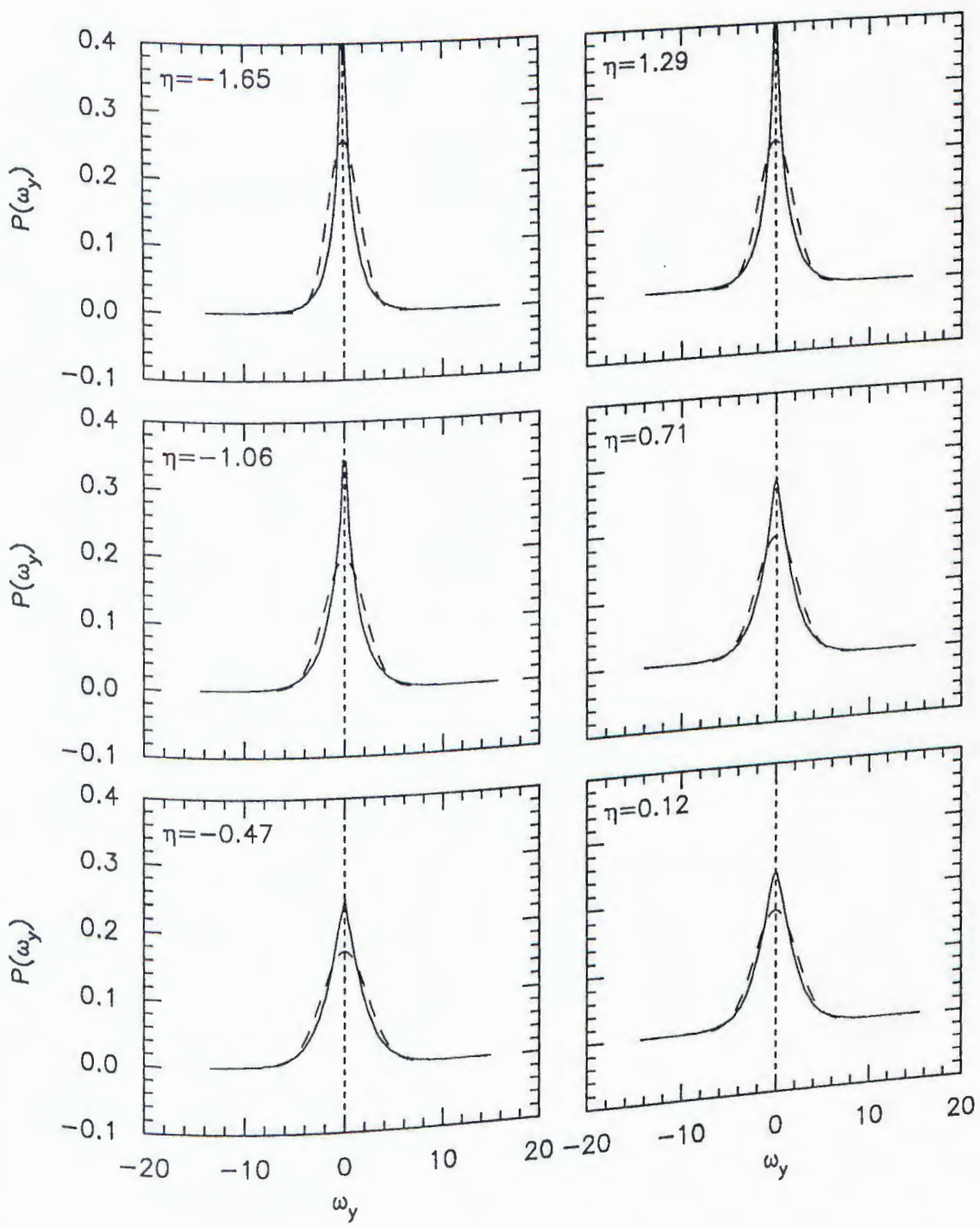

Fig. 5.13. PDF of the transverse vorticity. Gaussian distributions are shown as dashed lines.

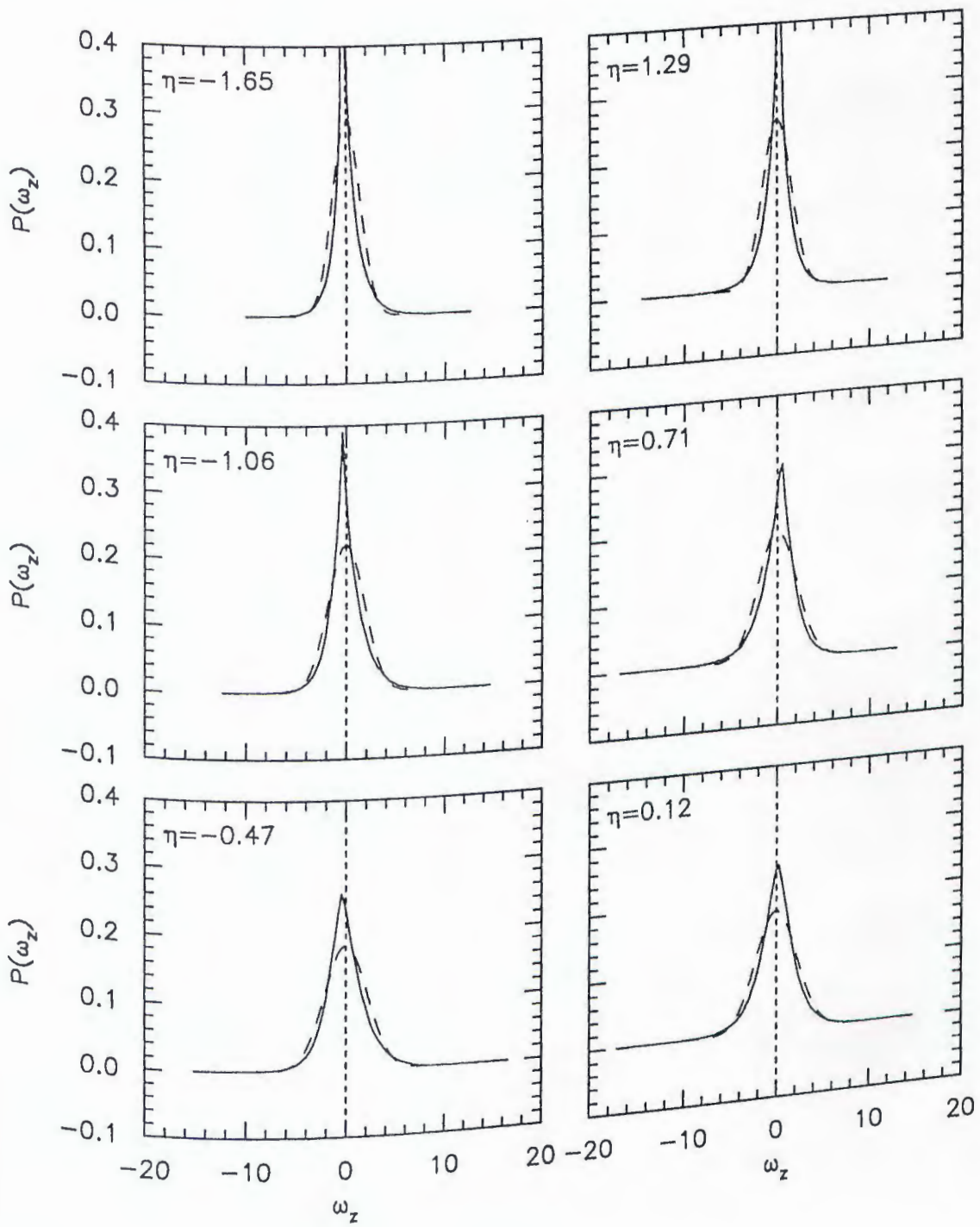

Fig. 5.14. PDF of the spanwise vorticity. Gaussian distributions are shown as dashed lines.

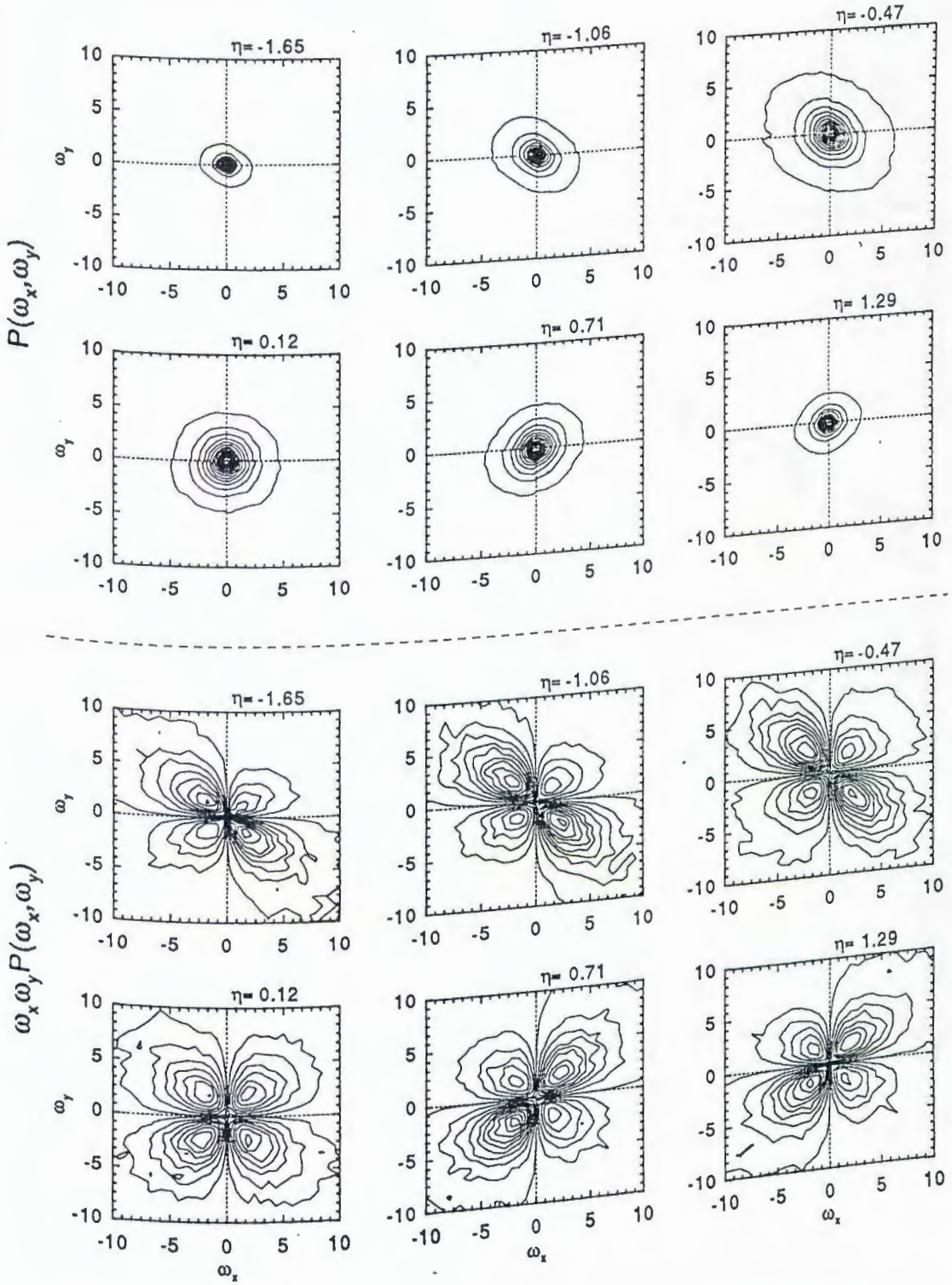

Fig. 5.15. Joint probability density function (JPDF) (top) and covariance integrand (bottom) contours for the streamwise and transverse vorticity components.

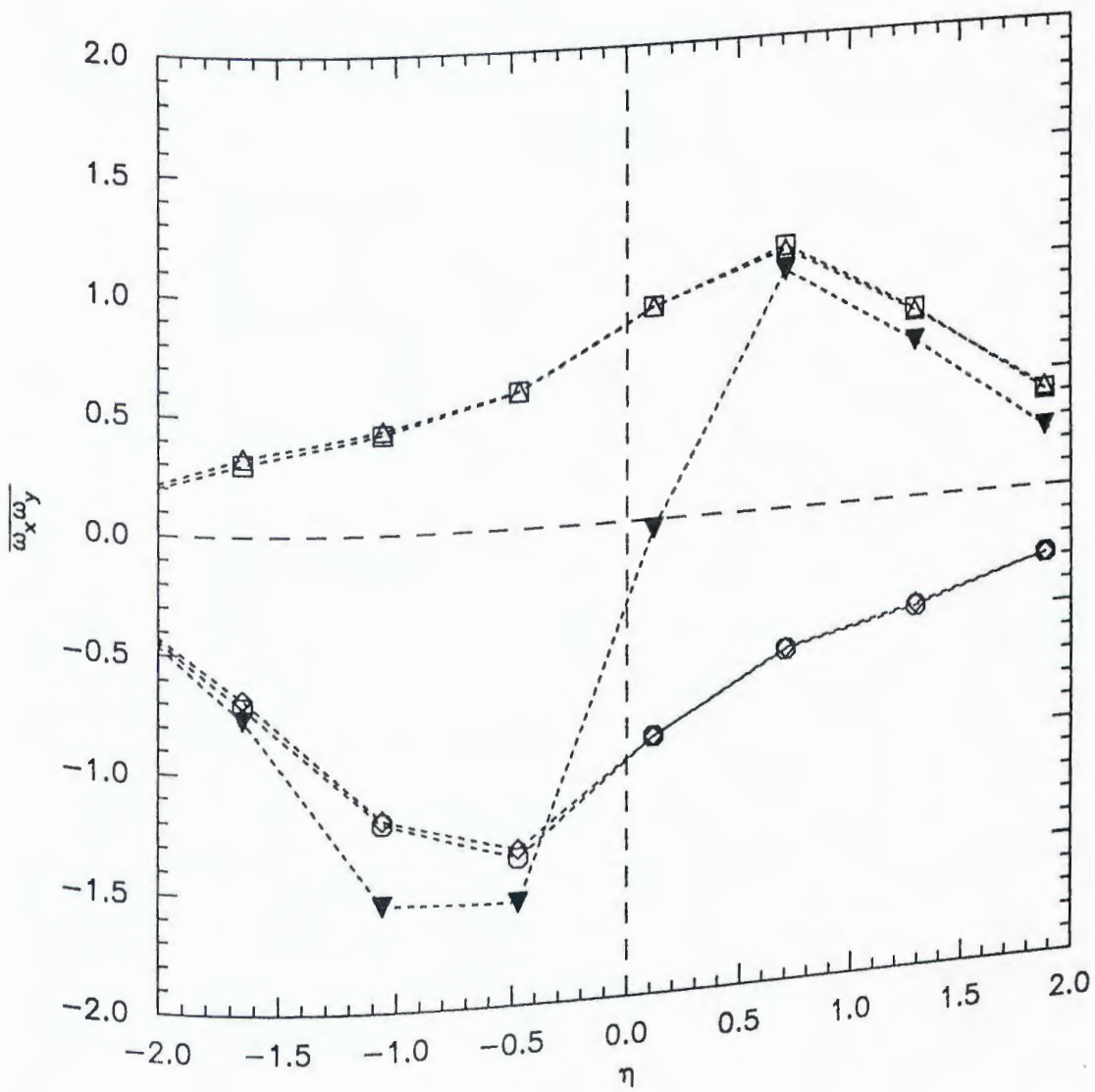

Fig. 5.16. Quadrant analysis for the correlation of the streamwise and transverse vorticity components: □, Q1; ○, Q2; △, Q3; ◇, Q4; and ▼, total (sum of quadrant values in this and subsequent figures).

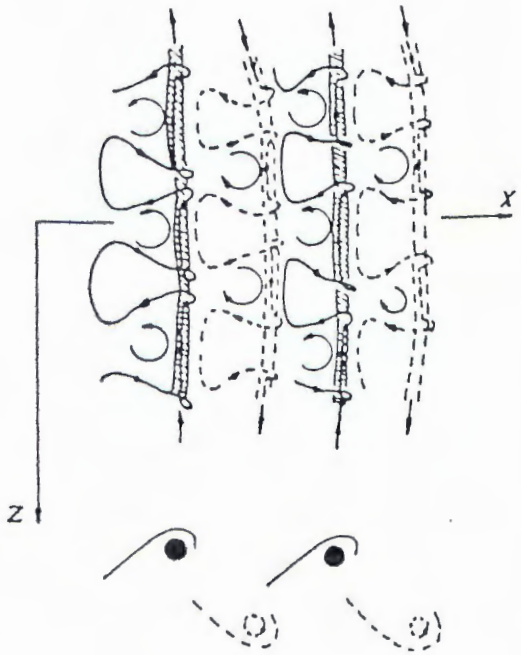

Fig. 5.17. Schematic sketches of the vortex loops calculated by Meiburg & Lasheras [39] for the laminar wake of a flat plate with a corrugated trailing edge. Shaded regions represent the spanwise shed Kármán vortices.

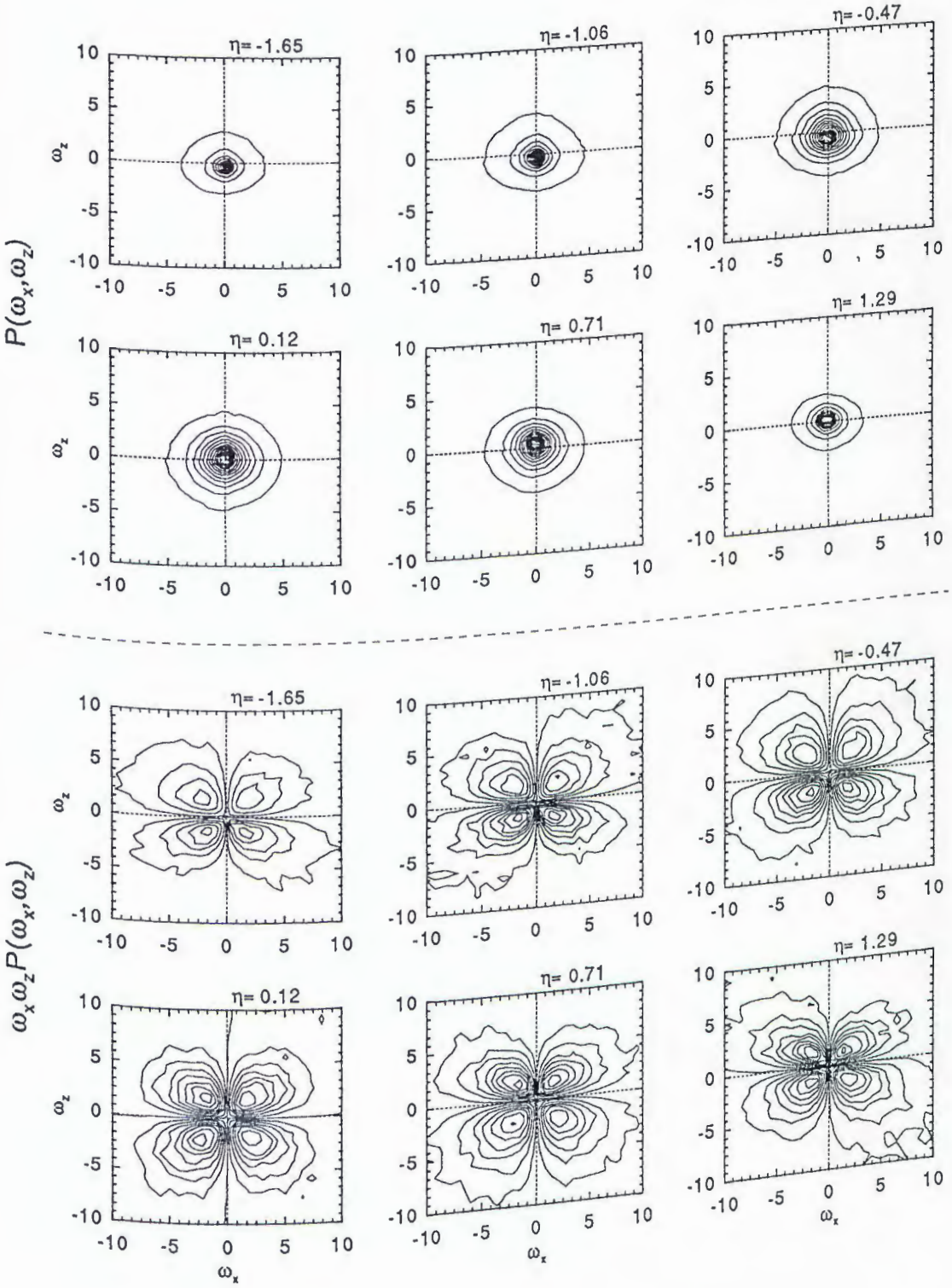

Fig. 5.18. JPDF (top) and covariance integrand (bottom) contours for the streamwise and spanwise vorticity components.

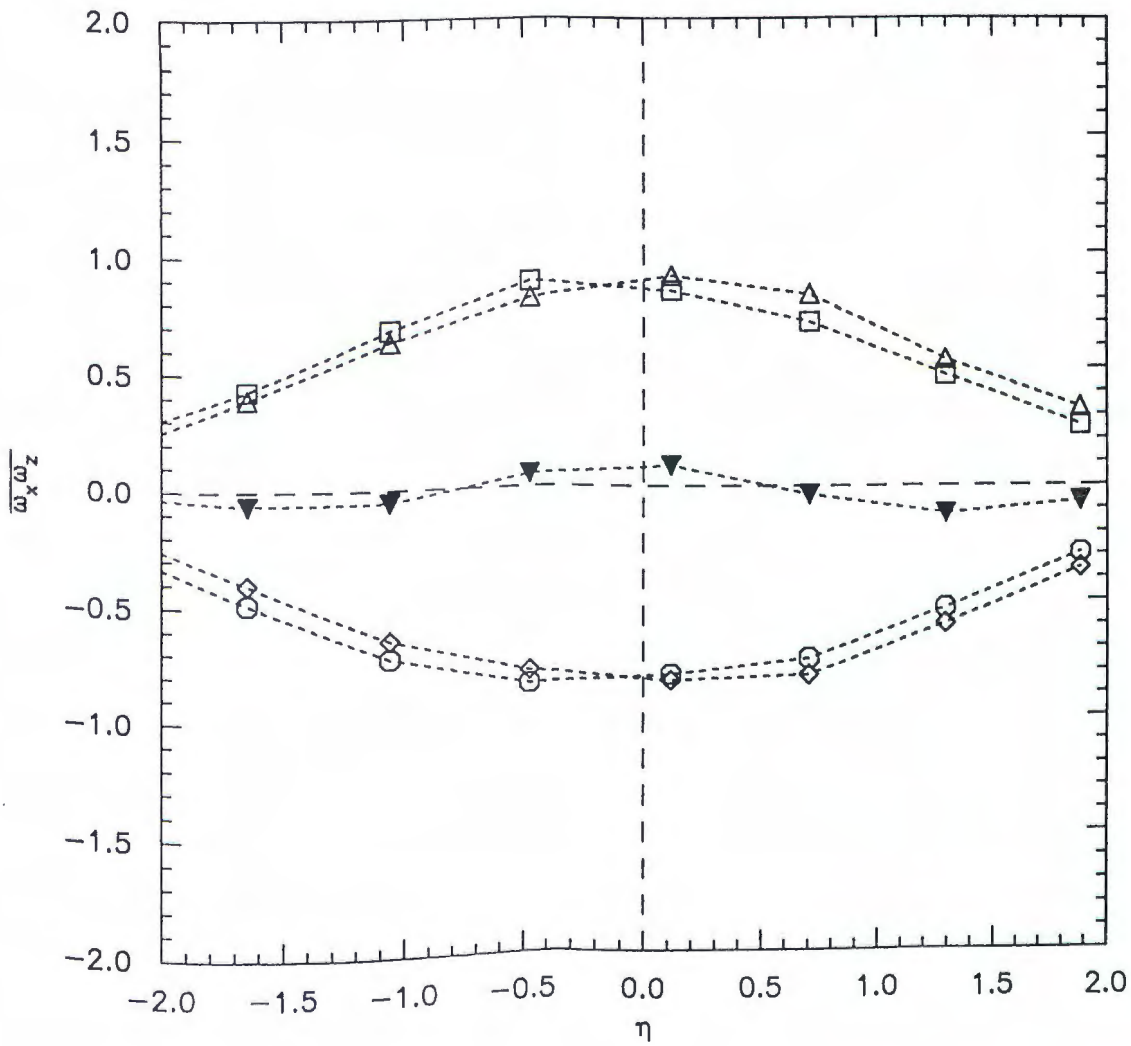

Fig. 5.19. Quadrant analysis for the correlation of the streamwise and spanwise vorticity components: □, Q1; ○, Q2; △, Q3; ◇, Q4; and ▼, total.

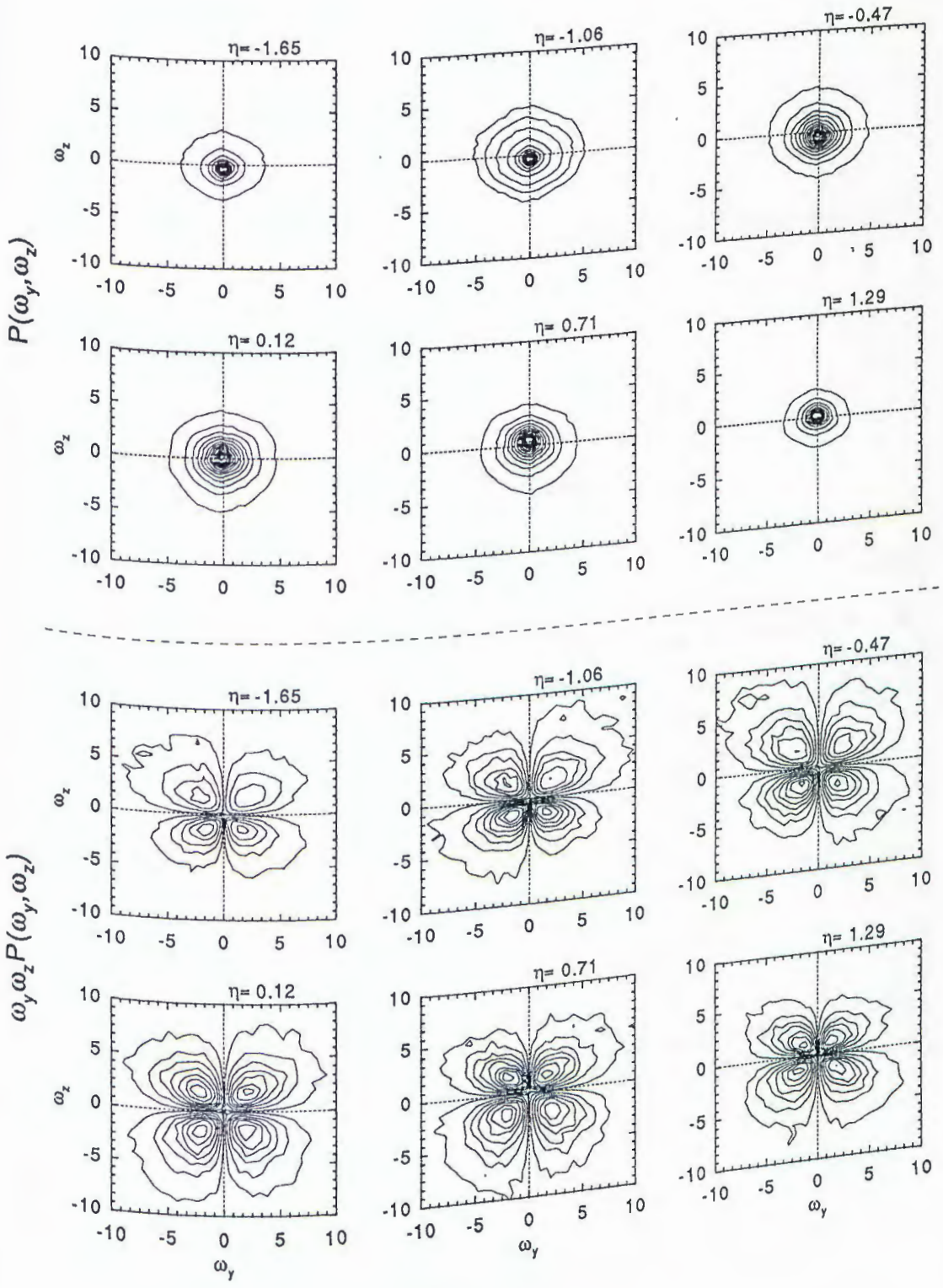

Fig. 5.20. JPDF (top) and covariance integrand (bottom) contours for the transverse and spanwise vorticity components.

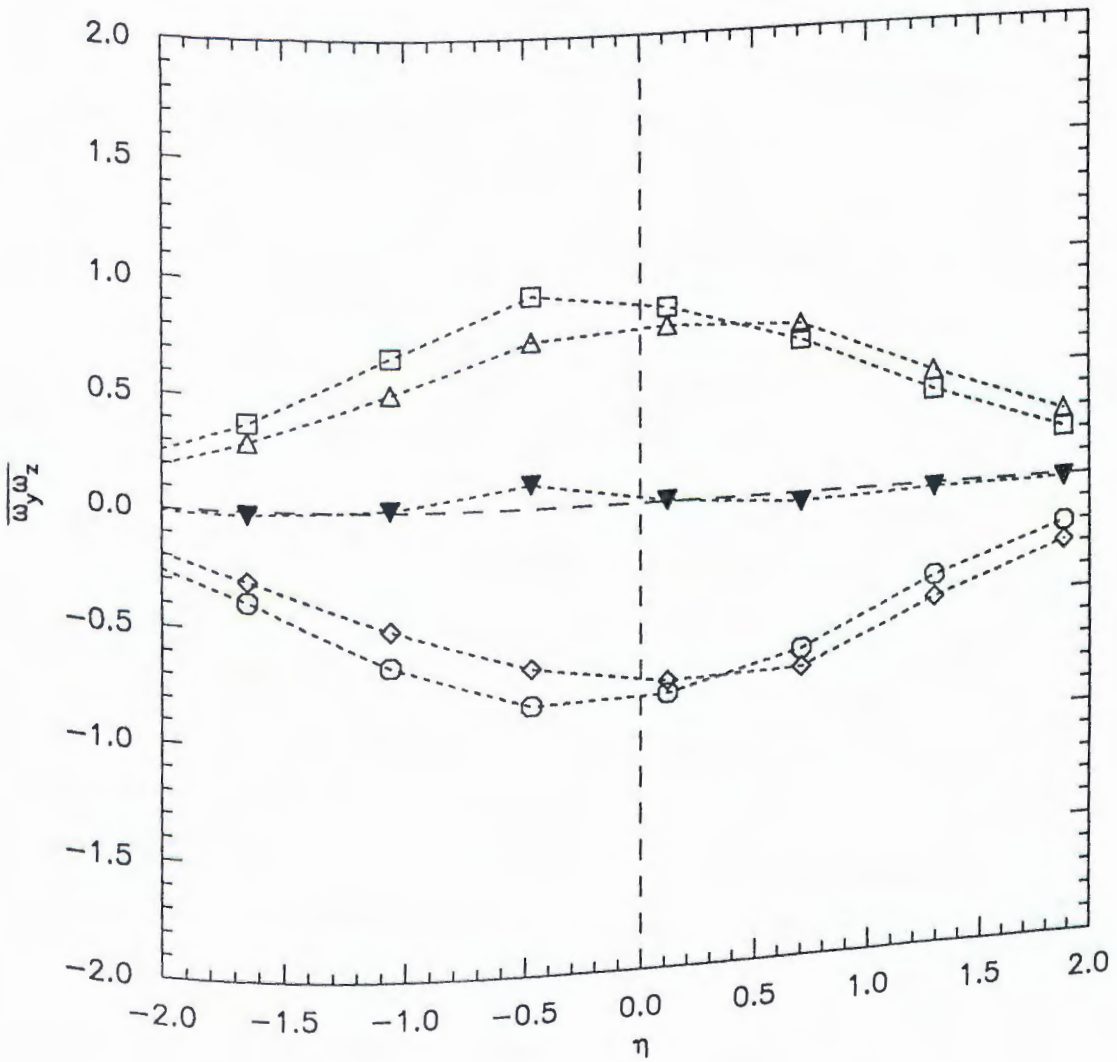

Fig. 5.21. Quadrant analysis for the correlation of the transverse and spanwise vorticity components: □, Q1; ○, Q2; △, Q3; ◇, Q4; and ▼, total.

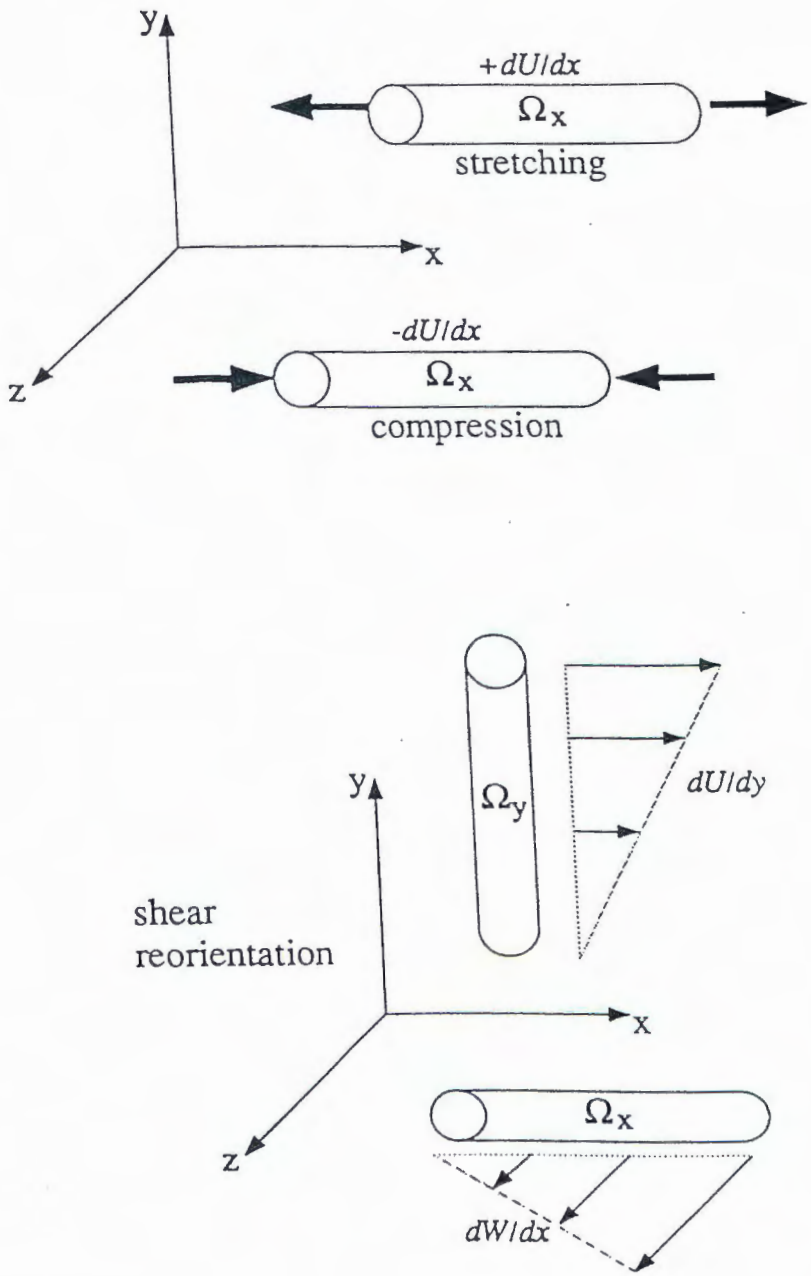

Fig. 5.22. Schematic sketches of vortex stretching (top) and reorientation due to shearing (bottom) by velocity gradients.

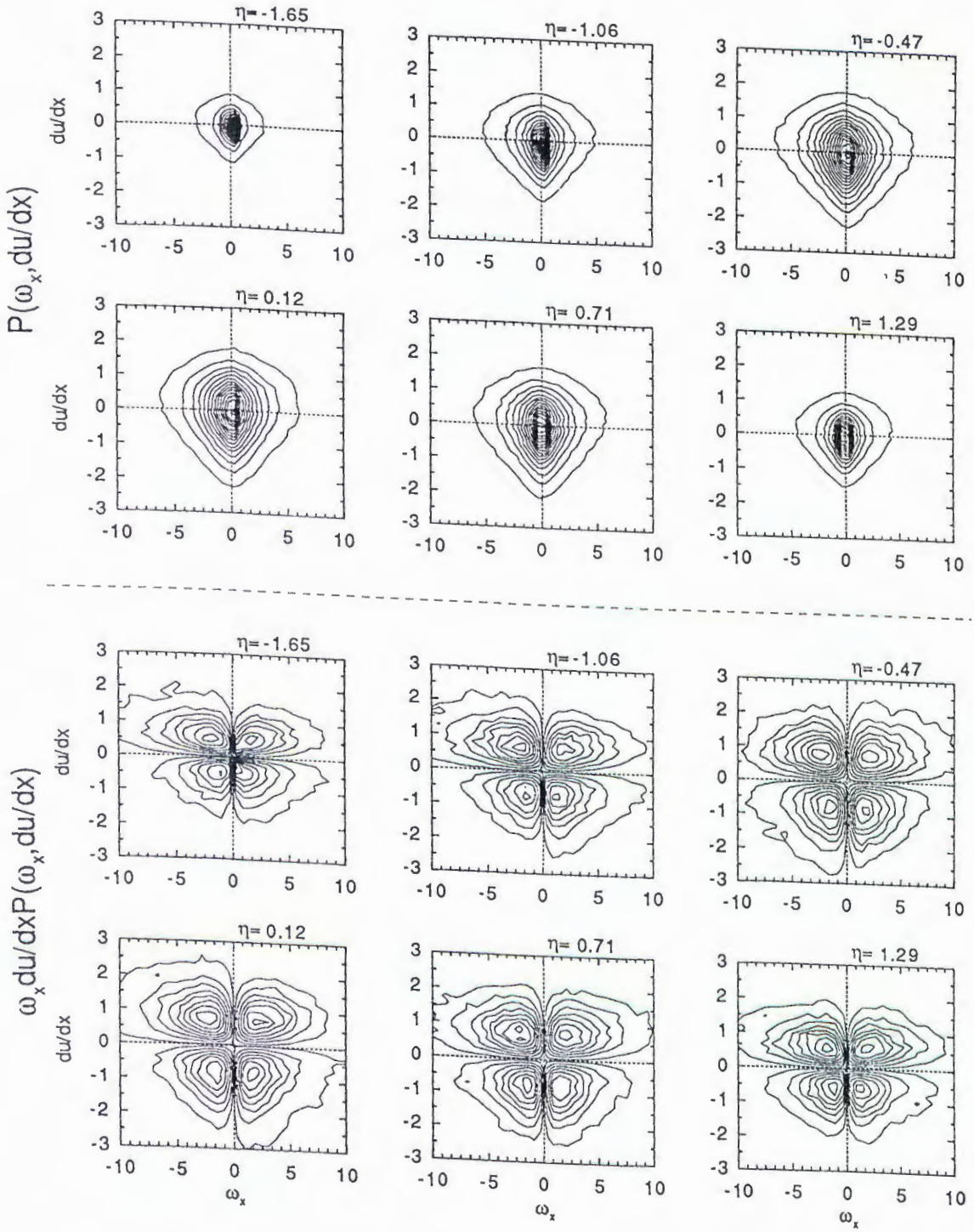

Fig. 5.23. JPDF (top) and covariance integrand (bottom) contours for ω_x and du/dx.

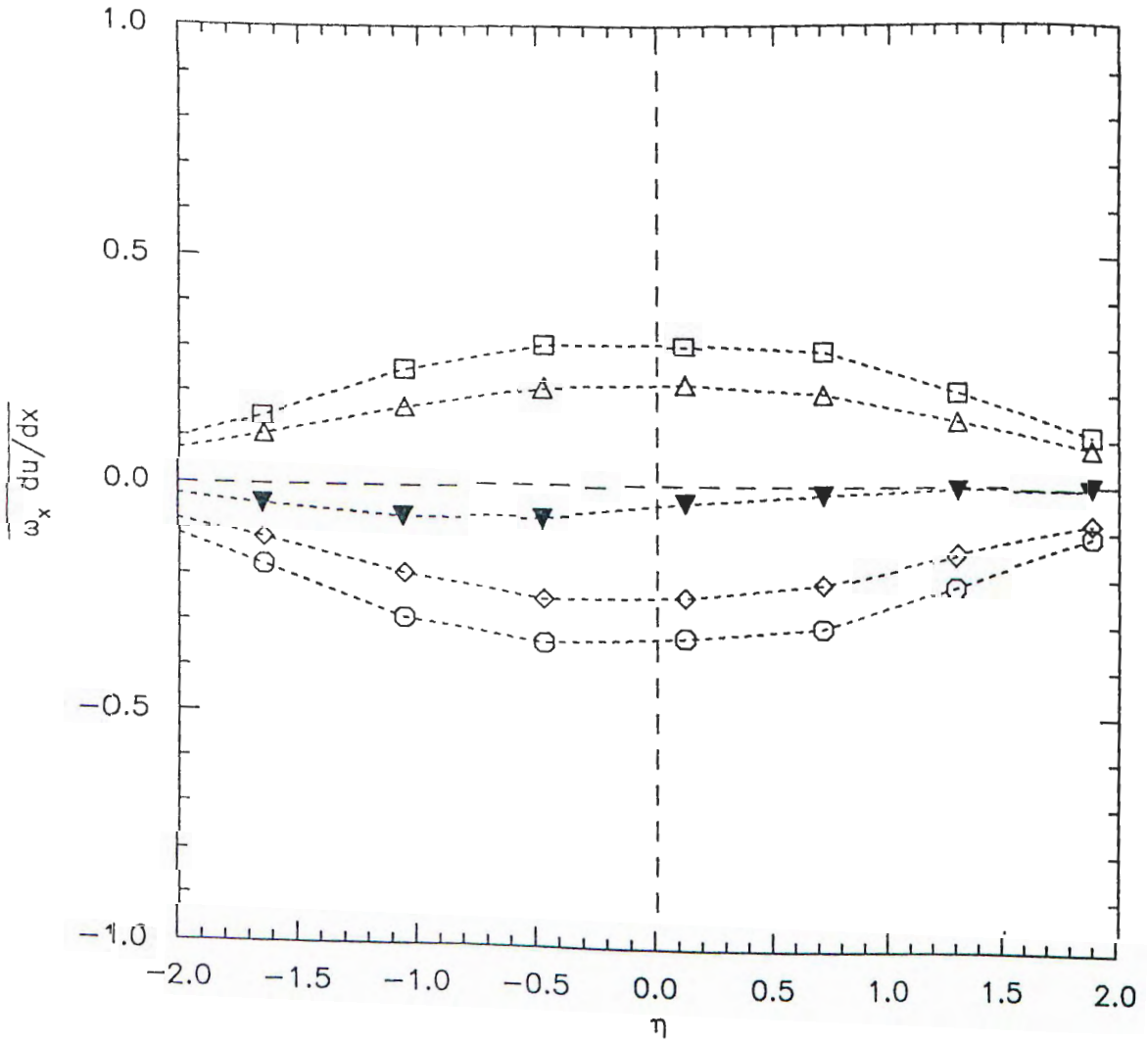

Fig. 5.24. Quadrant analysis for the correlation of ω_x and du/dx. □, Q1; ○, Q2; △, Q3; ◇, Q4; ▼, total.

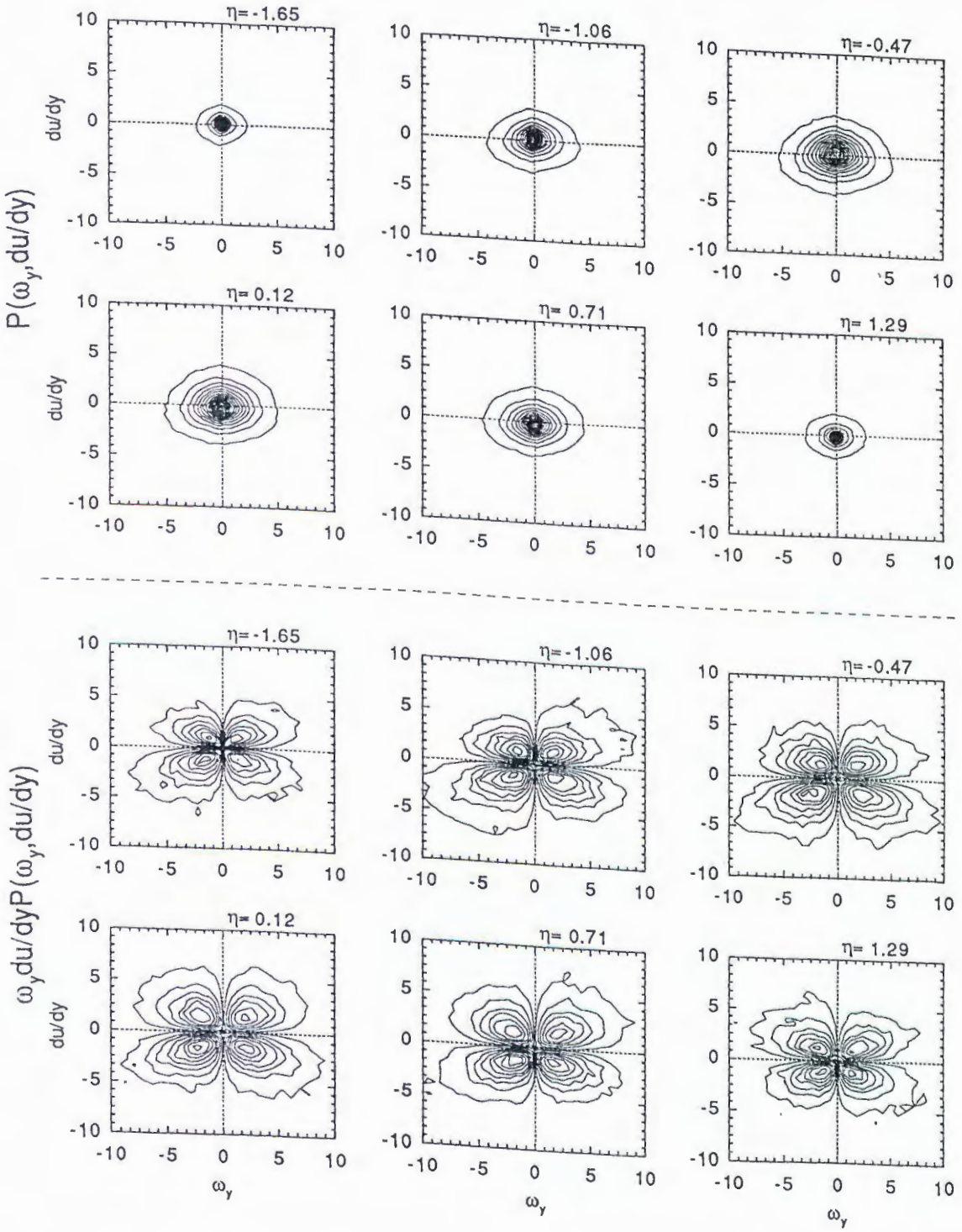

Fig. 5.25. JPDF (top) and covariance integrand (bottom) contours for ω_y and du/dy.

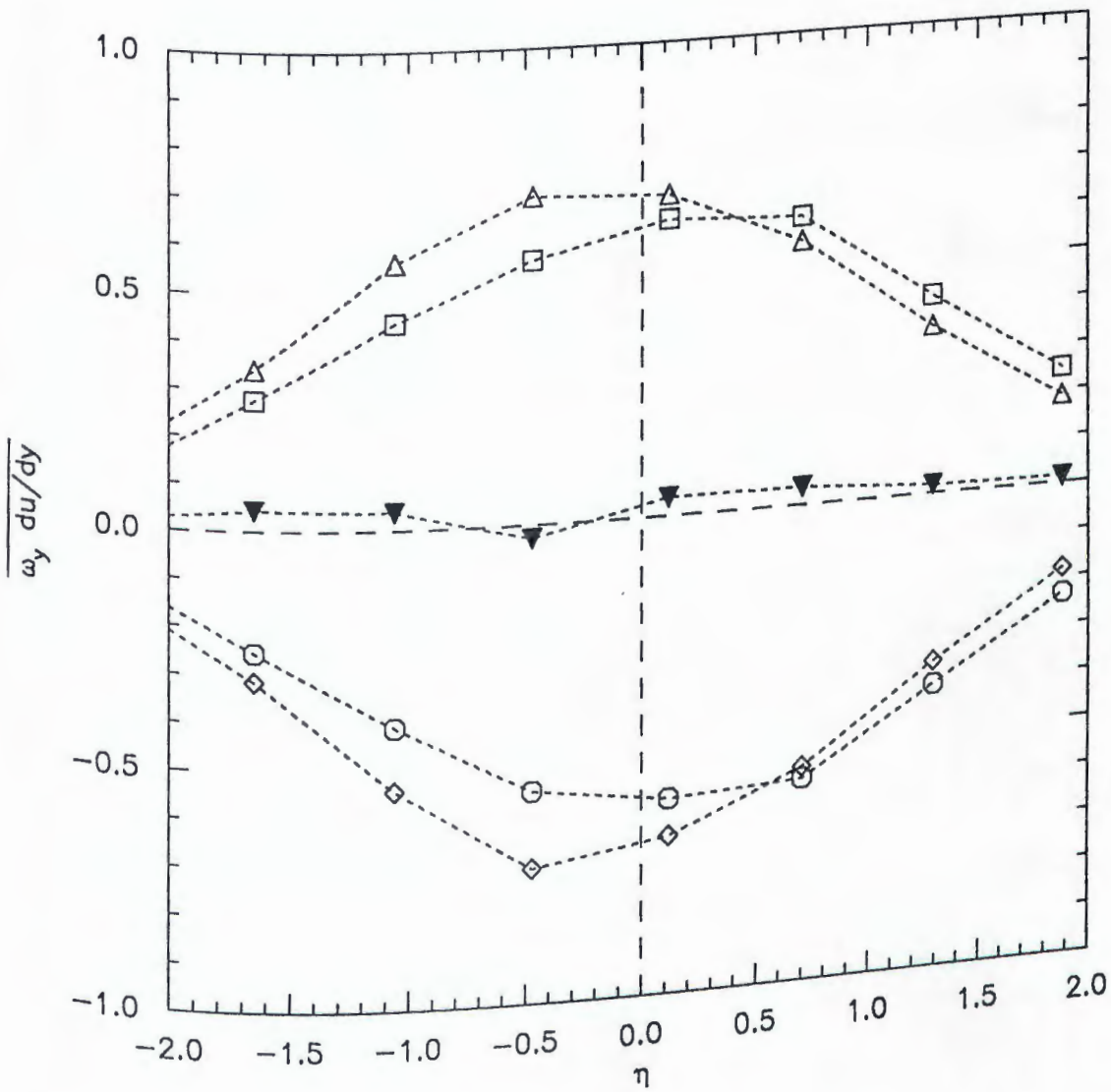

Fig. 5.26. Quadrant analysis for the correlation of ω_y and du/dy.
□, Q1; ○, Q2; △, Q3; ◇, Q4; ▼, total.

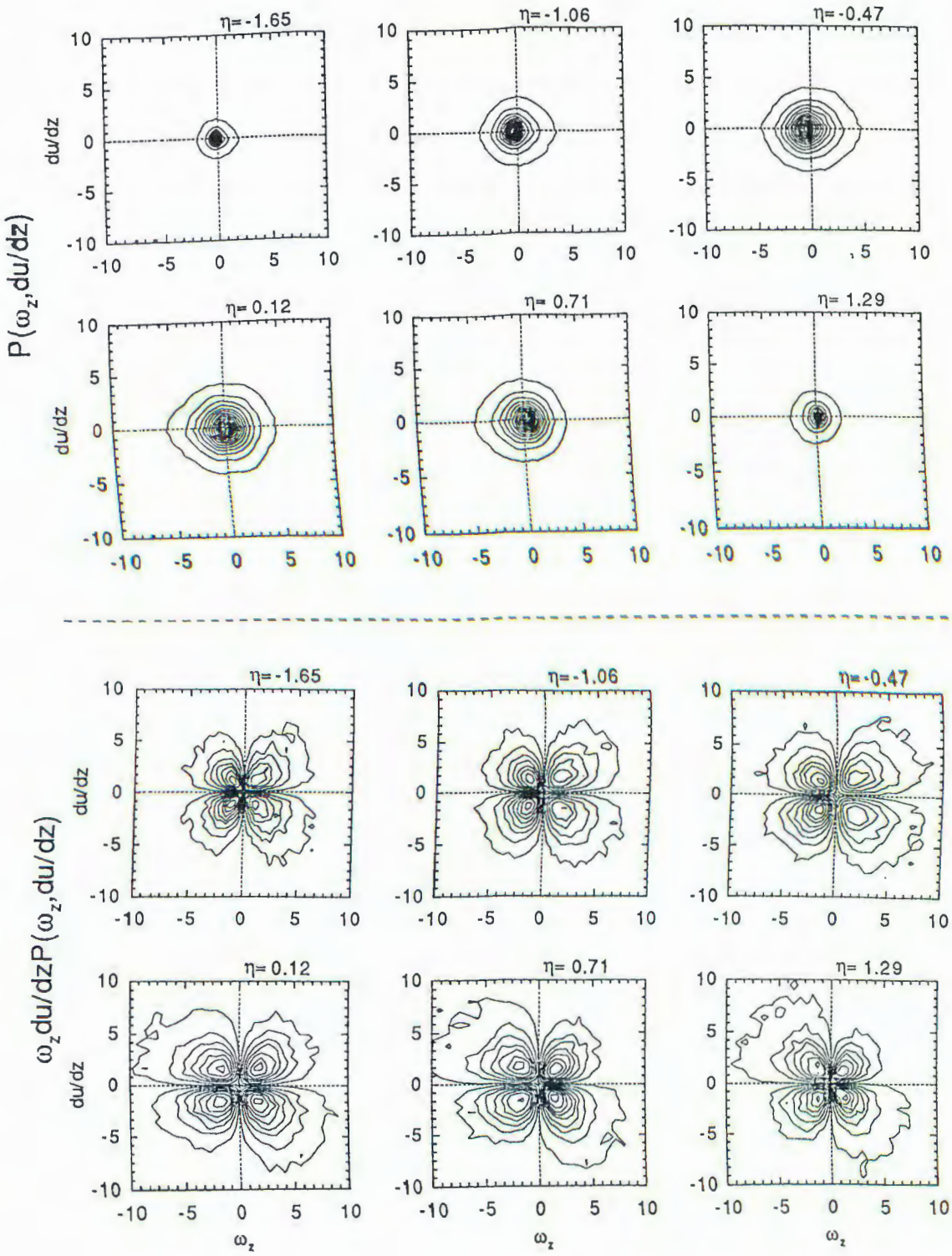

Fig. 5.27. JPDF (top) and covariance integrand (bottom) contours for ω_z and du/dz.

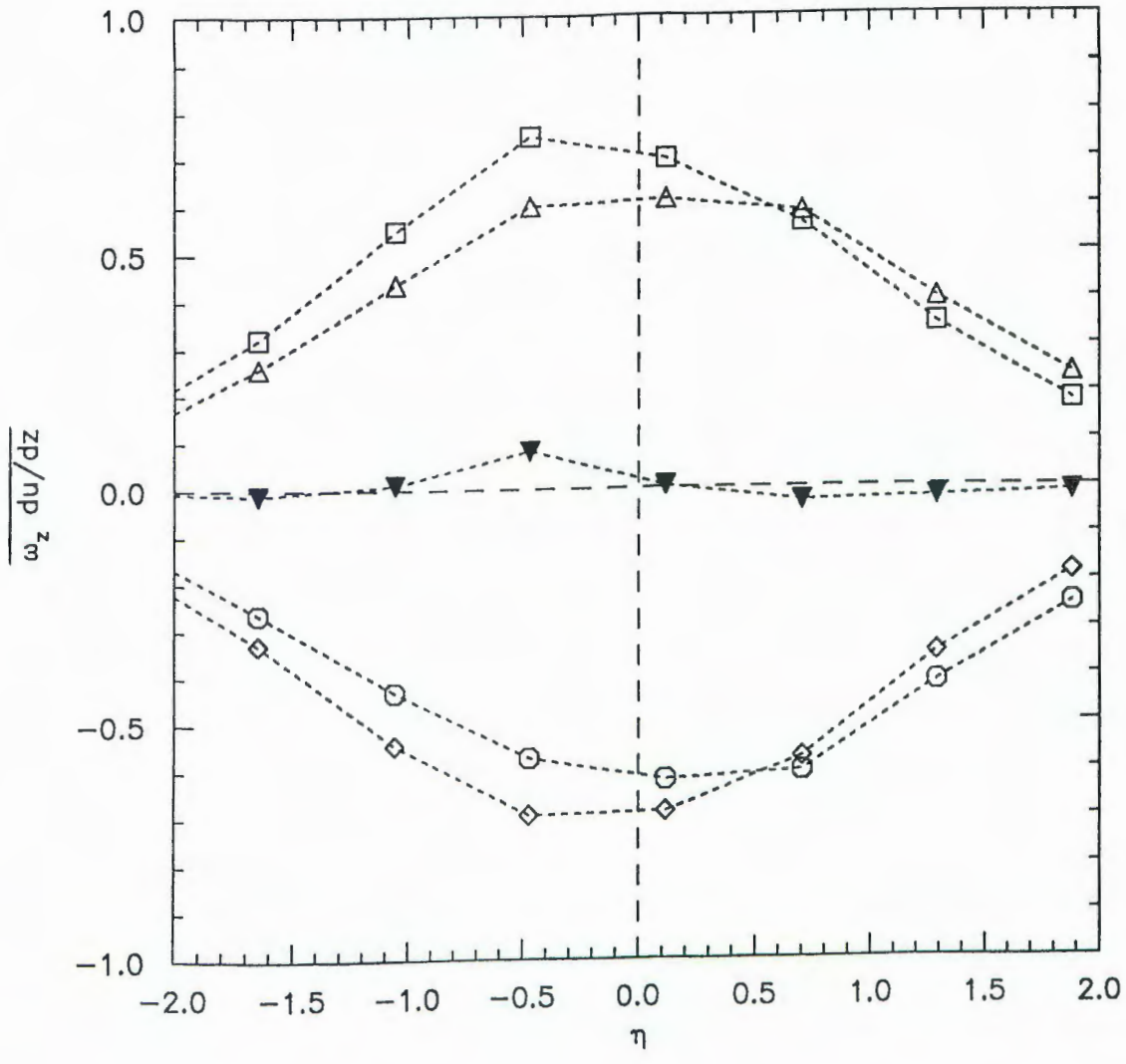

Fig. 5.28. Quadrant analysis for the correlation of ω_z and du/dz. □, Q1; ○, Q2; △, Q3; ◇, Q4; ▼, total.

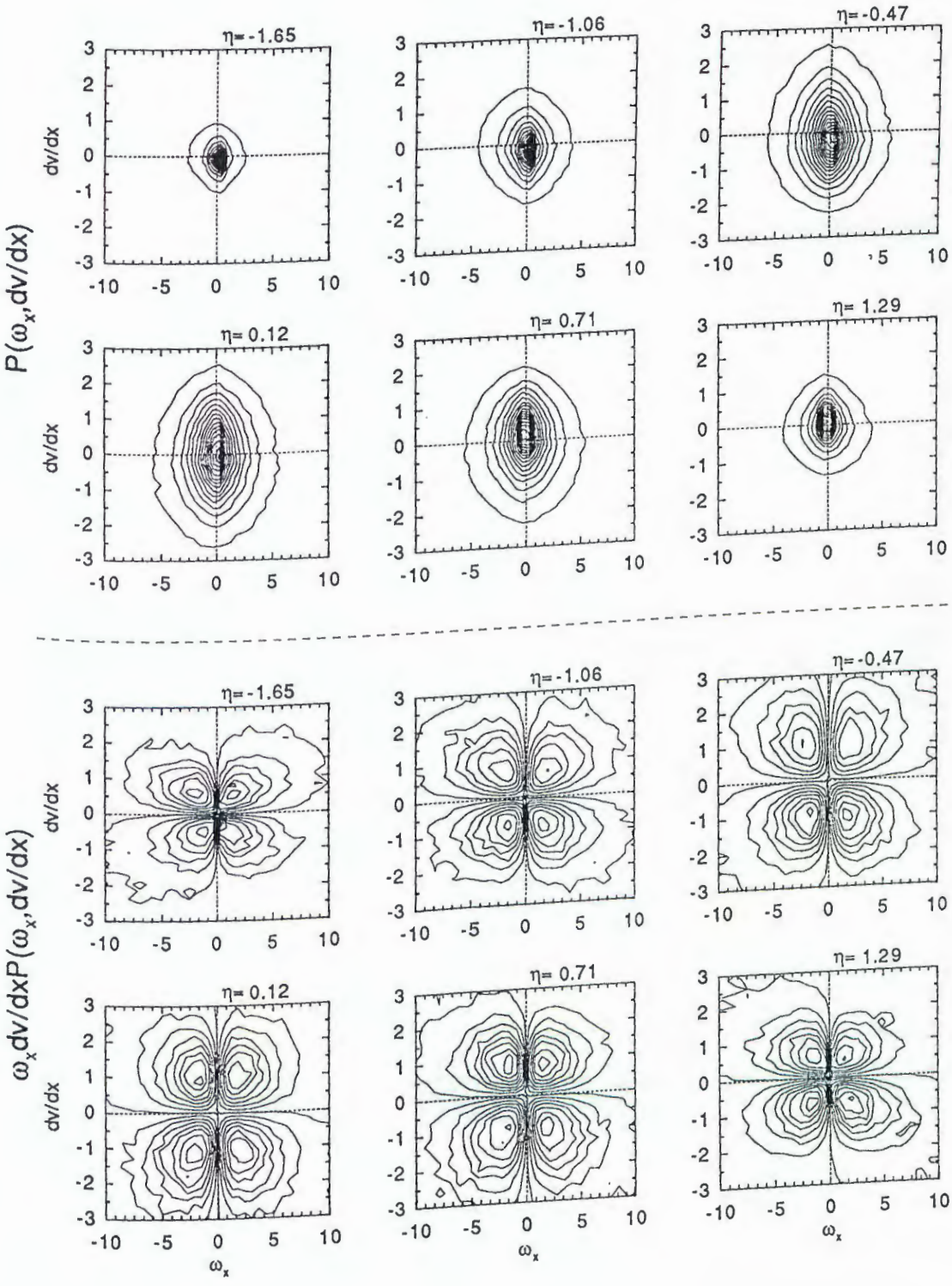

Fig. 5.29. JPDF (top) and covariance integrand (bottom) contours for ω_x and dv/dx.

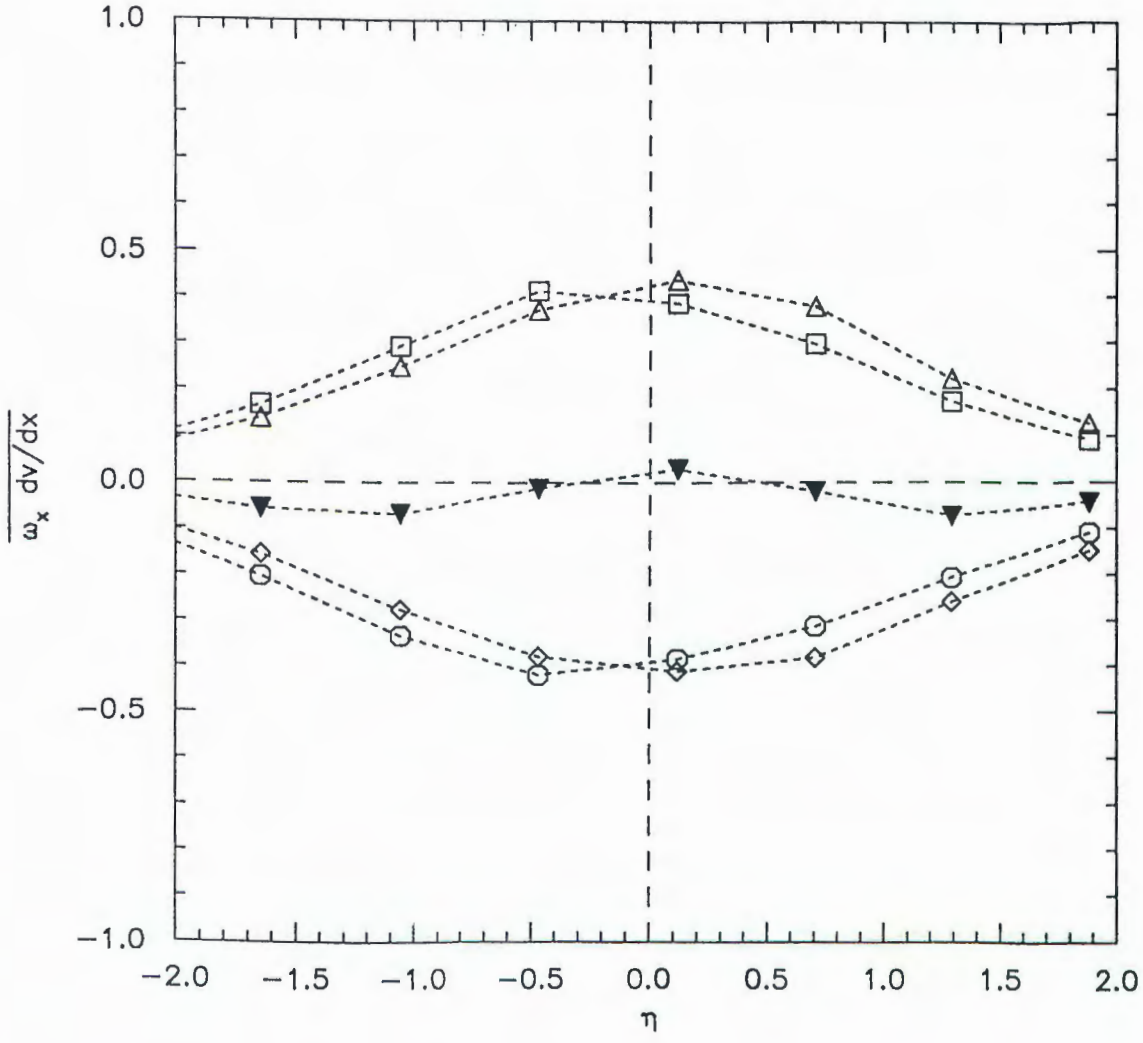

Fig. 5.30. Quadrant analysis for the correlation of ω_x and dv/dx. □, Q1; ○, Q2; △, Q3; ◇, Q4; ▼, total.

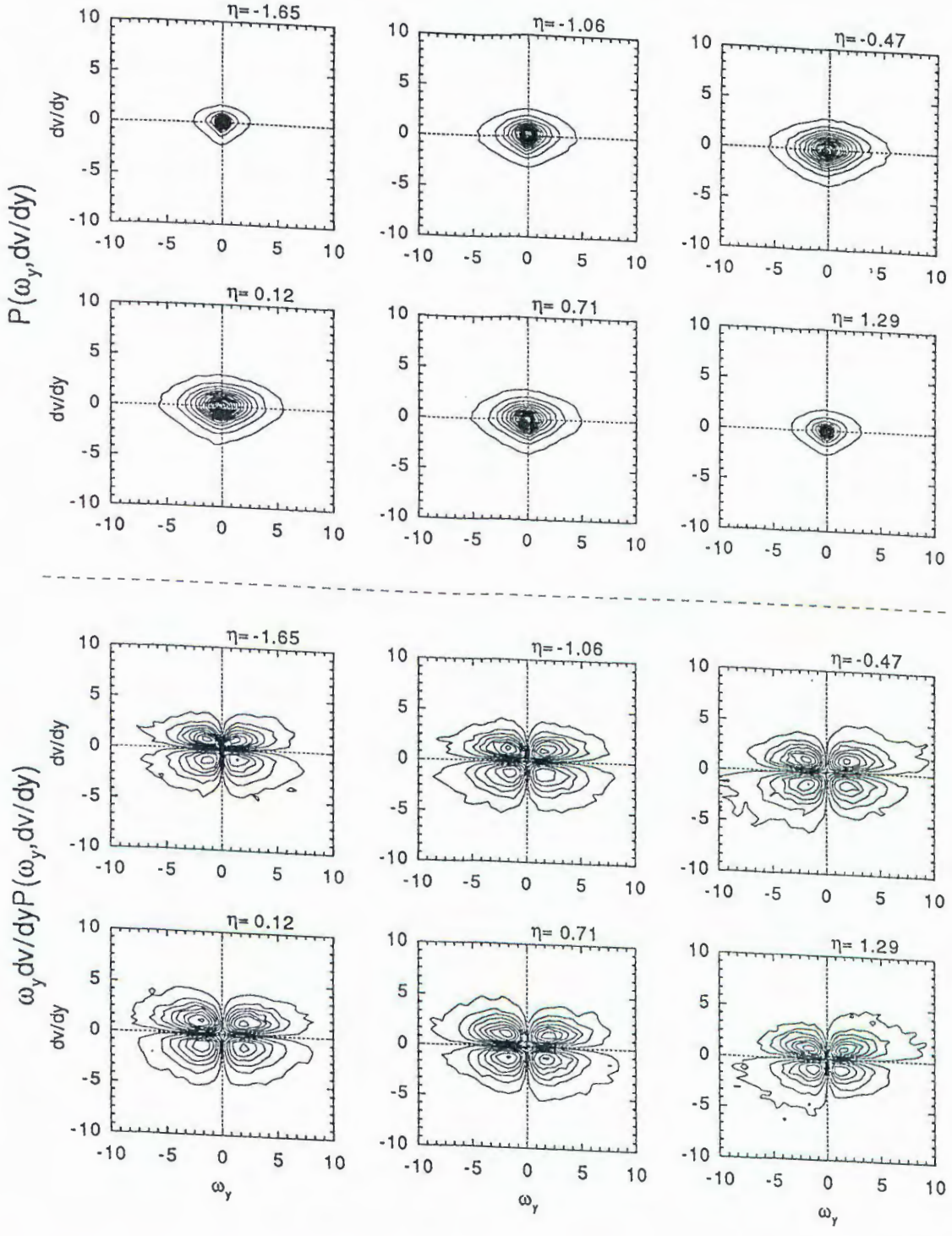

Fig. 5.31. JPDF (top) and covariance integrand (bottom) contours for ω_y and dv/dy.

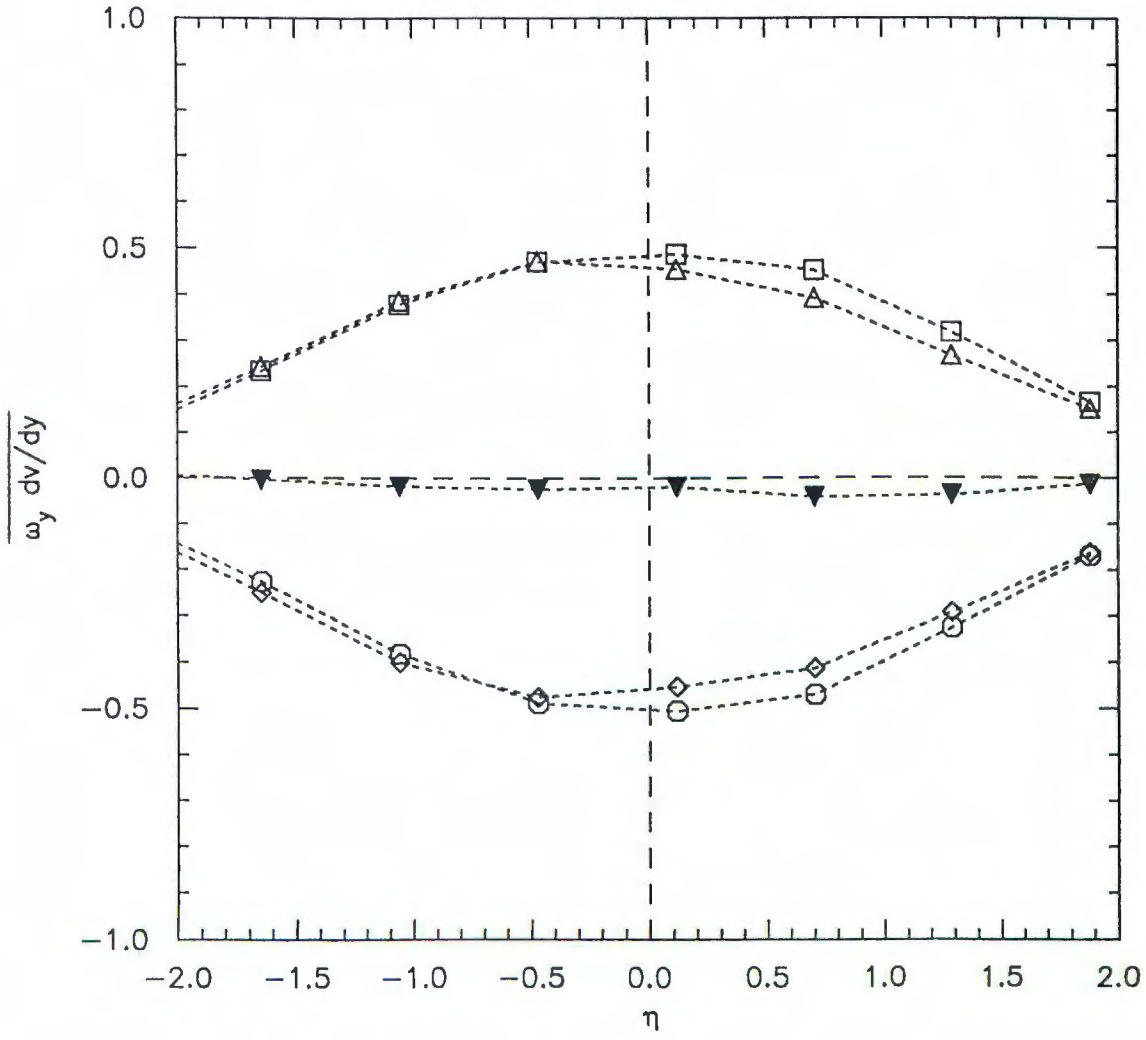

Fig. 5.32. Quadrant analysis for the correlation of ω_y and dv/dy. □ , Q1; ○ , Q2; △ , Q3; ◇ , Q4; ▼ , total.

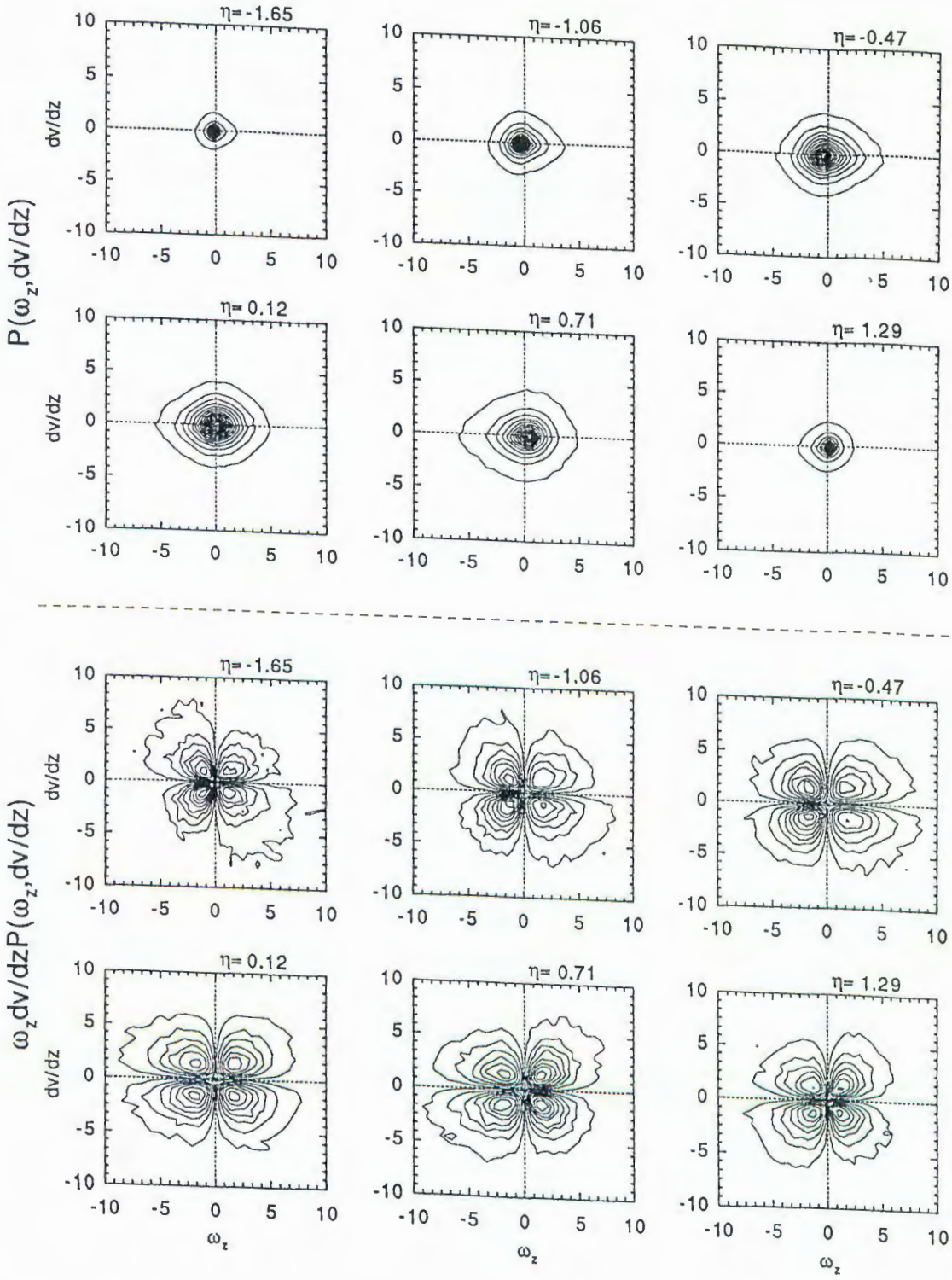

Fig. 5.33. JPDF (top) and covariance integrand (bottom) contours for ω_z and dv/dz.

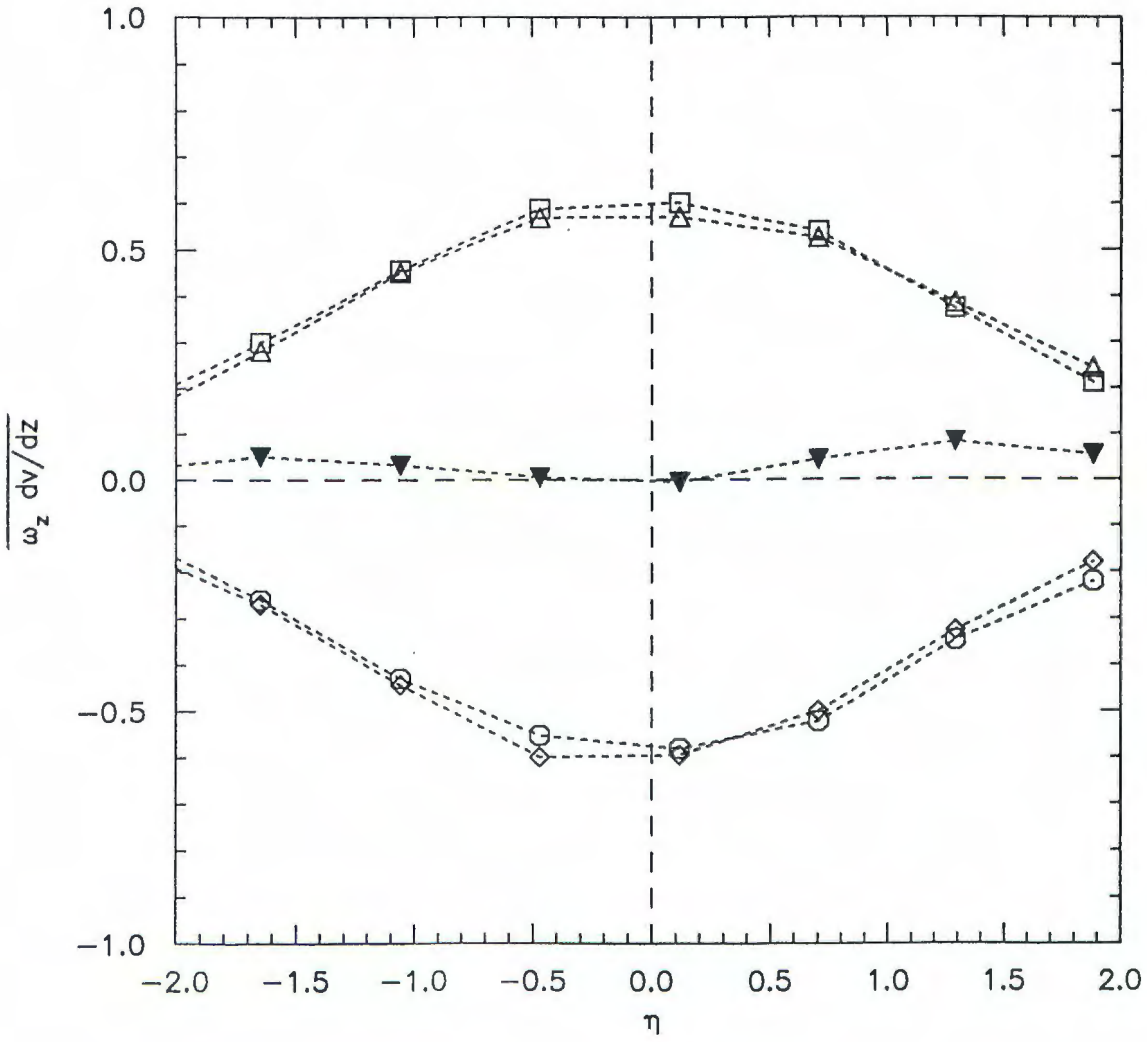

Fig. 5.34. Quadrant analysis for the correlation of ω_z and dv/dz. □, Q1; ○, Q2; △, Q3; ◇, Q4; ▼, total.

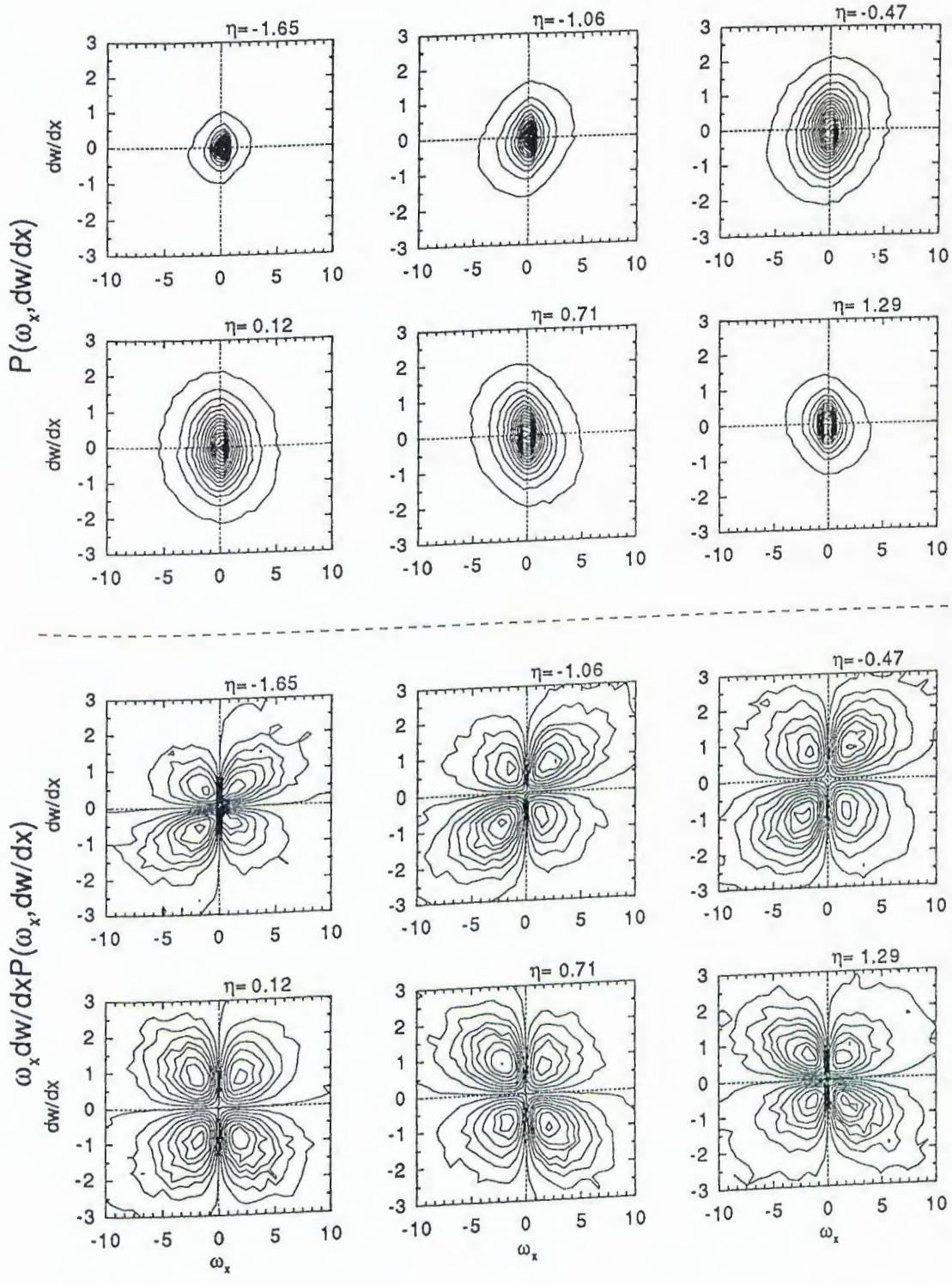

Fig. 5.35. JPDF (top) and covariance integrand (bottom) contours for ω_x and dw/dx.

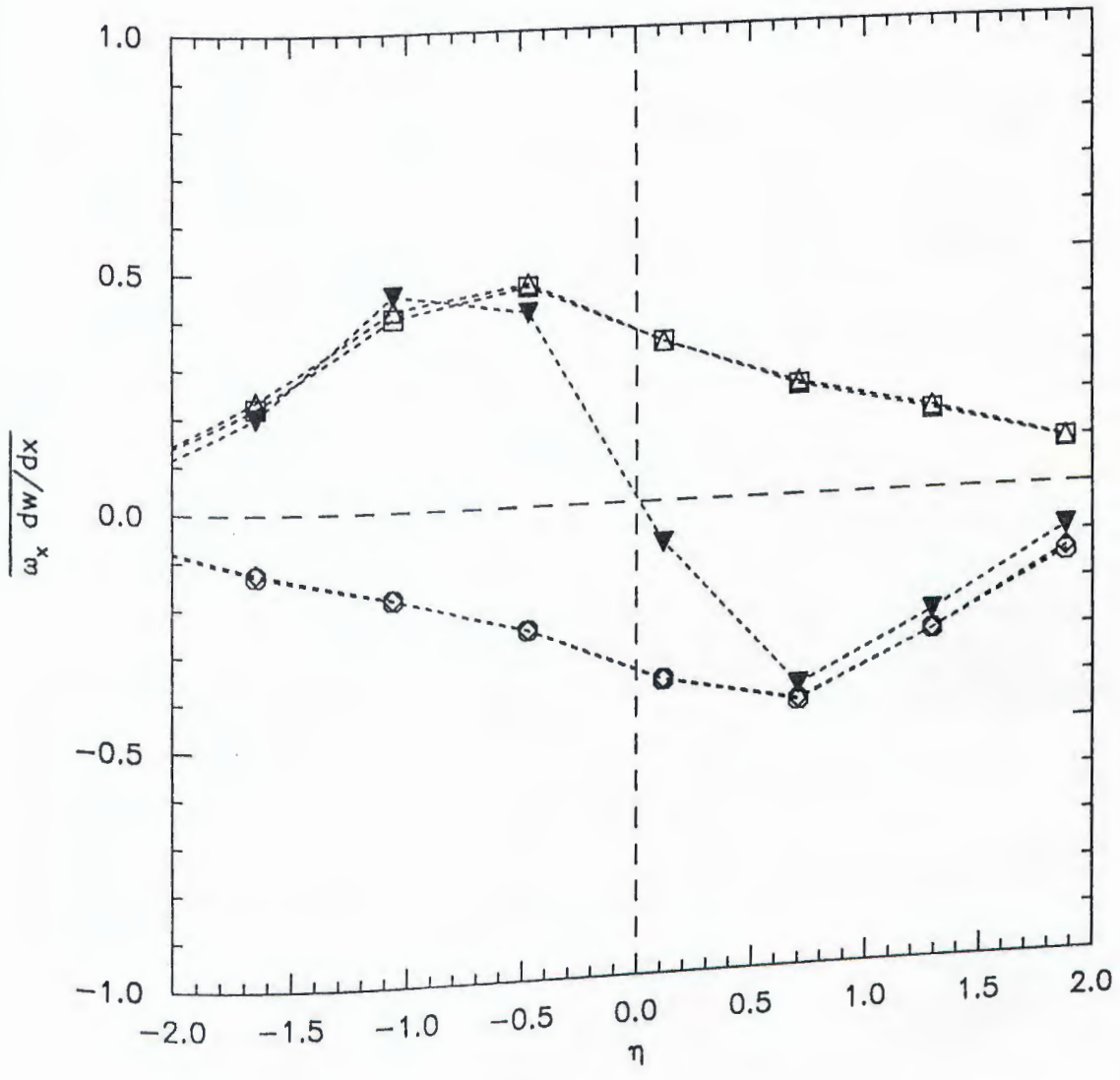

Fig. 5.36. Quadrant analysis for the correlation of ω_x and dw/dx.
□, Q1; ○, Q2; △, Q3; ◇, Q4; ▼, total.

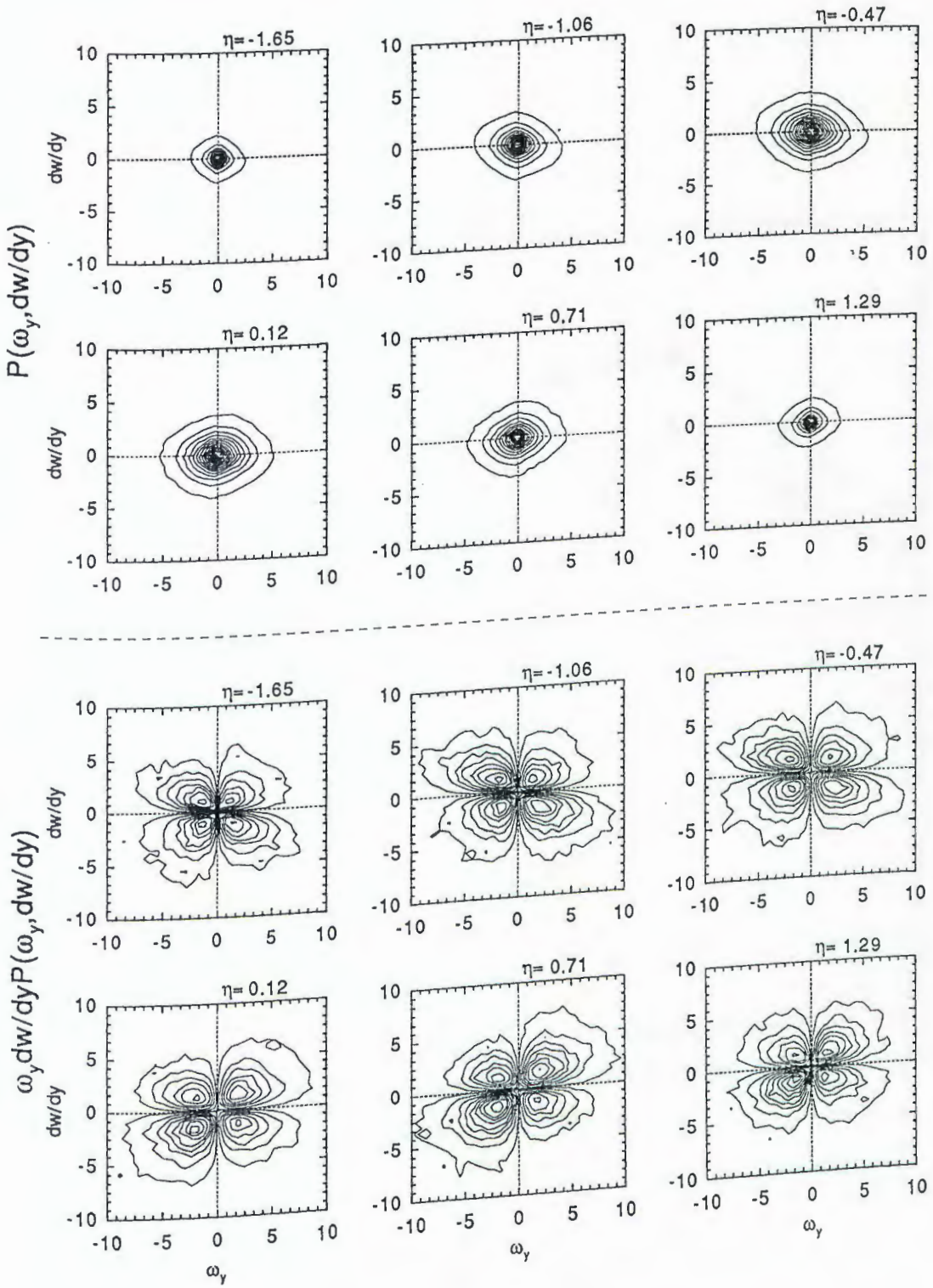

Fig. 5.37. JPDF (top) and covariance integrand (bottom) contours for ω_y and dw/dy.

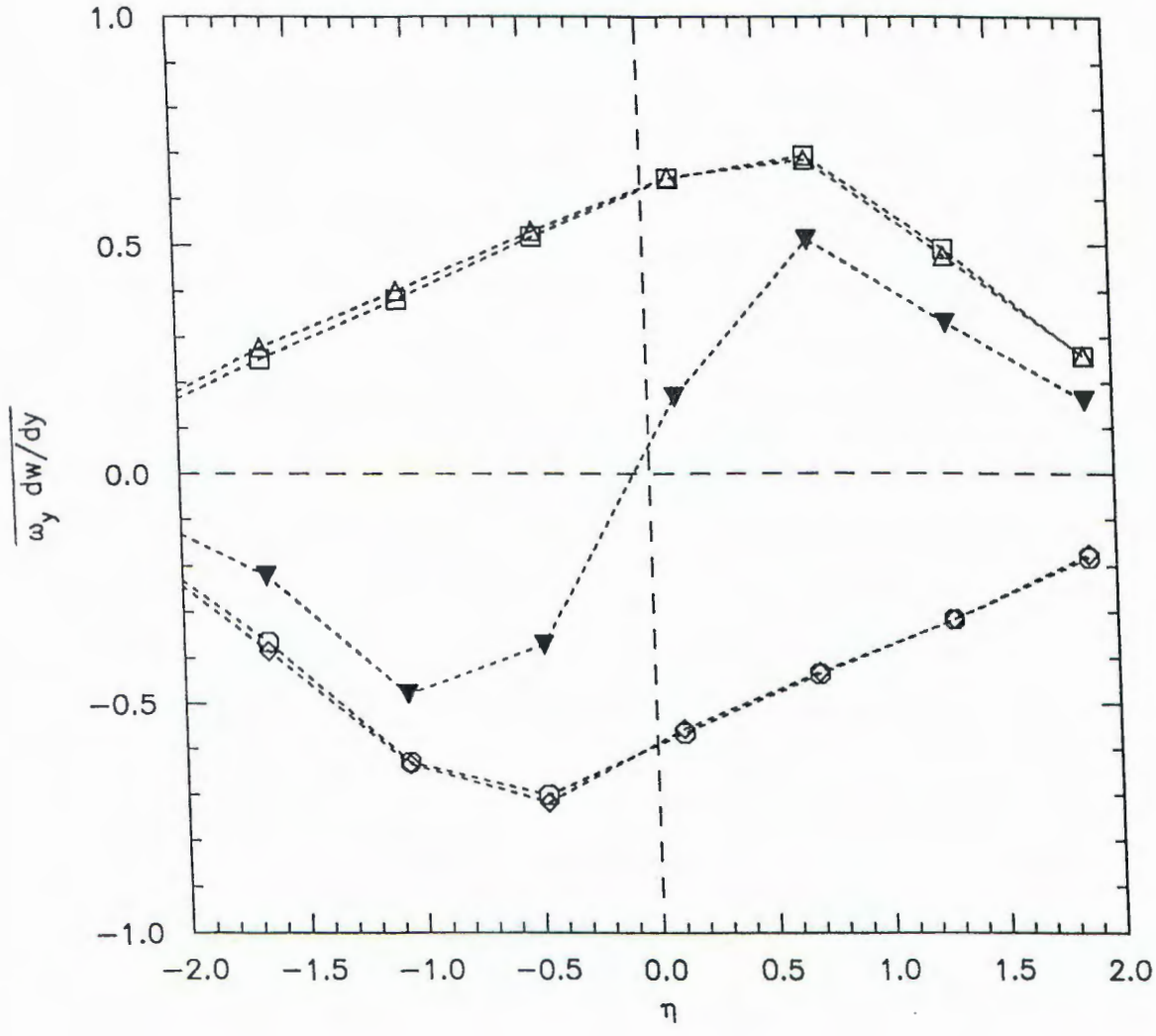

Fig. 5.38. Quadrant analysis for the correlation of ω_y and dw/dy. □, Q1; ○, Q2; △, Q3; ◇, Q4; ▼, total.

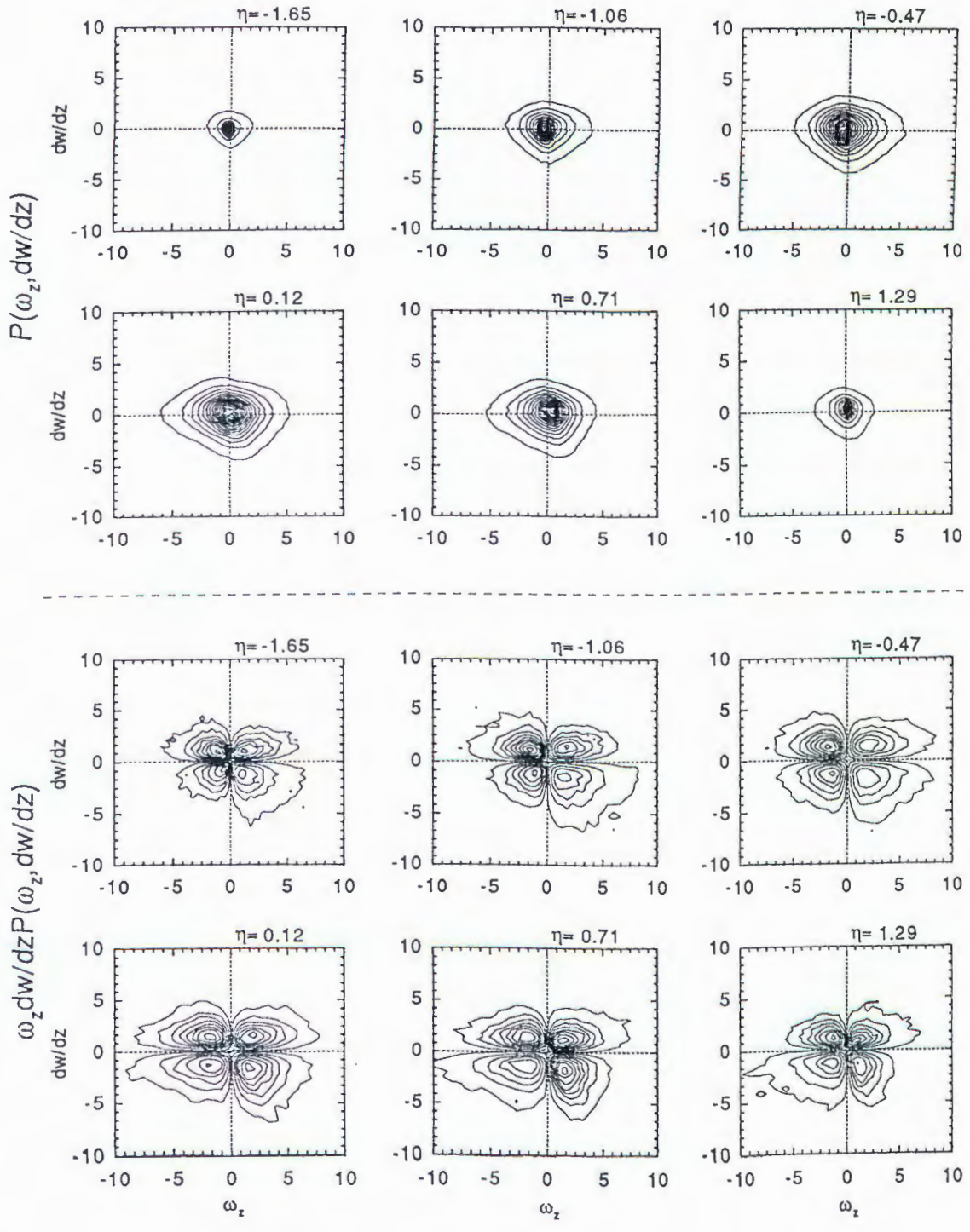

Fig. 5.39. JPDF (top) and covariance integrand (bottom) contours for ω_z and dw/dz.

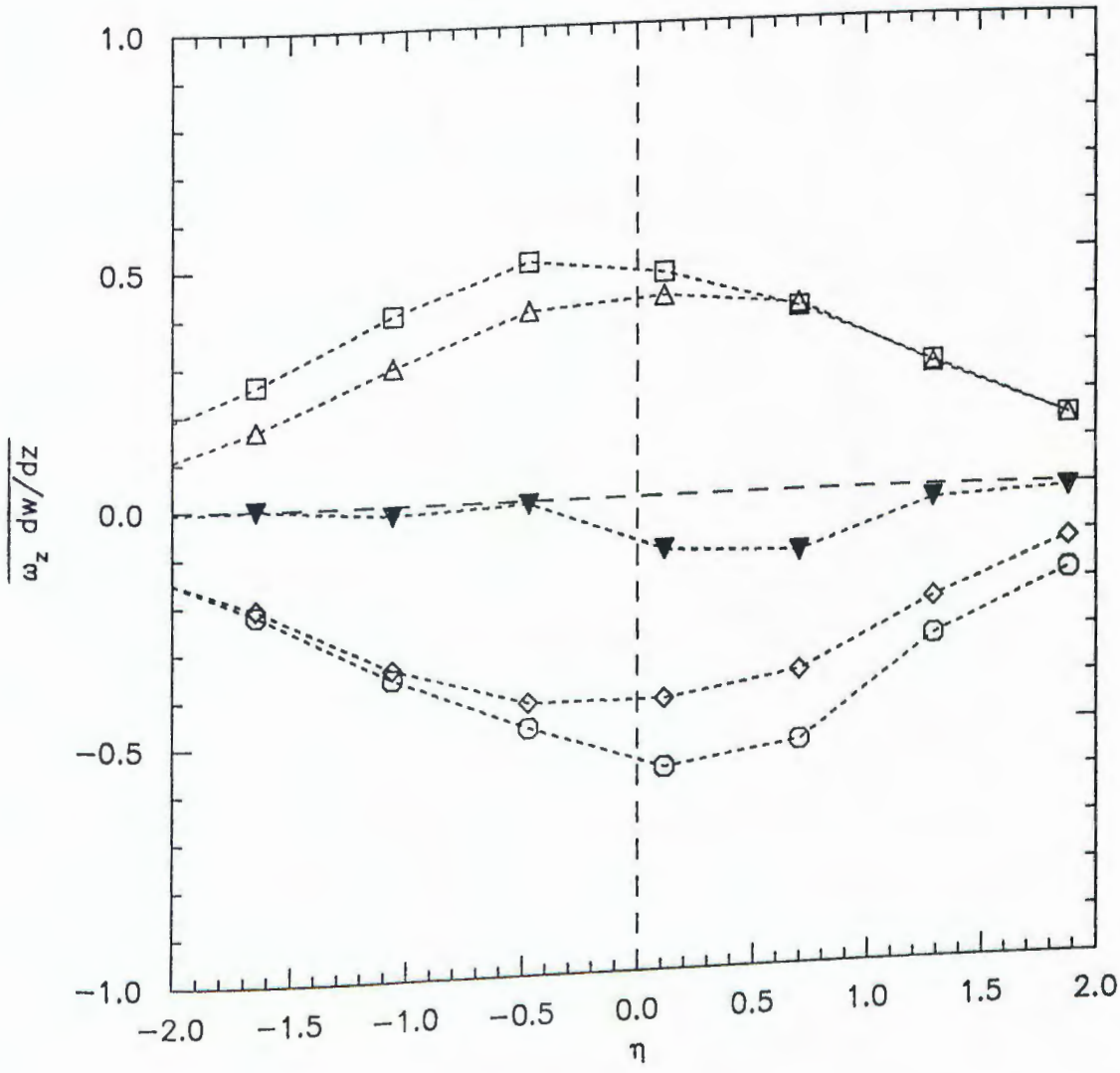

Fig. 5.40. Quadrant analysis for the correlation of ω_z and dw/dz.
□, Q1; ○, Q2; △, Q3; ◇, Q4; ▼, total.

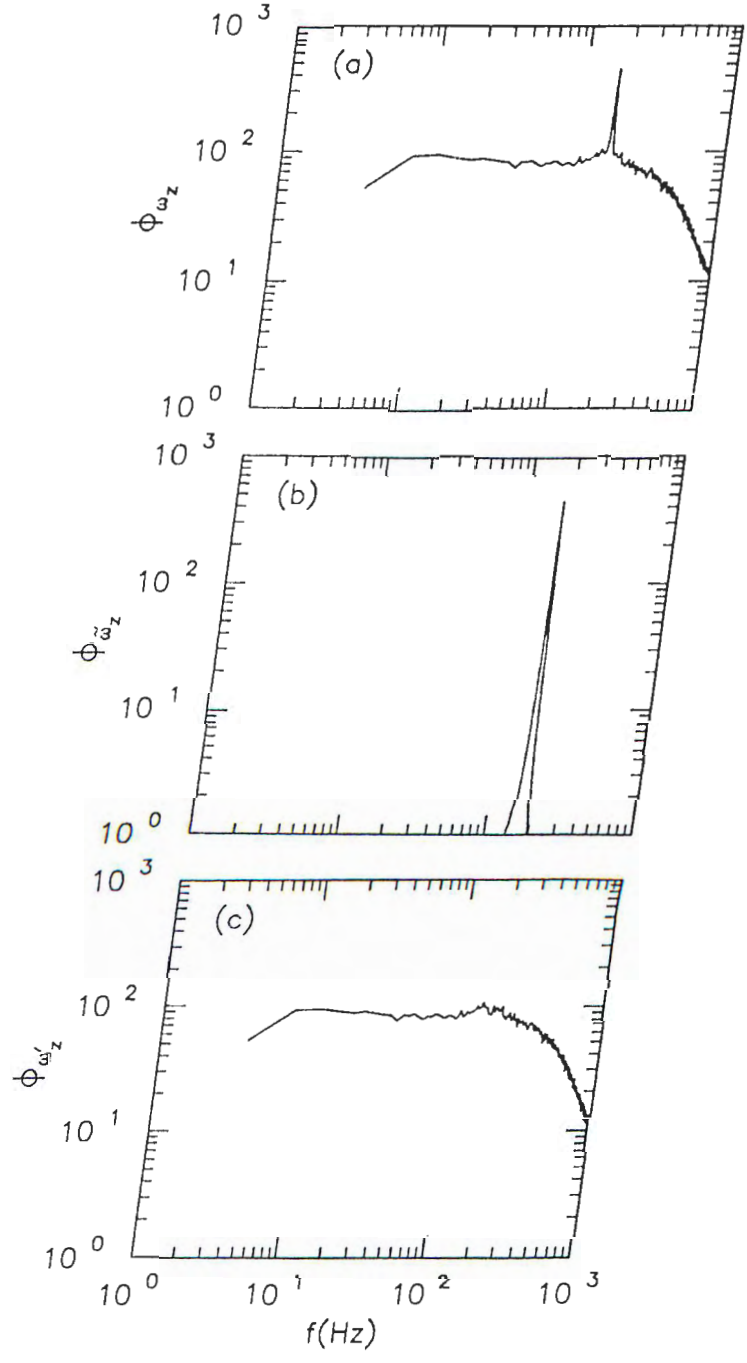

Fig. 6.1. Spectra of ω_z signals at η=0.12: (a) total fluctuating (ω_z), (b) phase reference ($\tilde{\omega}_z$), and (c) incoherent (ω'_z). The phase reference signal is used for conditional analysis of all measured variables.

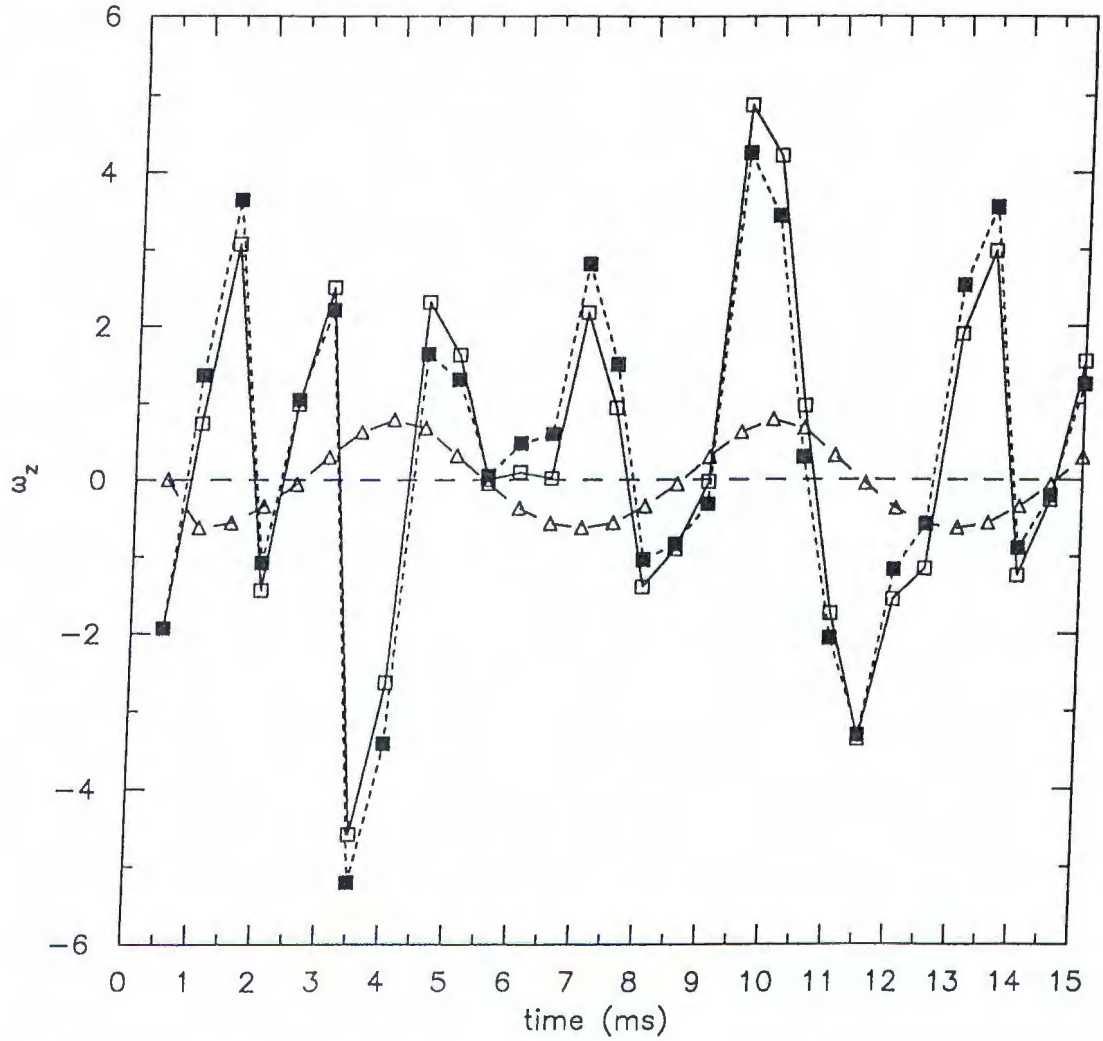

Fig. 6.2. Time series for the three parts of the nondimensional spanwise vorticity. □, total fluctuating (ω_z); △, coherent ($\tilde{\omega}_z$); ■, incoherent (ω_z').

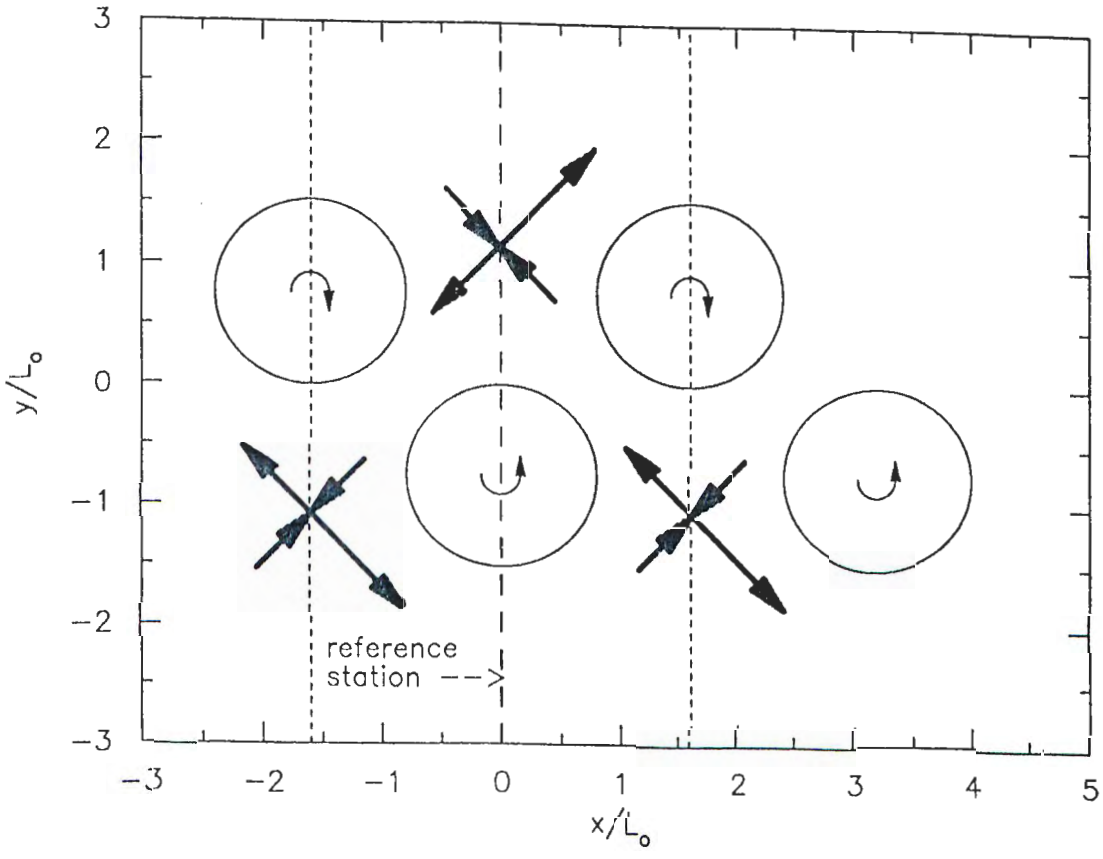

Fig. 6.3. Schematic sketch of the vortex shedding and the saddle regions. The dimensions are estimated from current database and from Hussain & Hayakawa [26] at x/d=30. The reference station at $x/L_o=0$ indicates the detected events across the wake.

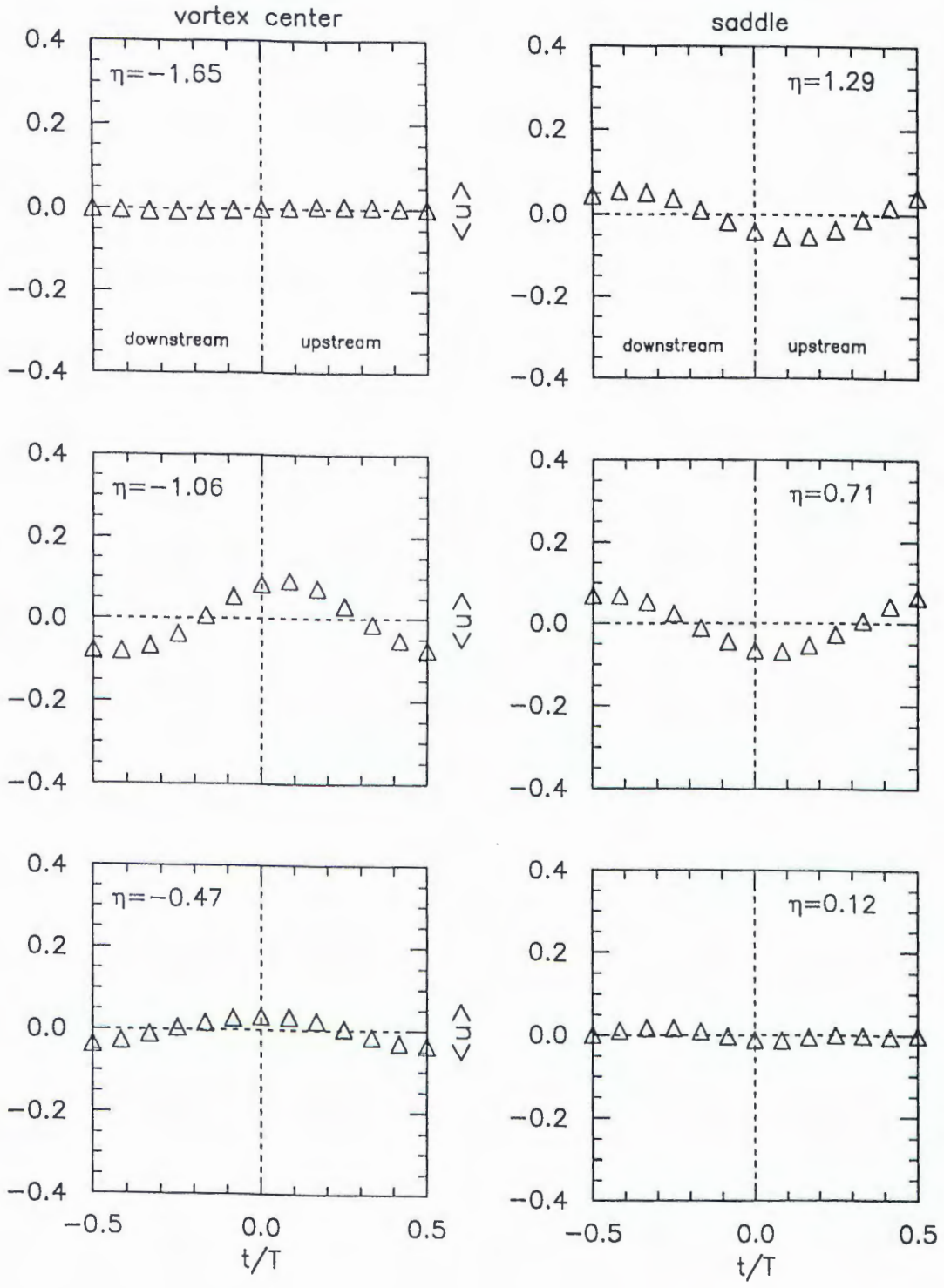

Fig. 6.4. Conditional averages of u fluctuations.

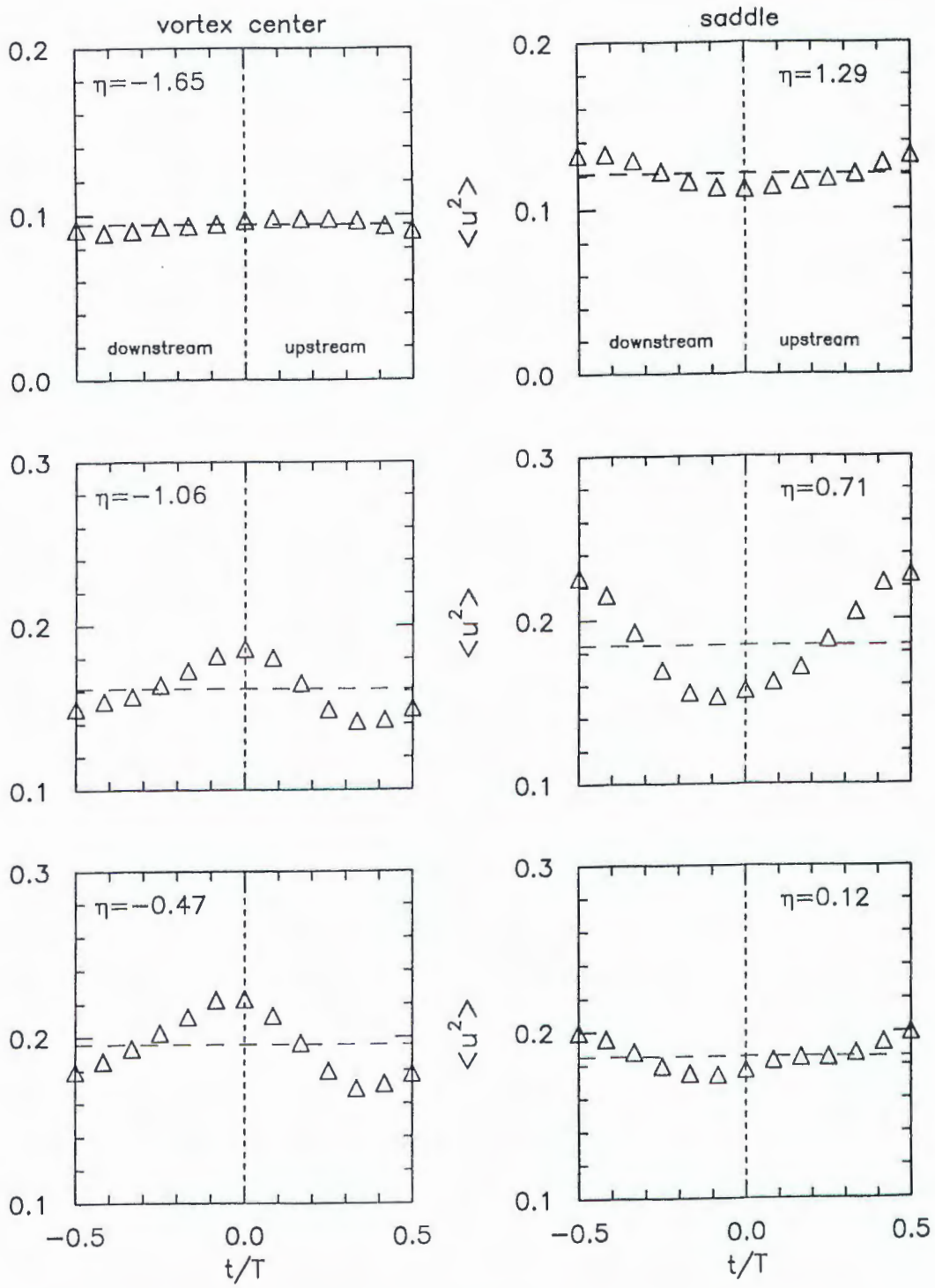

Fig. 6.5. Conditional averages of the total u^2 fluctuations. The incoherent contribution is almost the same as the total therefore not shown. The long dashed lines indicate the time averages.

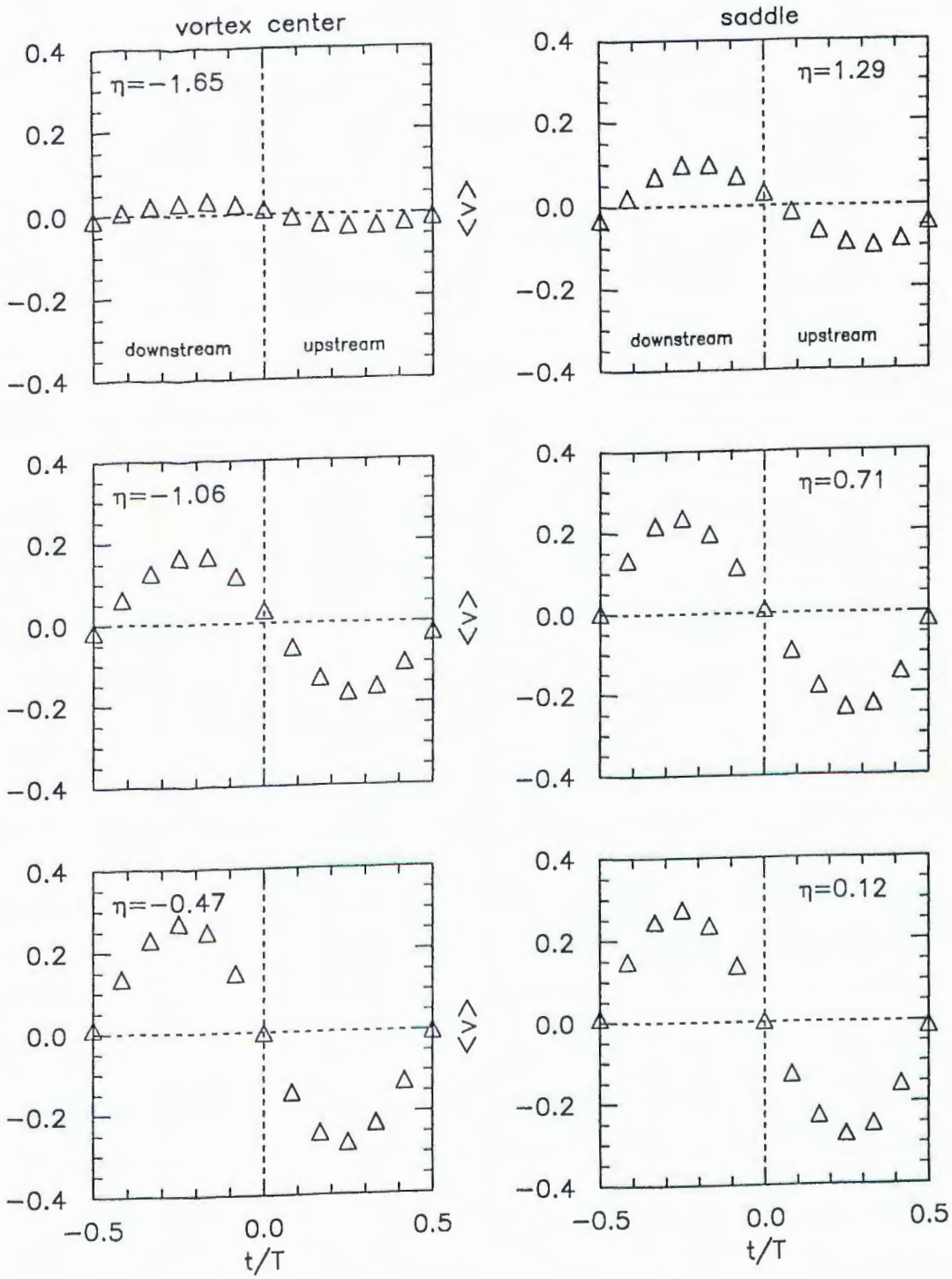

Fig. 6.6. Conditional averages of v fluctuations.

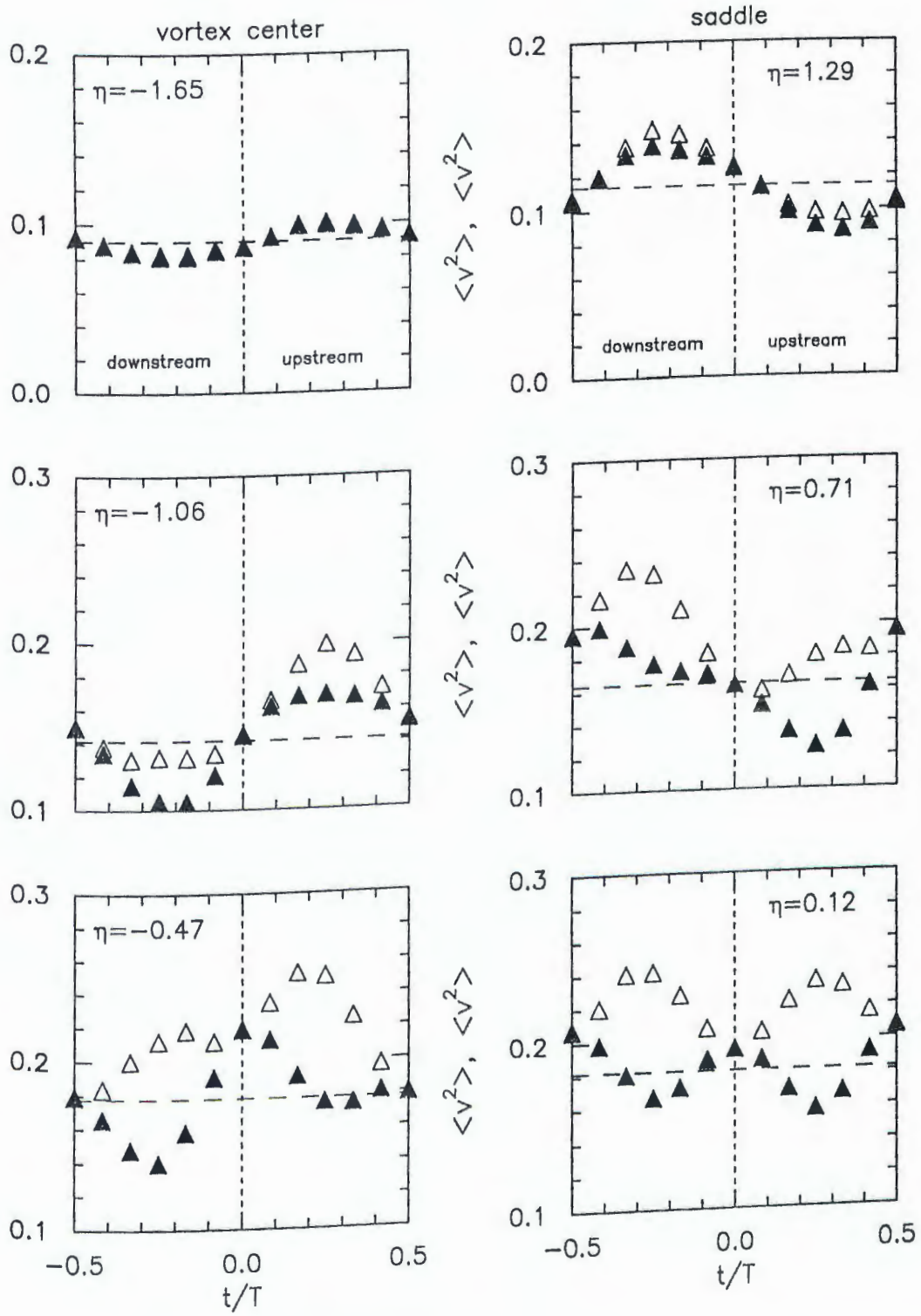

Fig. 6.7. Conditional averages of the total and incoherent v^2 fluctuations. The closed symbols are for the incoherent fluctuating field. The open symbols are for the total fluctuating field. The long dashed lines indicate the time averages of the incoherent field.

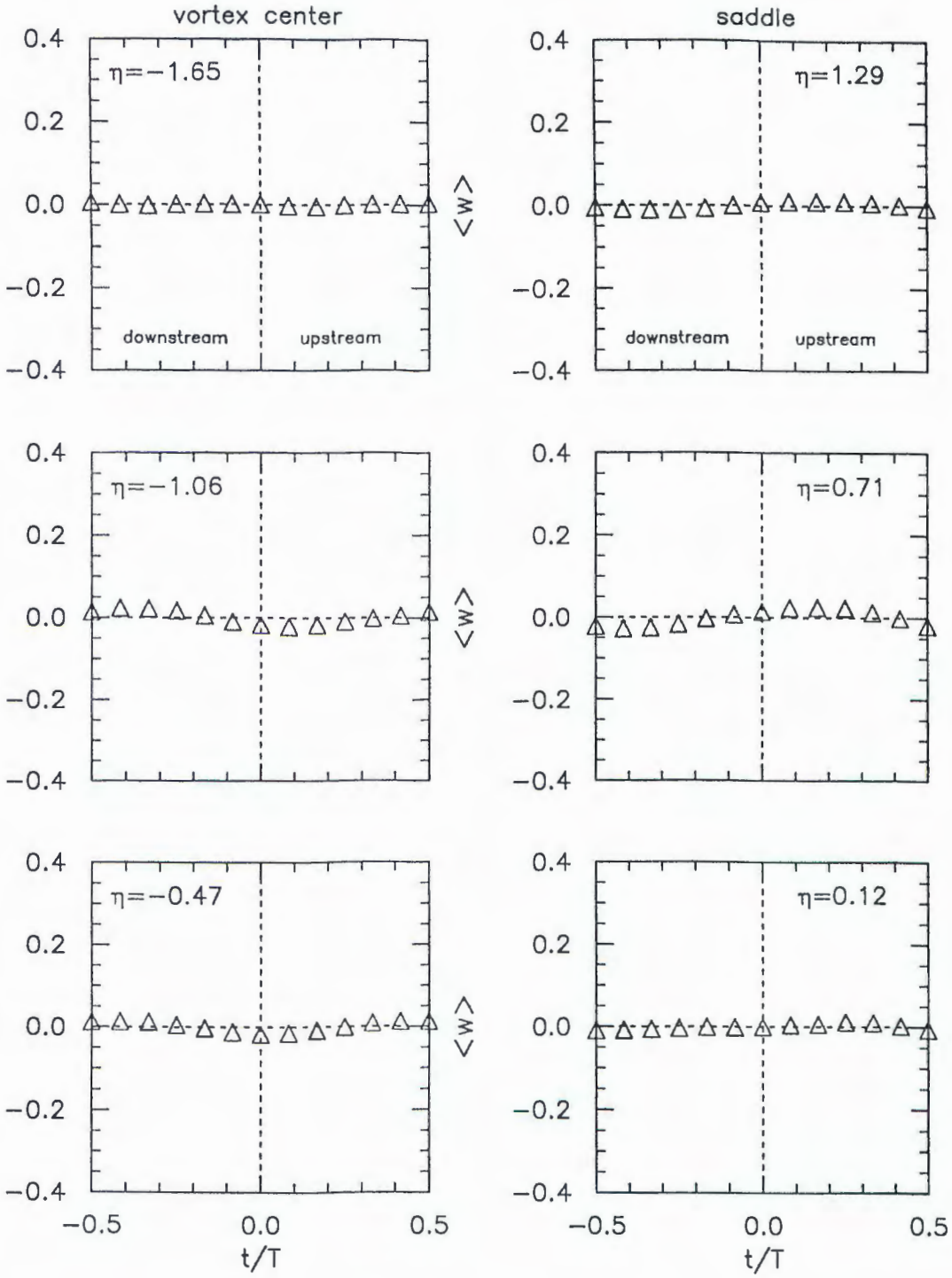

Fig. 6.8. Conditional averages of w fluctuations.

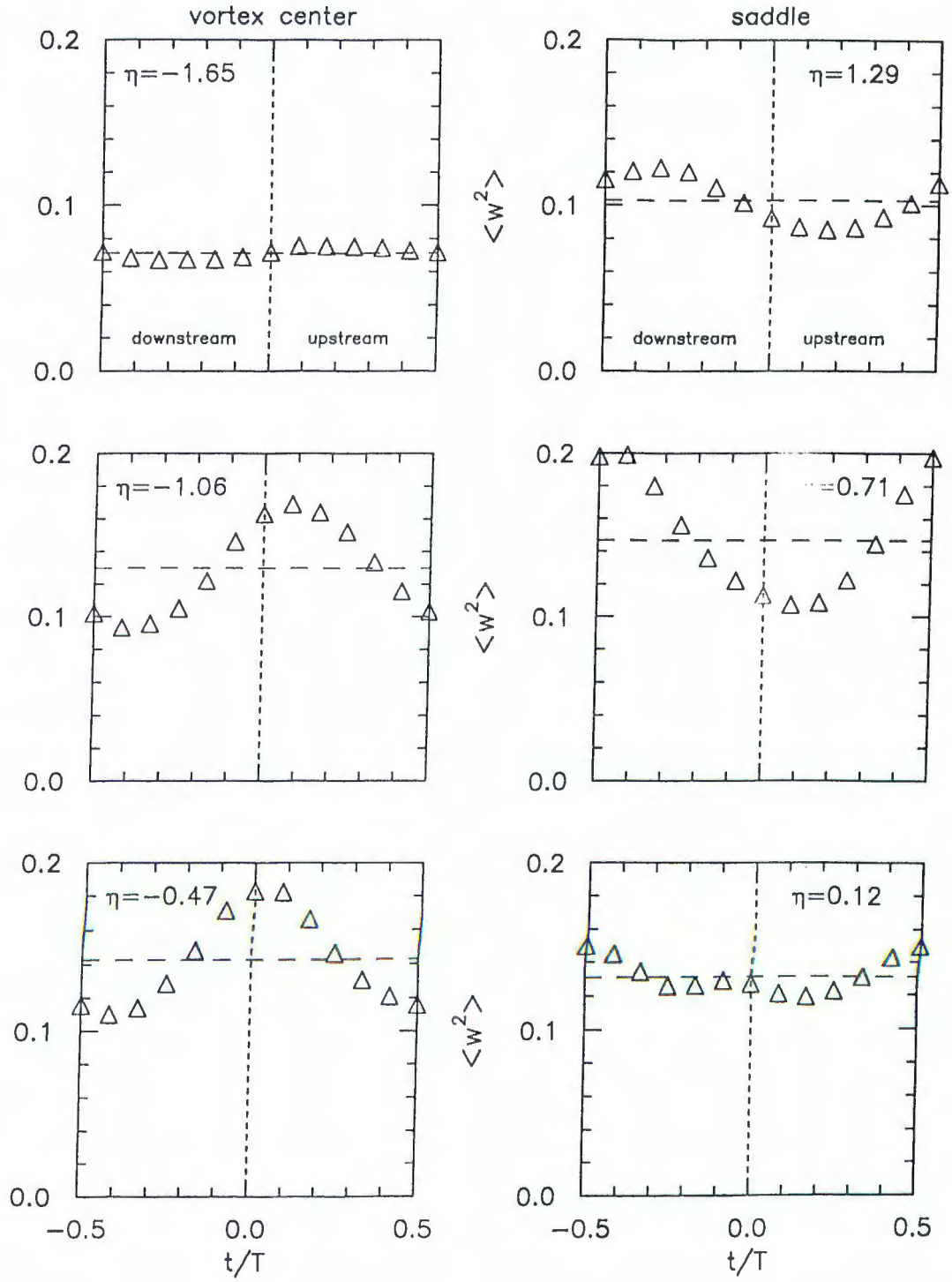

Fig. 6.9. Conditional averages of the total w^2 fluctuations. The incoherent contribution is almost the same as the total therefore not shown. The long dashed lines indicate the time averages.

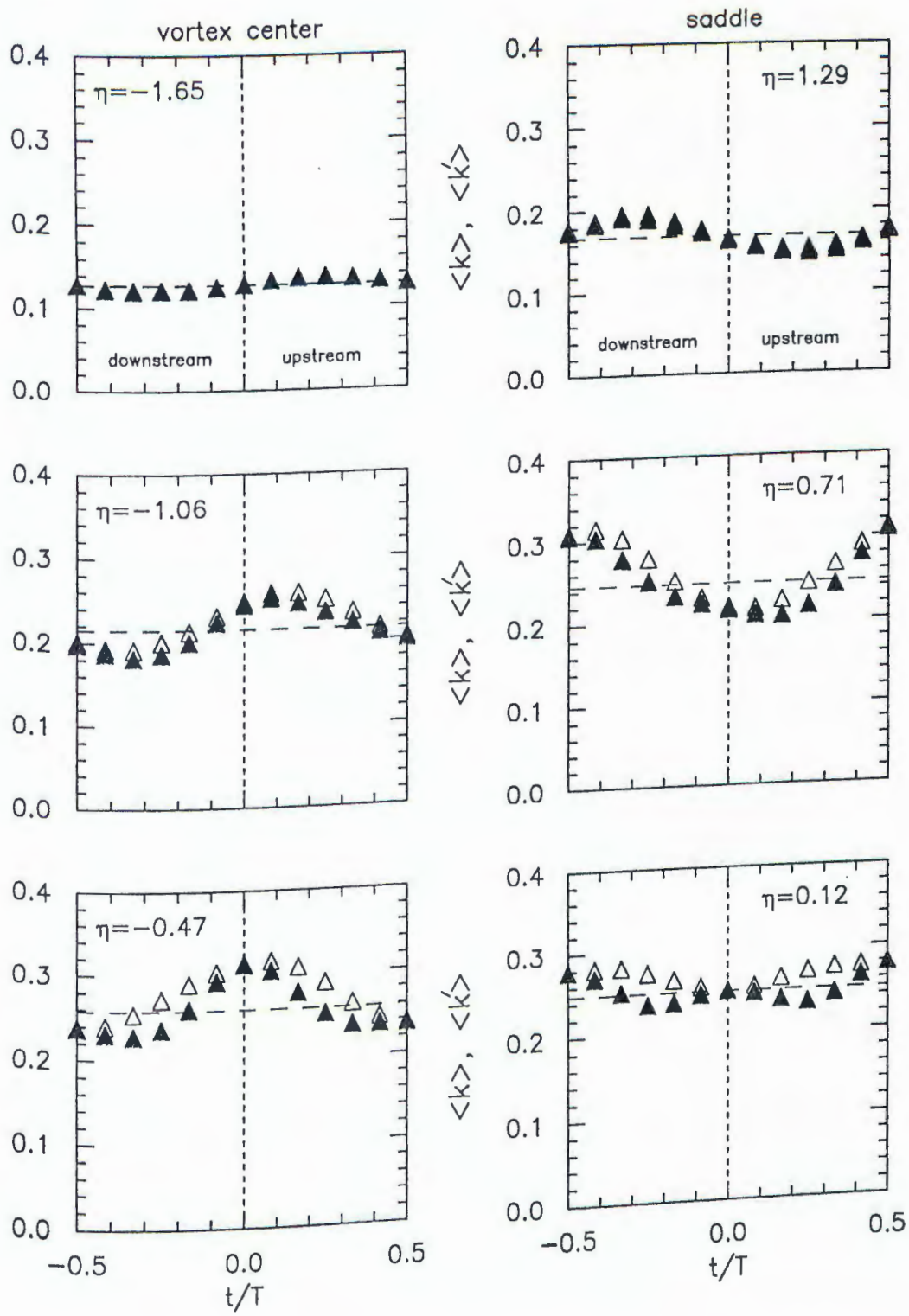

Fig. 6.10. Conditional averages of the total and incoherent k fluctuations. The closed symbols are for the incoherent fluctuating field. The open symbols are for the total fluctuating field. The long dashed lines indicate the time averages of the incoherent field.

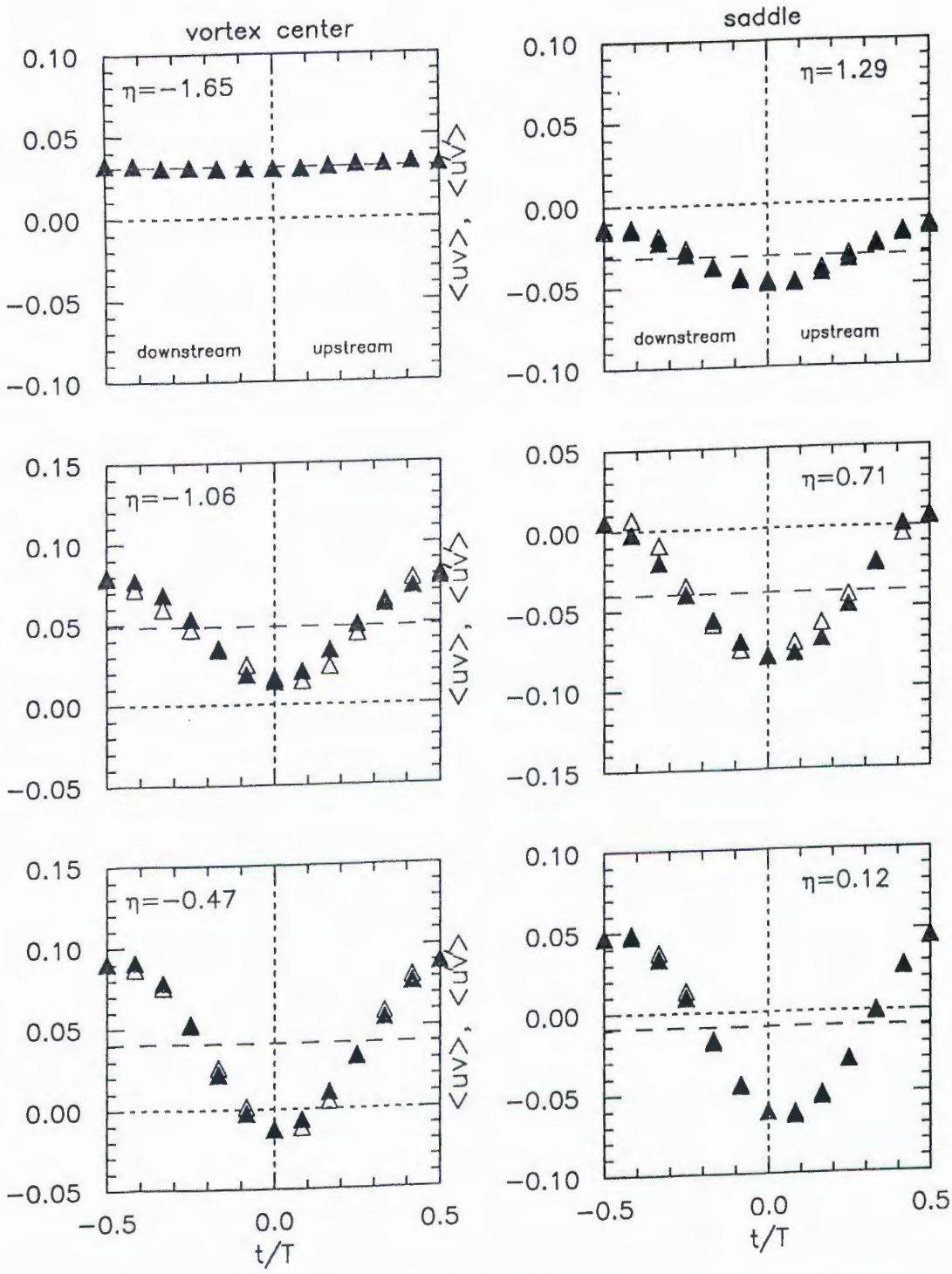

Fig. 6.11. Conditional averages of the total and incoherent uv fluctuations. The closed symbols are for the incoherent fluctuating field. The open symbols are for the total fluctuating field. The long dashed lines indicate the time averages of the incoherent field.

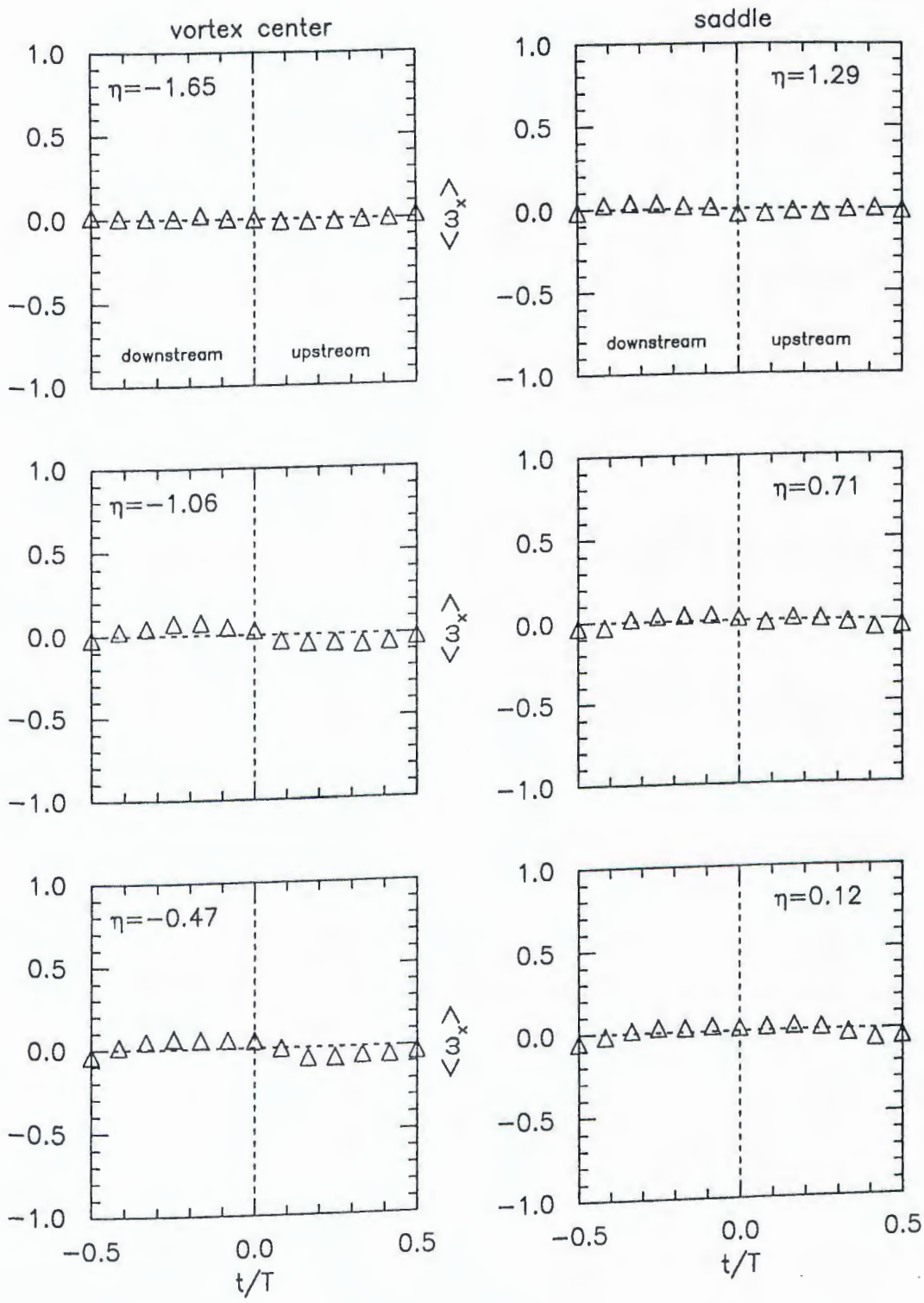

Fig. 6.12. Conditional averages of ω_x fluctuations.

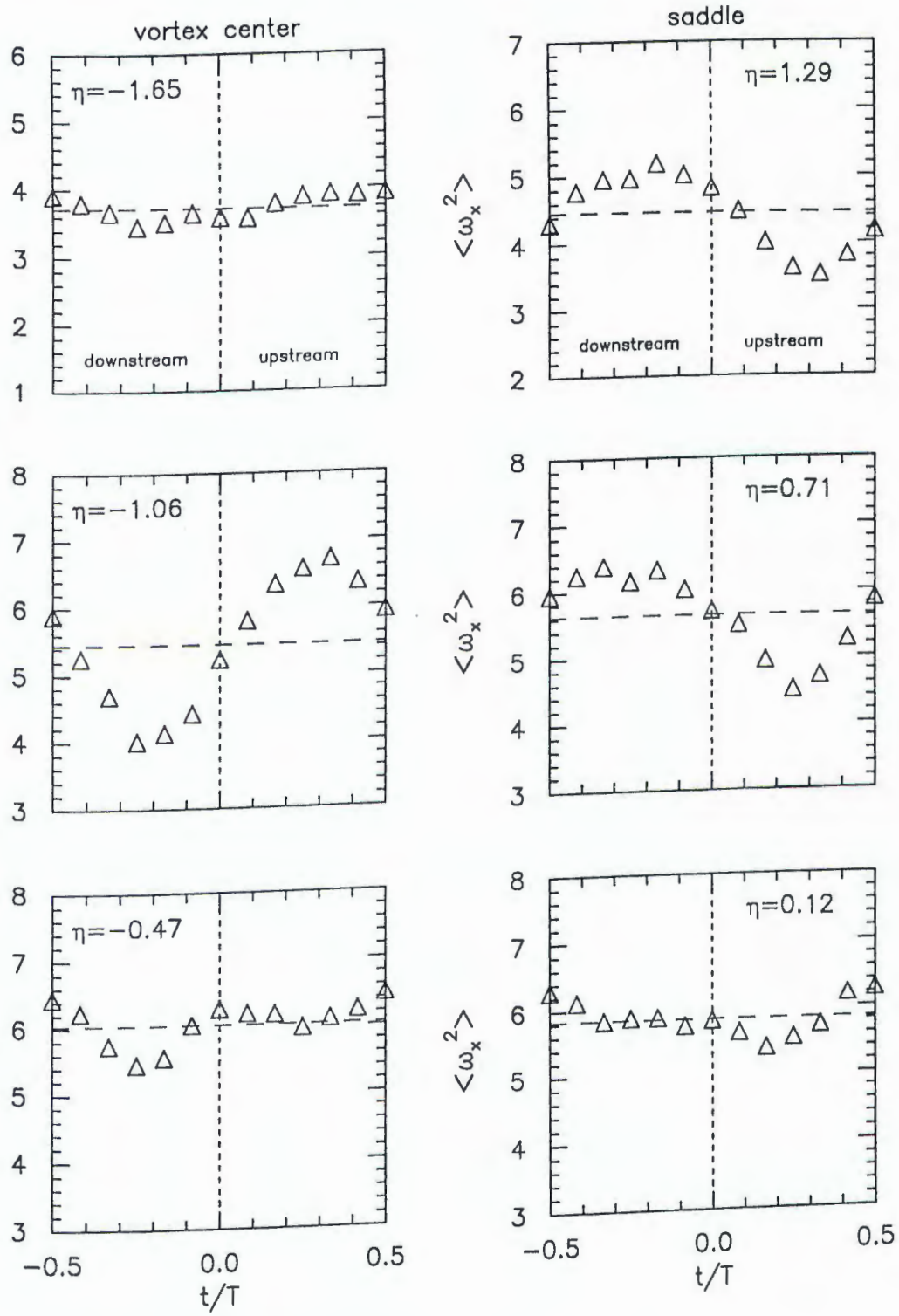

Fig. 6.13. Conditional averages of the total ω_x^2 fluctuations. The incoherent contribution is almost the same as the total therefore not shown. The long dashed lines indicate the time averages.

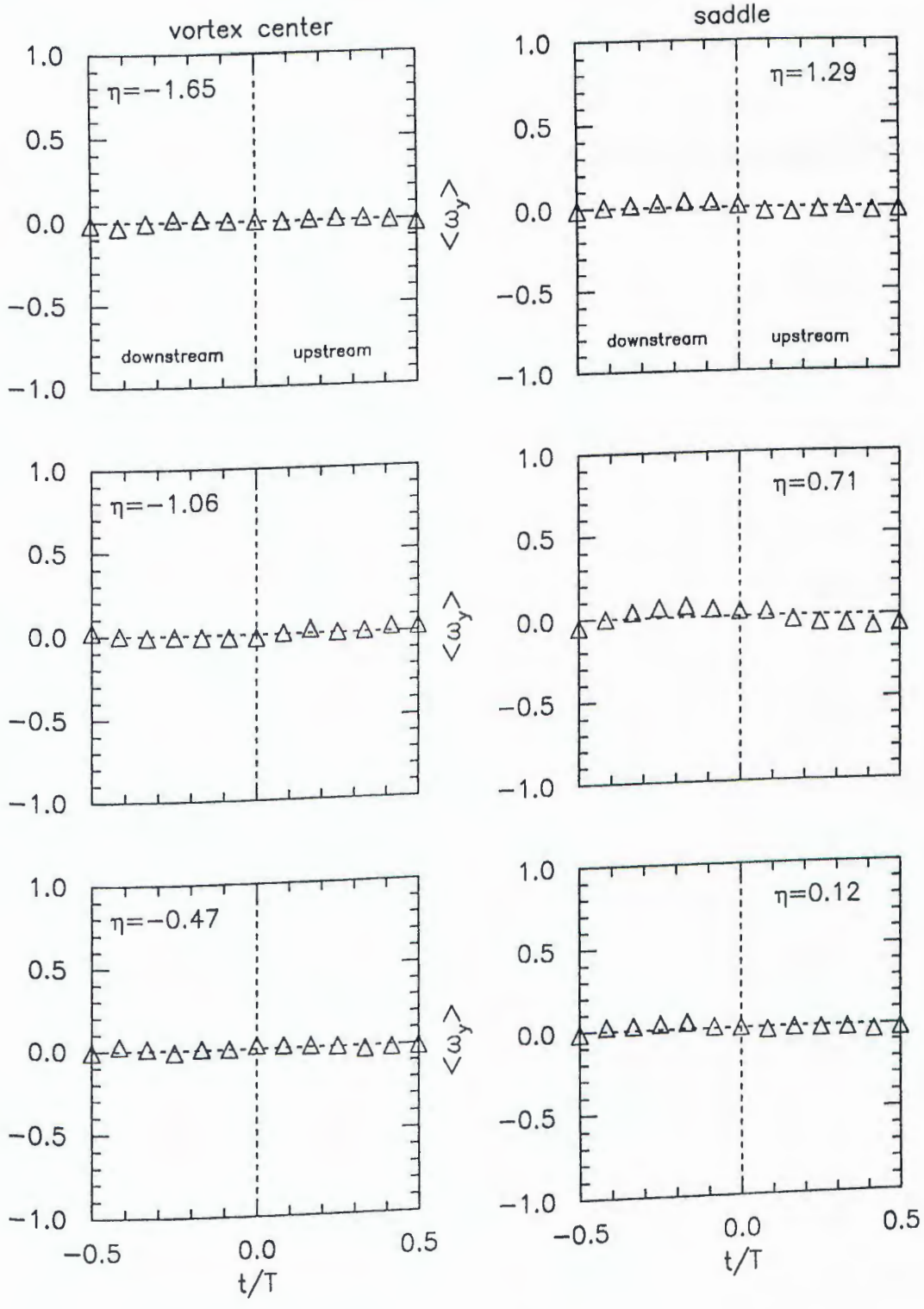

Fig. 6.14. Conditional averages of ω_y fluctuations.

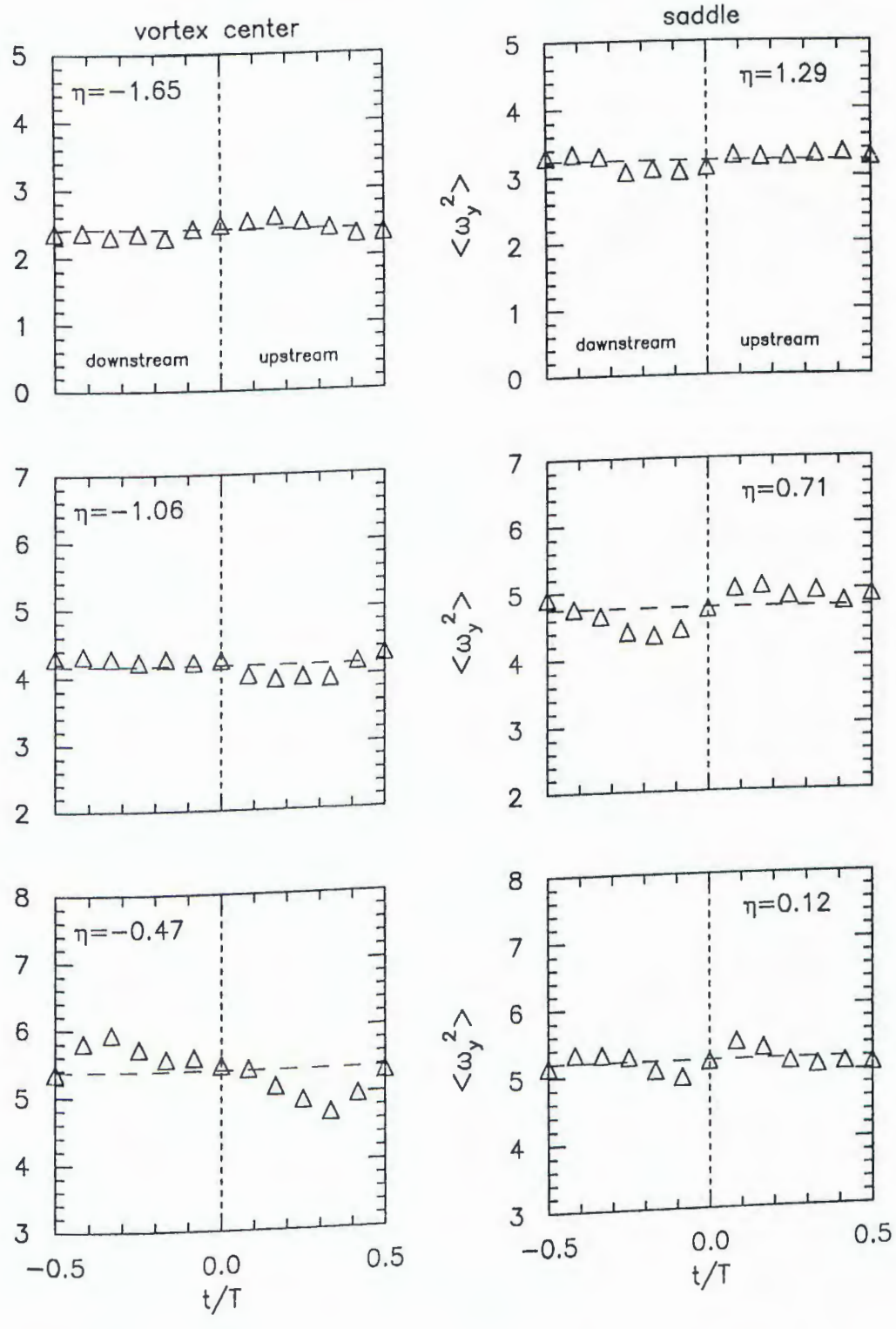

Fig. 6.15. Conditional averages of the total ω_y^2 fluctuations. The incoherent contribution is almost the same as the total therefore not shown. The long dashed lines indicate the time averages.

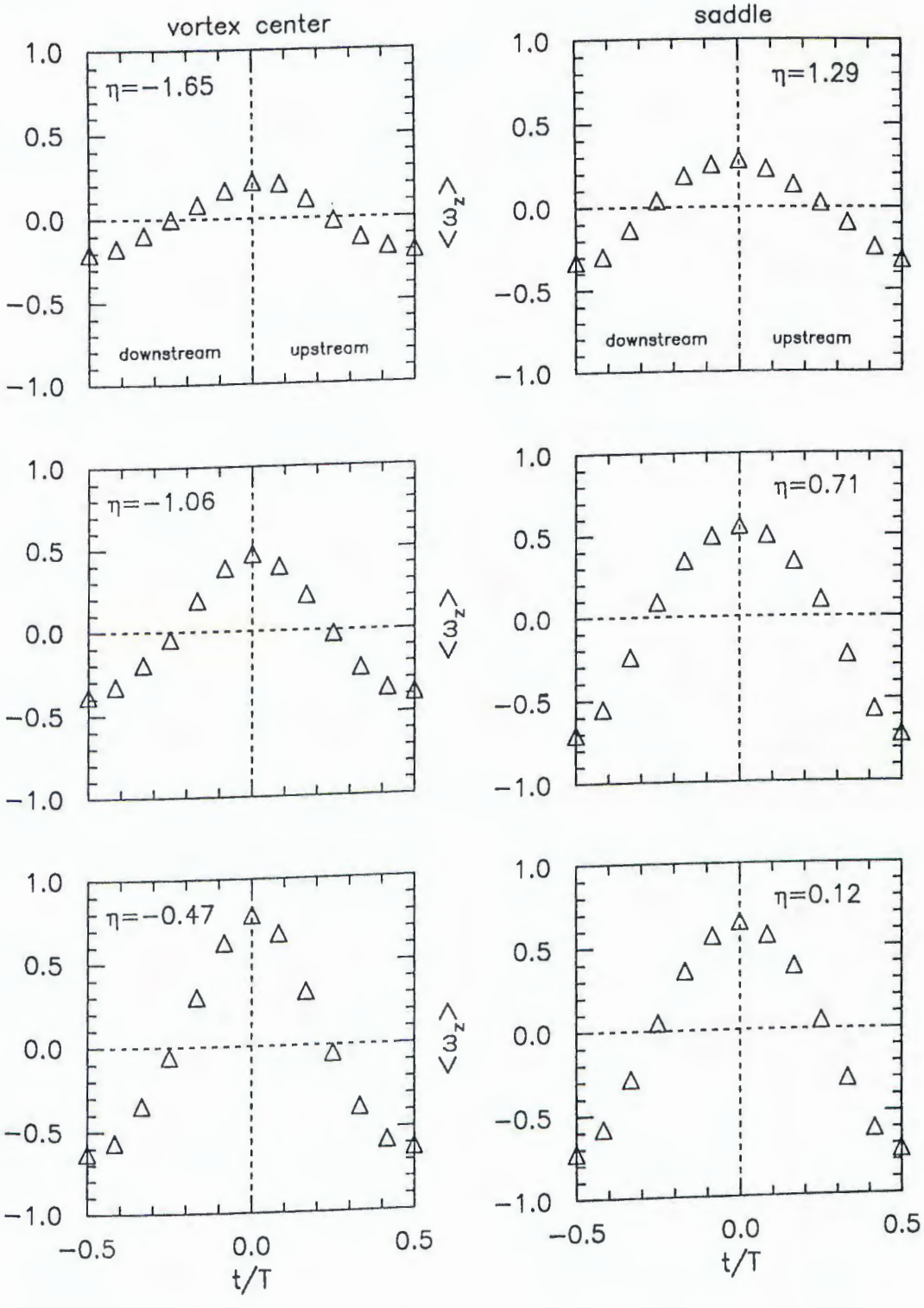

Fig. 6.16. Conditional averages of ω_z fluctuations.

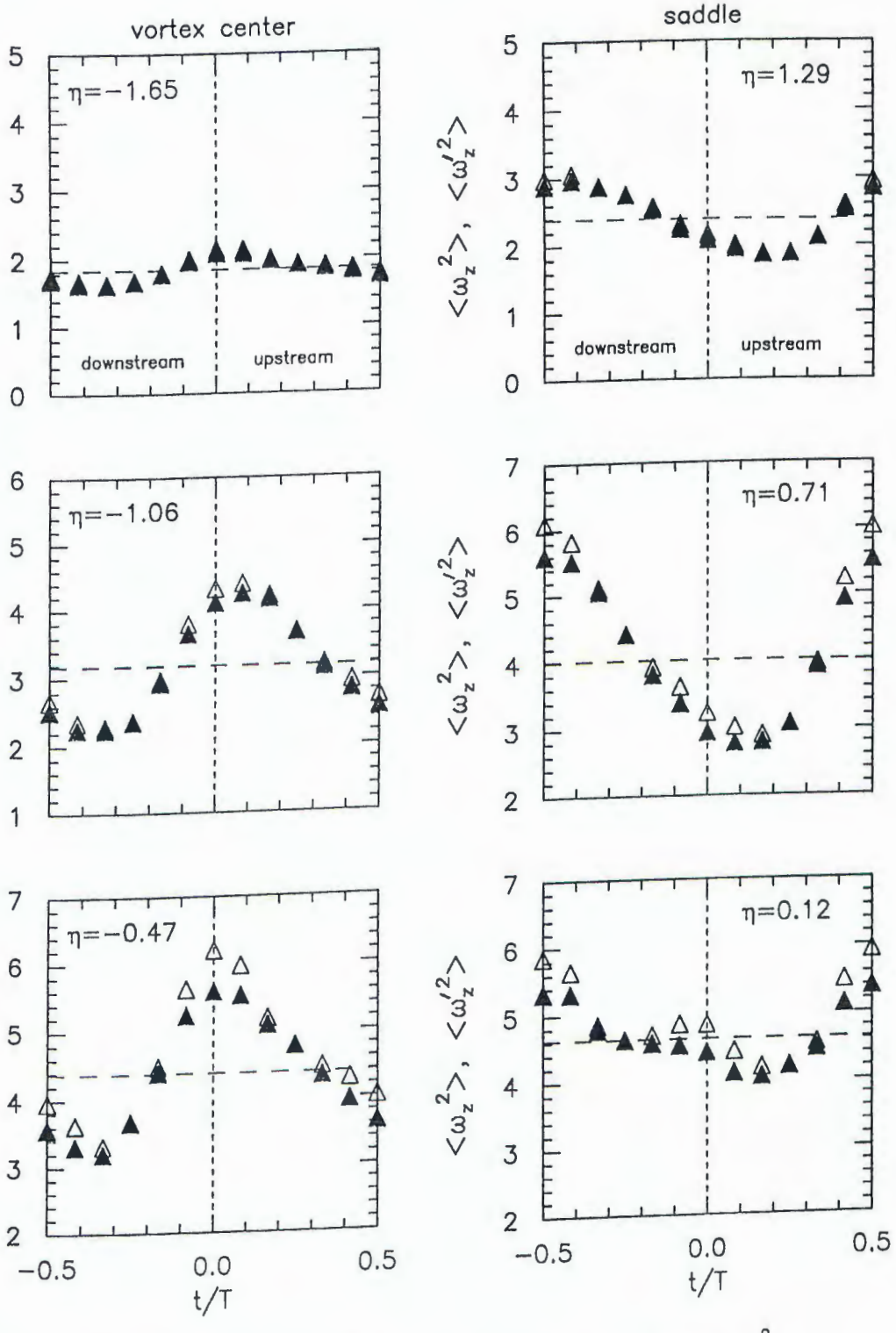

Fig. 6.17. Conditional averages of the total and incoherent ω_z^2 fluctuations. The closed symbols are for the incoherent fluctuating field. The open symbols are for the total fluctuating field. The long dashed lines indicate the time averages of the incoherent field.

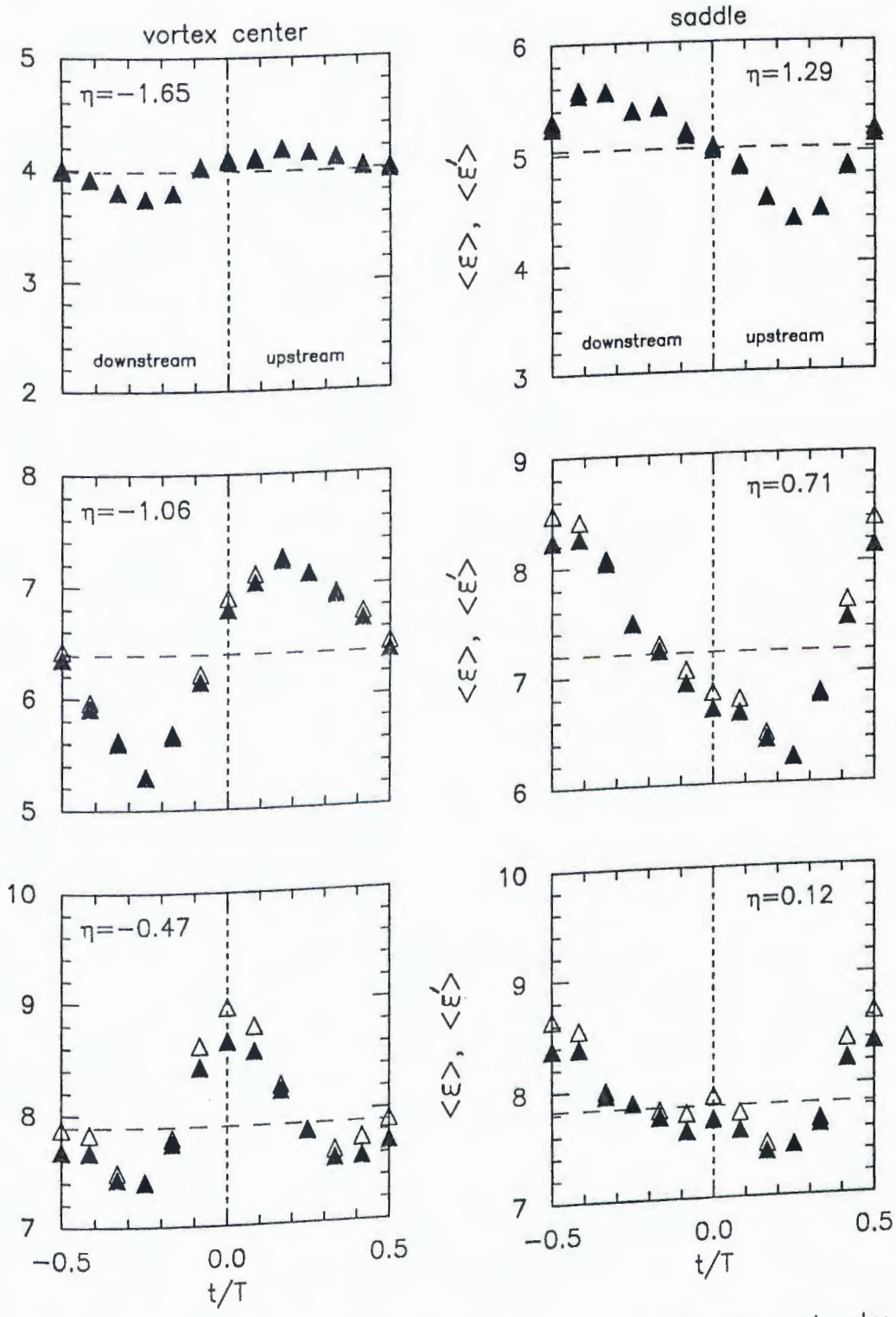

Fig. 6.18. Conditional averages of the total and incoherent enstrophy fluctuations. The closed symbols are for the incoherent fluctuating field. The open symbols are for the total fluctuating field. The long dashed lines indicate the time averages of the incoherent field.

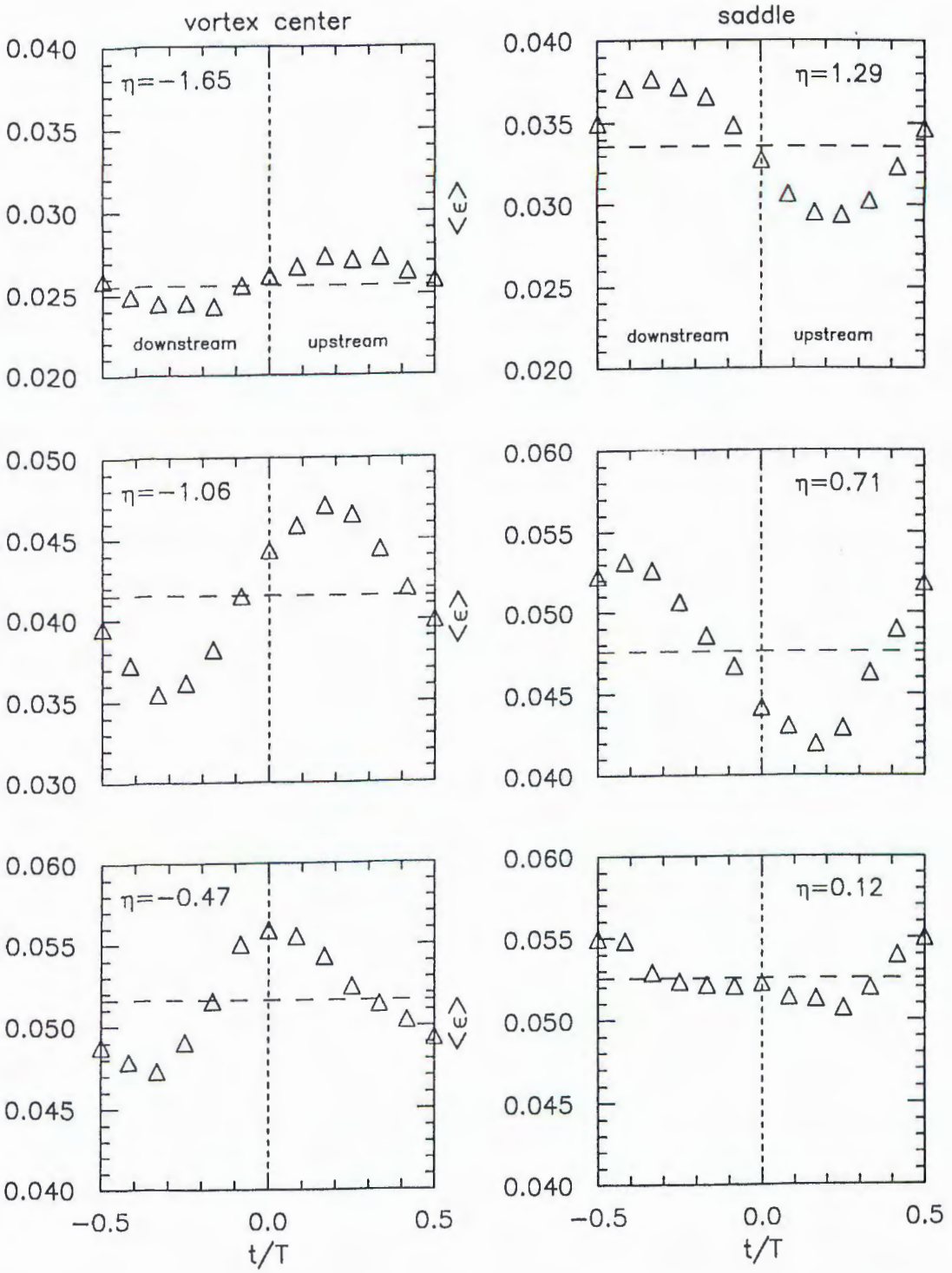

Fig. 6.19. Conditional averages of the total dissipation rate fluctuations. The incoherent contribution is almost the same as the total therefore not shown. The long dashed lines indicate the time averages.

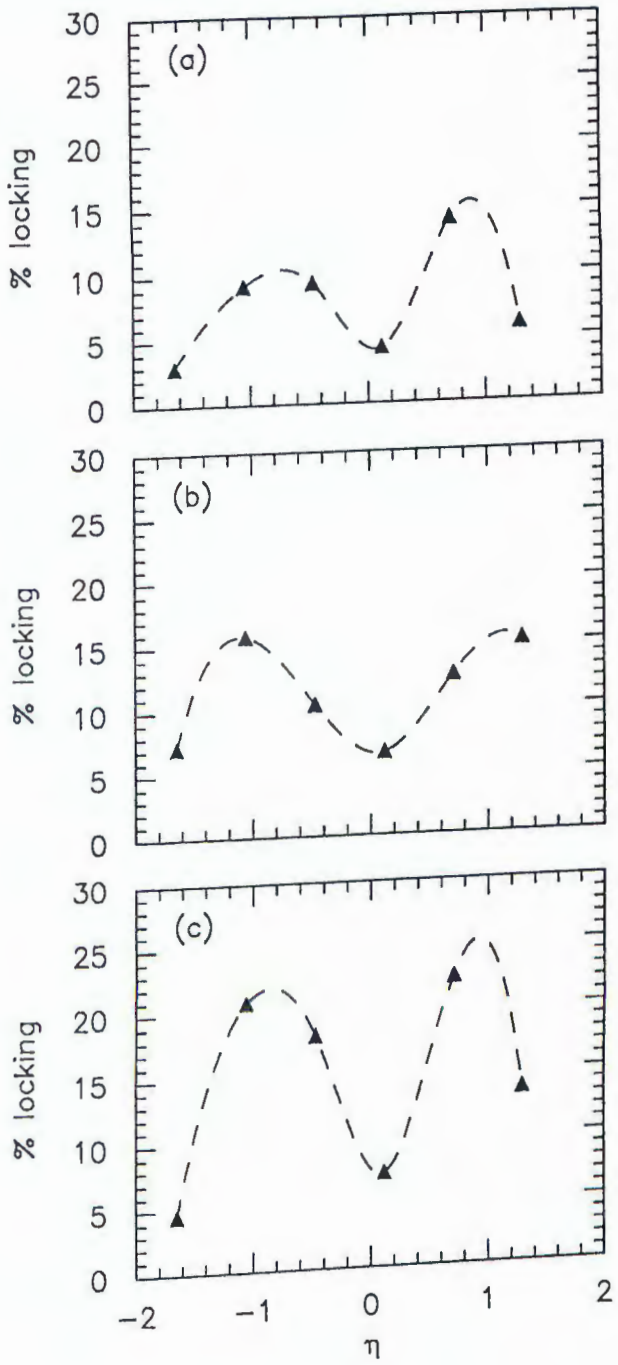

Fig. 6.20. Phase locking of the incoherent velocity flow field with the vortex shedding: (a) $\langle u'^2 \rangle$, (b) $\langle v'^2 \rangle$, and (c) $\langle w'^2 \rangle$.

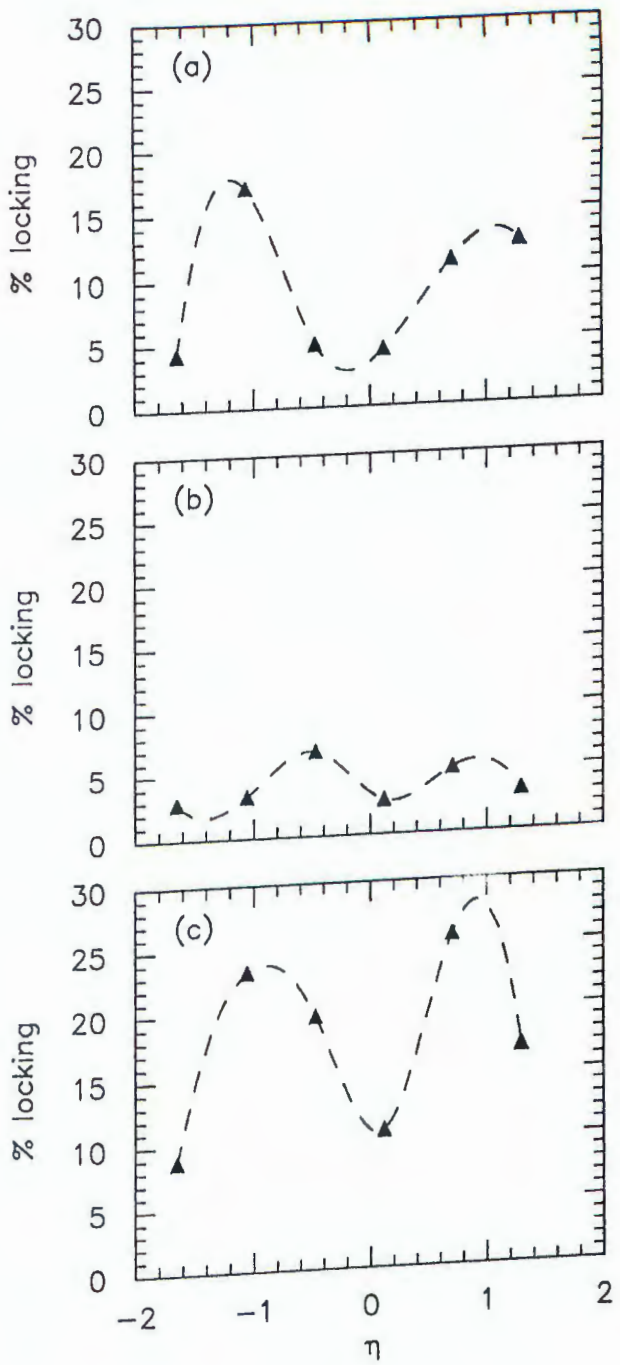

Fig. 6.21. Phase locking of the incoherent vorticity flow field with the vortex shedding: (a) $\langle \omega_x'^2 \rangle$, (b) $\langle \omega_y'^2 \rangle$, and (c) $\langle \omega_z'^2 \rangle$.

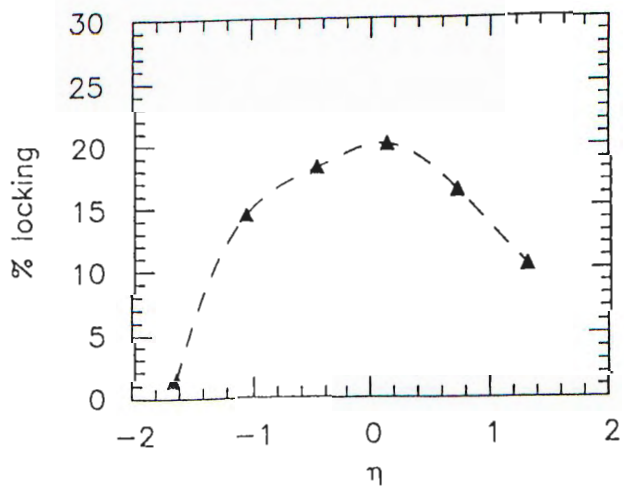

Fig. 6.22. Phase locking of the incoherent Reynolds shear stress field $\langle u'v' \rangle$ with the vortex shedding.

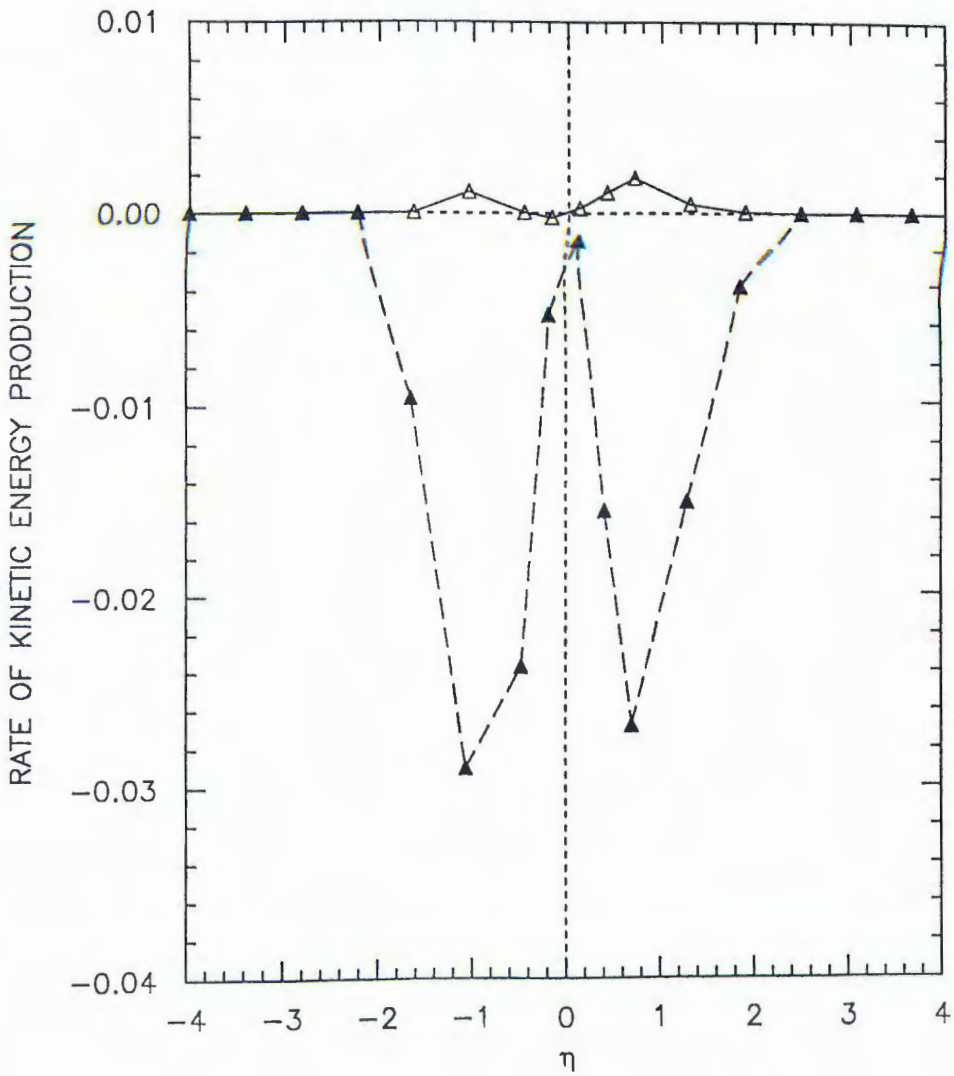

Fig. 7.1. Distributions of the rate of mean kinetic energy production by the mean velocity gradient. The open symbols are for production due to interaction with the coherent field, and the closed symbols are for the incoherent field.

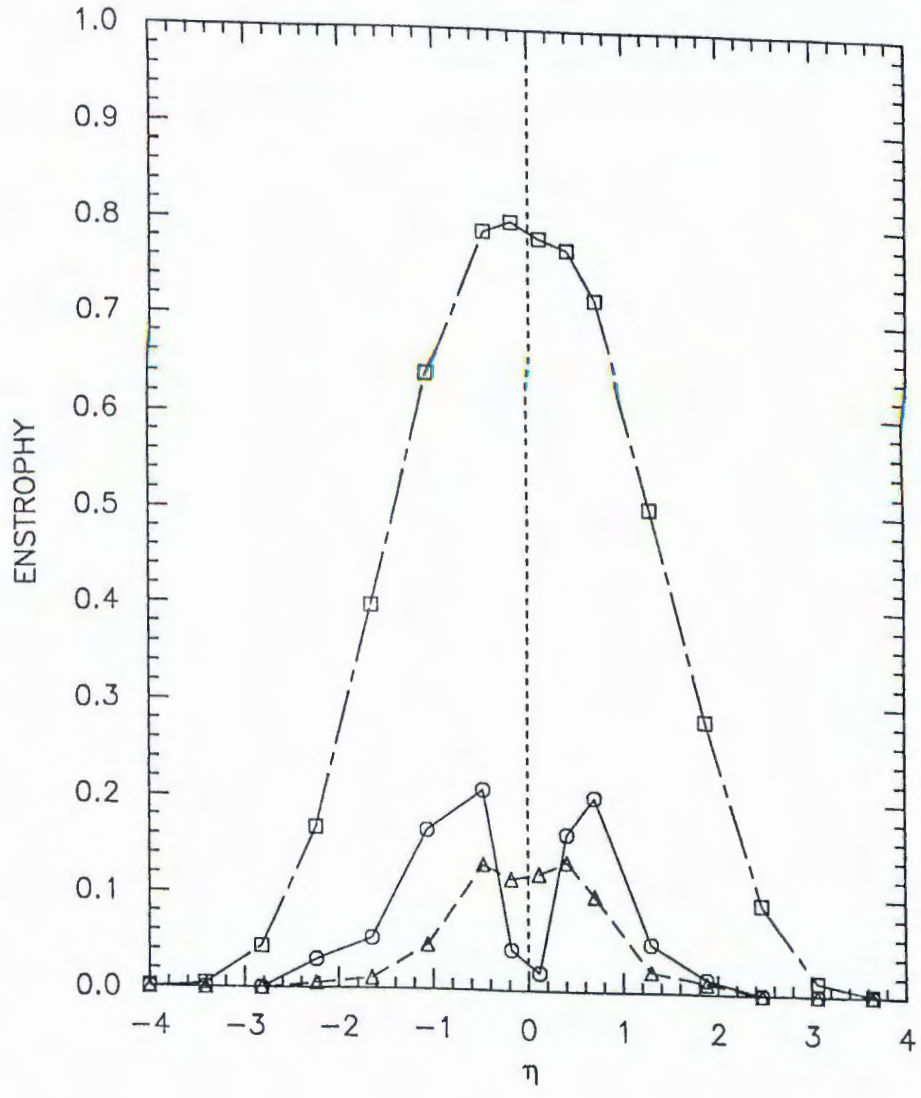

Fig. 7.2. Enstrophy distributions at x/d=30.
○, mean; △, coherent; □, incoherent/10.

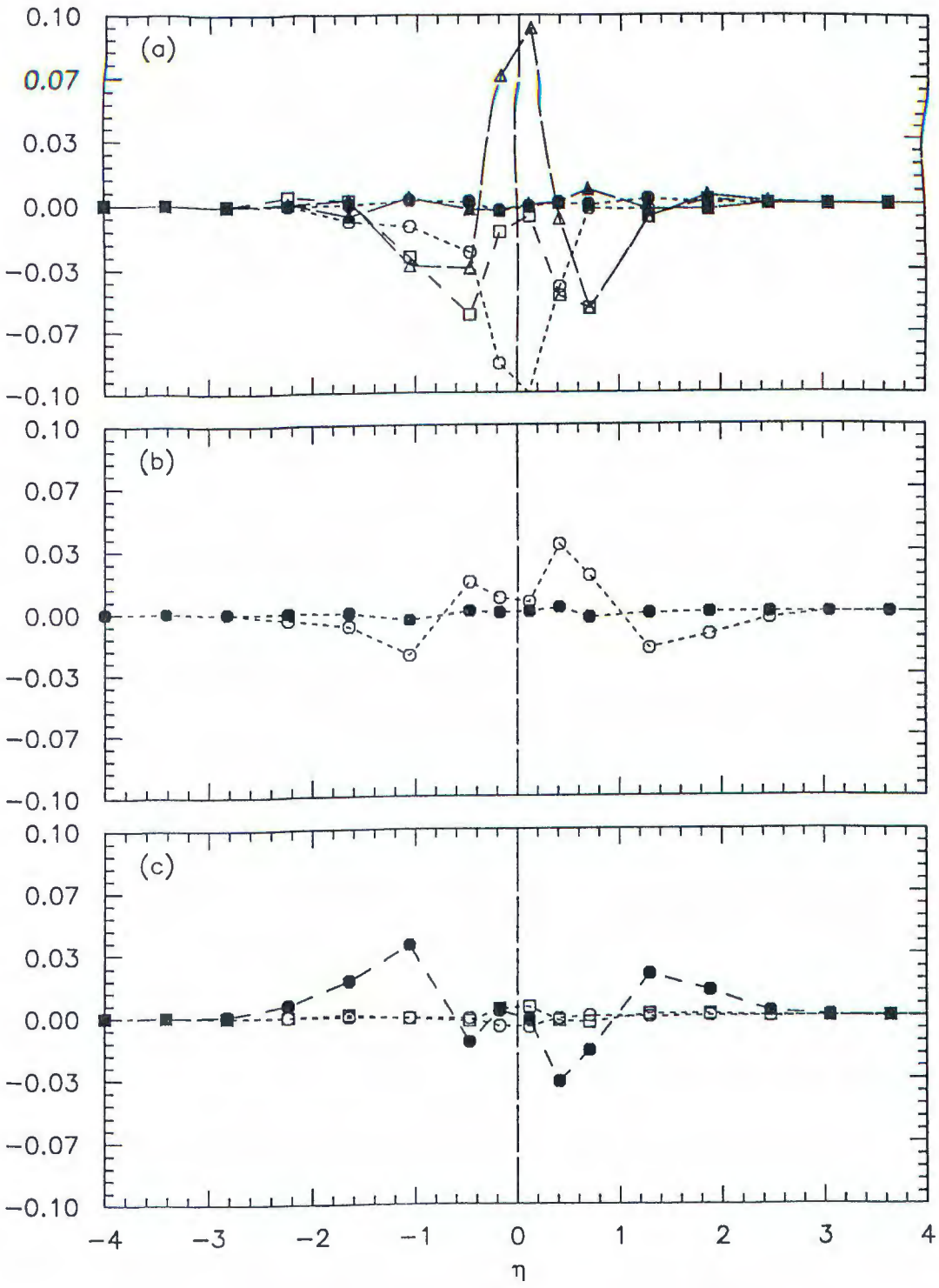

Fig. 7.3. Balance of the mean enstrophy at x/d=30.
(a) □, (1); ○, (2a); ●, (2b); △, (3a); ▲, (3b).
(b) ○, (5a); ●, (5b).
(c) □, (6); ○, (7); ●, residual.

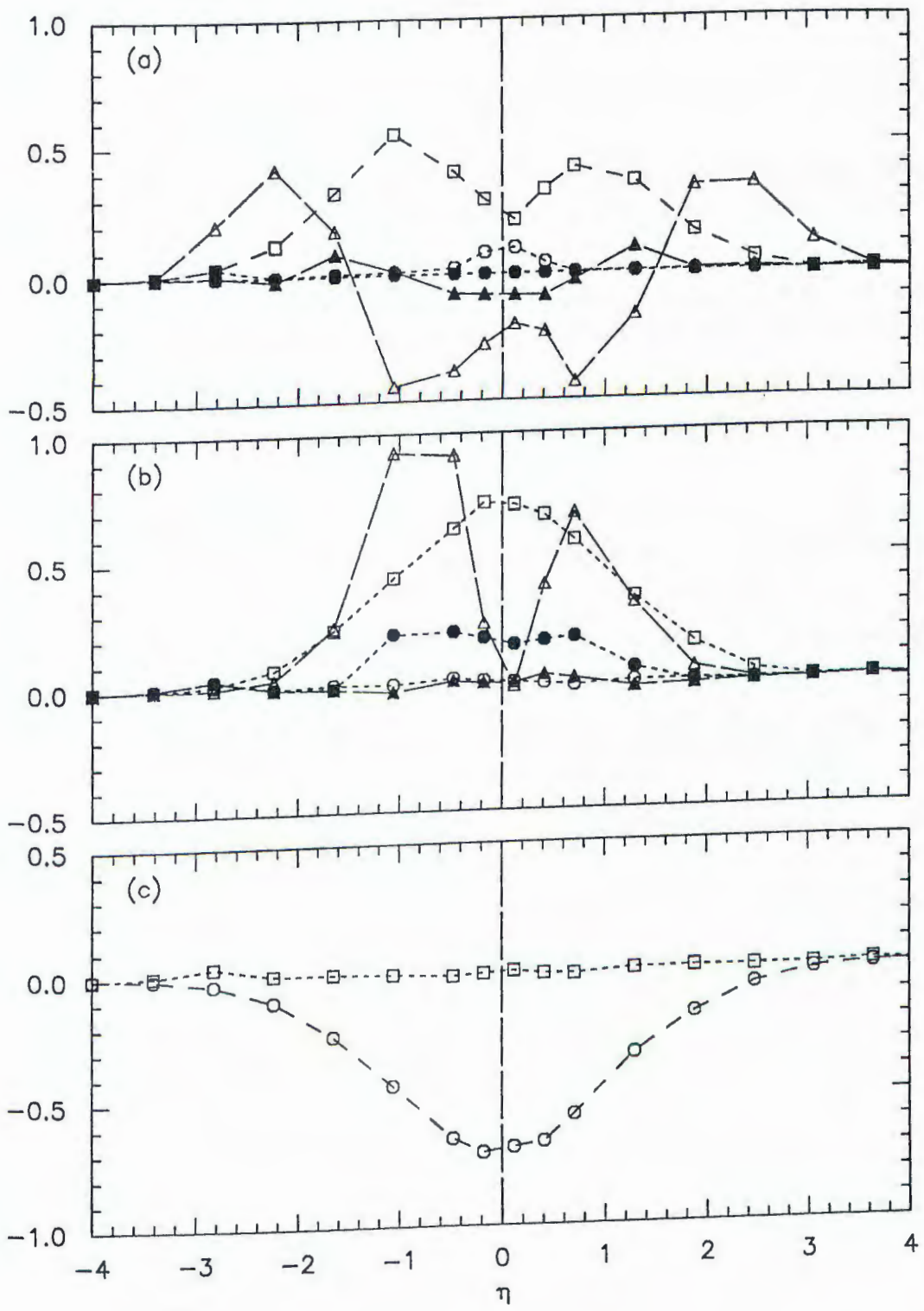

Fig. 7.4. Balance of the incoherent enstrophy at x/d=30.
(a) □, (1); ○, (2a); ●, (2b); △, (3a); ▲, (3b).
(b) □, (4a)/10; ○, (4b); ●, (4c); △, (5a); ▲, (5b).
(c) □, (6); ○, (dissipation rate and residual)/10.

REFERENCES

1. I.E. Alber, "Turbulent Wake of a Thin, Flat Plate," *AIAA J.* (1980), **18**, pp. 1044-1051.

2. J. Andreopoulos and P. Bradshaw, "Measurements of Interacting Turbulent Shear Layers in the Near-Wake of a Flat Plate," *J. Fluid Mech.* (1980), **100**, pp. 639-668.

3. R.A. Antonia, L.W.B. Browne and D.A. Shah, "Characteristics of Vorticity Fluctuation in a Turbulent Wake," *J. Fluid Mech.* (1988), **189**, pp. 349-365.

4. J.L. Balint, P. Vukoslavčević and J.M. Wallace, "The Transport of Enstrophy in a Turbulent Boundary Layer," Zoran Zarić Memorial Conference, Dubrovnik, May 1988.

5. J.L. Balint, J.M. Wallace and P. Vukoslavčević, "The Velocity and Vorticity Vector Fields of a Turbulent Boundary Layer. Part 2. Statistical Properties," *J. Fluid Mech.* (1991), **228**, pp. 53-86.

6. P.S. Bernard and B.S. Berger, "A Method for Computing Three-Dimensional Turbulent Flows," *SIAM J. Appl. Math.* (1982), **42**, pp. 453-470.

7. D.K. Bisset, R.A. Antonia and D. Britz, "Structure of Large-Scale Vorticity in a Turbulent Far Wake," *J. Fluid Mech.* (1990), **168**, pp. 463-482.

8. P. Bradshaw, An Introduction to Turbulence and its Measurements, Pergamon Press, pp. 106-131, 1975.

9. L.W.B Browne, R.A. Antonia and D.K. Bisset, "Coherent Structures in the Far Field of a Turbulent Wake," *Phys. Fluids* (1986), **29**, pp. 3612-3617.

10. B. Cantwell and D. Coles, "An Experimental Study of Entrainment and Transport in the Turbulent Near Wake of a Circular Cylinder," *J. Fluid Mech.* (1983), **136**, pp. 321-374.

11. A. Cenedese, G.P. Romano and F. Di Felice, "Experimental Testing of Taylor's Hypothesis by L.D.A. in Highly Turbulent Flow," *Experiments in Fluids* (1991), **11**, pp. 351-358.

12. J.M. Cimbala, H.M. Nagib and A. Roshko, "Large Structure in the Far Wakes of Two-Dimensional Bluff Bodies," *J. Fluid Mech.* (1988), **190**, pp. 265-298.

13. T. Dracos, M. Kholmyansky, E. Kit and A. Tsinober, "Some Experimental Results on Velocity-Velocity Gradients Measurements in Turbulent Grid Flows," Topological Fluid Mechanics, ed. by H. K. Moffatt & A. Tsinober, pp. 564-584, Cambridge, 1989.

14. K. Döbbeling, B. Lenze and W. Leuckel, "Basic Considerations Concerning the Construction and Usage of Multiple Hot-Wire Probes for Highly Turbulent Three-Dimensional Flows," *Meas. Sci. Technol.* (1990), **1**, pp. 924-933.

15. H. Eckelmann, S.G. Nychas, R.S. Brodkey and J.M. Wallace, "Vorticity and Turbulence Production in Pattern Recognized Turbulent Flow Structures," *Phys. Fluids* (1977), **20**, pp. 225-231.

16. Eisenlohr, H. and H. Eckelmann, "Vortex Splitting and its Consequences in the Vortex Street Wake of Cylinders at Low Reynolds Number," *Phys. Fluids* A (1989), **1** (2), pp. 189-192.

17. G. Fabris, "Higher-Order Statistics of Turbulent Fluctuations in the Plane Wake," *Phys. Fluids* (1983), **26** (6), pp. 1437-45.

18. J.F. Foss, "Advanced Techniques for Transverse Vorticity Measurements," Proc. of the 7th Bienial Symp. on Turbulence, 1977.

19. J.F. Foss and J.M. Wallace, "The Measurement of Vorticity in Transitional and Fully Developed Turbulent Flows," in *Advances in Fluid Mechanics Measurements* (1989), ed. by M. Gad-el-Hak. Lecture Notes in Engineering, Vol. 45, pp. 263-321. Springer.

20. J. Gershfeld, W.K. Blake and C.W. Kinsley, "Trailing Edge Flows and Aerodynamic Sound," AIAA, ASME, ASCE, SIAM, APS 1st National Fluid Dynamics Congress, Cincinnati, Ohio, paper 88-3826-CP, July 1988.

21. H.T. Grant, "Large Eddies of Turbulent Motion," *J. Fluid Mech.* (1958), **4**, pp. 149-190.

22. A. Haji-Haidari and C.R. Smith, "Development of the Turbulent Near-Wake of a Tapered Thick Flat Plate," *J. Fluid Mech.* (1988), **189**, pp. 135-163.

23. M. Hayakawa, and A.K.M.F. Hussain, "Three-Dimensionality of Organized Structures in a Plane Turbulent Wake," *J. Fluid Mech.* (1989), **206**, pp. 375-404.

24. T.T. Huang, L.P. Purtell and Y.T. Lee, "Turbulence Characteristics of Trailing-Edge Flows on Thick and Thin Hydrofoils," Proc. of the 4th Symp. of Numerical and Physical Aspects of Aerodynamics Flows, CSU Long Beach, 1989.

25. A.K.M.F. Hussain, "Coherent Structures–Reality and Myth," *Phys. Fluids* (1983) **26**(10), pp. 2816-2850.

26. A.K.M.F. Hussain and M. Hayakawa, "Eduction of Large-Scale Organized Structures in a Turbulent Plane Wake," *J. Fluid Mech.* (1987), **180**, pp. 193-229.

27. B.M. Jones, "The Measurements of Profile Drag by the Pitot Traverse Method," ARC R&M 1688, (1936).

28. F.E. Jorgensen, "Directional Sensitivity of Wire and Fiber Film Probes," DISA Inform. **11**, pp. 31-37, 1971.

29. E.G. Kastrinakis, H. Eckelmann and W.W. Willmarth, "Influence of the Flow Velocity on a Kovasznay-type Vorticity Probe," *Rev. Sci. Instrum.* (1979), **50**, pp. 759-767.

30. J.H. Kim and H. Fiedler, "Vorticity Measurements in a Turbulent Mixing Layer," Advances in Turbulence, Vol. 2, pp. 267-271, 1989.

31. J. Kim and P. Moin, "The Structure of the Vorticity Field in Turbulent Channel Flow. Part 2. Study of Ensemble-Averaged Fields," *J. Fluid Mech.* (1986), **162**, pp. 339-363.

32. A.L. Kistler, "The Vorticity Meter," 1952 M.S. Thesis, Johns Hopkins University.

33. L.S.G. Kovasznay, "Turbulence Measurements," in *Physical Measurements in Gas Dynamics and Combustion* (1954), ed. by R.W. Landenbuerg, B. Lewis, R.N. Pease & H.S. Taylor. Vol. 10, pp. 213. Princeton University Press.

34. D.B. Lang and P.E. Dimotakis, "Measuring Vorticity Using the Laser Doppler Velocimeter," *Bull. Am. Phys. Soc.* (1982), **27**, p. 1166.

35. I.C. Lekakis, R.J. Adrian and B.G. Jones, "Measurement of Velocity Vectors with Orthogonal and Non-Orthogonal Triple-Sensor Probes," *Experiments in Fluids* (1989), **7**, pp. 228-240.

36. B. Marasli, F.H. Champagne and I. Wygnanski, "Effect of Travelling Waves on the Growth of a Plane Turbulent Wake," *J. Fluid Mech.* (1992), **235**, pp. 511-528.

37. B. Marasli, P.N. Nguyen and J.M. Wallace, "The Vortical Structure of the Near Wake of a Circular Cylinder," *Experiments in Fluids* (1993), **15**, pp. 209-218.

38. G.E. Mattingly and W.O. Criminale, "The Stability of an Incompressible Two-Dimensional Wake," *J. Fluid Mech.* (1972), **51**, pp. 233-272.

39. E. Meiburg and J.C. Lasheras, "Experimental and Numerical Investigation of the Three-Dimensional Transition in Plane Wakes," *J. Fluid Mech.* (1988), **190**, pp. 1-37.

40. E.W. Miner, T.F. Swean, Jr., R.A. Handler and R.I. Leighton, "Evaluation of the Near-Wall k-ϵ Turbulence Model by Comparison with Direct Simulations of Turbulent Channel Flow," NRL Memorandum Report 6499, 1989.

41. J.C. Mumford, "The Structure of the Large Eddies in Fully Developed Turbulent Shear Flows. Part 2. The Plane Wake," *J. Fluid Mech.* (1983), **137**, pp. 447-456.

42. R. Narasimha and H. Prabhu, "Equilibrium and Relaxation in Turbulent Wakes," *J. Fluid Mech.* (1972), **54**, pp. 1-17.

43. P.N. Nguyen and J.J. Gorski, "Navier-Stokes Analysis of Turbulent Boundary-Layer and Wakes for 2-D Lifting Bodies," Proc. of the 18th Naval Hydrodynamics Symp., University of Michigan, 1990.

44. P.N. Nguyen, B. Marasli and J.M. Wallace, "The Vortical Structure of the Near Wake of a Circular Cylinder," ASME Separated Flow Symposium, Washington, D.C., June 1993.

45. L. Ong, "Visualization of Turbulent Flows with Simultaneous Velocity and Vorticity Measurements," 1992 PhD Dissertation, University of Maryland.

46. S.-R. Park and J.M. Wallace, "The Influence of Velocity Gradients on Turbulence Properties Measured with Multi-Sensor Hot-Wire Probes," Proc. of the 13th Symp. on Turbulence (1992), University of Missouri, Rolla.

47. F.R. Payne and J.L. Lumley, "Large Eddy Structure of the Turbulent Wake behind a Circular Cylinder," *Phys. Fluids* (1967), pp. S194-S196.

48. U. Piomelli, J.L. Balint and J.M. Wallace, "On the Validity of Taylor's Hypothesis for Wall-Bounded Turbulent Flows," *Phys. Fluids* A (1989), **1**, pp. 609-611.

49. P.J. Pot, "Measurements in a 2-D Wake and in a 2-D Wake Merging into a Boundary Layer," Data Report NLR TR-79063 U, the Netherlands, 1979.

50. W.H. Press, B.P. Flannery, S.A. Teukolsky and W.T. Vetterling, Numerical Recipes, Cambridge University Press, pp. 307-312, 1990.

51. B.R. Ramaprian, V.C. Patel and M.S. Sastry, "The Symmetric Turbulent Wake of a Flat Plate," *AIAA J.* (1982), **20**, pp. 1228-1235.

52. W.C. Reynolds and A.K.M.F. Hussain, "The Mechanics of an Organized Wave in Turbulent Shear Flow. Part 3. Theoretical Models and Comparison with Experiments," *J. Fluid Mech.* (1972), **54**, pp. 263-288.

53. A. Roshko, "On the Development of Turbulent Wakes from Vortex Streets," NACA 1191, 1954.

54. M. Samet and S. Einav, "A Hot-Wire Technique for Simultaneous Measurement of Instantaneous Velocities in 3-D Flows," *J. Phys. E: Sci. Instrum.* (1987), **20**, pp. 683-690.

55. H. Schlichting, Boundary Layer Theory, McGraw-Hill, pp. 590-610, 1960.

56. Y. Suzuki and N. Kasagi, "Evaluation of Hot-Wire Measurements in Wall Shear Turbulence Using a Direct Numerical Simulation Database," *Experimental Thermal and Fluid Science* (1992), **5**, pp. 69-77.

57. M. Tagawa,T. Tsuji and Y. Nagano, "Evaluation of X-Probe Response to Wire Separation for Wall Turbulence Measurements," *Experiments in Fluids* (1992), **12**, pp. 413-421.

58. G. I. Taylor, "The Spectrum of Turbulence," Proceedings of the Royal Society of London (1938), Series A, Vol. 164, p.476.

59. H. Tennekes and J.L. Lumley, A First Course in Turbulence, The MIT Press, pp. 75-93, 1972.

60. A.A. Townsend, "The Fully Developed Turbulent Wake of a Circular Cylinder," *Aust. J. Sci. Res.* (1949), **2**, p. 451.

61. A.A. Townsend, "Flow Patterns of Large Eddies in a Wake and in a Boundary Layer," *J. Fluid Mech.* (1979), **95**, pp. 515-537.

62. P. Vukoslavčević and J.M. Wallace, "Influence of Velocity Gradients on Measurements of Velocity and Streamwise Vorticity with Hot-Wire X-Array Probes," *Rev. Sci. Instrum.* (1981), **52** (6), pp. 869-879.

63. P. Vukoslavčević, J.M. Wallace and J.L. Balint, "The Velocity and Vorticity Vector Fields of a Turbulent Boundary Layer. Part 1. Simultaneous Measurement by Hot-Wire Anemometry," *J. Fluid Mech.* (1991), **228**, pp. 25-51.

64. J.M. Wallace, "Methods of Measuring Vorticity in Turbulent Flows," *Experiments in Fluids* (1986), **4**, pp. 61-71.

65. J.M. Wallace and R.S. Brodkey, "Reynolds Stress and Joint Probability Density Distributions in the $u - v$ Plane of a Turbulent Channel Flow," *Phys. Fluids* (1977), **20** (3), p. 351.

66. W.W. Wassmann and J.M. Wallace, "Measurement of Vorticity in Turbulent Shear Flow," *Bull. Am. Phys. Soc.* (1979), **24**, p. 1142.

67. W.W. Willmarth, in Advances in Applied Mechanics, ed. by C.S. Yi, Academic, New York, Vol. 15, p. 159, 1975.

68. C.H.K. Williamson, "The Existence of Two Stages in the Transition to Three-Dimensionality of a Cylinder Wake," *Phys. Fluids* (1988), **31** (11), pp. 3165-3168.

69. I. Wygnanski, F. Champagne and B. Marasli, "On the Large-Scale Structures in 2-D, Small Deficit Turbulent Wakes," *J. Fluid Mech.* (1986), **168**, pp. 31-71.

70. H. Yamada, Y. Kuwata, H. Osaka, and Y. Kageyama, "Turbulence Measurements in a Two-dimensional Turbulent Wake," Technical Reports of the Yamaguchi University, **2** (4), Japan, 1980.